Universidad de Granada
Programa Oficial de Doctorado en Química
Nucleation in small volumes and confinement
Tesis Doctoral
Isaac Rodríguez Ruiz

INSTITUTO ANDALUZ DE CIENCIAS DE LA TIERRA

CONSEJO SUPERIOR DE INVESTIGACIONES CIENTÍFICAS

Universidad de Granada

Nucleation in small volumes and confinement

Isaac Rodríguez Ruiz

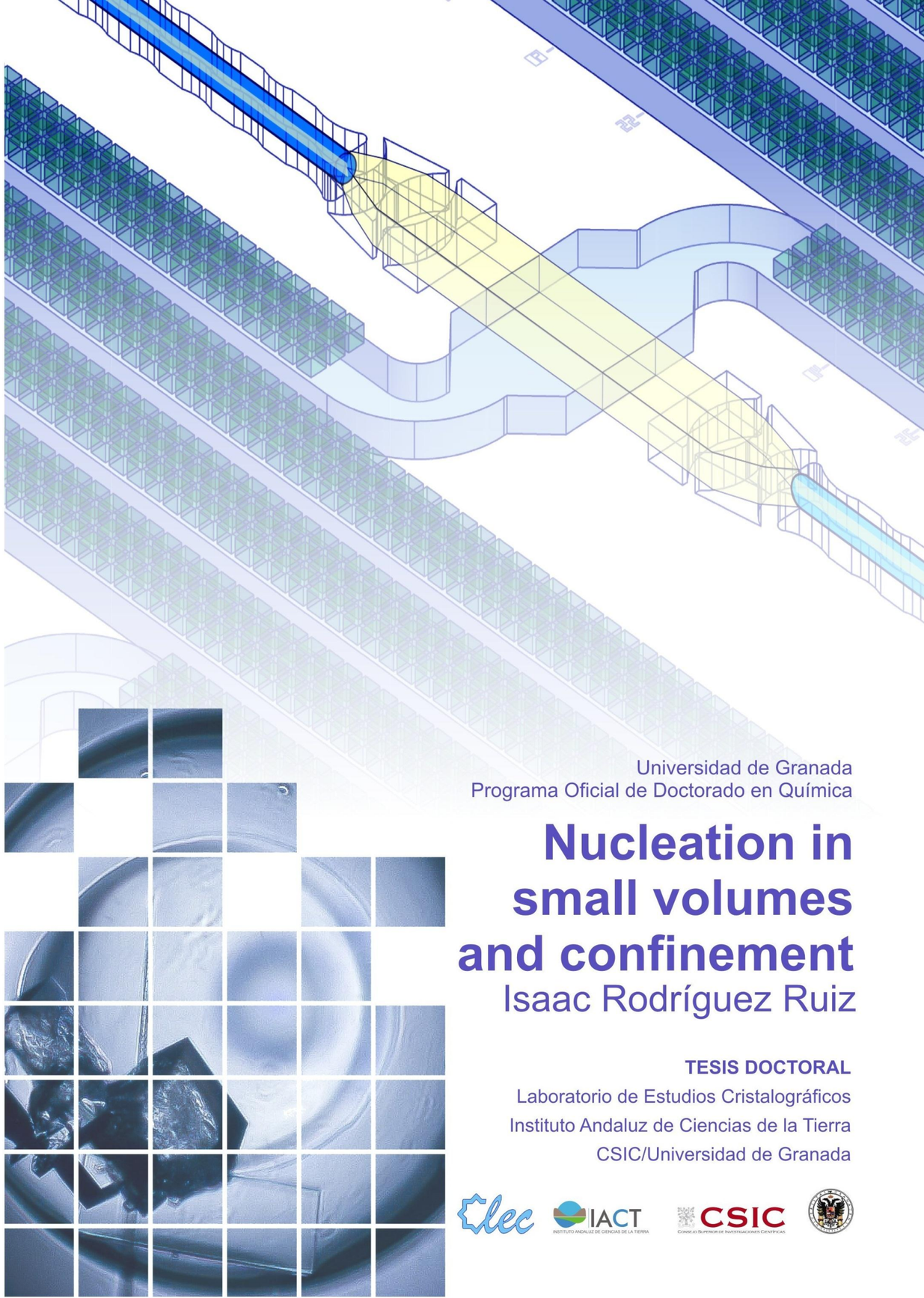

Universidad de Granada
Programa Oficial de Doctorado en Química

Nucleation in small volumes and confinement

Isaac Rodríguez Ruiz

TESIS DOCTORAL

Laboratorio de Estudios Cristalográficos
Instituto Andaluz de Ciencias de la Tierra
CSIC/Universidad de Granada

Editor: Universidad de Granada. Tesis Doctorales
Autor: Isaac Rodríguez Ruiz
ISBN: 978-84-9163-185-9
URI: http://hdl.handle.net/10481/46066

Laboratorio de Estudios Cristalográficos

Instituto Andaluz de Ciencias de la Tierra

CSIC – Universidad de Granada

Nucleation in small volumes and confinement

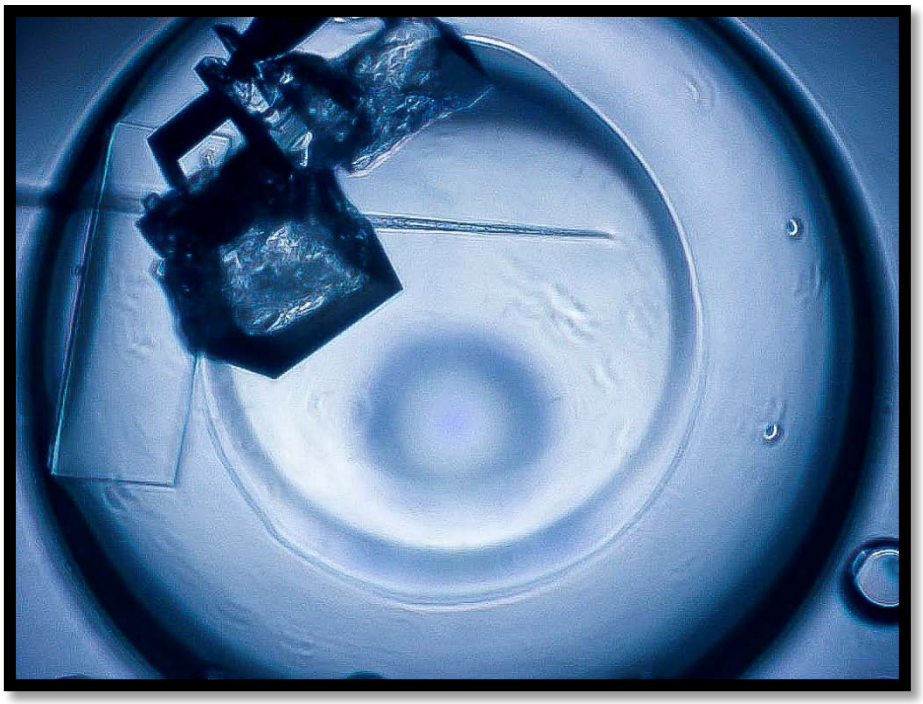

TESIS DOCTORAL

Isaac Rodríguez Ruiz

Laboratorio de Estudios Cristalográficos
Instituto Andaluz de Ciencias de la Tierra
CSIC – Universidad de Granada

Nucleation in small volumes and confinement

Isaac Rodríguez Ruiz

TESIS DOCTORAL

GRANADA

2013

Laboratorio de Estudios Cristalográficos
Instituto Andaluz de Ciencias de la Tierra
CSIC – Universidad de Granada

Memoria presentada para optar al Grado de Doctor

dentro del Programa Oficial de Doctorado en Química de la Universidad de Granada

El doctorando, Isaac Rodríguez Ruiz y los directores de la tesis, Juan Manuel García Ruiz y Jaime Gómez Morales garantizamos, al firmar esta tesis doctoral, que el trabajo ha sido realizado por el doctorando bajo la dirección de los directores de la tesis y hasta donde nuestro conocimiento alcanza, en la realización del trabajo, se han respetado los derechos de otros autores a ser citados, cuando se han utilizado sus resultados o publicaciones.

Granada, 15 de Julio de 2013

Fdo: Isaac Rodríguez Ruiz

Ingeniero Químico por la Universidad de Granada

Directores de la tésis:

Fdo:
Juan Manuel García Ruiz
Profesor de investigación
Instituto Andaluz de Ciencias de la Tierra
Laboratorio de Estudios Cristalográficos
CSIC-UGR

Fdo:
Jaime Gómez Morales
Científico titular
Instituto Andaluz de Ciencias de la Tierra
Laboratorio de Estudios Cristalográficos
CSIC-UGR

"Whatever you can do, or dream you can do, begin it.
Boldness has genius, power, and magic in it"

Johann Wolfgang von Goethe

Acknowledgements

This Ph.D. thesis has been carried out thanks to a predoctoral (JAE-Pre) research contract within the *Junta para la Ampliación de Estudios* of CSIC, co-founded by the European Social Found (ESF). The work on this thesis has been carried out in four different research laboratories: *Laboratorio de Estudios Cristalográficos "LEC"* of *Instituto Andaluz de Ciencias de la Tierra* (*CSIC*- University of Granada), *"Grupo de Transductores Químicos"* of *Barcelona Microelectronics Institute* , *"IMB-CNM"* (*CSIC)*, *Sources et Sondes Ponctuelles* department of the *Centre Interdisciplinaire de Nanoscience de Marseille*, "*CINaM*" (*CNRS),* and the *Dipartimento di Chimica "G. Ciamician"* belonging to the Italian *Alma Mater Studiorum Università di Bologna.*

The present thesis has been developed within the framework of the projects: *"Factoría de cristalización"*, CSD2006-00015 (Consolider-Ingenio) of *MEC-CSIC*-Junta de Andalucía, *"Enfrentar Problemas Geológicos Clave desde una perspectiva de Crecimiento Cristalino"*, CGL2010-16882 of *MICINN*, *"Multifunctional drug-loaded antibody-targeted inorganic nanoparticles for biomedical use"*, IT2009-0028 of MICINN, *"Cristalización y funcionalización de apatitos nanocristalinos. Relevancia en la formación de la nanoestructura ósea y en aplicaciones terapéuticas"*, MAT2011-28543 of *MINECO*, *"Producción y caracterización de cristales de proteínas reforzados y entrecruzados con aplicaciones biotecnológicas"*, BIO2010-16800, of MICINN and *"Técnología Cristalográfica: contribuyendo al desarrollo socioeconómico en y desde Andalucía"* of Junta de Andalucía.

My work would not have been possible without the help and contribution of several people to whom I would like to express my deepest gratitude.

First of all, I would like to thank Prof. Juan Manuel García Ruiz for having accepted me in his research group, for placing his trust in me, and for unconditionally offering me his support and direction along these years.

I am gratefully indebted to Dr. Jaime Gómez Morales for his continuous supervision and advice, and for the confidence he has always had in my work. I am sure that without his help this thesis could hardly have been possible.

My sincere appreciation goes to Dr. Fermín Otálora Muñoz for his helping hand, especially during the first year of the Ph.D. I would also like to extend my appreciation to Dr. Germán Luzón González, from University of Granada, for his continuous assistance.

I want to express my most sincere thanks to Dr. José Manuel Delgado López and Dr. Alexander Van Driessche who continuously helped me during this work. They both are brilliant scientist and great teachers from whom I have learned a lot about science and scientific world in general. I would also like to express my gratitude to Dr. Luis David Patiño López and Dr. José Antonio Gavira Gallardo for their constant support and for showing continuous and truly interest in my work. I want also to extend my sincere gratitude to Dr. Duane Choquesillo Lazarte for his always convenient suggestions. From all of them I always got words of encouragement and support in those days where things were complicated.

Special thanks to Miguel Durán Olivencia for our long conversations at untimely hours. Because of them today I ignore a bit less about nucleation. Also thanks to Pilar Ramírez García for her valuable help and technical assistance during the last period of this work. Of course I also thank to the rest of *LEC* group, so many competent and devoted partners, for their companion, friendship and daily help, which always made my work a little bit easier.

I acknowledge Dr. Stéphane Veesler, from *CINaM*, for opening to me the doors of his laboratories and his home in Marseille for two consecutive years, and for his advices and attention to my work. Also my sincere gratitude to Dr. Andreu Llobera Adán for demonstrating an unquenchable energy and for all the resources and facilities he has offered to my disposal at *IMB-CNM.* I would also like to thank Dr. Michele Iafisco from *Università di Bologna* for his always clever observations and suggestions and for his

hospitality during our stay in Bologna. Thanks to all my co-authors (in the recently published, but also in the future publications related with this work) as well, for their interesting and always constructive advices, and for their dedication to this work.

Finally last, but not least, I would like to thank my beloved family and Naïma for their unconditional love, patience, caring and determined support along these years. This work is gratefully dedicated to them.

Nucleation in Small Volumes and Confinement

Abstract

The formation of a crystalline phase from solution is a key subject in a wide range of interdisciplinary fields, from materials and pharmaceutical research to biochemistry, molecular biology or physical chemistry, among many others. In most of those fields, the studies performed in small volumes are motivated by four main interests: low (high added value) reagents consumption, emulation of crystallization conditions in natural or biological environments, location of crystallization events in a confined space for their study, and the study and exploitation of the effects that confinement itself exerts in the precipitating material. Along the present thesis, we have explored the application of small volumes for the study of different systems and substances of interest:

In **chapter 3** we have taken advantage of small volumes to study gypsum ($CaSO_4 \cdot 2H_2O$) nucleation at low supersaturations, and in absence of stirring. We have applied the whole classical nucleation theory model for the interpretation of our own experimental data, obtained from studies in small 100 µL vials and low supersaturations, and to re-interpret values reported in literature, in large volumes and higher supersaturations, with the aim of comparison.

Chapter 4 evaluates the precipitation of calcium phosphates in large volumes, by batch thermal-decomplexing methods, and in small volumes, at microliter scale, by pH-decomplexing methods (with the help of the "*crystallization mushroom*" to perform droplet vapour diffusion experiments), trying to obtain biomimetic and biocompatible apatite nanoparticles (whose composition of the model stoichiometric compound – hydroxyapatite – is $Ca_5(OH)(PO4)_3$) for biomedical applications.

In **chapter 5** we have applied microfluidic and microinjection techniques to investigate the effects of confinement at nano-and pico-volumes in two different systems of interest: a) Evaporation of sodium chloride (NaCl) solutions in nano- and picoliter

droplets, as a model system to understand natural crystallization conditions, i.e. in the small pores and cracks of stone and other building materials, in order to understand the mechanisms of degradation of buildings, statuary and cultural heritage, in general, by the action of weathering and pollution. b) Calcium carbonate ($CaCO_3$) nucleation and phase transition in small volumes and medium to high supersaturations due to the great interest of calcium carbonate in industrial and pharmaceutical applications, and its starring role in nature and biomineralization processes.

Finally, **chapter 6** is devoted to the development of new technologies for applied crystallization studies requiring low consumption of reactants and special design characteristics. Spectrophotometric detection systems were implemented in the design of microfluidic systems with the help of optical microlenses and fiber optics inserts, and a low cost procedure for obtaining solvent-resistant microfluidic structures is presented, for the study of nucleation of small organic molecules in nanoliter volumes. This chapter concludes with some outlooks concerning the logical continuation of the present work and, in addition, a microfluidic solid base reactor for enzymatic catalytic reactions, using enzyme crystals as catalysts, is designed and presented.

KEYWORDS: scaling down, nucleation, microfluidics, confinement, biomineralization.

Resumen

La cristalización en disolución es objeto de interés para una gran variedad de áreas científicas y tecnológicas interdisciplinares, tales como la ciencia de materiales, la investigación farmacéutica, la bioquímica y la biología molecular, o la química-física, entre muchas otras. En todos estos campos, el uso de pequeños volúmenes en la realización de estudios de cristalización viene motivado por cuatro intereses principales: la minimización del consumo de reactivos de alto valor añadido, la simulación de condiciones de cristalización en entornos naturales o biológicos, la localización de los eventos de cristalización en espacios confinados para su estudio, y el propio estudio y aprovechamiento de los efectos que este confinamiento ejerce en la sustancia precipitada. A lo largo de esta tesis hemos investigado la aplicación de pequeños volúmenes en el estudio de la cristalización en diferentes sistemas y sustancias de interés:

El **capítulo 3**, aprovecha las ventajas que ofrecen los pequeños volúmenes para estudiar la nucleación de yeso ($CaSO_4 \cdot 2H_2O$) a bajas sobresaturaciones y en ausencia de agitación mecánica de la disolución. Aplicando la teoría clásica de la nucleación en su forma íntegra, y con la intención de realizar una comparativa, se han interpretado los datos experimentales obtenidos (para estudios realizados en viales de 100 µL, en las condiciones de sobresaturación y mezcla anteriormente citadas), y se han reinterpretado los resultados experimentales publicados con anterioridad para estudios realizados en grandes volúmenes y mayores sobresaturaciones.

En el **capítulo 4** se evalúa la precipitación de fosfatos de calcio a partir de disoluciones metaestables a través de dos sistemas diferenciados: en grandes volúmenes, utilizando métodos de descomplejación térmica en batch, y en pequeños volúmenes, en el rango de microlitros, mediante descomplejación por variación de pH, con la ayuda de la "*seta de cristalización*" (dispositivo diseñado para realizar experimentos de difusión de vapor en gotas). El propósito de esta evaluación es la de explorar métodos para la obtención de nanopartículas biomiméticas y biocompatibles de apatitos (cuya fórmula

estequiométrica para su compuesto modelo – hidroxiapatito – es $Ca_5(OH)(PO_4)_3$), para su uso en aplicaciones biomédicas.

A lo largo del **capítulo 5,** se aplican distintas técnicas de microfluídica y de microinyección, para investigar los efectos que el confinamiento en nano- y picovolúmenes ejerce en dos sistemas de enorme interés: a) La evaporación de cloruro sódico (NaCl) en nano- y pico-gotas, con la aplicación hacia una mayor comprensión de los mecanismos naturales de cristalización en los pequeños poros y grietas de las rocas y de diferentes materiales de construcción. El estudio nos perimte profundizar en los mecanismos de degradación de las construcciones arquitectónicas, estatuas, y patrimonio cultural en general, expuestos a la intemperie y a la polución. b) La nucleación y transición de fase del carbonato cálcico ($CaCO_3$), en el mismo rango de volúmenes, y a sobresaturaciones medias y altas, debido a su gran interés en muchas aplicaciones industriales y farmacéuticas, así como por su papel protagonista en determinados procesos de biomineralización naturales.

Finalmente, el **capítulo 6** está dedicado al desarrollo de nuevas tecnologías, enfocadas a la elaboración de estudios de cristalización aplicados que requieren un bajo consumo de reactivos y unas características de diseño especiales. Se han implementado sistemas de detección espectrofotométrica en el diseño de distintos sistemas de microfluídica, mediante el uso de microlentes ópticas e inserción de fibras ópticas. Asimismo, se ha desarrollado un procedimiento de bajo coste para la fabricación de estructuras microfluídicas resistentes a la corrosión por disolventes orgánicos, para su aplicación en estudios de nucleación de pequeña molécula en nanovolúmenes. Este capítulo concluye con algunas perspectivas en relación con la continuación lógica del presente trabajo y, conjuntamente, se presenta el diseño y fabricación de un micro reactor de lecho fijo para reacciones catalíticas enzimáticas, usando como catalizadores cristales entrecruzados de proteína.

PALABRAS CLAVE: reducción a escala, nucleación, microfluídica, confinamiento, biomineralización.

Table of contents

CHAPTER 1

Introduction and objectives

CHAPTER 1

Introduction and objectives

Nucleation is a phenomenon that refers to the formation of a new phase (solid or liquid), precipitating from a gas, or a homogeneous solution or melt. Concretely, the subject of this thesis focuses its attention in nucleation phenomena occurring from solution, which represents, in its initial step, a first order phase transition, from a liquid (solution) to a solid phase. Such phase transition, crystallization from solution, requires the solution to be supersaturated with respect to the solid phase, in order to take place. Supersaturation is the driving force for nucleation to occur, and refers to a state in which the liquid (solvent) contains more dissolved solids (solute) than can ordinarily be accommodated at those conditions of pressure and temperature.

Depending on the way matter is internally structured in the nucleating phase, the new solid phase can be classified into two different categories. Amorphous materials exhibit an internal structure, in which its constituent units (atoms, molecules or ions) do not display order, being essentially indistinguishable from a liquid in its structure. On the other hand, crystalline materials are those whose constituent units are arranged in an ordered pattern extending in all three spatial dimensions. A crystalline material may display different possible spatial arrangements of its constituent units (phases), depending its stability on the crystallizing conditions, or also include solvent molecules in its structure (solvates).

Nucleation from solution, and concretely crystallization (nucleation of a crystalline phase) is a key issue in a wide range of interdisciplinary fields, as materials research, biochemistry, molecular biology, pharmaceutical research, or physical chemistry, among many others. From the chemical engineering point of view, crystallization is essentially a solid-liquid separation technique, and probably one of the oldest existing unit operations. Not going so far, sodium chloride, for example, has been manufactured by crystallization processes since ancient times. But crystallization is also found in nature, both occurring in the inorganic world (in geological and mineralogical formations) and living organisms,

through biomineralization processes, which consists in the selective extraction and uptake of elements from the local environment and their incorporation into functional (and partially inorganic) structures, under strict biological control [1]. Conversely to the interest of industries based in mass productions, nucleation and crystallization in nature frequently occur in small volumes. Whilst crystallization of many inorganic salts takes place in the pores, cracks, and small cavities of rocks and mineral structures [2, 3], many biomineralization processes happen in small and defined compartmented volumes, controlled by the presence of organic macromolecules in living organisms [1, 4].

Nowadays, the study of crystallization has reached a great importance in a wide variety of fields, from material and life sciences (where biomineralization attracts an important part of interest), to food industry or base chemicals. Crystallization is massively present in chemical industry wherein, at some stage, it is used as a method of production, purification or recovery of solid material. In this sense, crystallization is one of the best and cheapest methods available for the production of pure solids from impure solutions [5]. In contrast, it can also be present as an undesirable phenomenon to be avoided (for example, generating the obstruction of pipelines and membranes by scaling effect [6-11], which also occurs initially in confined spaces), or yielding byproducts to be separated from the material of interest [12, 13].

Crystallization is also important in alimentary industry, in many aspects of food preparation and storage, as well as in creating and refining the ingredients for foods and household products. Here, it is commonly used to purify sugars and fats [14, 15], and also is an important factor affecting the texture of things such as ice cream, fondant, and chocolate [16-18]. Additionally, controlling crystallization is important for maintaining the organoleptic properties when freezing foods [19]. Ice cream, for example is smooth due to the small size of the micron-sized ice crystals by which it is composed. Higher crystal sizes (caused by a low quality manufacture or a non proper storage) result in a non desired grainy texture.

For the pharmaceutical industry, crystallization is a major technological process for particle precipitation and, in addition, it plays an important role in defining the stability and drug release properties of the final dosage forms, depending on the crystallized phase [20]. Crystallization from solution is widely used for manufacturing bioactive drug substances and formulation excipients during final and also intermediate stages of purification and separation. Drug chemical purity and physical properties, such as solubility, crystal habit and size are defined by this process [20-22]. Consequently, different crystalline phases of a substance are responsible for a wide range of pharmaceutical formulation problems, such as bio-inequivalence [23], as well as chemical and physical instability of the solid drugs in their final dosage forms. The crystallization process requires considerable time and energy resources and defines such economical issues as the efficiency of solvent recycling, separation of waste (impurities) and consumption of raw materials. For that reason, in the early stages of research and development of new pharmacological compounds (when the added value of the new synthesis compounds is extremely high), the scaling down processes are essential for making more profitable investigations by working with the smallest possible volumes, reducing the consumption of reactants. Furthermore, as we will discuss lately below, the confinement of solutions in small volumes exerts effects in the stabilization of crystalline phases which would not nucleate and grow in higher volumes in the same conditions [24-26]. Hence, this property of small volumes also opens the possibility of characterizing not only the stable, but also the metastable precipitates, of pharmaceutical interest, permitting a higher protection of the business around the new products and its synthesis by creation of patents [27].

In life sciences, crystallization is one of the most important tools applied in structural biology, which is concerned in studying the functionality of biological macromolecules (especially proteins and nucleic acids) as a function of their three-dimensional shape and conformation. These conformations and 3D structure are determined through X-ray crystallography, by previously crystallizing the macromolecules. With this purpose, many different techniques have been developed during the last decades [28, 29] to obtain high

quality macromolecule crystals for crystallographic purposes, through the screening of the maximum possible crystallization conditions. Again, the reduction of reactant consumption for the crystallization screening process is a key factor that saves lots of money in the time consuming process of the expression, purification, and concentration of limited amounts of valuable proteins.

As it has been briefly shown, there are abundant and very diverse scientific, industrial, and economic interests, with direct applications, behind the necessity of a deeper comprehension of the mechanisms by which nucleation of a new phase takes place from solution. A few cases of relevance, which are also in relation with the work developed in this thesis are found in, for example, the degradation of buildings, statuary and cultural heritage, in general, by the effect of crystallization of salts in the pores and cracks of the constructing materials (natural stones or human manufactured materials)[3], the above mentioned scaling effect in industrial processes [6-9], the control of the physic-chemical properties of the precipitates, interesting for industrial and pharmaceutical applications [30-32], the importance of the mechanisms of bone and other hard tissues formation (biomineralization) [30, 33, 34] for the synthesis of biomimetic and biocompatible materials [35, 36], or the direct implications in protein structure resolution through X-ray crystallography [37, 38]. For all these cases, further insights into nucleation and crystal growth are a must.

Nucleation phenomena have been under theoretical investigation since late 19th century, when the first thermodynamic theories were implemented. Since then, the thermodynamic approach has been updated in many ways, and so the analytical techniques for detection of nucleation have also been improved. Several models have been applied in order to give an interpretation to the experimental observations. The next section of this introductory chapter will give a quick overview to the usual definition of a nucleation event, and the most extended theoretical approaches for nucleation, which are a necessary instrument for the analysis, comprehension and discussion of the experimental observations presented along the next chapters of the thesis.

Nucleation

1. Definition

Nucleation is the initiation of a phase change in a small region, such as the formation of a solid crystal from a liquid solution. It is a consequence of rapid local fluctuations on a molecular scale in a homogeneous phase that is in a state of metastable equilibrium. The mechanism by how a stable crystal nucleus is formed from solution is still unknown with certainty. To take a simplified example, the condensation of a supersaturated vapour to the liquid phase only occurs after the formation of microscopic droplets (condensation nuclei), on a condensing surface. However, as the vapour pressure at the surface of these micro droplets is very high, droplets tend to evaporate quickly, yet the surrounding vapour is supersaturated. New nuclei form while present ones evaporate, until finally stable droplets are formed either by coalescence or under very high vapour supersaturation conditions. To depict the formation of crystal nuclei is an even more difficult duty. Not only the aggregation of molecules/ions has to occur, opposing the tendency to redissolve, but molecules also have to become orientated into a fixed lattice to form a crystal. The number of molecules in a stable crystal nucleus can vary from about ten to several thousand, depending on the specie and supersaturation. Nonetheless, a stable nucleus could hardly result from the simultaneous collision of the required number of molecules, since this would constitute an extremely improbable event. More likely, ions or molecules in a solution would locally interact to form short-lived clusters in those regions of higher local supersaturation, which mostly will redissolve due to their instability. However, if the nucleus grows beyond a certain critical size, it will become stable under the non local, but average supersaturation conditions in the bulk of solution.

A vast majority of the existing nucleation theories are based in two assumptions: first, the supersaturated media where phase transition occurs, is characterized by an equilibrium cluster distribution, given by

$$N_n = N_1 \exp\left(\frac{\Delta G_{(n)}}{k_B T}\right) \tag{1.1}$$

where N_n represents the number or concentration of n-clusters (clusters consisting of n molecules), $\Delta G_{(n)}$ is the Gibbs free energy of formation of an n-cluster, k_B is the Boltzmann constant, and T is absolute temperature; second, the system is considered to be in a pseudo-steady state. The concentration of each cluster size remains constant, but there is a steady current through the system, clusters over the critical size n^* being constantly removed from the system. Thermodynamically, supersaturation, the driving force for the first-order phase transition and, hence, for the nucleation process, can be expressed as [39]

$$\Delta\mu \equiv \frac{(G_{old} - G_{new})}{M} \equiv \mu_{old} - \mu_{new} \tag{1.2}$$

Physically, the supersaturation $\Delta\mu$ is the gain in free energy per molecule or atom (M represents the number of molecules/atoms) associated with the passage of the phase from the minimum with higher Gibbs free energy G_{old} to the minimum with lower Gibbs free energy G_{new} (μ_{old} and μ_{new} are, respectively, the chemical potentials of the old and the new phases at the corresponding minima). Supersaturation is also commonly expressed as

$$S = \frac{c}{c^*} \tag{1.3}$$

where c is the solution concentration and c^* is the equilibrium saturation at the given temperature. $\Delta\mu$ and S are related through the next expression:

$$\sigma = \frac{\Delta\mu}{k_B T} = \frac{c - c^*}{c^*} = S - 1 \tag{1.4}$$

A large supersaturation driving force is necessary to initiate nucleation from a bulk solution. This can occur in two conditions. The first is homogeneous nucleation, which is nucleation occurring in the bulk solution by aggregation of molecules and clusters of the nucleating material. The second condition occurs when, in contrast with homogeneous nucleation, the new phase nucleates preferentially over solid particles of foreign substances. This is called heterogeneous nucleation.

2. Classical nucleation theory approach

An adequate theoretical description of clustering processes is of considerable interest because, as we have seen, they are responsible of a huge variety of processes in nature, and in scientific and technological applications. One of the tools allowing the theoretical description of such processes are the nucleation theories. From all these theories, the most extended theoretical approaches, predominantly employed in the interpretation of experimental results of nucleation-growth processes are based on the classical theory of nucleation (CNT), its extensions and modifications. The CNT has the exceptional advantage that its basic principles are equally well applicable to quite a variety of different systems. As a reflection of this general applicability, CNT is used in an extended variety of systems such as condensation, boiling, crystallization, melting, self-organization of ferroelectric domains and nanofilms, formation of micellar solutions or formation and growth of diamonds from vitreous carbon [40]. In contrast, the series of simplifications and assumptions that are implicit in this theory, makes of CNT a model that, despite of offering a good approach to experimental observations, it has been demonstrated to fail giving a real explanation to the nucleation phenomenon. There have been several attempts to improve the classical droplet model used in the classical nucleation theory. The most widely used modified liquid drop models are suggested by Lothe and Pound [41], Fisher [42], and Dillmann and Meier [43]. According to [41], the classical theory formulation of the nucleation rate requires a correction factor to describe correctly the translational and rotational motions of the cluster. These contributions were calculated from the Boltzmann distribution. The formulation described at [42] also accounts for the translational and rotational degrees of freedom of the cluster. An additional term for the free energy of formation expression was suggested there, whose magnitude would be normalized to experimental values. The droplet model described at [43] was simply an addition of another factor to the free energy of formation equation, accounting for the difference between the surface energy of a small cluster and a macroscopic droplet. Even though the modifications listed above have improved the performance of the classical theory for certain systems (species), the general performance

has not been improved and, in fact, the improvements have even worsened the discrepancy. Thus, despite of the more sophisticated models the classical nucleation theory in its original form is still widely used, and it is how we are going to describe it next.

Considering the (previously mentioned) assumptions of equilibrium cluster distribution (Eq (1.1)) and the pseudo steady state of the system, the nucleation stage can be described by means of a balance equation in the size axis. This equation, the so-called Master Equation of Nucleation (MEN) [39] considers that each cluster can grow or shrink by any amount and therefore, it has not an analytical closed solution. Nonetheless, assuming the clusters can only grow or shrink by jumps of unitary size (Szilard's limit) one readily obtains the Zeldovich-Frenkel Equation of nucleation (ZFEN) [39, 44, 45]. The main advantage of this approximation is the ZFEN has an exact steady-state solution which, indeed, looks like an Arrhenius law, i. e.:

$$Z_{eq}(N) \sim \exp\left(-\beta \Delta\Omega(N^*)\right) \tag{1.5}$$

where $\beta = 1/k_B T$ and $\Delta\Omega = \Omega(N) - \Omega_\infty$ is the work of cluster formation, i.e. the energy needed by the system to build up an N-sized cluster and, finally $Z_{eq}(N)$ is the cluster size distribution, i.e. the number of N-sized clusters per unit volume ($[Z] = [m^{-3}]$). With the aid of the ZFEN one can evaluate a very useful kinetic magnitude, the nucleation rate, hereafter denoted as J_{CNT}. After some manipulations, we can deduce the following expression for this quantity

$$J_{CNT} \simeq z_d k^+(N^*) C_{eq}^0 exp\left(-\beta \Delta\Omega(N^*)\right), \tag{1.6}$$

where

$$z_d = \sqrt{\frac{1}{2\pi k_B T}\left|\frac{\delta^2 \Omega(N)}{\delta N^2}\right|_{N^*}} \tag{1.7}$$

$$k^+(N^*) = k_{eq}^+(N)\, S \tag{1.8}$$

being z_d the Zeldovich's factor, S the supersaturation ratio described in eq (1.3) and $k_{eq}^{+}(N)$ the equilibrium attachment rate of monomers to a cluster of size N, and by definition of N^*

$$\frac{\delta\beta\Omega(N^*)}{\delta N} = 0 \tag{1.9}$$

In most cases, C_{eq}^{0} (the concentration of nucleation centers) is simply substituted by the limiting monomer concentration, which in the case of mono-component systems is equivalent to $C_1 \equiv \rho_1$, despite of not having a precise definition. Applying this criterion we can reach the most widely known expression for J_{CNT}

$$J_{CNT} \simeq z_d k_{eq}^{+}(N^*)\rho_1 S\, exp\big(-\beta\Delta\Omega(N^*)\big) \tag{1.10}$$

Since the analytical expression of $\Omega(N)$ depends on the type of nucleation considered (3D or 2D, homogeneous or heterogeneous) and $k_{eq}^{+}(N^*)$ depends both the cluster geometry and the mechanism which governs the attachment of monomers to the clusters, there exists a wide range of expressions for J_{CNT}. Considering the particular case of 3D-heterogeneous nucleation, with collision rates governed by monomer diffusion, equation (1.10) can be rewritten as [39]:

$$J_{CNT} \simeq z_d \gamma_N \rho_1 \sqrt{4\pi c^2}\, v_0^{1/3} D_1 [N^*]^{1/3} S\, exp\left(-\beta \frac{4\varepsilon^3 v_0^2 \sigma^3 \psi(\Theta_\omega)}{27\,(\Delta\mu)^2}\right) \tag{1.11}$$

where $\psi(\Theta_\omega)$ is the wetting function dependent on the wetting angle between nucleating phase and heterogeneous substrate (Θ_ω).

$$\psi(\Theta_\omega) = \frac{1}{4}(2 + \cos\Theta_\omega)(1 - \cos\Theta_\omega)^2 \tag{1.12}$$

It can be observed that when $\Theta_\omega = \pi$ the nucleation rate expression for 3D homogeneous nucleation governed by monomer diffusion is recovered. $\Delta\mu$, the chemical potential, can also be expressed as $\Delta\mu = \beta^{-1}\ln S \equiv k_B T \ln S$, where γ_N is the sticking coefficient, corresponding to the critical cluster, that can be considered as $\gamma_N \sim 1$ for a low saturated system, v_0 is the molecular volume and ε is a shape volume factor. Given for spherical nuclei $\varepsilon = (36\pi)^{1/3}$. Gathering the pre exponential variables

$z_d \gamma_N \rho_1 \sqrt{4\pi\varepsilon^2} \nu_0^{1/3} D_1 [N^*]^{1/3} = A\, S = \mathfrak{A}$ and introducing the previous modifications we reach the most extended equation for J_{CNT}:

$$J_{CNT} \simeq \mathfrak{A}\, exp\left(-\frac{16\pi\nu_0^2\sigma^3\psi(\Theta_\omega)}{3k_B{}^3T^3\ln^2 S}\right) \tag{1.13}$$

3. Generating Supersaturation

Metastable zone and induction time

The possibility of the existence of thermodynamically metastable states is a characteristic feature of the first-order phase transitions [39]. This is physically explained by the threshold character of the dependence of the nucleation rate on the supersaturation. After the initial moment $t = 0$ of the onset of supersaturation, a certain time, τ, called induction time (or induction period) may elapse prior to the formation of an appreciable amount of the new phase. This time is experimentally observable and is indicative of the capability of the system to remain in metastable equilibrium. The metastable zone results from the metastability of a supersaturated solution, and the dependence of supersaturation with different parameters. Therefore, its width (the critical point in which nucleation is detected when one of the parameters is changed) is a characteristic crystallization property for each system, and depends mainly on initial temperature, solution, cooling rate, presence of impurities, mechanical effects, etc. Nevertheless, most of these parameters are also closely connected with the description of nucleation behavior in the solution. Metastable zone width in nucleation is important for experimental performance, and also in industrial crystallization processes of unseeded and highly supersaturated solutions, for two main reasons:

- Industrially, conditions of metastability permits, for a determined period, the handling and transport of solutions avoiding the undesired precipitation of secondary byproducts. In contrast, a metastable situation is usually desired for the mixing of solutions, allowing to a higher homogeneity in the mixture,

favoring the latter precipitation of particles with more homogeneous properties, such as size, shape, and size distribution. For example, batch crystallizers, (in which spontaneous nucleation has to be considered and controlled), are commonly used in the chemical industry, from the production of explosives [46] or latex [47], to the synthesis of nanoparticles [35].

- As we will see in chapter 3, the experimentally determined induction periods for metastable solutions provide a connection between measurable quantities and thermodynamic variables. This allows us to experimentally estimate the value of the surface free energy between a crystalline phase and its surrounding solution for a given system, or the activation energy necessary for triggering nucleation processes. Obtained parameters allow us to describe and characterize systems, with the further purpose of controlling nucleation and crystallization events.

Methods for creating and controlling supersaturation

There are four main approaches to achieve supersaturation in a given system: by a chemical reaction, by the action of a precipitating agent that reduces solubility of a compound in a given solution (anti-solvent), by a temperature change, affecting solubility of this compound, and by concentration of the solution. Experimentally, these approaches can be reached by batch mixing or vapour diffusion of an agent or reactive in a solution, for the case of chemical reactions and anti-solvent precipitation, and by solvent evaporation in the case of solution concentration.

Precipitation by batch reaction consists in the addition of a reactant solution to another, appearing a new product by a chemical reaction. This product is formed in concentrations that create supersaturation, and therefore nucleation and precipitation occurs. In this case (an also in the case of batch precipitation by the addition of anti-solvents), supersaturation strongly depends on the mixing conditions. Mixing can be described macroscopically (describing the overall mixing of the bulk solution) and also

microscopically (locally describing the mixing, at the smallest scale of fluid motion). Chemical reactions, and therefore nucleation and crystal growth tend to be fast, so the mixing at micro-scale generates local supersaturations that differ from the macroscopic one, thus strongly affecting the crystallization process. This will be lately considered, observed and discussed in chapters 3, 4 and 5 of the present manuscript. In order to achieve a spatially homogeneous supersaturation, the use of stirrers is widely extended in industrial and laboratory processes to obtain a homogeneous mixing of the reactant solutions at the micro-scale. However, in highly supersaturated solutions, the metastability of the mixture is not large enough to delay precipitation until the homogeneous mixing is achieved. In these cases, the use of complexing agents allows to homogeneously distribute reactants in the solution at micro-scale, lately precipitating a more homogeneous product [48, 49].

Another extended method for crystallization involves the vapour diffusion techniques [50-52]. They consist on allowing the equilibration of a solution droplet with a larger reservoir of a second solution in a closed volume. This reservoir would contain:

a) A solution of similar composition with respect to the first one, but in higher concentrations

b) A solution with a volatile reactant

c) A solution consisting of a volatile precipitant agent.

Initially, the droplets of solution contain an insufficient concentration of precipitant for crystallization, but as solutions equilibrate, in case a), water vaporizes from the drop and transfers to the reservoir, and the precipitant concentration increases to a level optimal for crystallization. Since the system is in equilibrium, these optimum conditions are maintained until the crystallization is complete. In case b) vapour pressure of the volatile reactant increases in the closed volume, lately diffusing into the droplet until reaching equilibrium with the solution, and therefore generating supersaturation by reaction with the reactants contained in the droplet. Similarly, in case c), anti-solvent

diffuses in the droplet, and reduces solubility of the compound in the solution, creating supersaturation.

The most commonly used method for achieving supersaturation by concentration of a solution is the evaporation of the solvent [53, 54]. Evaporation can be performed at a fixed temperature by heating a solution to its boiling point, which can be lowered by operating the system under a vacuum. In the case of solvents with low boiling points, or when a low evaporation rate is desired, it can also be performed at room temperature. Since the surface from which the evaporation takes place is usually more supersaturated than the bulk solution, crystals tend to nucleate and grow in the interface and fall into the solution.

Finally, the cooling method is also widespread for crystallization of compounds with temperature dependent solubility [55, 56]. The solution temperature is lowered below the saturation temperature for that solution. At this point, crystallization may be spontaneous or it may be induced by seeding or by applying energy to the system (agitation) [57-59]. Changes in solution cooling rate have important effects on nucleating phases, as metastable solution can reach different supersaturation values [55, 58].

Scaling down and confinement

We have commented above the relevance of small volumes in crystallization occurring in nature, as well as its interest for studies which involve high added value products and which otherwise could represent unaffordable costs. For all these cases, different approaches have been widely proposed in literature, from mimicking the crystallization conditions in nature in order to reproduce and study the crystallization process at laboratory [60], to the use of sophisticated devices and techniques permitting a wide range of studies with a low consumption of reactants [61, 62]. In addition, there are occasions in which there is also a need for scaling down in industry, mainly when existing processes are subject to modifications and improvements. Here, the main interest for scaling down consists in the optimization of the process in terms of productivity, selectivity and/or safety, under the restriction of an existing and mostly fixed reactor design. To study possible problems in the future production, low cost small scale trials and best mimicking comportment are usually adapted. However, examples of this approach in the literature are not common, as due to confidential reasons, scale-down industrial approaches are not generally published.

But the use of small volumes for studying crystallization has further implications that the ones of natural conditions emulation, or the simple reduction of reactant consumption. First, nucleation phenomena are very difficult to observe, due to its stochastic nature [63]. The confinement of a solution in a compartmented domain permits to locate nucleation events in a specific space. Consequently, working with small quantities of solution permits the monitoring of the whole volumes of study, allowing the observation of crystal formation. Moreover, another great benefit of physically scaling down systems, from an analytical point of view, is not only a reduction in size but rather an improvement of the analytical performance [64]. One more consequence of scaling

down results from the relation of nucleation rate, $J_{CNT,}$ with volume and induction period, τ, which can be expressed, through CNT as:

$$\tau = \frac{1}{2VJ_{CNT}} \tag{1.14}$$

For a given supersaturation, determining a nucleation rate through equation (1.13), a reduction of volume reduces the probability of a nucleating event to occur, obtaining higher induction periods for nucleation, and therefore extending in time the metastability of the supersaturated solution. Additionally, there is also a substantial interest in the scientific community in the study of confinement from a fundamental point of view [63]. In the last years, the increasing number of technical developments has permitted the confinement and study of phase transition of solutions and melts in more and more reduced volumes (from micron sized domains to nanoporous media, with the help of controlled-pore glasses, membranes and other nanoporous materials [65-67]), showing in most cases that these transitions are fundamentally different from those observed in bulk [68]. One of the peculiarities of a confined system at micro- and nano-scale is that supersaturation can no longer be taken as a constant throughout the nucleation process. In an ideal solution, the consumption of molecules during the nucleation of a supersaturated solution can be neglected in comparison with the rest of molecules remaining in solution. On the contrary, in a micro- or nano- confined system, only a reduced number of molecules exists in solution, and each molecule joining a new emerging cluster counts in the total, no longer contributing to the supersaturation of the solution [63].

Studies of confinement constraints are nowadays present in literature [63] and have revealed interesting effects on nucleation barrier and nucleation kinetics in different systems, from condensation of droplets in superheated vapour [69-72] or microemulsions [73] to crystallization in solution [74, 75], where also effects on crystal habit have been found. In particular, generation of small droplets [25, 76-78], gathers the main interest of studying effects of confinement in nucleation together with the possibility of optically observing and monitoring nucleation events in a confined space. On this sense, regular

arrays of microdroplets have been generated by different techniques and with different purposes: patterned self-assembled monolayers have been used for droplet generation and storage in order to study polymorphism of organic compounds [24-26] or calcium carbonate heterogeneous nucleation [79]; droplet based microfluidic techniques [80, 81] (which will be explained below)have been used for investigating nucleation kinetics of different substances, from big macromolecules [76, 82] to small molecules of pharmaceutical interest [77, 83]; and finally, the novel microinjection technique [84] have been demonstrated to be a powerful tool to easily generate microdroplet arrays for the study of nucleation in a controlled evaporation environment [85].

Microfluidics

Contrary to microinjection, which is a very recent technique that is not extended yet in the field of crystallization, microfluidic techniques have been developed, improved, and intensively studied in the last two decades, appearing to be nowadays an established field of scientific research. Microfluidic techniques consist in a series of processes or systems created for handling small amounts of fluids, using channels with dimensions of tens to hundreds of microns [86]. The main advantages of microfluidics come in terms of small volume consumption and manipulation, low cost, short reaction time and high-throughput, making them one of the most widespread techniques when referring to scaling down processes. Since the appearing of micro total analysis system (μ-TAS), also known as "lab-on-a-chip" in the 1990s [64], microfluidics has been considered as a potential technology to miniaturize the conventional equipments and technologies [87]. It is gradually changing, since then, the way of performing many analytical processes from biological and gene analysis or clinical diagnosis [88-91] to drug discovery or material synthesis [92, 93].

Microfluidics are physically differentiated from "macrofluidics" by characteristic laminar flows (attributable to the small size of microchannels), described by low Reynolds numbers. This indicates the importance of flow inertia in the microchannels, compared with viscous stress [80]. Their intrinsic laminar flows and the absence of convective forces due to the small size of the channels [76, 94] only allows the mixing of different streams flowing in contact with each other by diffusion. But whilst, in the field of crystallization, a diffusive media is desired for improving the crystalline quality of growing crystals [29, 95] (for molecular structural resolution by X-ray diffraction), the homogeneity of the mix of reactants (or solution and precipitant agents) is also of extreme importance [96]. Homogeneity at micro-scale is a requirement not only for controlling the properties of crystallized materials, but also for studying nucleation by performing high temporal resolution kinetic measurements [76]. Therefore, together with the advantages of low consumption of reagents, overcoming the diffusive microfluidic

media to obtain a rapid mixing of reagents becomes necessary. For this purpose, the use of chaotic advection has been proved to be effective for rapid mixing of streams at microfluidic scale [97, 98]. Lately, this concept has been used and combined to microfluidic droplet methods [80, 81] for introducing chaotic mixing in unsteady, time-periodic flows inside droplets by the use of winding microchannels [76, 99]. Winding channels creates chaotic mixing by folding, stretching and reorienting the fluid volume [76]. The use of droplet based methods together with chaotic mixing has been shown to be especially valuable for performing kinetic experiments with samples which are available only in small quantities, permitting measurements in the millisecond time-scale [100]. For that reason and due to the application of these techniques in the experimental work developed for this manuscript, the principle of droplet based microfluidic methods will be detailed below.

Microfluidic droplet methods

Droplet based microfluidics consist on creating and manipulating discrete droplets using immiscible phases flow in microfluidic channels. Droplets form spontaneously when a stream of solution is injected into a solvent-immiscible carrier fluid [99]. The droplets are generally used as isolated and independent microreactors, in which reactions can be carried out without interference between samples or reagents. Droplets are widely also referred as "plugs" in literature, as they are usually large enough to be in contact with the walls of the channels, although they are surrounded by the inmiscible carrier fluid (usually silicone oil, fluorinert oil, or mineral oil), which avoids the wetting of the channels with the solution [76]. Accordingly, the microfluidic devices designed for creating droplets are also referred in literature as "plug factories" [77, 101]. Athough droplet techniques were firstly introduced for performing experiments in aqueous solutions, they have also been applied to non-polar solvents, permitting the study of organic molecule crystallization [77, 83].

Objectives

The main objectives of this thesis are to:

- Offer a complete analysis of the classical nucleation theory, for a better understanding and interpretation of the processes of crystallization from solution.
- Analyze the procedure for scaling down crystallization processes and the effect on the obtained precipitates
- Explore the effects of confinement in the metastability of solutions and in the stabilization of metaestable phases.
- Apply novel techniques and develop new technologies and analytical systems for the manipulation of small volumes, allowing the performance of kinetic studies of nucleation and chemical reactions in general, with small quantities of reagents.

For these purposes we will:

- Apply the whole CNT theoretical model to the study of calcium sulfate nucleation, for our own experimental data, obtained from studies in small 100 uL vials and low supersaturations, and from values reported in literature, in large volumes and higher supersaturations.
- Evaluate the precipitation of calcium phosphates in large volumes, by batch thermal-decomplexing methods, and in small volumes, by pH-decomplexing methods, with the help of the "*crystallization mushroom",* with the aim of obtaining biomimetic and biocompatible apatite nanoparticles for biomedical applications.
- Take advantage of the previously mentioned microinjection and microfluidic techniques to investigate the effects of confinement in two different systems of interest:
    - we have studied the evaporation of microdroplets (from nano- to picoliter volumes) of sodium chloride (and other inorganic salts) solutions, with a view to mimic natural crystallization conditions in

the small pores and cracks of stone and other building materials. This is important in order to understand the mechanisms of degradation of buildings, statuary and cultural heritage, in general, by the action of weathering and pollution.

  - we have investigated calcium carbonate nucleation and phase transition in small volumes and medium to high supersaturations. Calcium carbonate is of great interest in industrial and pharmaceutical applications, and one of the main protagonists in natural biomineralization processes. Additionally, the mixing of solutions at micro-scale and its significance in generating supersaturation has been evaluated.

- Develop new tools for applied crystallization studies that require low consumption of reactants and special design requirements:
  - We have developed a low cost procedure for obtaining solvent-resistant microfluidic structures for the study of small organic molecules nucleation in nanoliter volumes.
  - We have developed a microfluidic solid base reactor for enzymatic catalytic reactions using enzyme crystals as catalysts.
  - We have implemented spectrophotometric detection systems to both microfluidic systems with the help of optical lenses and fiber optics inserts, allowing following the nucleation events for the solvent resistant microdevices, and the conversion of the catalytic reaction for the microfluidic solid base reactor.

References

1. Mann S. Biomineralization: principles and concepts in bioinorganic materials chemistry. Oxford: University Press; 2001.

2. Rodriguez-Navarro C, Linares-Fernandez L, Doehne E, Sebastian E. Effects of ferrocyanide ions on NaCl crystallization in porous stone. Journal of Crystal Growth. 2002;243(3):503-16.

3. Rodriguez-Navarro C, Doehne E, Sebastian E. How does sodium sulfate crystallize? Implications for the decay and testing of building materials. Cement and concrete research. 2000;30(10):1527-34.

4. Meldrum FC. Calcium carbonate in biomineralisation and biomimetic chemistry. International Materials Reviews. 2003;48(3):187-224.

5. Mullin JW. Crystallization1993.

6. Mi B, Elimelech M. Gypsum Scaling and Cleaning in Forward Osmosis: Measurements and Mechanisms. Environmental Science & Technology. 2010;44(6):2022-8.

7. Rosenberg YO, Reznik IJ, Zmora-Nahum S, Ganor J. The effect of pH on the formation of a gypsum scale in the presence of a phosphonate antiscalant. Desalination. 2012;284(0):207-20.

8. McCool BC, Rahardianto A, Cohen Y. Antiscalant removal in accelerated desupersaturation of RO concentrate via chemically-enhanced seeded precipitation (CESP). Water Research. 2012;46(13):4261-71.

9. Lee R-W, Glater J, Cohen Y, Martin C, Kovac K, Milobar MN, et al. Low-pressure RO membrane desalination of agricultural drainage water. Desalination. 2003;155(2):109-20.

10. Black SN, Bromley LA, Cottier D, Davey RJ, Dobbs B, Rout JE. Interactions at the organic/inorganic interface: Binding motifs for phosphonates at the surface of barite crystals. Journal of the Chemical Society, Faraday Transactions. 1991;87(20):3409-14.

11. Zafiropoulou A, Dalas E. The effect of benzotriazoles on calcium carbonate scale formation. Journal of Crystal Growth. 2000;219(4):477-80.

12. Cherdron E, Forster H-J, Potencsik I. Method of precipitating radium to yield high purity calcium sulfate from phosphate ores. Google Patents; 1976.

13. Lane MK, Anderson WC. By-product gypsum fillers for mica-free joint compounds consisting of synthetic calcium sulphate dihydrate having a mean particle size of 11 or 12 microns. Google Patents; 1976.

14. Omran AM, King CJ. Kinetics of ice crystallization in sugar solutions and fruit juices. AIChE Journal. 1974;20(4):795-803.

15. Metin S, Hartel RW. Crystallization of fats and oils. Bailey's Industrial Oil and Fat Products. 2005.

16. Hartel RW. Ice crystallization during the manufacture of ice cream. Trends in Food Science & Technology. 1996;7(10):315-21.

17. Stapley AG, Tewkesbury H, Fryer PJ. The effects of shear and temperature history on the crystallization of chocolate. Journal of the American Oil Chemists' Society. 1999;76(6):677-85.

18. Hartel RW. Controlling crystallization in foods. Crystal growth of organic materials. 1996:172.

19. Blanshard J, Franks F. Ice crystallization and its control in frozen-food systems. Academic Press, London; 1987. p. 51-65.

20. Rodríguez-hornedo N, Murphy D. Significance of controlling crystallization mechanisms and kinetics in pharmaceutical systems. Journal of Pharmaceutical Sciences. 1999;88(7):651-60.

21. Ludlam-Brown I, York P. The crystalline modification of succinic acid by variations in crystallization conditions. Journal of Physics D: Applied Physics. 1993;26(8B):B60.

22. Blagden N, De Matas M, Gavan P, York P. Crystal engineering of active pharmaceutical ingredients to improve solubility and dissolution rates. Advanced Drug Delivery Reviews. 2007;59(7):617-30.

23. Haidar SH, Davit B, Chen M-L, Conner D, Lee L, Li QH, et al. Bioequivalence approaches for highly variable drugs and drug products. Pharm Res. 2008;25(1):237-41.

24. Lee AY, Lee IS, Myerson AS. Factors Affecting the Polymorphic Outcome of Glycine Crystals Constrained on Patterned Substrates. Chemical Engineering & Technology. 2006;29(2):281-5.

25. Lee I, Lee A, Myerson A. Concomitant Polymorphism in Confined Environment. Pharm Res. 2008;25(4):960-8.

26. Lee IS, Kim KT, Lee AY, Myerson AS. Concomitant Crystallization of Glycine on Patterned Substrates: The Effect of pH on the Polymorphic Outcome. Cryst Growth Des. 2008;8(1):108-13.

27. Shekunov BY, York P. Crystallization processes in pharmaceutical technology and drug delivery design. Journal of Crystal Growth. 2000;211(1):122-36.

28. Durbin S, Feher G. Protein crystallization. Annual Review of Physical Chemistry. 1996;47(1):171-204.

29. Otálora F, Gavira JA, Ng JD, García-Ruiz JM. Counterdiffusion methods applied to protein crystallization. Progress in Biophysics and Molecular Biology. 2009;101(1–3):26-37.

30. Lowenstam HA, Weiner S. On Biomineralization. Oxford: University Press; 1989.

31. Hasson D, Avriel M, Resnick W, Rozenman T, Windreich S. Mechanism of calcium carbonate scale deposition on heat-transfer surfaces. Industrial & Engineering Chemistry Fundamentals. 1968;7(1):59-65.

32. Garcia-Carmona J, Gomez-Morales J, Fraile-Sainz J, Rodriguez-Clemente R. Morphological characteristics and aggregation of calcite crystals obtained by bubbling CO2 through a Ca (OH) 2 suspension in the presence of additives. Powder Technology. 2003;130(1-3):307-15.

33. Kawasaki K, Buchanan AV, Weiss KM. Biomineralization in Humans: Making the Hard Choices in Life. Annual Review of Genetics. 2009;43:119-42.

34. Olszta MJ, Cheng X, Jee SS, Kumar R, Kim Y-Y, Kaufman MJ, et al. Bone structure and formation: A new perspective. Materials Science and Engineering: R: Reports. 2007;58(3-5):77-116.

35. Gómez-Morales J, Iafisco M, Delgado-López JM, Sarda S, Drouet C. Progress on the preparation of nanocrystalline apatites and surface characterization: Overview of fundamental and applied aspects. Progress in Crystal Growth and Characterization of Materials. 2013;59(1):1-46.

36. Al-Kattan A, Girod-Fullana S, Charvillat C, Ternet-Fontebasso H, Dufour P, Dexpert-Ghys J, et al. Biomimetic nanocrystalline apatites: Emerging perspectives in cancer diagnosis and treatment. International Journal of Pharmaceutics. 2012;423(1):26-36.

37. Weiss MS. Global indicators of X-ray data quality. Journal of Applied Crystallography. 2001;34(2):130-5.

38. Ducruix A, Giegé R. Crystallization of nucleic acids and proteins: A practical approach: IRL Press at Oxford University Press; 1992.

39. Kashchiev D. Nucleation: Basic Theory with Applications2000.

40. Mostany JL, Scharifker B, Saavedra KD, editors. Consistency of the Classical Theory of Nucleation with Nanometric Phenomena: A Comparison from Overpotential and Temperature Studies. Meeting Abstracts; 2006: The Electrochemical Society.

41. Lothe J, Pound GM. Reconsiderations of nucleation theory. The Journal of Chemical Physics. 1962;36:2080.

42. Fisher ME. The theory of condensation and the critical point. Physics. 1967;3(1):255.

43. Dillmann A, Meier G. Homogeneous nucleation of supersaturated vapors. Chemical Physics Letters. 1989;160(1):71-4.

44. Farkas L. Keimbildungsgeschwindigkeit in übersättigten Dämpfen. Z phys Chem. 1927;125:236-42.

45. Zeldovich JB. On the theory of new phase formation; cavitation. Acta physicochim URSS. 1943;18(1):1-22.

46. Kim K-J, Kim K-M. Nucleation kinetics in spherulitic crystallization of explosive compound: 3-nitro-1, 2, 4-triazol-5-one. Powder Technology. 2001;119(2):109-16.

47. Hansen FK, Ugelstad J. Particle nucleation in emulsion polymerization. I. A theory for homogeneous nucleation. Journal of Polymer Science: Polymer Chemistry Edition. 1978;16(8):1953-79.

48. López-Macipe A, Gómez-Morales J, Rodríguez-Clemente R. Nanosized Hydroxyapatite Precipitation from Homogeneous Calcium/Citrate/Phosphate Solutions Using Microwave and Conventional Heating. Adv Mater. 1998;10(1):49-53.

49. Delgado-Lopez JM, Iafisco M, Rodriguez I, Tampieri A, Prat M, Gomez-Morales J. Crystallization of bioinspired citrate-functionalized nanoapatite with tailored carbonate content. Acta Biomaterialia. 2012;8(9):3491-9.

50. García-Ruiz J, Hernández-Hernández M, Gómez-Morales J. D-36 CRYSTALLISATION MUSHROOM: A NEW CRYSTALLISATION TOOL BY VAPOUR DIFFUSION TECHNIQUE. VDI BERICHTE. 2005;1901(2):963.

51. Chayen NE. Comparative studies of protein crystallization by vapour-diffusion and microbatch techniques. Acta Crystallographica Section D: Biological Crystallography. 1998;54(1):8-15.

52. Mikol V, Rodeau J-L, Giegé R. Changes of pH during biomacromolecule crystallization by vapor diffusion using ammonium sulfate as the precipitant. Journal of Applied Crystallography. 1989;22(2):155-61.

53. Strickland-Constable RF. Kinetics and Mechanism of Crystallization from the Fluid Phase and of the Condensation and Evaporation of Liquids: Academic P.; 1968.

54. Sattler K, Feindt HJ. Solvent Evaporation, Crystallization. Thermal Separation Processes: Principles and Design. 1995:475-532.

55. Ozawa T. Kinetics of non-isothermal crystallization. Polymer. 1971;12(3):150-8.

56. Worlitschek J, Mazzotti M. Model-based optimization of particle size distribution in batch-cooling crystallization of paracetamol. Crystal Growth & Design. 2004;4(5):891-903.

57. Feng L, Berglund KA. ATR-FTIR for determining optimal cooling curves for batch crystallization of succinic acid. Crystal Growth & Design. 2002;2(5):449-52.

58. Doki N, Seki H, Takano K, Asatani H, Yokota M, Kubota N. Process control of seeded batch cooling crystallization of the metastable α-form glycine using an in-situ ATR-FTIR spectrometer and an in-situ FBRM particle counter. Crystal Growth & Design. 2004;4(5):949-53.

59. Kubota N, Doki N, Yokota M, Sato A. Seeding policy in batch cooling crystallization. Powder Technology. 2001;121(1):31-8.

60. Van Driessche AES, García-Ruíz JM, Tsukamoto K, Patiño-Lopez LD, Satoh H. Ultraslow growth rates of giant gypsum crystals. Proceedings of the National Academy of Sciences. 2011.

61. Gómez-Morales J, Hernández-Hernandez A, Sazaki G, García-Ruiz JM. Nucleation and Polymorphism of Calcium Carbonate by a Vapor Diffusion Sitting Drop Crystallization Technique. Crystal Growth & Design. 2010;10(2):963-9.

62. Leng J, Salmon J-B. Microfluidic crystallization. Lab on a Chip. 2009;9(1):24-34.

63. Grossier R, Veesler Sp. Reaching One Single and Stable Critical Cluster through Finite-Sized Systems. Crystal Growth & Design. 2009;9(4):1917-22.

64. Manz A, Graber N, Widmer HM. Miniaturized total chemical analysis systems: A novel concept for chemical sensing. Sensors and Actuators B: Chemical. 1990;1(1–6):244-8.

65. Jackson CL, McKenna GB. The melting behavior of organic materials confined in porous solids. The Journal of Chemical Physics. 1990;93(12):9002-11.

66. Ha J-M, Wolf JH, Hillmyer MA, Ward MD. Polymorph Selectivity under Nanoscopic Confinement. Journal of the American Chemical Society. 2004;126(11):3382-3.

67. Haller W. Chromatography on glass of controlled pore size. Nature. 1965;206(4985):693-6.

68. Christenson HK. Confinement effects on freezing and melting. Journal of Physics: Condensed Matter. 2001;13(11):R95.

69. Rao M, Berne BJ. Nucleation in finite systems: theory and computer simulation. Astrophysics and Space Science. 1979;65:39-46.

70. Vogelsberger W. Thermodynamics of finite systems: a possibility for interpretation of nucleation and condensation experiments. J Colloid Interface Sci. 1982;88:17-28.

71. Schmelzer J, Ulbricht H. Thermodynamics of finite systems and the kinetics of first-order phase transitions. Journal of colloid and interface science. 1987;117:325.

72. Schweitzer F, Schimansky-Geier L. Critical parameters for nucleation in finite systems. Journal of colloid and interface science. 1987;119:67-73.

73. Liu J, Nicholson CE, Cooper SJ. Direct Measurement of Critical Nucleus Size in Confined Volumes. Langmuir. 2007;23(13):7286-92.

74. Hartman P. Crystal growth: an introduction: North-Holland Publishing Company; 1973.

75. Andreazza P, Lefaucheux F, Mutaftschiev B. Nucleation in confined space: Application to the crystallization in gels. Journal of Crystal Growth. 1988;92:415-22.

76. Bringer MR, Gerdts CJ, Song H, Tice JD, Ismagilov RF. Microfluidic systems for chemical kinetics that rely on chaotic mixing in droplets. Philosophical Transactions of the Royal Society of London Series A: Mathematical, Physical and Engineering Sciences. 2004;362(1818):1087-104.

77. Ildefonso M, Candoni N, Veesler S. A Cheap, Easy Microfluidic Crystallization Device Ensuring Universal Solvent Compatibility. Organic Process Research & Development. 2012;16(4):556-60.

78. Gómez-Morales J, Torrent-Burgués J, Rodríguez-Clemente R. Nucleation of calcium carbonate at different initial pH conditions. Journal of Crystal Growth. 1996;169(2):331-8.

79. Stephens CJ, Kim Y-Y, Evans SD, Meldrum FC, Christenson HK. Early Stages of Crystallization of Calcium Carbonate Revealed in Picoliter Droplets. Journal of the American Chemical Society. 2011;133(14):5210-3.

80. Christopher G, Anna S. Microfluidic methods for generating continuous droplet streams. Journal of Physics D: Applied Physics. 2007;40(19):R319.

81. Zheng B, Tice JD, Roach LS, Ismagilov RF. A Droplet-Based, Composite PDMS/Glass Capillary Microfluidic System for Evaluating Protein Crystallization Conditions by Microbatch and Vapor-Diffusion Methods with On-Chip X-Ray Diffraction. Angewandte Chemie International Edition. 2004;43(19):2508-11.

82. Zheng B, Gerdts CJ, Ismagilov RF. Using nanoliter plugs in microfluidics to facilitate and understand protein crystallization. Current Opinion in Structural Biology. 2005;15(5):548-55.

83. Teychené S, Biscans B. Microfluidic Device for the Crystallization of Organic Molecules in Organic Solvents. Crystal Growth & Design. 2011;11(11):4810-8.

84. Grossier R, Hammadi Z, Morin R, Magnaldo A, Veesler S. Generating nanoliter to femtoliter microdroplets with ease. Applied Physics Letters. 2011;98(9):091916-3.

85. Grossier R, Magnaldo A, Veesler S. Ultra-fast crystallization due to confinement. Journal of Crystal Growth. 2010;312(4):487-9.

86. Whitesides GM. The origins and the future of microfluidics. Nature. 2006;442(7101):368-73.

87. Chen J, Chen D, Xie Y, Yuan T, Chen X. Progress of microfluidics for biology and medicine. Nano-Micro Letters. 2013;5 (1):66-80.

88. Demello AJ. Control and detection of chemical reactions in microfluidic systems. Nature. 2006;442(7101):394.

89. Fan X, White IM. Optofluidic microsystems for chemical and biological analysis. Nature photonics. 2011;5(10):591-7.

90. Chen J, Chen D, Yuan T, Chen X. Microfluidic PCR chips2011.

91. Du H, Wang Z, Yang Z, Chen D, Chen J, Hu R. Separation of Circulating Cancer Cells by Unique Microfluidic Chip in Colorectal Cancer. Oncology Research Featuring Preclinical and Clinical Cancer Therapeutics. 2012;19(10-11):10-1.

92. Dittrich PS, Manz A. Lab-on-a-chip: microfluidics in drug discovery. Nature Reviews Drug Discovery. 2006;5(3):210-8.

93. Song Y, Hormes J, Kumar CS. Microfluidic synthesis of nanomaterials. Small. 2008;4(6):698-711.

94. Bird R, Stewart W, Lightfoot E. Transport phenomena. 2nd. New York: John Wiley & Sons; 2002.

95. Lin H, Rosenberger F, Alexander J, Nadarajah A. Convective-diffusive transport in protein crystal growth. Journal of Crystal Growth. 1995;151(1):153-62.

96. Howard EI, Fernandez JM, Garcia-Ruiz JM. On the Mixing of Protein Crystallization Cocktails. Crystal Growth & Design. 2009;9(6):2707-12.

97. Liu RH, Stremler MA, Sharp KV, Olsen MG, Santiago JG, Adrian RJ, et al. Passive mixing in a three-dimensional serpentine microchannel. Microelectromechanical Systems, Journal of. 2000;9(2):190-7.

98. Stroock AD, Dertinger SK, Ajdari A, Mezić I, Stone HA, Whitesides GM. Chaotic mixer for microchannels. Science. 2002;295(5555):647-51.

99. Song H, Tice JD, Ismagilov RF. A Microfluidic System for Controlling Reaction Networks in Time. Angewandte Chemie International Edition. 2003;42(7):768-72.

100. Song H, Ismagilov RF. Millisecond kinetics on a microfluidic chip using nanoliters of reagents. Journal of the American Chemical Society. 2003;125(47):14613-9.

101. Ildefonso M, Revalor E, Punniam P, Salmon JB, Candoni N, Veesler S. Nucleation and polymorphism explored via an easy-to-use microfluidic tool. J Cryst Growth. 2012;342(1):9-12.

CHAPTER 2

Experimental techniques and devices

CHAPTER 2

Experimental techniques and devices

In this chapter, the experimental set ups and techniques, specifically used and/or developed for the different studies which have been carried out, will be described. With the purpose of increasing the readability of the manuscript, more commonly used and widespread analytical and experimental techniques, extensively explained and detailed in literature, have been omitted. Among these well known techniques, the use of optical microscopy, Scanning and Transmission Electron Microscopy (SEM and TEM respectively), Selected Area Electron Diffraction (SAED), Energy Dispersive X-ray Spectroscopy (EDS), RAMAN and Infrared (IR) Spectroscopy, UV-Vis Spectroscopy, Inductively Coupled Plasma-Optical Emission Spectrometry (ICP-OES), X-ray Diffraction (XRD) and X-ray Powder Diffraction (XRPD), Thermogravimetric Analysis (TGA), Dynamic Light Scattering (DLS) and electrophoretic mobility (ζ-potential) has been required to characterize the experiments carried out along the different chapters of this manuscript.

Devices

1. Peltier based thermostatic multi-well set up

The apparatus presented here is a homemade thermostatic control consisting in two different modules, independently thermostatted by Peltier elements and coupled to an inverted microscope (Nikon Eclipse TE2000-U) [1]. To reach temperature differences higher than 20 $^{\circ}$C with respect to room temperature, Peltier elements are cooled down by an external thermostatic bath. Different types of vials can be used in the modules by inserting them into metal blocks specifically designed for each type of vial. Metal blocks help to homogeneously distribute the temperature in all the inserted vials. Pictures of the experimental set up are shown in Figure 1. Standard HPLC glass vials with 0.5 mL capacity (figures 1b and 1d) were used for the experiments performed in chapter 3 of this

manuscript. Each thermostated block can hold up to 24 0.5 mL experiments/vials. The whole assembly is mounted on an automated X−Y translation stage. Temperature control, X-Y translation, as well as sequential image acquisition can be performed automatically and periodically (from minutes to hours) with the help of a software developed ad-hoc for this instrument.

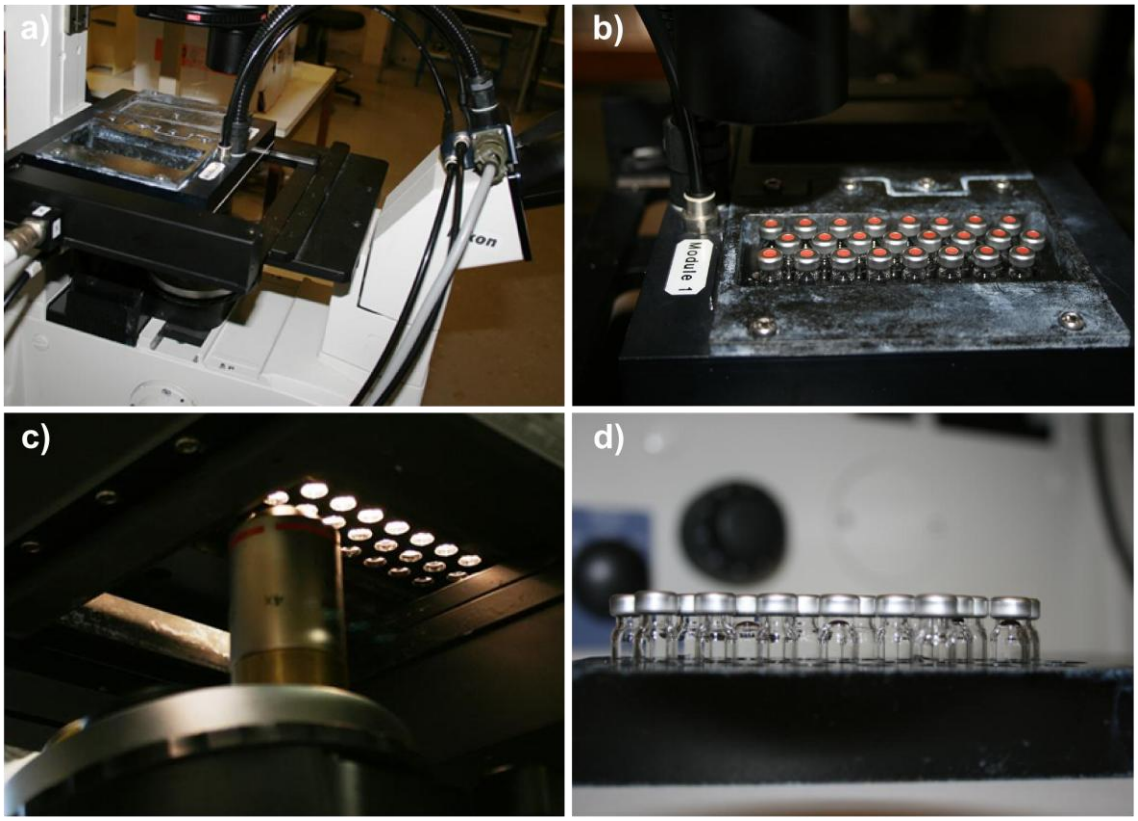

Figure 1. Descriptive images of the peltier based thermostatic multi-well set up. a) thermostatic control coupled to an inverted Nikon Eclipse TE2000-U microscope; b) detail of an independent thermostated module; c) rear view of the module and microscope objective; d) 0.5 mL vials inserted in the metal block that transmits temperature from the peltier elements.

2. Microinjection technique for droplet generation

The microinjection of small quantities of unsaturated reactant solutions under a layer of paraffin oil, that prevents them from instantaneous evaporation, is a novel technique that permits the quick generation of dozens of subnanoliter and picoliter sitting droplets (hundreds of picoliters and tens of picoliters, respectively), whose water molecules lately diffuse through the permeable layer of paraffin oil, generating supersaturation by

concentration of the reactant in the remaining water [2]. Determining the volume of the injected solutions, as well as its variation with time, caused by the controlled evaporation/diffusion of water molecules, allows us to evaluate the increase of concentration as a function of time for each sitting droplet, and therefore to follow in time its non stationary supersaturation. But under the same principles of this technique, and also determining the volume of the injected solutions for each droplet, it is also possible to generate instantaneous supersaturation by mixing of two different reactant solutions under oil, and estimate the total reactant concentration of the final batch. Both techniques have been applied in chapter 5 of the present manuscript with two substances of interest:

- NaCl, which is one of the major responsible of stone degradation in buildings, monuments and statuary, mainly situated near the sea. Due to its high solubility, NaCl present in ambient water crystallizes in small pores and cracks of stone by evaporation, generating precipitates that exert a high pressure on the inner walls of these cavities, leading to fractures and seriously damaging architectonical structures and the cultural heritage in general.
- $CaCO_3$, which is an important protagonist in biomineralization processes and biomaterial science, and one of the main inorganic biominerals in nature, as well as being of interest for its industrial applications as a filler in plastics, rubber, paper, paints and pigments, food and pharmaceutical industry, among many others [3-5]. Moreover, confinement is also of great interest for biomaterial science, as it is the natural mechanism for crystalline nucleation control in biomineralization processes (which occur in compartmented well defined volumes [6]).

For that reason and with the purpose of providing a useful tool to better characterize both types of microinjection experiments, a model to estimate the volume of a sitting droplet is proposed. This calculation consists on the indirect estimation of the contact angle of the droplet with the substrate, by the measurement of its height and width. The aim of this model is to describe the time evolution of volume in droplets of different

solutions generated by the microinjection technique [2, 7], under a layer of permeable paraffin oil. Water of these droplets would diffuse through the oil consequently shrinking, and thus generating a progressive increase of the concentration inside the droplets, $C=C_0$, only known in the initial moment t_0, when $V=V_0$ The interest of this volume estimation is to relate it with the concentration, being able to calculate it as a function of time for a running experiment.

Considering that

$$C_0 = \frac{m_0}{V_0} \tag{2.1}$$

where m_0 is the initial amount of solute in the solution, which remains constant until a certain supersaturation is reached, due to the loss of solvent by diffusion and nucleation takes place. While solution is undersaturated or in metaestable state, without precipitation, we can consider

$$C_t = \frac{m_0}{V_t} \tag{2.2}$$

and the time evolution can be expressed as:

$$\frac{dC_t}{dt} = \frac{-m_0}{V^2{}_t}\frac{dV_t}{dt} \tag{2.3}$$

Taking into account the following two assumptions, the shape of the droplets can be approached to a spherical cap as a good estimation:

- Droplets are considered symmetric about a central vertical axis: that means it is irrelevant from which direction the drop is viewed.

- Contact area of the droplets with the substrate is considered as a circular surface. Despite of that, there are small differences in shape because droplets are generated while the tip of the injector is in movement (see Figure 2). Those fluctuations from a circular contact area have a negligible effect on droplets volume. Thus, the effect of inertia in droplet deposition is not taken into account in order to simplify the model.

Model

Contact angles and volume of the droplet are estimated by fitting a rectangle of width W and height H to the shape of the drop and then relating the measured magnitudes, W and H, to the contact angle as described next:

Being the volume of a sphere, V_s of radius R:

$$V_s = \frac{4}{3}\pi R^3 \qquad (2.4)$$

where $R = W/2$ only when $H \geq R$, (Figure 3a), V_s can be related with the volume of a spherical cap of same radius R as [8-10]:

$$V_{cs} = \frac{1}{4}(2 + \cos\theta)(1 - \cos\theta)^2 V_s \qquad (2.5)$$

where θ is the contact angle of the spherical cap, and it is related with its complementary angle as

$$\delta + \theta = \pi \quad \text{thus,} \quad \theta = \pi - \delta \qquad (2.6)$$

δ is related with h and R trough cosine function as

$$\cos\delta = \frac{h}{R} \quad \text{thus,} \quad \delta = \cos^{-1}\frac{h}{R} \qquad (2.7)$$

In this case in which $H \geq R$, the contact diameter of the droplet is calculated by simple trigonometry as:

$$D = 2\sqrt{R^2 - h^2} \qquad (2.8)$$

For spherical caps in which $R<H$, (see Figure 3b) then R can be calculated as

$$R = \frac{a^2+h^2}{2h} \qquad (2.9)$$

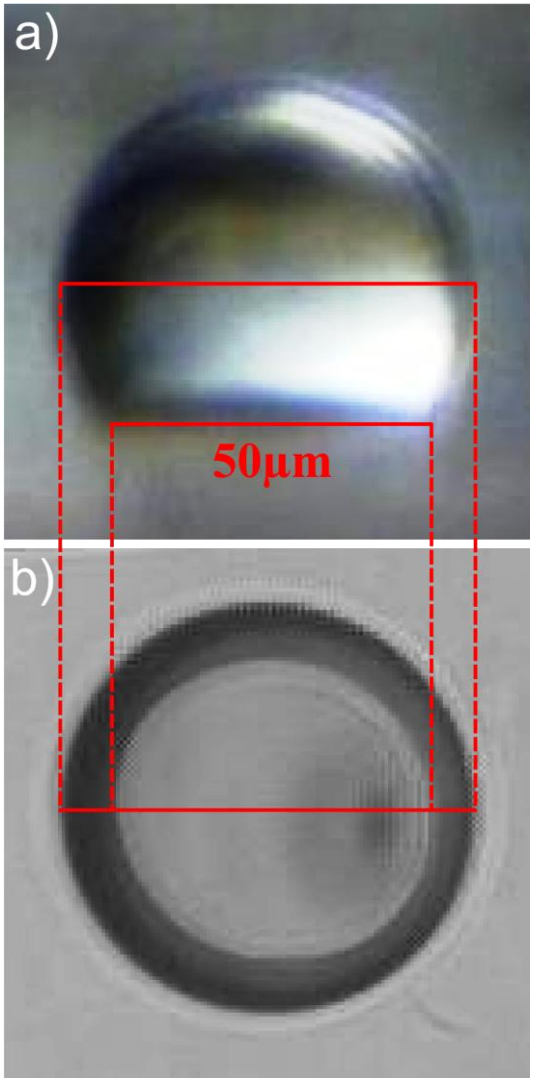

Figure 2. Two different views of a 0.16 nL droplet. NaCl Solution 2.71 M. Contact diameter ≈50 µm. a) Parallel to substrate view; b) bottom view of the same droplet.

where $a = W/2$ and $h = H$

And we can obtain the contact angle θ through the sin function as:

$$\sin\theta = \frac{a}{R} \quad \text{thus,} \quad \theta = \sin^{-1}\frac{a}{R} \tag{2.10}$$

While working with the bottom view of the droplets, and using the previous model, it is possible to estimate the volume of the droplets through the direct measurement of the contact diameter, D, and radius R by the calculation of θ. When the geometry of the droplet makes not possible to observe the radius R, we will be in the condition of $R<H$, previously determined, and the volume of the spherical cap could not be directly calculated, although it could be estimated fitting a curve to the plot of the volume time evolution in the experiment.

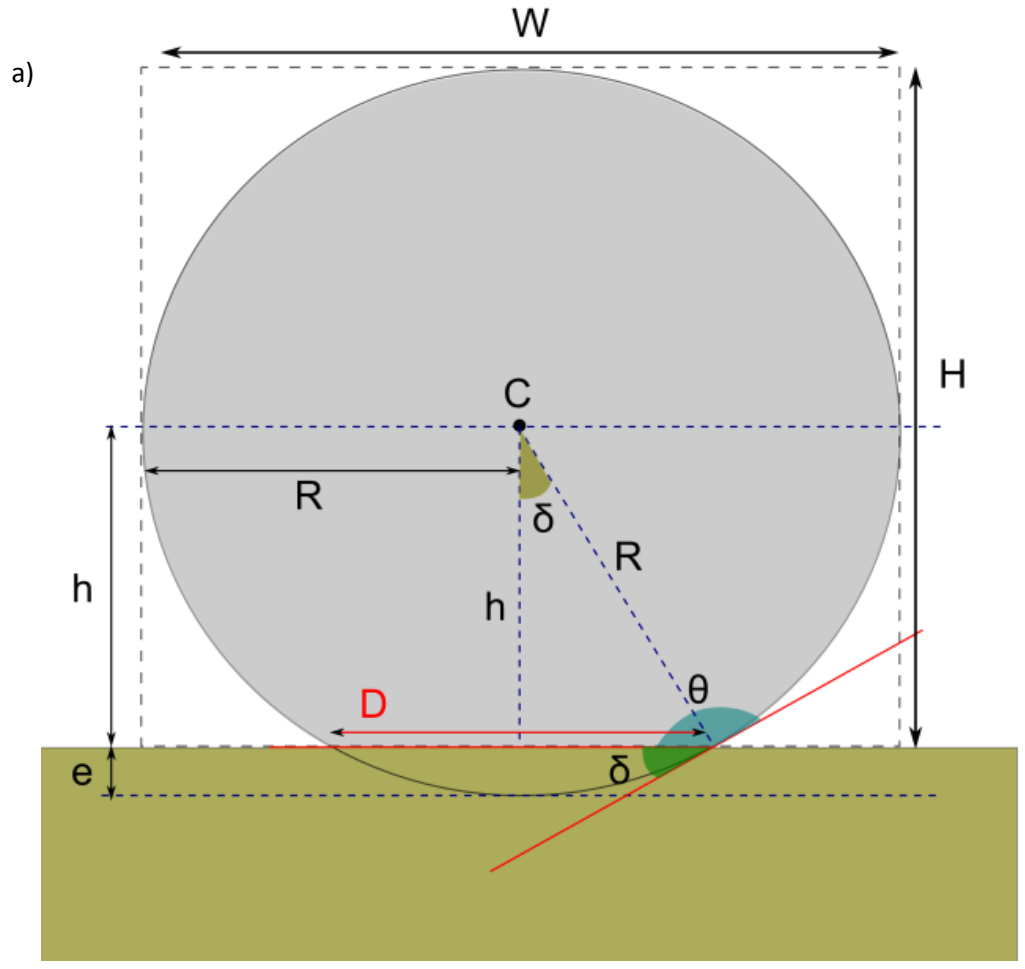

Figure 3. a) Schematic representation of a sitting droplet and its parameters for the describing model when $H \geq R$, which means $V_{cs} \geq V_s/2$.

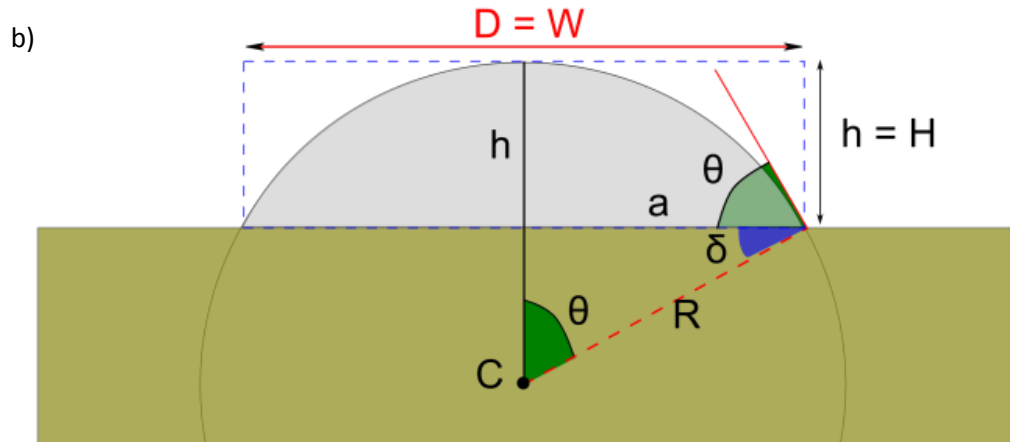

Figure 3 (continuation). b) Schematic representation of a sitting droplet and its parameters for the describing model when $R > H$, which means $V_{cs} < V_s/2$.

Description of the set up

The microinjection set up consists on a Femtojet microinjector (Eppendorf) which is able to inject really small quantities of volumes by liberating controlled quantities of compressed air at a controlled pressure over a capillary tip with a micron sized aperture (femtotips - Eppendorf). These materials are commonly used for cell injection and manipulation. For performing the experiments detailed in chapter 5.2, solutions are first introduced on different femtotips, and then injected under a 30 μL droplet of paraffin oil. Figure 4 shows a schematic representation of the microinjection setup (fig 4a) as well as descriptive images of an array of droplets of different sizes (fig 4b) and a detail of the injection tip (fig 4c).

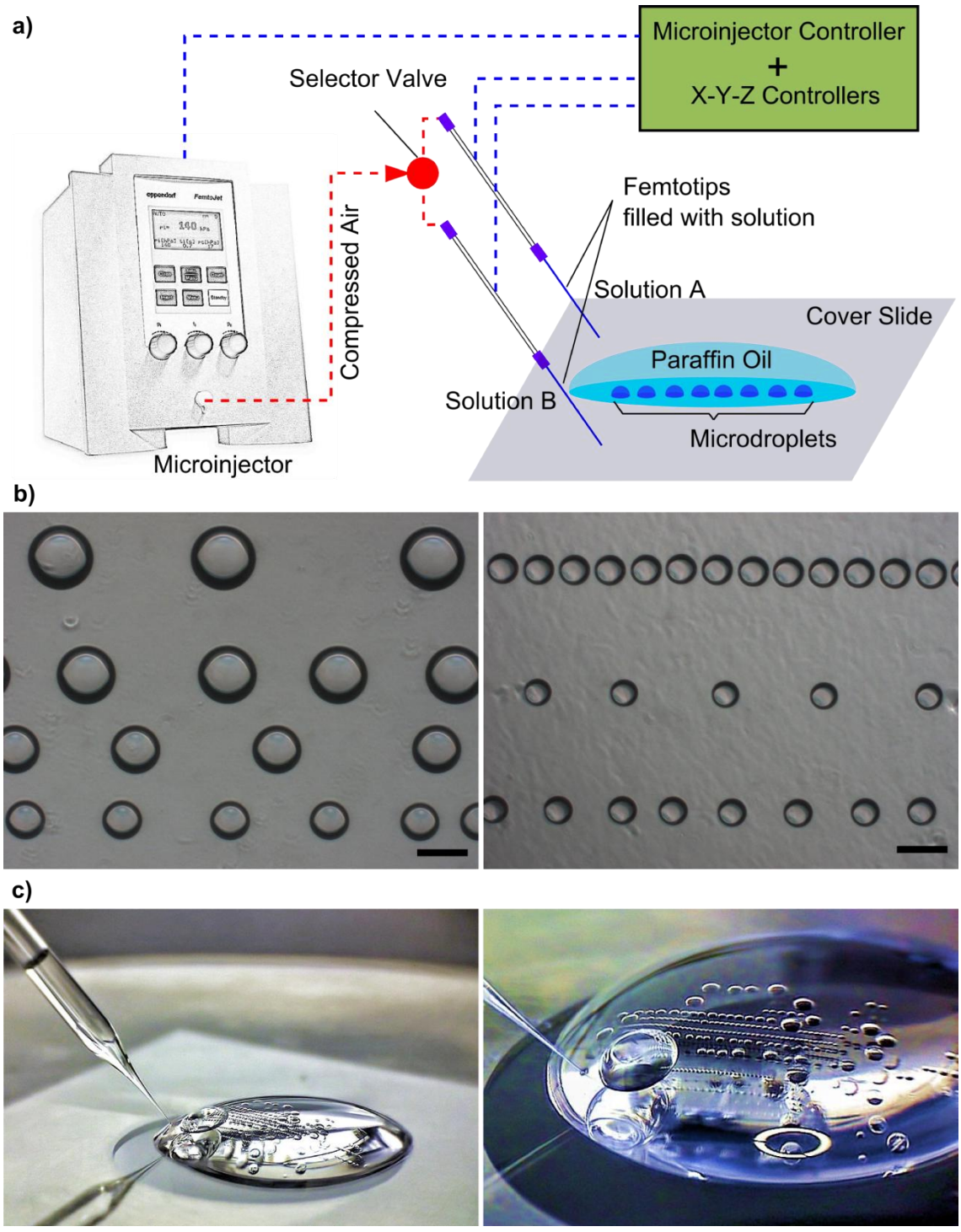

Figure 4. a) Schematic representation of the microinjection set up b) Array of different sized sitting droplets generated by microinjection. Scale bar = 100 µm; c) Femtotip injecting under a 30 µL paraffin oil droplet.

Arrays of microdroplets of a first solution were deposited over a plastic cover slip. Subsequently, an equimolar second solution was added with a second tip to the first droplets in different volume ratios, thus generating droplet mixtures with different molar ratios, directly in a confined space. Femtotips, attached to a capillary holder, were controlled by a home-made micromanipulator consisting of three miniature translation stages (piezo electric, MS30 mechonics) in X, Y and Z with a displacement of 18 mm in the 3 directions by steps of 16 nm [2]. Experiments were monitored with a Zeiss Axio Observer D1 inverted microscope, and initial and mixing volumes were determined through image analysis of the microdroplets, following the model described above. The principle of the experiments is to mix picoliter volumes of the reactant solutions under oil, generating an initial supersaturation. Lately water slowly diffuses from the crystallization drops through the layer of parffin oil, resulting in an increase in the concentration of solute. In situ observation of the precipitation process was carried out from the time of initial droplets mixture until complete crystallization of the droplets.

3. Droplet based microfluidics in teflon capillaries

Nanoliter experiments in chapter 5.2 were performed by applying droplet based microfluidic techniques in a low cost and resistant setup, affordable to any laboratory. Teflon capillaries have been discovered to be an easy-to-use, universally solvent-compatible and cheap microfluidic setup which avoids the use of surfactant and is easily transferable to the laboratory for crystallisation studies [11]. In this set up the plug factory is a T-junction made of PEEK (IDEX P-727 PEEK Tee) [12] being the output tube a Teflon storage tube. The T junction (Figure 5a) has an inner diameter or 152 μm and is connected to Teflon tubing of a diameter of 150 μm. The advantage of both Teflon and PEEK polymers is their compatibility with all solvents, the sole exception being concentrated acid (sulfuric or nitric acid). Equimolar solution volumes of reactants were pumped through a first PEEK T junction and mixed in a capillary (2.8 cm long) that connects this T junction to a second one, which works as the plug factory. The second T

junction is connected to an oil reservoir, which is used as the carrier fluid to generate the droplets (see Figure 5a). Fluorinated oil FC-70 (Hampton Research), which has no or very low miscibility with solvents in general and a good wettability with Teflon was chosen as a carrier fluid to generate arrays of 2 nL plugs inside the teflon capillaries, as shown in Figure 5b.

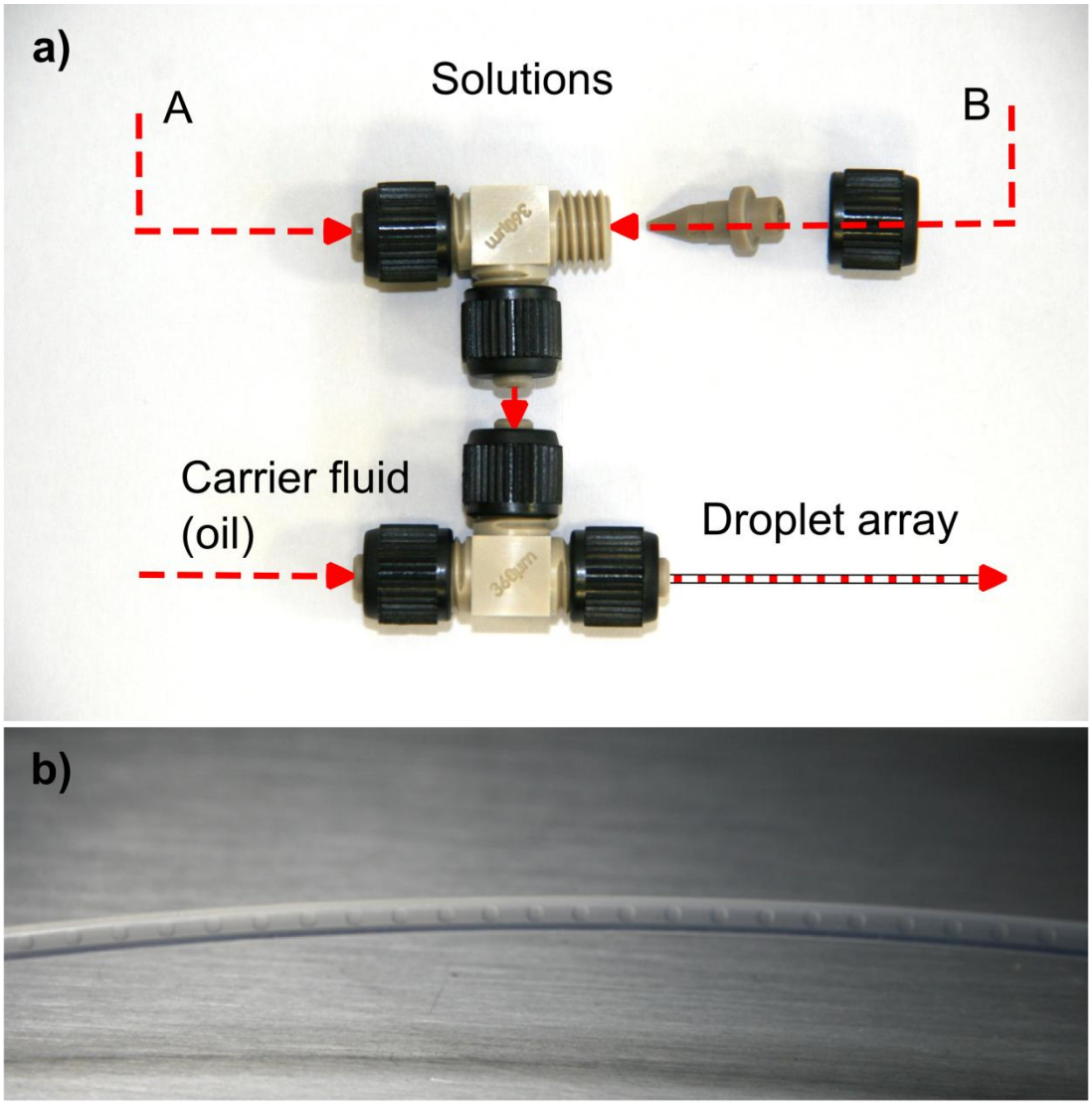

Figure 5. a) Schematic representation of the plug factory; b) Array of 2 nL droplets generated inside a 150 μm internal diameter teflon capillary.

Previously to the performance of experiments of chapter 5.2, three different types of Teflon capillaries were tested for their transparency for in situ observation of experiments and evaporation rate at two different temperatures, in order to explore their sealing capacity for long term experiments. Characteristics of the three materials are detailed below:

- TEFZEL (fluoropolymer):
    - Refractive index: 1.4
    - Permeability at 25 °C ($cm^3/100\ in^2 \cdot 24h \cdot atm/mil$):
        - $CO_2 = 250 - N_2 = 30 - O_2 = 100$
- HALAR (Ethylene - Chlorotrifluoroethylene polymer):
    - Refractive index: 1.447
    - Permeability at 25 °C ($cm^3/100\ in^2 \cdot 24h \cdot atm/mil$):
        - $CO_2 = 330 - N_2 = 10 - O_2 = 25$
- HPFA (fluoropolymer):
    - Refractive index: 1.340
    - Permeability at 25 °C ($cm^3/100\ in^2 \cdot 24h \cdot atm/mil$):
        - $CO_2 = 2260 - N_2 = 291 - O_2 = 881$

For the evaporation experiments only pure water was used to generate the plugs. After filling the capillaries with the droplet arrays, they were quickly sealed applying fire to the borders and closing them with a tong. Experiments were stored in temperature controlled chambers at 20 and 55 °C. Evaporation of aqueous solution through the three studied materials, TEFZEL, HALAR and HPFA was estimated by measuring on time the size of 3 different droplets on each capillary, in order to obtain a meaningful average. It is worth noting that, due to the specific characteristics of each material, the behavior of interfacial surfaces in absence of surfactants is completely different, and the size and shape of the aqueous droplets differ for each material in equal flow parameters. Figure 6 depicts this appreciation.

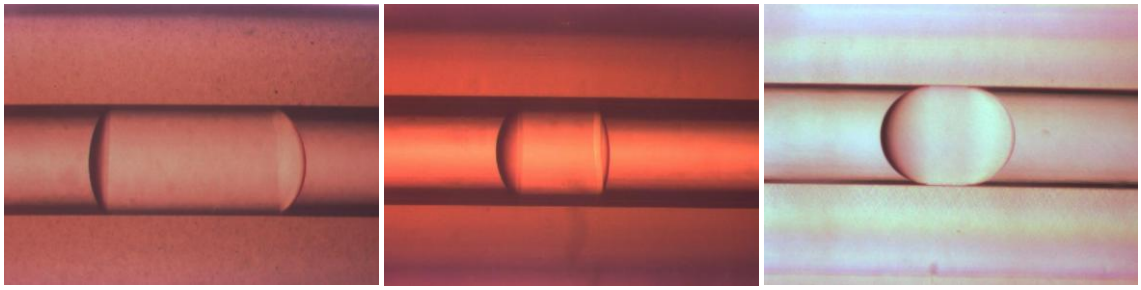

Figure 6. Water droplets inside 0,5 mm internal diameter different material capillaries. From left to right:TEFZEL, HALAR and HPFA.

Results after 6 days experiment are shown in Table 1 and Figure 8. It can be noticed an increment on volume for the droplets after 24 h in HPFA capillary at 55 °C. It is due to the formation of gas bubbles inside droplets because of evaporation of water (see Figure 7). The small variations appreciated during the experiments at 20 °C in all materials are a consequence of the accuracy limits for the length measurements of the droplets. Although we cannot observe any appreciable evaporation after 143 horus at 20°C, for the experiments at 55 °C it has been determined a clear evaporation rate, resulting HPFA capillaries the less evaporative system (Fig. 8).

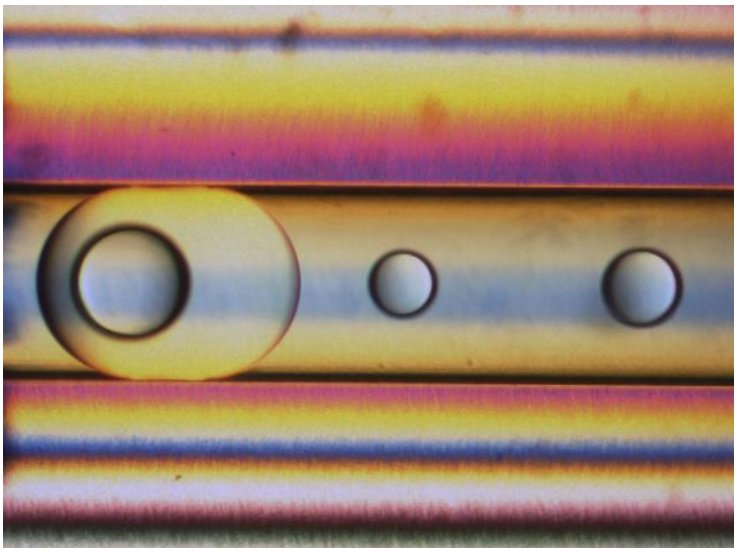

Figure 7. Water droplet inside 0,5 mm internal diameter HPFA capillary, after 24h at 55 ˚C.

Table 1. Measurement of droplets and estimated volume (considering cylinder volume to simplify calculus).

	HPFA						HALAR						TEFZEL					
20 °C	L (mm)			V (nl)			L (mm)			V (nl)			L (mm)			V (nl)		
t0	0,678	0,667	0,672	133	131	132	0,566	0,576	0,574	111	113	113	1,069	1,133	1,021	210	222	200
27 h	0,676	0,669	0,670	133	131	132	0,577	0,588	0,586	113	115	115	1,112	1,135	1,028	218	223	202
54 h	0,668	0,667	0,670	131	131	132	0,571	0,577	0,573	112	113	113	1,119	1,130	1,000	220	222	196
143 h	0,670	0,667	0,671	132	131	132	0,585	0,577	0,581	115	113	114	1,090	1,100	0,976	214	216	192
55 °C	L (mm)			V (nl)			L (mm)			V (nl)			L (mm)			V (nl)		
t0	0,678	0,667	0,672	133	131	132	0,566	0,576	0,574	111	113	113	1,069	1,133	1,021	210	222	200
1 day (27 h)	0,687	0,677	0,704	135	133	138	0,524	0,530	0,530	103	104	104	1,120	1,141	1,176	220	224	231
2 days (54 h)	0,622	0,605	0,641	122	119	126	0,502	0,508	0,502	99	100	99	1,012	1,061	1,048	199	208	206
6 days (143 h)	0,495	0,531	0,518	97	104	102	0,382	0,380	0,384	75	75	75	0,767	0,686	0,701	151	135	138

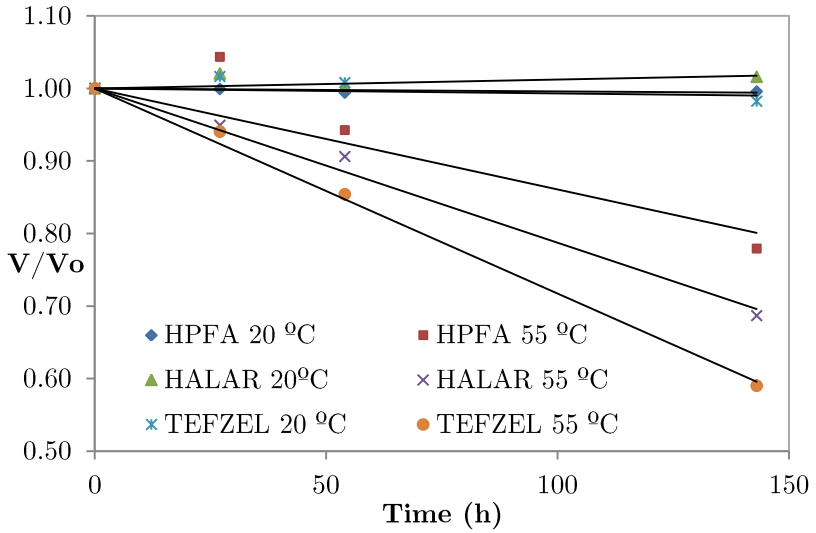

Figure 8. Representation of the estimated volume/initial volume ratio of the measured droplets versus time.

To determine the most appropriate material for in situ observation and monitoring nucleation events, a test has been carried out in two different optical microscopes: Wild Heerbrugg M420 Makroskop (light in reflexion) and Nikon Diaphot inverted microscope (transmission of light through the capillaries). Comparative images are shown in Figure 9. It can be noticed that HPFA capillaries are the most transparent of the three materials. Also a reduction of 0,15 mm in the capillary walls on this material (testing a capillary with higher internal diameter) improves drastically the transparency when monitoring experiments (see Figure 9D). In addition the inverted microscope is the most suitable system for a better observation through these capillaries.

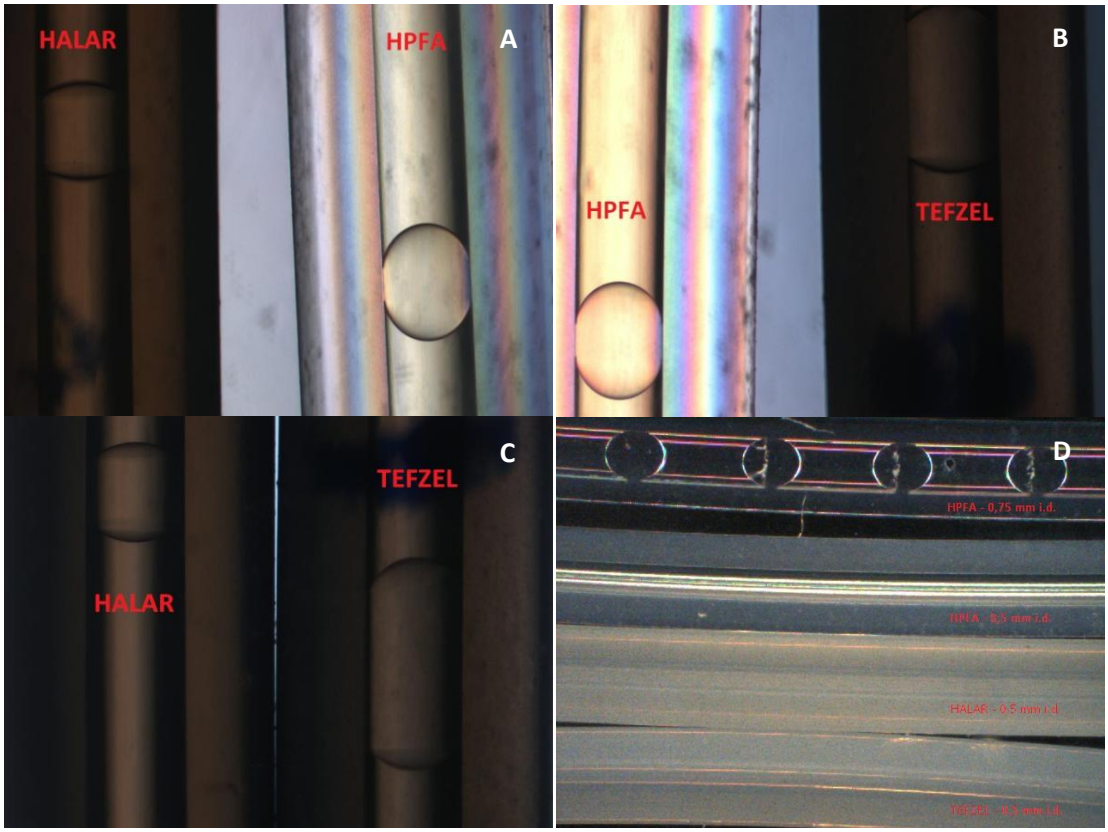

Figure 9. Comparative images, captured with the inverted microscope Nikon Diaphot for the different 0,5 internal diameter capillaries: A) HALAR (left) – HPFA (right), B) HPFA (left) – TEFZEL (right), C) HALAR (left) – TEFZEL (right). D) Comparative image captured with the Wild Heerbrugg M420 Makroskop. From up to down: 1)HPFA capillary (i. d. 0,75 mm, with aqueous droplets of $CaCO_3$), 2) HPFA capillary (i. d. 0,5 mm, empty), 3) HALAR (i.d. 0,5 mm, empty), 4) TEFZEL (i.d 0,5 mm, empty).

4. Crystallization mushroom

The characteristics of an innovative device called the "crystallization mushroom" [13, 14] is now described. In general lines, the crystallization mushroom consists of a controlled chamber in which vapour diffusion experiments can be performed with a high reproducibility due to its special characteristics. The advantages that the "crystallization mushroom" offers compared to other crystallization devices are the reduced consumption of reagents during the crystallization process, since it permits the study of micro-volumes (droplets around 40 μL), and the high reproducibility due to the possibility of running 12 batches of crystals for each experiment. Therefore, this set up may be suitable to evaluate interactions and/or the co-crystallization of many substances of interest with

small amounts of high added value products as proteins, polymers, or drugs for studies in the fields of biomineralization and biomaterials.

The experiments performed in chapter 4 of this manuscript were carried out in 2 "crystallization mushrooms" (Triana Science & Technology, S.L.) at 20 ± 2 °C and total pressure of 1 atm. Each crystallization mushroom is a chamber consisting of a glass Petri dish (2 × 10 cm diameter) placed on top of a cylindrical vessel 5 cm in diameter and 3 cm in height, connected to the Petri dish by a hole (Figure 10). The empty space contained inside the system (cylindrical vessel and Petri dish) has a total volume of 153.678 mL [12]. Each mushroom contained 12 polystyrene microbridges (small plastic blocks with a shallow well to facilitate sitting drop crystallization) concentrically placed inside the precipitation chamber (upper chamber). Each micro-bridge (Hampton Research, Inc) held 40 μL of a solution whose composition is 500 mM $Ca(CH_3COO)_2$ and 300 mM $(NH_4)_2HPO_4$ (Ca/P=5/3). A 3 mL aliquot of a 40 mM NH4HCO3 solution was placed inside the gas generation chamber (lowest reservoir of this device). The glass cover and the precipitation chamber were sealed with silicon grease. Once each "mushroom" was closed and sealed, the underlying NH_4HCO_3 solution started to release NH_3 and CO_2 gasses into the free space of this device (0.112 L). Both CO_2 and NH_3 gases diffused and re-dissolved into the aqueous droplets increasing their pH until it reached an asymptotic value.

Precipitation process was followed by pH measurements by using an electrode (Titan model, Sentron) placed on a hole located on a side wall of the upper chamber (as illustrated in Figure 10), which allows for the measurement of the pH in droplets.

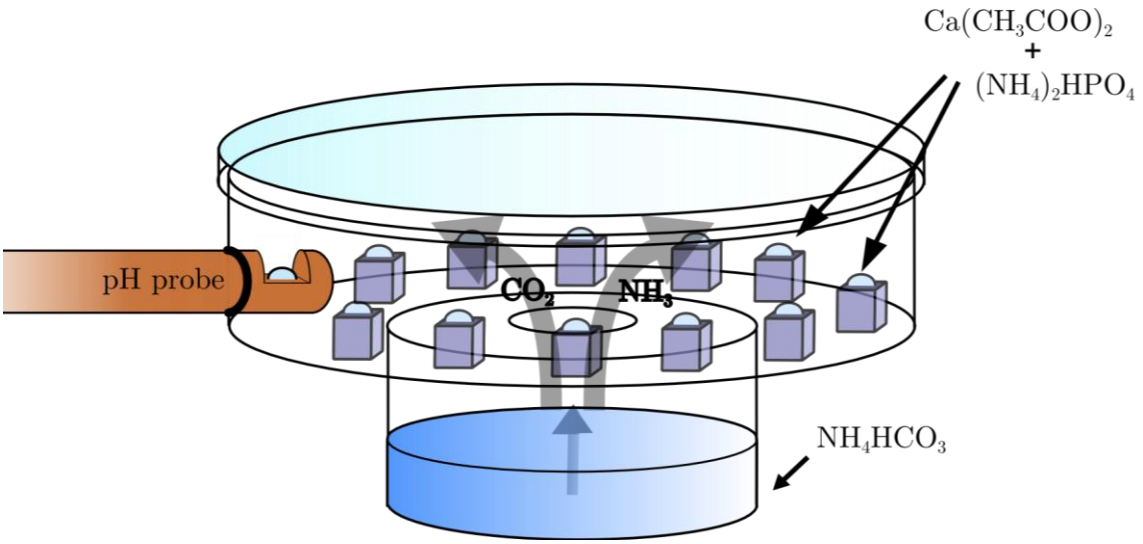

Figure 10. Schematic illustration of the "crystallization mushroom" and the experimental set up applied in chapter 4.

5. Modified Mach-Zehnder interferometer with phase shifting applied to mass transport characterization

Mach-Zehnder Interferometry (MZI) is a technique extensively used in fields as diverse as optical physics, fluid science, digital holographic microscopy, microgravity research and heat and mass transport [15-19]. Our purpose with this technique has been to use it as a refraction index mapping application, which is a helpful method for characterizing the mixing of two different solutions.

The principle of Mach-Zehnder interferometry is described as follows: A laser beam is divided in the reference and the sample (test) beams by means of a beamsplitter. The sample beam propagates through the experimental volume before being recombined with the reference beam. The result of the recombination is the generation of interference fringes (Interferogram) at imaging plane. The interferogram carries the information of the variation of the optical path between the object and the reference beam. A schematic view of a Mach-Zehnder interferometer is shown in Figure 11.

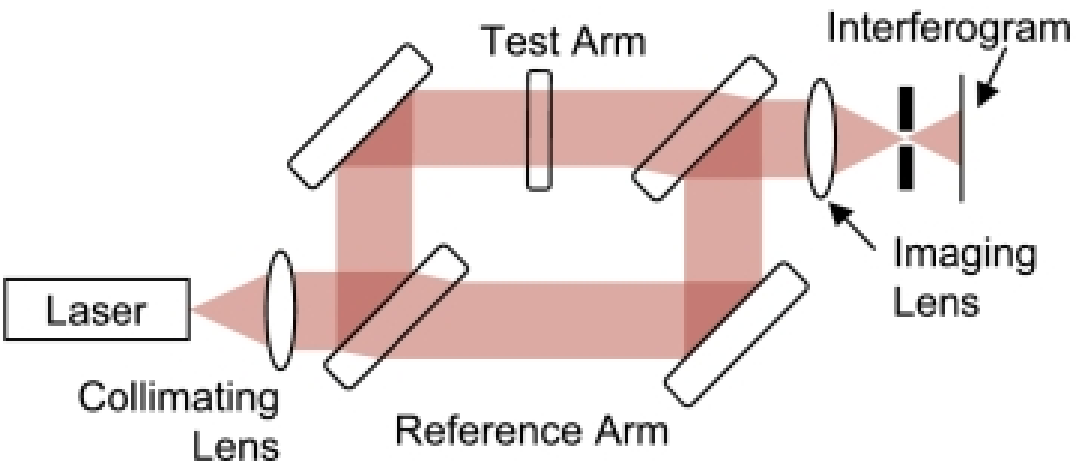

Figure 11. A typical Mach-Zehnder Interferometer setup

The intensity fringes resulting from the interference between the reference beam and the object beam is expressed as:

$$I(x,y) = I_0(1 + \gamma(x,y)cos[\psi(x,y)]) \tag{5.1}$$

where I_0 is the sum of the reference and sample beam intensities, γ is the fringe modulation and x,y are spatial coordinates. Fringe modulation is proportional to the ratio between the reference and sample intensities, according to: $\gamma \propto 2\frac{\sqrt{I_r I_s}}{I_r + I_s}$, but depends also on the illumination beam coherence.

$\Psi(x,y)$ is the integration of the phase difference between the reference and sample beams along the optical path z:

$$\psi(x,y) = \frac{2\pi}{\lambda}\int_{z_1}^{z_2}[n(x,y,z) - n_r]\,dz \tag{5.2}$$

where λ is the illumination wavelength, z_2-z_1 is the sample volume thickness along the laser propagation path, $n(x,y,z)$ is the local refractive index inside the sample volume and n_r is a reference refraction index.

Phase Shifting Interferometry

Phase cannot be directly extracted from a single interferogram (Eq. 5.1). Phase shifting interferometry (PSI) allows extracting the real phase for each pixel of the image. It consists in acquiring a minimum of 3 phase-shifted images of the same fluid status and in calculating the phase of each pixel with a phase shifting algorithm. The method consists on introducing a small (controlled) phase delay in the reference beam between the recorded images. The intensity distribution on the acquired images (j is the number of the image) is given by:

$$I_j(x,y) = I_0(1 + \gamma(x,y)cos[\psi(x,y) + j\alpha(x,y)]) \tag{5.3}$$

Generally, the phase step is calibrated to be $\alpha = \pi/2$ in such way that the set of images can be seen as a set of equations to be solved easily. Several methods are possible to introduce the phase shift. Phase shifting can be performed mechanically, by modulation of reference arm refraction index or by changes on illumination wavelength. The most extended method consists on introducing an optical path modification in the reference arm by displacing a mirror [20-22]. This mirror is either mounted on a piezoelectric transducer (PZT) or on a stepper motor. In refraction index modulation methods, the delay is introduced by means of liquid-crystal variable retarders (LCVR) and pockels cells [23, 24]. Such approaches provide satisfactory performances, but have some drawbacks (cost and time constants) that might limit its use depending on the application. An alternative way to achieve the phase shift is introducing very slight changes in the illumination wavelength. No moving parts or additional optical elements are then necessary for introducing the phase shift in this case.

LEC's Mach-Zehnder Interferometer

In our laboratory, we have developed a Phase-Shift Mach-Zehnder Interferometer based on wavelength modulation. Figure 12 shows a schematic view of our instrument. The interferometer follows an unbalanced Mach-Zehnder configuration. Indeed, the

reference arm is longer than the sample arm, in an amount of $2U$. This unbalance allows reducing the bias current range necessary to scan the phase shift range, as further explained below. The laser diode temperature, as well as bias current, both are controlled with a composite driver. Emitted light pass first through a Faraday isolator, so as to avoid any back-reflection towards the semiconductor laser cavity. A movable short focal length lens L1 and a rotating ground glass diffuser allow tuning the spatial coherence of the beam. L2 is a collimating lens. A half-wave plate is placed before a polarizing beam splitter PBS; the plate can be manually rotated in order to equilibrate the laser intensity between the interferometer arms. The sample beam is transmitted by the PBS whereas the reference beam is reflected and follows the reference path through the mirrors M1 and M2. As the reference and sample beams polarizations are orthogonal, another half-wave plate is placed on the reference beam path. Both beams are recombined by a non-polarizing beam splitter NPBS. Imaging of the sample and the interference is performed by a long working distance microscope and a CCD camera. The whole system is controlled and automated through a PC running Labview® based scripts, developed ad-hoc for the instrument.

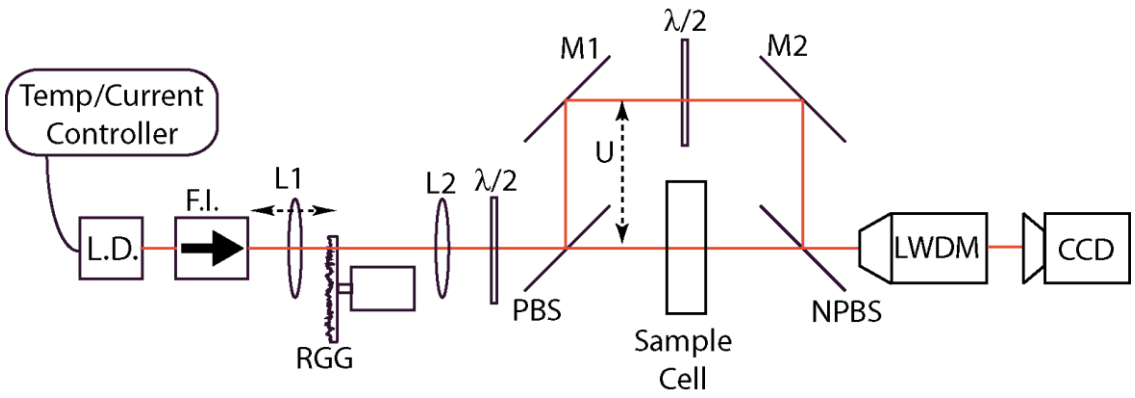

Figure 12. Schematic representation of the Mach-Zehnder interferometer developed at LEC.

For the unbalanced interferometer setup, the set of equations 1.3 is defined as follows:

$$I_j(x,y) = (I_0 + j\Delta I)\big(1 + \gamma(x,y)cos\big[\psi + \Delta\psi_j\big]\big) \tag{5.4}$$

where:

$$\psi + \Delta\psi_j \cong \frac{2\pi}{\lambda}\Big[\big(2U + \Delta S(x,y)\big) - j\frac{\Delta\lambda}{\lambda}\big(2U + \Delta S(x,y)\big)\Big] \tag{5.5}$$

where $\Delta S(x,y)$ is the contribution of the sample to the phase between the reference and the sample arm.

In practice, the interferometer unbalance is several orders of magnitude greater than variations in the optical path along the sample volume. The assumption $\Delta S(x,y) << 2U$ is therefore valid and set (5.5) can be rewritten as:

$$I_j(x,y) = (I_0 + j\Delta I)\Big[1 + \gamma(x,y)cos\Big(\frac{2\pi}{\lambda}\big(2U + \Delta S(x,y)\big) - j\frac{2\pi\Delta\lambda}{\lambda^2}2U\Big)\Big] \tag{5.6}$$

The phase step is then:

$$\alpha_i = j\frac{2\pi\Delta\lambda}{\lambda^2}2U \tag{5.7}$$

$$\Delta\lambda = C\Delta i \quad \text{with} \quad C = \frac{\partial\lambda}{\partial i} \tag{5.8}$$

$$\Delta I = D\Delta i \quad \text{with} \quad D = \frac{\partial I}{\partial i} \tag{5.9}$$

where i is the laser bias current , C and D stand for the linear dependencies of the Laser Diode Wavelength and Intensity on the bias current. Equation (5.7) illustrates the versatility of the unbalanced setup and wavelength tunability. Indeed, adjusting unbalance U, which varies within a ten of cm range, allows limiting the current variation necessary to scan the phase shift within a 0-2π range. This advantage is non-negligible as the current scan range should be as small as necessary to avoid undesirable laser mode hopes. Therefore, for N phase steps and a scan from 0-2π , the current step and unbalance are fixed according to:

$$N\Delta i < \varepsilon_{MH}\ ,\ \ L_{LD} > 2U \gg D\frac{\lambda^2}{CI_0} \tag{5.10}$$

where ε_{MH} is the laser diode current range between consecutive mode hopes and L_{LD} is the laser diode coherence length. Optionally, Intensity variation could be minimized according to the third inequality (in red).

Phase calculation algorithm

Varying laser bias currents unavoidably leads to laser intensity variations (Eq. 5.9). It is reasonable to minimize these variations, to an extent high enough to ignore them (Eq. 5.10) or kept them small so as to preserve the common background and noise cancellation advantages of PSI. When intensity variations cannot be ignored i.e. the third inequality in Eq. 5.10 is not fulfilled, there are two ways to proceed: One is correcting acquired images I_j intensity according to:

$$I_{corr,j} = I_j\left(\frac{I_0}{(I_0 + jD\Delta i)}\right) \tag{5.11}$$

$D\Delta i$ can be measured for each set of phase-shifted images with the laser diode internal photodiode. The second one is using an algorithm that takes into account intensity variations. For phase estimation purposes N can be varied from 3 to infinity. However, for only 3 images, there is not explicit feedback concerning the phase-step calibration. There's a multiplicity of algorithms, but Hariharan's algorithms (N=5) is one of the most used, as it provides a minimized phase error for a phase step of $\pi/2$ [24]. Phase map, fringe modulation and phase step can be estimated from the set of 5 phase-shifted interferograms:

$$\psi(x,y) = atan\left[\frac{2[I_2(x,y) - I_4(x,y)]}{2I_3(x,y) - I_1(x,y) - I_5(x,y)}\right] \tag{5.12}$$

$$\gamma(x,y) = \frac{3\sqrt{(I_4 - I_2)^2 + (I_1 + I_5 - 2I_3)^2}}{2[I_1 + I_2 + 2I_3 + I_4 + I_5]} \tag{5.13}$$

$$\cos[\alpha(x,y)] = \frac{[I_5(x,y) - I_1(x,y)]}{I_4(x,y) - I_2(x,y)} \tag{5.14}$$

The phase map is obtained by means of an expression involving the arctangent function (Eq. 5.12). This mathematical function returns values that are known between the limits π and -π. Hence the result is given modulus 2π and discontinuities with values near to 2π appear in the phase distribution. Unwrapping is the procedure by which these discontinuities are resolved; the result is converted into the desired continuous phase function. In the LEC laboratory setup, phase is unwrapped according to the algorithm PUMA, developed by Bioucas-Dias and coworkers from the Instituto de Telecomunicações, Lisboa [25].

When working with a time series experiment with assumed known starting conditions, it is possible to either subtract a starting reference plane fit or the first acquired phase image to all subsequent phase images in the series, hence, the phase variation is given:

$$\Delta\psi(x,y,t) = \frac{2\pi}{\lambda}\int_0^W \Delta n(x,y,z,t)\,dz - \psi(x,y,t_0) \tag{5.15}$$

where W is the sample volume thickness. The average index variation along the observation axis (z) is:

$$\overline{\Delta n(x,y,z,t)} = \frac{\lambda}{2\pi Z}\Delta\psi(x,y,t) \tag{5.16}$$

From equation Eq. 5.16 and a known refraction index concentration coefficient $^{\Delta n}/_{\Delta C}$ obtained from calibration, the concentration map variations $\Delta C(x,y,z,t)$ time series can be obtained:

$$\overline{\Delta C(x,y,z,t)} = \frac{\lambda}{2\pi Z\left\{^{\Delta n}/_{\Delta C}\right\}}\Delta\psi(x,y,t) \tag{5.17}$$

References

1. Detoisien T, Forite M, Taulelle P, Teston Jl, Colson D, Klein JP, et al. A Rapid Method for Screening Crystallization Conditions and Phases of an Active Pharmaceutical Ingredient. Org Process Res Dev. 2009;13(6):1338-42.

2. Grossier R, Hammadi Z, Morin R, Magnaldo A, Veesler S. Generating nanoliter to femtoliter microdroplets with ease. Appl Phys Lett. 2011;98(9):091916-3.

3. Hostomský J, Jones AG. Crystallization and agglomeration kinetics of calcium carbonate and barium sulphate in the MSMPR crystallizer. Industrial Crystallization '93. 1993:2-055.

4. Plummer LN, Wigley TML, Parkhurst DL. The kinetics of calcite dissolution in CO 2 -water systems at 5 degrees to 60 degrees C and 0.0 to 1.0 atm CO 2. American Journal of Science. 1978;278(2):179-216.

5. García-Carmona J, Gómez-Morales J, Rodríguez-Clemente R. Morphological control of precipitated calcite obtained by adjusting the electrical conductivity in the Ca(OH)2-H2O-CO2 system. J Cryst Growth. 2003;249(3-4):561-71.

6. Meldrum FC. Calcium carbonate in biomineralisation and biomimetic chemistry. Int Mater Rev. 2003;48(3):187-224.

7. Grossier R, Magnaldo A, Veesler S. Ultra-fast crystallization due to confinement. J Cryst Growth. 2010;312(4):487-9.

8. Kashchiev D. Nucleation: Basic Theory with Applications2000.

9. Volmer M. Kinetik der Phasenbildung: mit 15 Tab. im Text: T. Steinkopf; 1939.

10. Sigsbee R. Vapor to condensed-phase heterogeneous nucleation. Nucleation Zettlemoyer AC (ed) New York, Marcel Dekker. 1969:151-224.

11. Ildefonso M, Candoni N, Veesler S. A Cheap, Easy Microfluidic Crystallization Device Ensuring Universal Solvent Compatibility. Org Process Res Dev. 2012;16(4):556-60.

12. Dombrowski RD, Litster JD, Wagner NJ, He Y. Crystallization of alpha-lactose monohydrate in a drop-based microfluidic crystallizer. Chem Eng Sci. 2007;62(17):4802.

13. Hernández-Hernández A, Rodríguez-Navarro AB, Gómez-Morales J, Jiménez-Lopez C, Nys Y, García-Ruiz JM. Influence of Model Globular Proteins with Different Isoelectric Points on the Precipitation of Calcium Carbonate. Cryst Growth Des. 2008;8(5):1495-502.

14. García-Ruiz J, Hernández-Hernández M, Gómez-Morales J. D-36 Crystallisation Mushroom: A new crystallisation tool by vapour diffusion technique. VDI BERICHTE. 2005;1901(2):963.

15. Agble D, Mendes-Tatsis MA. The effect of surfactants on interfacial mass transfer in binary liquid-liquid systems. International Journal of Heat and Mass Transfer. 2000;43(6):1025-34.

16. Duan L, Kang Q, Hu WR, Li GP, Wang DC. The mass transfer process and the growth rate of protein crystals. Biophysical Chemistry. 2002;97(2-3):189-201.

17. Dworecki K, Wąsik S, Ślęzak A. Temporal and spatial structure of the concentration boundary layers in a membrane system. Physica A: Statistical Mechanics and its Applications. 2003;326(3-4):360-9.

18. Dworecki K, Ślęzak A, Ornal-Węsik B, Wąsik S. Effect of hydrodynamic instabilities on solute transport in a membrane system. Journal of Membrane Science. 2005;265(1-2):94-100.

19. Sajith V, Sobhan CB. Digital interferometric measurement of forced convection heat transfer in a miniature rectangular channel. Experimental Heat Transfer. 2008;21(4):314-33.

20. Bruno L, Poggialini A, Felice G. Design and calibration of a piezoelectric actuator for interferometric applications. Optics and Lasers in Engineering. 2007;45(12):1148-56.

21. Langoju R, Patil A, Rastogi P. Phase-shifting interferometry in the presence of nonlinear phase steps, harmonics, and noise. Optics Letters. 2006;31(8):1058-60.

22. Patil A, Rastogi P. Approaches in generalized phase shifting interferometry. Optics and Lasers in Engineering. 2005;43(3-5):475-90.

23. Schwider J, Burow R, Elssner KE, Grzanna J, Spolaczyk R, Merkel K. Digital wave-front measuring interferometry: Some systematic error sources. Applied Optics. 1983;22(1):3421-32.

24. Hariharan P, Oreb B, Eiju T. Digital phase-shifting interferometry: a simple error-compensating phase calculation algorithm. Applied Optics. 1987;26(13):2504-6.

25. Bioucas-Dias JM, Valadão G. Phase unwrapping via graph cuts. IEEE Transactions on Image Processing. 2007;16(3):698-709.

CHAPTER 3

Significance of heterogeneous nucleation mechanisms in calcium sulfate precipitation

CHAPTER 3

Significance of heterogeneous nucleation mechanisms in calcium sulfate precipitation

1. State of the art

A great deal of work has been undertaken in the past decades in order to improve our understanding of crystal growth from solution, from a fundamental point of view, but also from applied engineering approaches, with the main purpose of establishing a control over the industrial crystallization processes. One of the key parameters in these studies is the induction time, i.e. waiting time for crystals to appear after the creation of the supersaturated state of a solution. These waiting times can be measured as a function of experimental conditions (supersaturation, temperature, pressure, etc.). Employing the classical nucleation theory (CNT) the surface free energy between the crystalline phase and the surrounding solution can be estimated. In turn this parameter, characteristic of the thermodynamic behaviour of the studied substance, can be used to extrapolate induction times outside of the studied supersaturation range, which is of great interest in industrial crystallization [1, 2] and also to model crystallization processes from solution taking place in Nature, which occurs at time scales and supersaturations not attainable at laboratory.

One of the major mineral phases precipitating from solution is gypsum ($CaSO_4 \cdot 2H_2O$), and massive deposits are found on the Earth surface [3, 4], but also abundance of this mineral has been detected on the Mars surface [5-7]. Due to its geological importance, but also because of its industrial relevance as a construction material and as a major scalant, the precipitation dynamics of gypsum is a much investigated subject [8-11]. Multiple studies determining the induction period of gypsum nucleation as a function of solution parameters (temperature [12-14], salinity [14, 15], additives [16, 17], among others) can be found in literature. From these experimental

data the activation energy barrier and the interfacial tension, both obtained through the kinetics of the crystallization process, are usually determined considering a simplified version of the CNT [12-14, 18, 19]. This provides useful information that permits the interpretation of the nucleation process or the extrapolation of different nucleation conditions, being of interest for industrial application. In most of those studies the nucleation kinetics are determined for solutions that are continuously (and vigorously) mixed, but in natural conditions or in scale formation in pore membranes (occurring in desalination units) hydrodynamic conditions are much smoother, and mainly a consequence of natural (or gravity induced) convection, and thus it is not clear which effect stirring (or the absence of) exerts on the precipitation kinetics. To attain a meaningful extrapolation from kinetic data obtained in the laboratory to low supersaturation scaling processes, as well as to natural conditions, such data are a must.

The aim of the present work is to evaluate the importance of heterogeneous nucleation in the precipitation mechanism of $CaSO_4 \cdot 2H_2O$. Understanding the precise nucleation mechanisms is crucial for designing effective anti-scalant strategies. For that purpose we have applied the CNT model, without simplifications, for the interpretation of experiments performed in heterogeneous nucleation conditions, as well as for data extracted from literature, with the aim of determining gypsum interfacial energy. To do so we have tested two hypothesis: (I) Do nucleation kinetics of gypsum determined in known heterogeneous conditions differ from the more common industrially inspired experiments? (i.e. stirring versus non-stirring and high supersaturations versus low supersaturations); and (II) how much the simplification of the CNT model do affect the estimation of $CaSO_4 \cdot 2H_2O$ thermodynamic parameters?

2. Experimental

Preparation of supersaturated solutions of $CaSO_4$

Stock solutions of calcium chloride dihydrate ($CaCl_2 \cdot 2H_2O$, Bioxtra, ≥ 99,0 % pure, Sigma - Aldrich) and sodium sulfate (Na_2SO_4, ACS reagent, ≥ 99,5 % pure, Sigma - Aldrich) of 2.0 M concentration each were prepared with Milli-q water and filtered by using 0,22 µm Millipore filters. Reactant solutions were all prepared by dilution of the 2.0 M stock solutions, and a determined mass of sodium chloride (NaCl, ACS reagent, , ≥ 99,0 % pure, Sigma - Aldrich) was added to equilibrate ionic strength in each experiment with respect to the experiment of maximum concentration. Subsequently solutions were again filtered with 0,22 µm Millipore filters in order to eliminate as much as possible all foreign particles. Finally, the supersaturated solutions of calcium sulfate in our experiments were prepared by mixing directly into the reaction wells equal volumes of two equimolar aqueous reactant solutions for each experimental condition and gently mixed with the pipette tip for at least 10 seconds each. In order to avoid as much as possible the presence of impurities and foreign particles, all the material used to prepare, store, and manipulate the solutions was carefully cleaned by submersion in concentrated potassium permanganate oxidizing solution for 24 hours. After that, a concentrated solution of hydrogen peroxide and sulfuric acid was used to oxidize the remaining material. Subsequently all material was rinsed several times in bi-distilled water and finally cleaned with milli-q water.

Table 1. Saturation Index calculated by PHREEQ-C at 20°C for different initial solutions: a) Without considering any NaCl ion effect over the saturation of the system, b) considering just half of the concentration of NaCl, c) taking into account the real NaCl concentration for each experiment

T=20 °C	**Saturation Index, SI**		
Conc. (mM)	**NaCl (a)**	**NaCl (b)**	**NaCl (c)**
16	0,03	-0,02*	-0,07*
17	0,06	0,01	-0,03*
18	0,09	0,04	0**
19	0,12	0,07	0,01
20	0,15	0,1	0,05
21	0,18	0,12	0,08
22	0,2	0,15	0,11
23	0,23	0,17	0,13
24	0,25	0,19	0,15
25	0,27	0,22	0,17
26	0,29	0,24	0,19
27	0,31	0,26	0,21
28	0,33	0,28	0,23
29	0,35	0,3	0,25
30	0,37	0,31	0,27
31	0,39	0,33	0,29
32	0,4	0,35	0,3
33	0,42	0,36	0,32
34	0,44	0,38	0,33
35	0,45	0,39	0,35
36	0,47	0,41	0,36
37	0,48	0,42	0,38
38	0,49	0,44	0,39
39	0,51	0,45	0,41
40	0,52	0,46	0,41

*Undersaturated solutions.

**Solution in saturation conditions.

Solution speciation and supersaturation for each nucleation experiment was determined with PHREEQ-C software [20]. PHREEQ-C uses Davies equation and/or the extended Debye-Hückel equation to estimate the activity coefficients of the species, as a function of the ionic strength. PHREEQ-C expresses supersaturation by comparing the chemical activities of the dissolved ions of the mineral (ion activity product, IAP) with their solubility product (K_{sp}) through the Saturation Index, SI, which is defined as $SI=log(IAP/K_{sp})$. It was observed that the theoretical effect of NaCl concentration on the solubility of $CaSO_4 \cdot 2H_2O$, calculated by PHREEQ-C, is overestimated, as the program determines a range of concentrations in which experiments should be in undersaturated conditions but where we have found gypsum crystallization events. Table 1 shows the saturation index for three different conditions: without considering any NaCl ion effect on the saturation of the system, considering just half of the concentration of NaCl, and taking into account the real NaCl concentration for each experiment, at 20 °C. For our studies we selected the saturation index data calculated without the effect of diluted salt, as we considered that these data represent more faithfully our observations.

Nucleation experiments set-up

Preliminary experiments were carried out to determine the optimal volume for a correct monitoring of the experiments. The final choice was based on merging our interest of studying small volumes, which allows a faster homogenization without stirring, combined with the minimum volume that permits neglecting the effect of water evaporation during the trials. To reduce evaporation as much as possible, a layer of mineral oil was placed on top of the crystallization solution. All experimental conditions were reproduced from 6 to 12 times in order to obtain a reliable data set and being able to calculate a meaningful average. All nucleation experiments were carried out in 0.2 ml batch reactors prepared in HPLC sealed glass vials. For 20 °C, glass vials were maintained in a temperature control chamber, except during observation. Experiments at

higher supersaturations that did not permit stabilization at 20 °C during the storing/monitoring intervals were stored and monitored in the laboratory room at 25 °C. Finally, experiments at 55 and 58 °C were stored and monitored in a peltier based thermostatic multi-well set up, coupled to an inverted microscope (Nikon Eclipse TE2000-S) [21].

Experiments carried out using limestone as a substrate to favor heterogeneous nucleation where set up also at 20, 25, 55 and 58 °C by duplicate. For a first set of experiments, a piece of limestone of 2-3 mm size (previously cleaned several times with bi-distilled water and finally with milli-q water), was added to the crystallization solutions. For a second set of experiments a thin film of 30 um thickness and 2-3 mm^2 surface prepared on a glass substrate and cleaned in the same conditions was added. Considering the very low solubility of calcite in water (K_{sp} =3.36x10^{-9} at 25 °C and pH=7) the concentration of calcium was not significantly changed. All natural limestone samples used in our experiments were collected at the Naica mine (Mexico). All samples were immediately washed with bi-distilled water and ethanol after removal from crystallization solutions before their analysis.

Fitting and error calculations

The accuracy of the fitting curves was evaluated by using the first-order Taylor method for propagating uncertainties [22, 23]. The experimental values were fitted to equation (10) by means of the non-linear least squares method (NLS) represented as dashed lines by using ***R*** [24], a free software environment for statistical computing and graphics, and the ***R***-package *nls*. The confidence intervals of the fittings, calculated by quadratic propagation of the fitting parameters, were represented as shaded areas.

Classical nucleation theory, CNT

The cornerstone of Classical Theories of Nucleation is the definition of molecular cluster. Indeed, as described in the introduction chapter, a N-sized (molecular) cluster is nothing but a set of N molecules spatially arranged in such a way that even being very small it has associated the same physical properties as those of stable bulk phase (e.g. density, surface tension, etc.). The most extended equation for nucleation frequency J_{CNT}, as described in equation (1.13) from the introduction section is:

$$J_{CNT} \simeq \mathfrak{A}\, exp\left(-\frac{16\pi v_0^2 \sigma^3 \psi(\theta_\omega)}{3k_B{}^3 T^3 \ln^2 S}\right) \tag{1.13}$$

where $\mathfrak{A} = A\,S = z_d \gamma_N \rho_1 \sqrt{4\pi c^2}\, v_0^{1/3} D_1 [N^*]^{1/3}$, denoting the J_{CNT} relation with the concentration of clusters of critical size, N^*, which is S-dependent. It should be noted that the pre-exponential factor A has a dependence on S, which emerges not only through the factor $(N^*)^{1/3}$ but also through the factor z_d. Nevertheless, as Kashchiev discussed in his seminal work [25], the variation of A with S is rather weak and in some cases can be considered S-independent. Thus (equations (4.8) and (13.36) of [25]), $z_d \propto ln^2 S$, and $(N^*)^{1/3} \equiv N_*^{1/3} \propto \ln^{-1} S$, thus $z_d N_*^{1/3} \sim \ln S$.

However, the factor $\mathfrak{A}$ has been wrongly applied in several works and assumed to be constant. Indeed, as we have shown, by applying the above analysis we know that $\mathfrak{A} \propto S \ln S$. Figure 1 shows the graphical representation of A and $\mathfrak{A}$ S dependence. One immediately deduces from this figure that considering $\mathfrak{A}$ as S -independent is not an accurate approximation and, it could involve wrong interpretations of the experimental results.

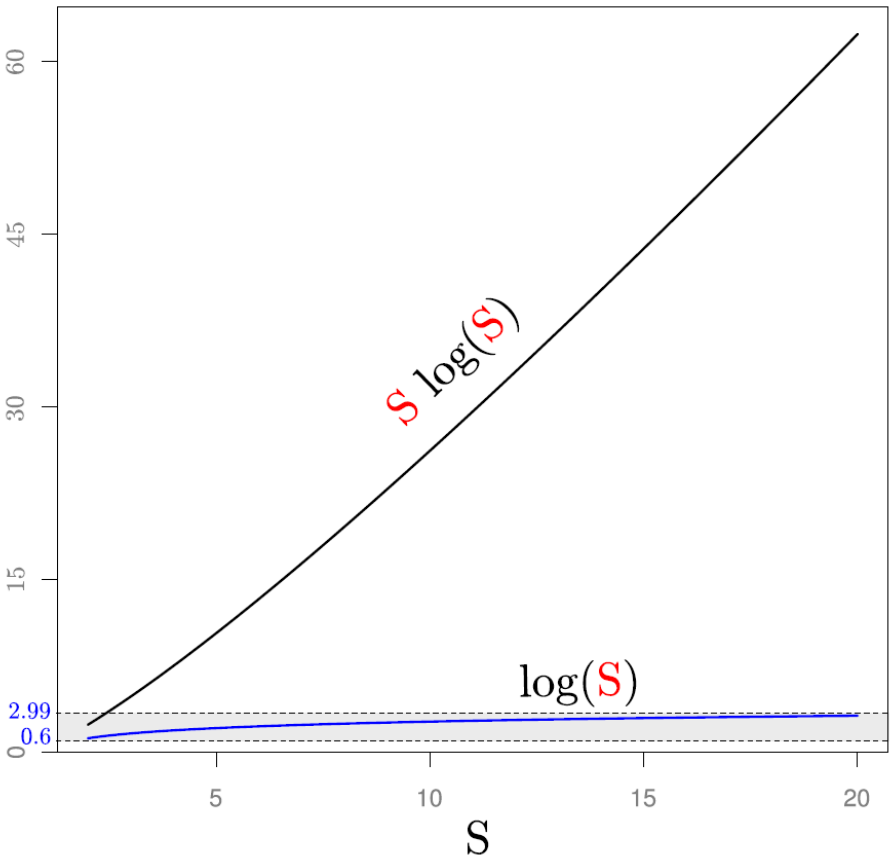

Figure 1. Variation of $A \propto \log S$ and $\mathfrak{A} \propto S \log S$ as a function of S for the supersaturation studied range in our experiments.

Determination of the waiting time (t_w)

One of the most important experimental parameters to consider for kinetic measurements is the induction time. It provides a connection between measurable quantities and thermodynamic variables, and allows us, for a given system, to experimentally estimate the value of the surface free energy of a crystalline phase with respect to its surrounding solution. Induction period is defined as the time which elapses between the onset of supersaturation and the formation of a critical nucleus. This time primarily depends on solution supersaturation and temperature. However, since it is very difficult to detect the formation of a critical nucleus, it is important to remark that, experimentally, we do not measure induction period but "waiting times for nucleation" as an approximation [26]. In order to be detected, it is necessary to let these nuclei grow

until they reach an observable size, which depends on the used technique [27]. Although the induction period is difficult to establish, the waiting time for nucleation is not. This waiting time is the sum of three factors [28]:

$$t_w = t_d + t_n + t_g = \tau + t_g \quad (1)$$

The first term t_d is the time needed to achieve a stationary size distribution of precritical clusters, the second term t_n is the time required to form nuclei of critical size, and the third term t_g accounts for the time required for those nuclei to grow to a size large enough to be experimentally detected. For a data set obtained with the same technique, the value of τ can be replaced by t_w .

Induction period has a very simple relation with the previously explained nucleation rate, given by [25, 29, 30]:

$$\tau \equiv t_w = \frac{1}{2VJ_{CNT}} = \frac{1}{2V}\mathfrak{A}^{-1} \exp\left(\frac{16\pi\nu_0^2\sigma^3\psi(\Theta_\omega)}{3k_B{}^3T^3 \ln^2 S}\right) \quad (2)$$

where V is the total volume of solution and τ the induction period (approximated by t_w).

In this work the waiting time for nucleation was determined by direct observation of the wells under optical microscopy. Due to the low supersaturation and the absence of stirring, the nuclei are expected to appear after a long induction period and in very low quantities, dropping to the bottom of the vials due to the gravity. For that reason other techniques like dynamic light scattering [12] might not be optimal for monitoring nucleation in our experimental set up, as the probability of detecting this low quantity of crystals without stirring is very low. On the other hand, the use of pH-probes, conductivity measurements or ion selective probes are not useful for long term experiments (from days to weeks) as they would need to be calibrated and re-adjusted. In addition, some interferences can be presented during the analyses of a given ion. Due to the different induction times, observation intervals, for each concentration and

temperature, were carefully selected by setting up a series of preliminary experiments to be able to estimate the waiting times for nucleation.

For the study of limestone substrate and precipitates, scanning electron microscopy and EDX spectrometry were performed in a SEM Hitachi S-510 (Hitachi High Technologies Europe, Germany) coupled with a Rontec-Edwin 98/NT (Rontec, Germany) X-ray spectrometer.

3. Results and discussion

As mentioned above in the introduction section, the classical model for describing nucleation has been frequently submitted to a series of particular assumptions and simplifications with the aim of facilitating data interpretation. Generally, in order to extract an analytical value of σ from the experimental values, the relationship between induction period and nucleation rate has been considered, e.g. [31-35]. Equation (2) has been usually rewritten and transformed into a linear equation, by applying natural logarithms to linearise the exponential term:

$$\ln(\tau) = -\ln(2V) - \ln(\mathfrak{A}) + \left(\frac{16\pi v_0^2 \sigma^3 \psi(\Theta_\omega)}{3k_B{}^3 T^3 \ln^2 S}\right) \quad (3)$$

The saturation index, *SI=log(IAP/K_{sp})*, can be written as *SI=log (S)*. For the simplicity of calculations in the current work decimal instead of natural logarithms are used, so a conversion factor needs to be applied, which is equal to *log (x) = 2.3ln (x)*. In this work, a value of $\Theta_\omega = \pi$ will be considered, therefore obtaining a surface tension value which involves the contribution of both, heterogeneous and homogeneous nucleation mechanisms simultaneously, as long as there is no experimental approach to estimate a wetting angle that reflects the heterogeneous mechanism in crystalline nucleation from solution. Thus including in a single variable $\mathcal{K}$ the pre-exponential factor $\mathfrak{A}$ as well as all the constant parameters, and considering the wetting function equal to 1 ($\Theta_\omega = \pi$) equation (3) can be rewritten as

$$log(\tau) = -\mathcal{K} + \left(\frac{16\,\pi\,\gamma_{cf}\Omega^2}{2.3^3 3 k_B{}^3 T^3 log^2 S}\right) \quad (4)$$

Equation (4) is the standard way to relate experimental induction period data with interfacial tension, through the representation and linearization of $\ln(\tau)$ vs $1/\ln^2(S)$. This linearization implies the assumption of a constant $\mathfrak{A}$, non dependent with S, inducing a significant error, as described above. Through this commonly used equation, if $\mathfrak{A}$ is considered as constant in a sufficiently wide range of supersaturation values, experimental induction times usually need two different values of σ to be fitted. That is reflected in several publications [12-14, 36-38], in which the authors identify two different regimes of nucleation, depending on the slope of the linearised CNT expression (heterogeneous nucleation for the lowest value and homogeneous nucleation for the highest value of supersaturation). Moreover, models considering the role of foreign particles in nucleation mechanisms have been developed with the purpose of explaining the observed variations in the slope of the linearised expression [39]. However, if the CNT expression is used taking into account the supersaturation dependence of the pre-exponential factor $\mathfrak{A}$ ($\mathfrak{A} \propto S\,ln^{2/3} S$ for the case of 3D nucleation as it was previously demonstrated) one value of σ can be enough to adequately fit the experimental data.

Experimental values of induction times (measured at different supersaturations and temperatures) obtained by Lancia and coworkers [12], and by Alimi and coworkers [13] are presented in Figure 2. With the aim of illustrating how the S dependence on the pre-exponential factor $\mathfrak{A}$ properly explains the experimental observations, data have been re-interpreted through a non linear least squares (NLS) fitting using equation (3). Figure 2a and 2b represents the experimental data of Lancia and coworkers and Alimi and coworkers respectively, considering two nucleation regimes by splitting S values in two smaller ranges. Figure 2c and 2d show the corresponding curve fitting (calculated through Non Linear Square fitting) considering a single nucleation regime for the whole supersaturation range, and consequently arising a unique σ value. From the fitting curve, a value of $\sigma = 2.8 \pm 0.7$ mJ m^{-2} is obtained from the data of Lancia *et al.* The experimental values of interfacial tensions obtained through the application of the CNT

model to experimental data from Alimi *et al.*[13], as well as from Lancia *et al.* [12] and our experiments, are summarized in Table 2.

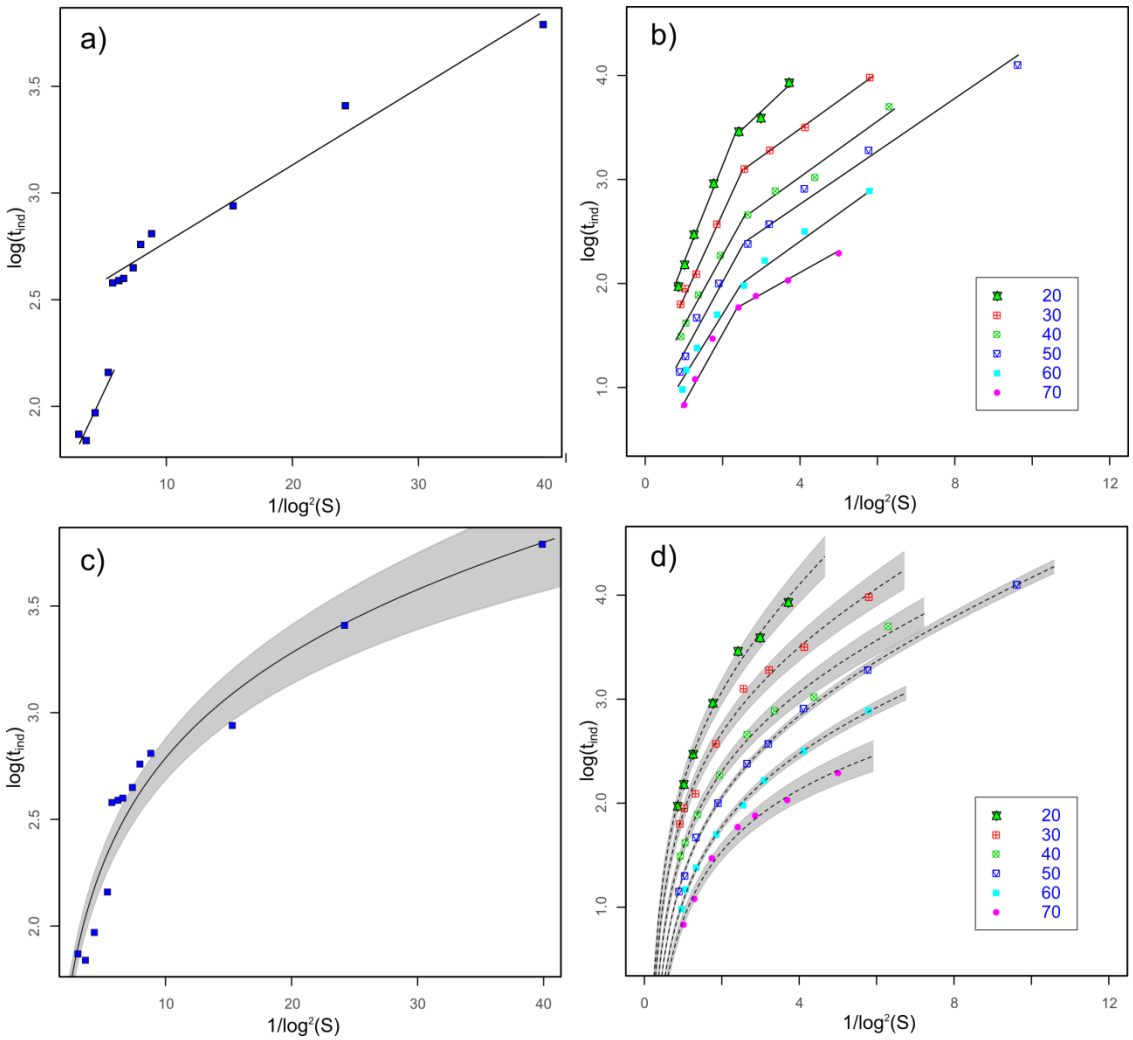

Figure 2. a) Experimental data for induction periods of $CaSO_4 \cdot 2H_2O$ nucleation determined by Lancia and coworkers at 50 ° C [12]; b) Experimental data for induction periods of $CaSO_4 \cdot 2H_2O$ nucleation determined by Alimi and coworkers [13] at different temperatures, depicted in the graphs); a), b) considering two nucleation regimes (as reported by the authors); c), d) re-evaluation of the data considering one single nucleation regime. The grey areas represent the analytical error, calculated by quadratic propagation, for the fitting parameters.

Table 2. σ values (mJ/m^{-2}) calculated from [13] and [12] and for our own experimental data, as well as σ values reported in the mentioned works.

	Alimi*			Lancia**		This work
T (K)	σ	σ_{hom}	σ_{het}	σ_{hom}	σ_{het}	σ
293	(9.1 ± 0.4)	48.5	14.3			(9.1 ± 0.4)
298						(7.8 ± 0.4)
303	(7.8 ± 0.4)	45.8	13.9			
313	(7.3 ± 0.3)	47.4	13.7			
323	(7.8 ± 0.1)	46.7	14.3	(2.8 ± 0.7)	37	
328						(7.3 ± 0.3)
331						(7.8 ± 0.1)
333	(7.0 ± 0.2)	49.9	13.9			
343	(4.6 ± 1.2)	46.2	14.9			

Values of σ_{hom} and σ_{het} reported at *[13]and **[12] considering homogeneous and heterogeneous nucleation, respectively.

The relationship between the measured induction periods $\tau \sim t_w$ and supersaturation for our experimental data, obtained at different temperatures, is represented in Figure 3. Experiments at 55 °C and 58 °C were carried out since the transition temperature of gypsum to anhydrite is proposed to occur in the temperature interval 56-58 °C [40, 41]. Below this temperature anhydrite becomes unstable with respect to gypsum while it is the stable thermodynamic phase at temperatures hotter than mentioned. For that reason a different σ value, from anhydrite nucleation, might be expected at temperatures higher than 55 °C. Other temperatures were also scanned in order to test a temperature dependence of surface free energy in the range of studied temperatures, as also has been reported in literature [13, 14]. Very similar values of surface energy are found for all temperatures (Table 2), and thus, for the studied temperature range, no significant dependence of σ on temperature exists. Also no significant change on the slope of the curves (and therefore in the value of σ) was observed at the transition temperature of gypsum-anhydrite.

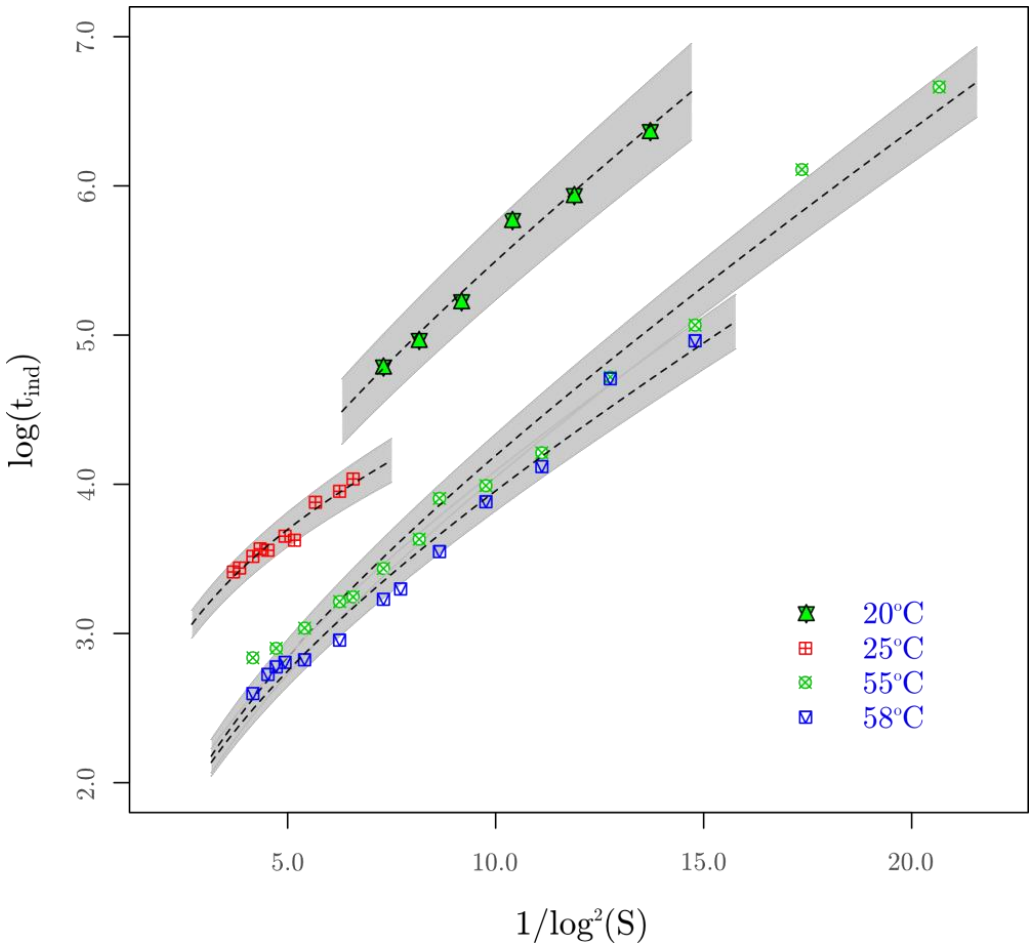

Figure 3. Dependence of log (τ) on $1/(\log S)^2$ for $CaSO_4 \cdot 2H_2O$ nucleating at different temperatures from aqueous solutions.

Despite of finding really similar values of σ for all the experiments performed, as well as for the values obtained from de data found in literature, there is a small difference between our values and those obtained by Lancia and Alimi experimental data. While differences between our results and those obtained from Alimi *et al.* are within the experimental error, value obtained from Lancia *et al.* experiments is sensibly lower. This difference can be easily explained by the narrower region of supersaturations studied in both, our work and the work of Alimi *et al.*, in comparison with the range of supersaturations studied by Lancia *et al.* Considering a more extensive region of supersaturations should result in a more accurate σ value, as these experiments would provide a wider range of points for adjusting the fitting curve, from where the value of σ is obtained. To further illustrate this appreciation, Figure 4 shows an example of possible

fitting curves related to a Lancia *et al.* data set. Labeling every experiment of the data set, from 1 to 13 from highest to lowest supersaturation, black line represents the fitting of the range between experiment 4 and experiment 8 of the set. Red line represents the range 3 to 9, green line represents the range 2 to 10, blue line represents the range 1 to 11, orange line represents the range 1 to 12 and finally red line represents the whole dataset. Table 3 shows σ value calculated from each one of the fittings. It is noticeable that while selecting only the experiments which are within Alimi studied supersaturation range (or our own supersaturation range), the obtained σ value for this supersaturation window is in complete agreement with the rest of calculated values. Selecting data for the fitting in a wider range of supersaturations leads to lower σ values. Therefore, as the σ value proposed from Lancia and coworkers experimental data is the one calculated from the broader supersaturation interval, it should be considered as the more reliable one.

Table 3. Summary of σ values calculated from fitting different data intervals for Lancia *et al.* [12] experimental dataset.

Interval of experiments considered	σ_{fit} (mJ/m^{-2})
Experiment 4 to 8	6.97
Experiment 3 to 9	7.41
Experiment 2 to 10	6.89
Experiment 1 to 11	3.3
Experiment 1 to 12	2.91
Whole dataset (Experiment 1 to 13)	2.82

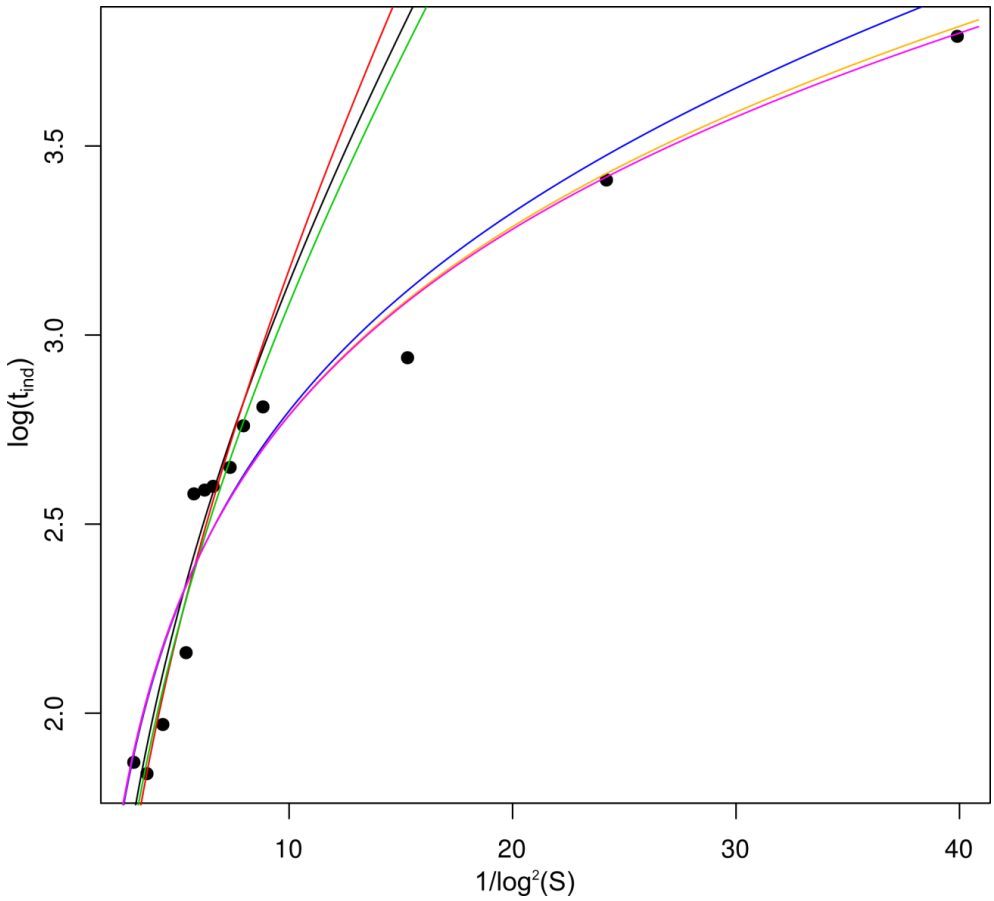

Figure 4. Calculated fitting curves corresponding to 6 different ranges of supersaturation for Lancia *et al.* dataset [12]. Labeling every experiment of the data set, from 1 to 13 from highest to lowest supersaturation, black line represents the fitting of the range between experiment 4 and experiment 8 of the set. Red line represents the range 3 to 9, green line represents the range 2 to 10, blue line represents the range 1 to 11, orange line represents the range 1 to 12 and finally red line represents the whole dataset.

Promoting (heterogeneous) nucleation

In order to provide a substrate for controlled heterogeneous nucleation to be promoted, nucleation experiments in the presence of limestone were performed. Limestone rock has been found as a common nucleation substrate for gypsum in nature [42-44], as well as forming crusts and contributing to limestone degradation in buildings and statuary [45, 46]. Moreover, limestone offers a substrate for gypsum epitaxial

nucleation and grow and it is commonly used in industrial applications for SO_2 removal and neutralization of sulfuric acid solutions [47, 48].

Remarkably, for these nucleation experiments, no reproducible results were obtained from both, untreated samples and 30 micron thin limestone films. Although a meaningful fit of the data is not possible, in comparison with the experiments without limestone substrate an important reduction of the measured induction period is appreciated. Crystals have been found on the limestone rock for supersaturations in which no crystals were detected in the experiments without substrate after two months at room temperature. For example at a concentration of 20 mM with respect to $CaSO_4 \cdot 2H_2O$ crystals were found to nucleate within less than 2 weeks (see Table 2). Since most of the growing crystals are not easily observed by optical microscope (even through a transparent limestone thin film), SEM was used to visualize the heterogeneous nucleation of gypsum on the limestone substrates, finding a major density of gypsum crystals on the small stones than on the thin films. Figure 5 shows SEM images of gypsum crystals nucleated on the limestone substrate. Elemental analysis was used to search for a possible preferential composition on the substrate for the localization and growth of these nuclei. No clear correlation could be found between substrate composition and nucleation density (data not shown). A possible explanation of the large scatter in the data could be the different roughness of natural limestone samples (e.g. more nucleation on the rougher small stones compared to the smoother thin films), but further experimental work would be needed to confirm or refute this hypothesis.

Table 2. Different induction periods obtained for experiments with and without limestone substrate, at 20 °C. Influence of substrate in nucleation can be clearly seen for the lower studied supersaturations of $CaSO_4 \cdot 2H_2O$.

	τ (days) 20°C	
C (mM)	**limestone substrate**	**no substrate**
16	7 (1)	*(12)
17	7 (1)	*(12)
18	12.5 (3)	*(12)
19	9.9 (3)	*(12)
20	13 (1)	*(12)

Number of experiments shown between brackets "()" for each measured induction time.
*no available data after 2 months

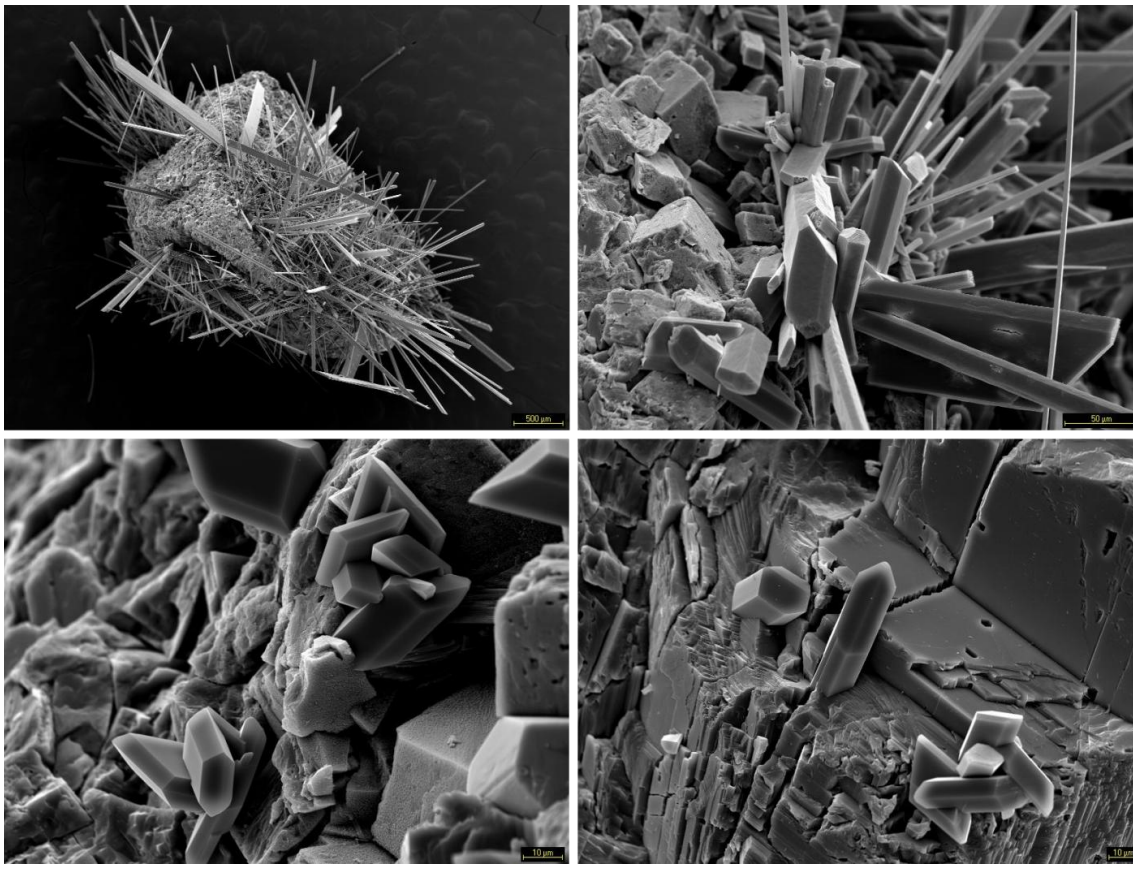

Figure 5. SEM images for two different limestone substrate nucleation experiments. Both experiments were prepared at 25 mM concentration.

Nucleation mechanism

It is important to elucidate if the dominant mechanism of nucleation for gypsum is homogeneous or heterogeneous. In view of our experimental conditions, in which only low supersaturations were scanned, according to literature, it would be reasonable to think that heterogeneous nucleation is the dominant mechanism [26, 49, 50]. We have found as well that gypsum crystals mainly nucleate and grow in the meniscus formed at the oil/solution interface, before dropping down to the bottom of the vial. This observation would be in agreement with a heterogeneous nucleation mechanism for gypsum in our experiments, concurring with the work of Lancia and coworkers [10], who suggest that even at relatively high supersaturations heterogeneous nucleation is an important mechanism.

However, from a probabilistic point of view, the monomer attachment rate for the reactants in solution is expected to reach higher values within the oil/solution interface. While the walls of the containers are generally assumed to be ideal interfaces (and therefore the collision frequency per particle should be similar to that in the bulk of solution), mineral oil is permeable to water molecules. This permeability generates a diffuse interface that could generate an increase of viscosity in this region and, thus, lower the average velocity of the particles in the region closer to the interface meniscus. Consequently, the collision frequency would be expected to be increased in this region, as particles would spend, in average, higher periods of time there. Hence, nucleation probability in the meniscus would be favored by the longer waiting times for nucleation which are expected for the studied supersaturation range. That is to say, a small concentration gradient in the solution/oil interface meniscus explains localized (not necessarily heterogeneous) nucleation. Moreover, the oil/water interface also presents a modified dielectric constant, with respect to those of the solution and mineral oil, thus affecting solubility of $CaSO_4$, as ionic compounds and have a higher interaction with polar solvents (like dissolves like [51]) . While water has a dielectric constant of $\varepsilon_w = 80.37$ [52], mineral oil, which is a non polar solvent, has a low dielectric constant, $\varepsilon_{oil} \approx 2.3$ [53]. The diffuse interface behaves as a mixture of oil and water of a particular

thickness. There, dielectric constant of the media, ε_i, would be an intermediate value from both water and mineral oil, resulting from their mixture, thus locally lowering solubility of $CaSO_4$ with respect to its solubility in water. For a better understanding, figure 6 shows a schematic representation of the oil/water interface and its properties. The joint effect of a higher collision rate and a lower local solubility is certainly generating an environment that significantly enhances nucleation probability.

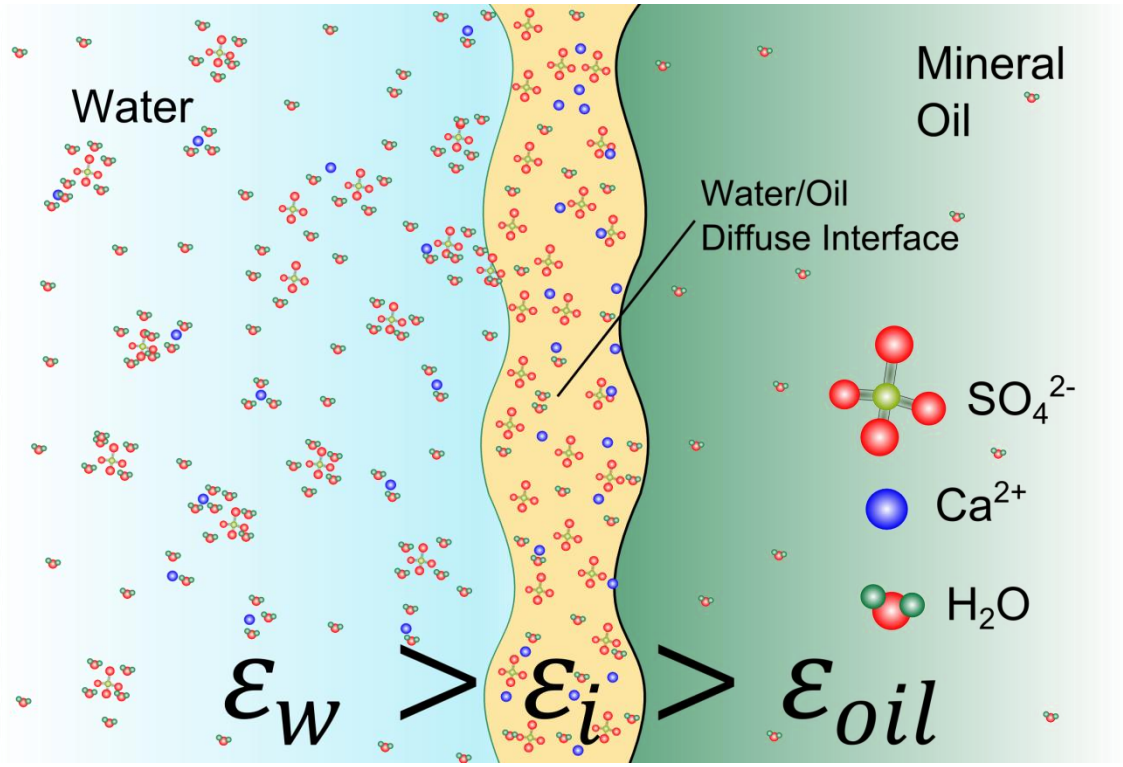

Figure 6. Schematic representation of the oil/water interface for a $CaSO_4$ solution. A higher collision frequency in a more viscous environment, together with a lower value of dielectric constant, caused by the partial mix of oil (non polar solvent) with water (polar solvent) are significantly increasing the nucleation probability in the water/oil interface.

In order to illustrate the nucleation and growth of the $CaSO_4$ crystals in the water/oil interface, figure 7 shows some representative images of those crystals formed in the meniscus of such interface. To make the figure more illustrative, shown experiments were selected at the higher temperature and supersaturations studied. In these conditions the

lowest induction periods were measured, and the highest quantity of crystals was formed, making them more easily observable in the picture. Nevertheless, the same behavior was observed for all the experiments.

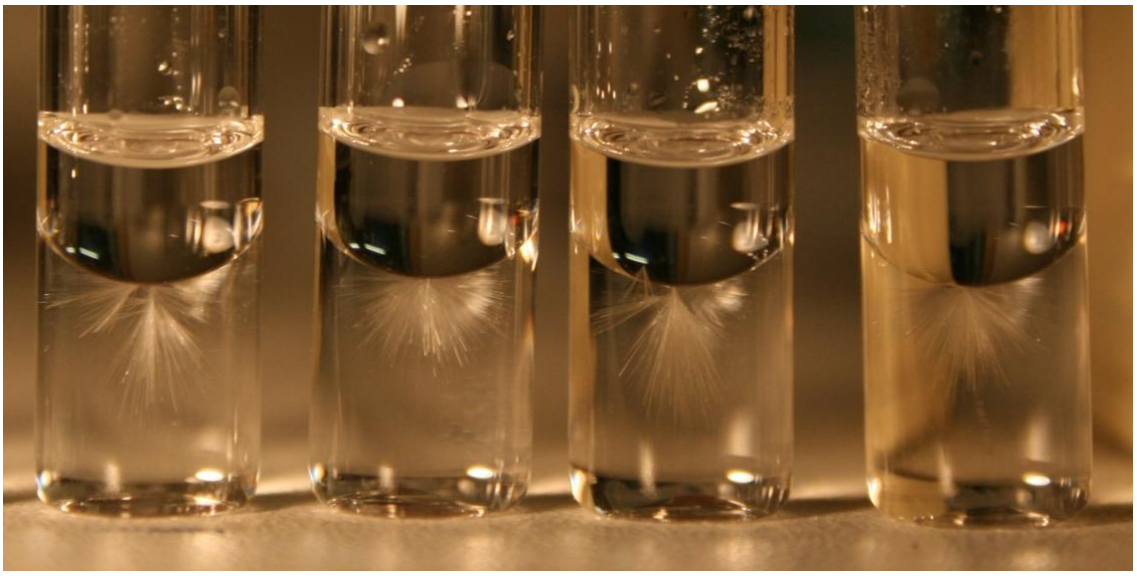

Figure 7. Representative images of gypsum crystals formed in the meniscus formed at the oil/solution interface. Experiments were performed at 58 °C, with a 40 mM $CaSO_4$ solution (SI = 0.5).

Even though, as previously mentioned, obtained values of surface free energy are in very good agreement with σ values determined from experimental data found in literature. Heterogeneous nucleation takes place on a substrate which lowers the energy barrier for nucleation, by reducing the area of the cluster of aggregated molecules in contact with the surrounding solution. But the presence of foreign bodies/surfaces is not the sole condition needed for heterogeneous nucleation to be promoted. A higher affinity with the heterogeneous surface than the one of the nucleating substance with solution, is also necessary with the foreign material for heterogeneous nucleation to occur (i.e. the interaction potential should be of similar magnitude for nucleating phase and foreign bodies). Otherwise, foreign particles would just affect diffusivity of the media, supposing that an important number of particles exist. If, in contrast, only a few foreign particles

are present, as it is expected to happen when high purity reagents, solution, and optimal cleaning conditions are achieved, even if these particles have a high interaction potential, the heterogeneous mechanism of nucleation would be masked by a more abundant number of homogeneous nucleation events.

For the diverse experimental setups found in literature for gypsum nucleation studies, it is clear that materials with different compositions have been in contact with the solutions (different types of glass, plastic or metal containers and tubes, stirrers, limestone and mineral oil in our case...etc). Nevertheless, and apart from the experiments in which gypsum was promoted to nucleate on a preferential substrate for heterogeneous nucleation (limestone), the values of interfacial energies calculated from the obtained induction times for all the experimental setups are very similar. Hence, it is reasonable to consider that these and other nucleation experiments at laboratory scale are mainly governed by a similar nucleation mechanism.

In view of the obtained results, which points out a common nucleation mechanism for all the experiments, heterogeneous nucleation should be ruled out because of all the considerations explained above. Thus, homogeneous nucleation appears to be the common nucleation mechanism that governs the gypsum nucleation studies reported to date. This hypothesis, supported by our observations, is in agreement with the nucleation of a Lennard-Jones liquid, simulated and reported by Wang *et al.* [54] who found that the free energy barrier for heterogeneous nucleation is a minimum when the lattice spacing of the impurity equals the lattice spacing of the equilibrium crystalline phase, whereas the crystal grows into the bulk instead of wetting the impurity if its lattice spacing is different. Accordingly, experiments performed using a limestone substrate for favoring the epitaxial nucleation and growth of gypsum are displaying an heterogeneous nucleation mechanism, (suggested by the lower induction times measured in comparison with experiments performed in equal conditions without limestone), while experiments performed without substrate are nucleating by a homogeneous mechanism, common to all the experiments reported in literature.

4. Conclusions

Induction times for gypsum nucleation at low supersaturations were measured at temperatures of 20, 25, 55, and 58 °C in 0.2 ml batch reactors with no stirring, with the purpose of favoring heterogeneous nucleation. Through a non simplified interpretation of the Classical Nucleation Theory (CNT), values of interfacial tension between gypsum crystals and solution were estimated from these data, and the same model was applied to re-evaluate experimental data found in literature in order to contrast our results. No temperature dependence of the interfacial tension was found in the studied temperature range (20-58 °C), and estimated values in heterogeneous conditions were in high accordance with values calculated from previously reported experimental datasets. Despite of the significant differences between experimental setups and materials, the estimation of a common value for surface free energy suggests a common nucleation mechanism for all the experiments, which might be homogeneous nucleation. In agreement with the observation of a common mechanism for nucleation, differenced experiments carried out with limestone (to promote epitaxial nucleation and growth of gypsum) presented important differences in measured induction times with respect to similar experiments performed in absence of limestone. Consequently, this result suggests a different mechanism for nucleation. However, a more insightful investigation of the nucleation mechanisms implies the consideration of a nucleation theory for multicomponent systems to be investigated. Further investigation will be carried out on this sense for the future.

References

1. Freyer D, Voigt W. Crystallization and Phase Stability of CaSO4 and CaSO4 – Based Salts. Monatshefte für Chemie. 2003;134(5):693-719.

2. Omran AM, King CJ. Kinetics of ice crystallization in sugar solutions and fruit juices. AIChE Journal. 1974;20(4):795-803.

3. Buick R, Dunlop JSR. Evaporitic sediments of Early Archaean age from the Warrawoona Group, North Pole, Western Australia. Sedimentology. 1990;37(2):247-77.

4. Warren JK. Evaporites: sediments, resources and hydrocarbons: Springer Berlin; 2006.

5. Kuzmin RO, Mironenko MV, Evdokimova NA. Spectral and thermodynamic constraints on the existence of gypsum at the Juventae Chasma on Mars. Planetary and Space Science. 2009;57(8–9):975-81.

6. Massé M, Bourgeois O, Le Mouélic S, Verpoorter C, Spiga A, Le Deit L. Wide distribution and glacial origin of polar gypsum on Mars. Earth and Planetary Science Letters. 2012;317–318(0):44-55.

7. Robertson K, Bish D. Constraints on the distribution of CaSO4 · nH2O phases on Mars and implications for their contribution to the hydrological cycle. Icarus. 2013;223(1):407-17.

8. Mi B, Elimelech M. Gypsum Scaling and Cleaning in Forward Osmosis: Measurements and Mechanisms. Environmental Science & Technology. 2010;44(6):2022-8.

9. Rosenberg YO, Reznik IJ, Zmora-Nahum S, Ganor J. The effect of pH on the formation of a gypsum scale in the presence of a phosphonate antiscalant. Desalination. 2012;284(0):207-20.

10. McCool BC, Rahardianto A, Cohen Y. Antiscalant removal in accelerated desupersaturation of RO concentrate via chemically-enhanced seeded precipitation (CESP). Water Research. 2012;46(13):4261-71.

11. Lee R-W, Glater J, Cohen Y, Martin C, Kovac K, Milobar MN, et al. Low-pressure RO membrane desalination of agricultural drainage water. Desalination. 2003;155(2):109-20.

12. Lancia A, Musmarra D, Prisciandaro M. Measuring induction period for calcium sulfate dihydrate precipitation. AIChE Journal. 1999;45(2):390-7.

13. Alimi F, Elfil H, Gadri A. Kinetics of the precipitation of calcium sulfate dihydrate in a desalination unit. Desalination. 2003;158(1–3):9-16.

14. He S, Oddo JE, Tomson MB. The Nucleation Kinetics of Calcium Sulfate Dihydrate in NaCl Solutions up to 6 m and 90°C. Journal of Colloid and Interface Science. 1994;162(2):297-303.

15. Prisciandaro M, Lancia A, Musmarra D. Gypsum nucleation into sodium chloride solutions. AIChE Journal. 2001;47(4):929-34.

16. El-Shall H, Rashad MM, Abdel-Aal EA. Effect of phosphonate additive on crystallization of gypsum in phosphoric and sulfuric acid medium. Crystal Research and Technology. 2002;37(12):1264-73.

17. Badens E, Veesler S, Boistelle R. Crystallization of gypsum from hemihydrate in presence of additives. Journal of Crystal Growth. 1999;198–199, Part 1(0):704-9.

18. Amathieu L, Boistelle R. Crystallization kinetics of gypsum from dense suspension of hemihydrate in water. Journal of Crystal Growth. 1988;88(2):183-92.

19. Nielsen AE, Söhnel O. Interfacial tensions electrolyte crystal-aqueous solution, from nucleation data. Journal of Crystal Growth. 1971;11(3):233-42.

20. Parkhurst DL. User's guide to PHREEQC. US Geol. Surv. Water Resour. Inv. Rep1999.

21. Detoisien T, Forite M, Taulelle P, Teston Jl, Colson D, Klein JP, et al. A Rapid Method for Screening Crystallization Conditions and Phases of an Active Pharmaceutical Ingredient. Organic Process Research & Development. 2009;13(6):1338-42.

22. Mekid S, Vaja D. Propagation of uncertainty: Expressions of second and third order uncertainty with third and fourth moments. Measurement. 2008;41(6):600-9.

23. Fornasini P. Uncertainty in Indirect Measurements. The Uncertainty in Physical Measurements. Springer New York; 2009. p. 149-62.

24. Development Core Team, R: A language and environment for statistical computing. R Foundation for Statistical Computing, Vienna, Austria. ISBN 3-900051-07-0. 2005.

25. Kashchiev D. Nucleation: Basic Theory with Applications2000.

26. Söhnel O, Mullin JW. A method for the determination of precipitation induction periods. Journal of Crystal Growth. 1978;44(4):377-82.

27. Martin J, Alcantara R, Garcia-Ruiz JM. The Detection of Salting-out. A Comparative Study. Crystal Research and Technology. 1991;26(1):35-42.

28. Mullin JW. Crystallization1993.

29. Lundrigan SE, Saika-Voivod I. Test of classical nucleation theory and mean first-passage time formalism on crystallization in the Lennard-Jones liquid. The Journal of Chemical Physics. 2009;131:104503.

30. Hänggi P, Talkner P, Borkovec M. Reaction-rate theory: fifty years after Kramers. Reviews of Modern Physics. 1990;62(2):251.

31. García-Ruiz JM. Nucleation of protein crystals. Journal of Structural Biology. 2003;142(1):22-31.

32. Söhnel O, Mullin JW. Precipitation of calcium carbonate. Journal of Crystal Growth. 1982;60(2):239-50.

33. Gómez-Morales J, Torrent-Burgués J, Rodríguez-Clemente R. Nucleation of calcium carbonate at different initial pH conditions. Journal of Crystal Growth. 1996;169(2):331-8.

34. Kashchiev D. Nucleation2000. 17 p.

35. Kashchiev D, Verdoes D, van Rosmalen GM. J Cryst Growth. 1991;110:373.

36. Mahajan AJ, Kirwan DJ. Nucleation and growth kinetics of biochemicals measured at high supersaturations. Journal of Crystal Growth. 1994;144(3–4):281-90.

37. Mydlarz J, Jones AG. Crystallization and agglomeration kinetics during the batch drowning-out precipitation of potash alum with aqueous acetone. Powder Technology. 1991;65(1–3):187-94.

38. Söhnel O, Mullin JW, Jones AG. Crystallization and agglomeration kinetics in the batch precipitation of strontium molybdate. Industrial and Engineering Chemistry Research®. 1988;27(9):1721-8.

39. Liu X. A new kinetic model for three-dimensional heterogeneous nucleation. The Journal of Chemical Physics. 1999;111:1628.

40. Hardie LA. The Gypsum-Anhydrite Equilibrium at One Atmosphere Pressure. American Mineralogist. 1967;52:29.

41. Blount CW, Dickson FW. Gypsum-anhydrite equilibria in systems $CaSO_4$–H_2O and $CaSO_4$-NaCl-H_2O. American Mineralogist. 1973;58:8.

42. Cuevas-González J, Fernández-Cortés A, Muñoz-Cervera MC, Benavente D, García del Cura MA, Andreu JM, et al. Mineral-Forming Processes at Canelobre Cave (Alicante, SE Spain). In: Andreo B, Carrasco F, Durán JJ, LaMoreaux JW, editors. Advances in Research in Karst Media: Springer Berlin Heidelberg; 2010. p. 503-8.

43. Offeddu FG, Cama J, Soler JM, Ganor J, Casanova I, Putnis CV, et al. Experimental Study of Calcite Dissolution and Gypsum Precipitation in Acid Solutions. Macla.15:155-6.

44. Braithwaite C, editor. Calcitization and compaction in the Upper Permian Concretionary Limestone and Seaham formations of North-east England. Proceedings of the Yorkshire Geological and Polytechnic Society; 1988: Geological Society of London.

45. Camuffo D, Monte M, Sabbioni C. Origin and growth mechanisms of the sulfated crusts on urban limestone. Water Air Soil Pollut. 1983;19(4):351-9.

46. Torok A. Gypsum-induced Decay on Limestone Buildings in the Urban Environment of Budapest. Restoration of Buildings and Monuments. 2005;11(2):71.

47. Warych J, Szymanowski M. Model of the Wet Limestone Flue Gas Desulfurization Process for Cost Optimization. Industrial & Engineering Chemistry Research. 2001;40(12):2597-605.

48. Huminicki DMC, Rimstidt JD. Neutralization of sulfuric acid solutions by calcite dissolution and the application to anoxic limestone drain design. Applied Geochemistry. 2008;23(2):148-65.

49. Chernov AA, Givargizov EI. Modern crystallography III: crystal growth: Springer-Verlag Berlin; 1984.

50. Skripov V. Homogeneous nucleation in melts and amorphous films. Current Topics in Materials Science. 1977;2:327-78.

51. Anslyn EV, Dougherty DA. Modern physical organic chemistry: University Science Books; 2006.

52. Akerlof G. DIELECTRIC CONSTANTS OF SOME ORGANIC SOLVENT-WATER MIXTURES AT VARIOUS TEMPERATURES. Journal of the American Chemical Society. 1932;54(11):4125-39.

53. Shkol'nikov V, Bronshtein L, Shekhter YN, Drozdova O. Electrical and viscosity properties of mineral oil components. Chemistry and Technology of Fuels and Oils. 1977;13(7):479-81.

54. Wang H, Gould H, Klein W. Homogeneous and heterogeneous nucleation of Lennard-Jones liquids. Physical Review E. 2007;76(3):031604.

CHAPTER 4

Scaling down processes for the study of calcium phosphates nucleation and its interest for biomedical applications

CHAPTER 4

Scaling down processes for the study of calcium phosphates nucleation and its interest for biomedical applications

Calcium phosphate precipitation by using Ca^{2+} complexing agents

1. State of the art

Calcium phosphates (CaP) are abundant minerals in both nature and living organisms. In biological systems, (ortho)phosphates are the main inorganic constituent of normal (bones, enamel, dentine, fish enameloid, deer antlers and some species of shells) and pathological (dental and urinary calculus and stones, atherosclerotic lesions) biological calcifications. By definition, all calcium (ortho)phosphates consist of three major chemical elements: Ca(II), P(V) and O(II), as a part of phosphate anions (PO_4^{3-}). In addition, the chemical composition of many CaPs includes hydrogen, either as part of an acidic orthophosphate anion (for example, HPO_4^{2-} or $H_2PO_4^-$), hydroxide (for example, $Ca_{10}(PO_4)_6(OH)_2$) and/or incorporated water (for example, $CaHPO_4 \cdot 2H_2O$). Diverse combinations of CaO and P_2O_5 (both in the presence of water and without it) provide a large variety of calcium phosphates. There are twelve [1] known non-ion-substituted calcium orthophosphates. The most relevant ones, from the biological point of view, as well as for biomaterial science, are listed in table 1. Their most important parameters, in terms of biological activity, are the molar Ca/P ratio, basicity/acidity and solubility. These parameters strongly correlate with the solution pH. The lower the Ca/P molar ratio is, the more acidic and water-soluble the CaP is [2-4]. In order to illustrate this, figure 1 shows the solubility of the main CaP phases, as a function of pH at human body temperature conditions. The solubility ranges from high values for acidic compounds, to very low values for basic compounds, such as apatites, allow CaP to be dissolved by the living organisms, transported from one place to another and precipitated, when necessary.

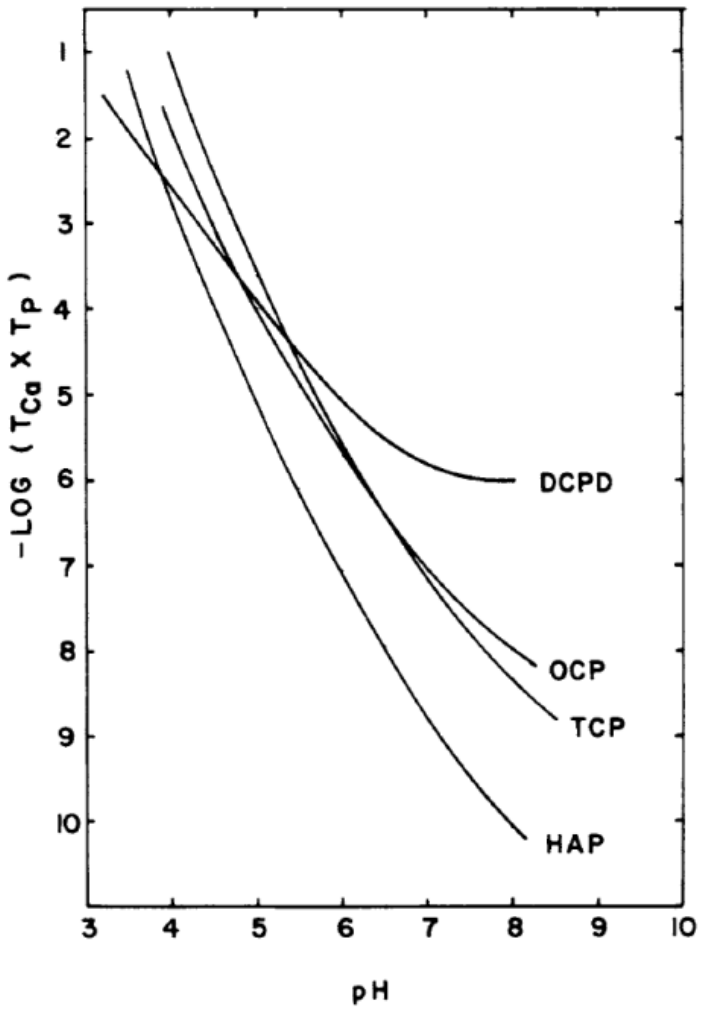

Figure 1. Solubility isotherms of CaP phases at 37 °C and 0.1 mol · L^{-1} ionic strength. Figure obtained from ref. [5]

Table 1. List of most important calcium phosphates from the biological point of view , their Ca/P ion ratio and their crystal structure [1].

Compound	Chemical formula	Ca/P ratio	Space group
Dicalcium phosphate dihydrate (DCPD)	$CaHPO_4 \cdot 2H_2O$	1	monoclinic*I*a
Amorphous calcium phosphate (ACP)	$Ca_xH_y(PO_4)_z \cdot nH_2O$, n = 3 –4.5; 15 – 20% H_2O	1.2-2.2	Amorphous
Octacalcium phosphate (OCP)	$Ca_8(HPO_4)_2(PO_4)_4 \cdot 5H_2O$	1.33	triclinic *P* -1
Tricalcium phosphate (TCP)	α-$Ca_3(PO_4)_2$ β-$Ca_3(PO_4)_2$	1.5	α-monoclinic $P2_1/a$ β-rhombohedral *R*3cH
Hydroxyapatite (HA)	$Ca_{10}(PO_4)_6(OH)_2$	1.67	or hexagonal P6*3*/m

Dicalcium phosphate dihydrate (DCPD or brushite) is of biological importance because it is often found in pathological calcifications (dental calculi, crystalluria, chondrocalcinosis and urinary stones) and some carious lesions [2, 6-8]. This phase is rarely seen in vivo, although it has been reported that the apparent absence of this phase may be due to difficulties of detection as a consequence of its weak X-ray diffraction pattern [5, 9]. DCPD has been proposed as an intermediate in both bone mineralization and dissolution of enamel in acids (dental erosion) [2, 6, 7]. In medicine, DCPD is used in CaP cements [10-12] and as an intermediate for tooth remineralization.

Amorphous calcium phosphate (ACP) is often encountered as a transient phase during the formation of CaPs in aqueous systems. Usually, ACP is the first phase precipitated from a supersaturated solution prepared by rapid mixing of solutions containing ions of calcium and orthophosphate [13-16] . ACP is thought to be formed at the beginning of the precipitation due to a lower surface energy than that of OCP and apatites [13]. The lifetime of ACP in aqueous solution was reported to be a function of the presence of additive molecules and ions, pH, ionic strength and temperature. Thus, ACP may persist for appreciable periods and retain the amorphous state under some specific experimental conditions [17]. However, it has been discovered by extended X-ray absorption fine structure (EXAFS), on biogenic and synthetic samples, that ACP has an apatitic short-range structure, but with a crystal size so small that it appears to be amorphous by X-ray analysis [18-20]. Biologically, ACP (often containing ions of Na, Mg, carbonate and pyrophosphate) is found in soft-tissue pathological calcifications (e.g., heart valve calcifications of uremic patients) [2, 6-8]. In medicine, pure ACP is used in calcium orthophosphate cements [11, 12, 21] and as a filling material in dentistry. Bioactive composites of ACP with polymers have properties suitable for use in dentistry [22, 23] and surgery [24, 25].

Octacalcium phosphate (OCP) has a significant biological relevance. It is often found as an unstable transient intermediate during the precipitation of the

thermodynamically more stable calcium orthophosphates (*e.g.* hydroxyapatites) in the hard tissues of vertebrates and in aqueous solutions. The triclinic structure of OCP displays apatitic layers (with atomic arrangements of calcium and orthophosphate ions similar to those of HA) separated by hydrated layers (with atomic arrangements of calcium and orthophosphate ions similar to those in DCPD) [2-4, 26]. A similarity in crystal structure between OCP and HA is one reason why the epitaxial growth of these phases is observed. OCP is of a great biological importance because it is one of the stable components of human dental and urinary calculi [27, 28]. OCP was first proposed to participate as the initial phase in enamel mineral formation and bone formation through subsequent precipitation and stepwise hydrolysis of OCP by W. E. Brown [29, 30]. It plays an important role in *in vivo* formation of apatitic biominerals. Although OCP has not been observed in vascular calcifications, it has been strongly suggested as a precursor phase to biological apatite found in natural and prosthetic heart valves [31, 32]. In surgery, OCP is used for implantation into bone defects [33, 34].

Tricalcium phosphates cannot be precipitated from aqueous solutions. β-TCP is a high temperature phase, which can only be prepared at temperatures above 800 °C by thermal decomposition of calcium deficient hydroxyapatites, or by solid-state interaction of acidic calcium orthophosphates. Ion-substituted β-TCP can also be prepared by calcination of bones: such type of β-TCP is occasionally called "bone ash". α-TCP is usually prepared from β-TCP by heating above ~ 1125 °C and it might be considered a high temperature phase of β-TCP. Pure β-TCP never occurs in biological calcifications. Only the Mg-substituted form called whitlockite [35, 36] is found in dental calculi and urinary stones, dentinal caries, salivary stones, arthritic cartilage, as well as in some soft-tissue deposits [2, 6-8, 37]. However, it has not been observed in enamel, dentin or bone. In biomedicine, β-TCP is used in CaP bone cements [38, 39]. Although α-TCP and β-TCP have exactly the same chemical composition, they differ by the crystal structure and solubility. β-TCP is more stable than the α-phase [40]. Therefore, α-TCP is more reactive in aqueous systems, has a higher specific energy and it can be hydrolyzed to a mixture of other calcium phosphates. α-TCP never occurs in biological calcifications but

in medicine chemically pure α-TCP is used in calcium phosphate cements [10-12, 21, 41, 42].

Finally, **Hydroxyapatite** (HA) is the most stable CaP phase in physiological conditions and the model compound to designate the mineral component of bone and dentin [43, 44]. Even under the ideal stoichiometric conditions, the precipitates are generally non-stoichiometric, suggesting intermediate formation of precursor phases. In fact, biological apatites are calcium deficient crystals with Ca/P ratio lower than the theoretical value of stoichiometric hydroxyapatite (1.67)[43, 44]. They are plate-shaped nanoparticles with a length of about 30-50 nm, width of 30-50 nm and thickness of 2-10 nm [44, 45], in contrast to the much larger micron-sized HA crystals. In addition, biological nanocrystalline apatites usually present several foreign ions into the crystalline structure such as carbonate (4-6%), Na (0.9%) and Mg (0.5%) among others [44, 45], and recently, the presence of a considerable amount of strongly bonded citrate ions has been found in natural bone apatite [46]. Pure HA never occurs in biological systems. However, due to the chemical similarities to bone and teeth mineral, apatite crystallization has been the object of extensive research in numerous interdisciplinary areas to better understand its formation mechanism in natural mineralization processes [47] as well as to investigate its preparation as biomaterial due to its well known biomedical properties [48]. Hereafter, in order to differentiate pure HA from the biological-like one, we will refer to apatite or Ap instead. It is noteworthy that the crystallinity degree of synthetic Ap nanocrystals is rather low. Nevertheless, it is important to remark that their crystallinity degree is similar to that of biological apatites from bone or dentin [49]. This is another reason why synthetic nanocrystalline apatites are considered as good models for mimicking biological mineral, in contrast to stoichiometric and well crystallized HA. From a chemical point of view, the composition of nanocrystalline apatites differs widely from that of HA, responding to the global chemical composition [49]:

$$Ca_{10-x}(PO_4)_{6-x}(HPO_4 \text{ or } CO_3)_x(OH \text{ or } \tfrac{1}{2} CO_3)_{2-x} \quad \text{with } 0 \leq x \leq 2$$

This composition points out to the presence of vacancies in both Ca and OH sites. Moreover, the analysis of various cortical bone specimens leaded to the following reported [50] constant composition, in accordance with the previously mentioned general formula for x = 1.7

$$Ca_{8.3}(PO_4)_{4.3}\ (HPO_4 \text{ or } CO_3)_{1.7}\ (OH \text{ or } ½\ CO_3)_{0.3} \quad \text{with } 0 \leq x \leq 2$$

Indeed, synthetic Ap have important biological applications, including osteologic implant coatings, grafts, scaffolds and bone cavity fillings and vehicles for drug, protein and gene delivery [51-56].

Many different methodologies have been proposed to prepare nanosized and/or nanocrystalline apatites both in the absence and in the presence of additives [57]. These methods include wet chemical precipitation, co-precipitation, sol–gel synthesis, pyrolysis of aerosols, microemulsion, hydrothermal reactions, and microwave precipitation, among others [58]. Despite of the large number of synthetic strategies to synthesize nanoapatites, the preparation of apatites with similar morphological characteristics and physic-chemical bulk and surface properties to those of the bone mineral phase, still remains an intellectual and technological challenge [59]. The interest for biomimetic apatites comes from their exceptional biological properties, such as non-toxicity, inflammatory and immunitary responses, and high bioresorbability. These properties can be significantly increased by improving their biomimetism [60].

Another property required for the obtained precipitates is to display a monodisperse size distribution, thus providing particles with more homogeneous physic-chemical properties. In this context, the use of complexing agents, with the purpose of controlling the release of calcium ions in the precipitation of calcium phosphates, has been proved to be an excellent approach towards high quality biomimetic particle generation. The objective of controlled release of precipitating cations from metal complexes is to homogenize the chemical composition of the solution to produce such monodisperse crystals. Indeed, particles are normally formed through a sequential process of nucleation and growth by diffusion of growth units onto the existing nuclei. With this method, the

generation of growth units in solution can be controlled by thermal treatment or pH variations, in order to keep them below the critical supersaturation after the nucleation period. This allows to strictly separating the two steps, avoiding nucleation during the growth period, which is the necessary condition to obtain monodisperse particulate systems [61]. López-Macipe *et al.* developed a thermal decomplexing method for the synthesis of apatite nanoparticles using citrate ($C_3H_5O(COO)_3^{3-}$) as a Ca-complexing agent [52]. Lately we have modified this route by introducing CO_3^{2-} as a doping anion, since it is present in natural bone apatite nanoparticles. We were able to tune up the apatite carbonation degree, particle size and morphology, as well as its crystallinity, obtaining particles with a composition and specific surface area (SSA) similar to natural bone nanoapatites [62]. Main conclusions and findings of this work will be presented in this chapter.

However, batch methods in large volumes (macro-methods) for studying nucleation of CaPs present limitations. The mechanisms by which supersaturation is created in large volumes only permit to explore a window of supersaturations, always limited by the (meta)stability of the mixture of reactant solutions and the use of additives. On one hand, citrate has been proved to be a Ca^{2+}-complexing agent of intermediate strength between EDTA and acetate, malate and other carboxylic acids, which only releases Ca^{2+} by increasing the temperature. Figure 2a shows the chemical structure of the Ca-citrate ligand ($Ca_3[C_3H_5O(COO)_3]_2$). On the other hand, the costs of studying the effect of high added value *additives* in CaP nucleation (as proteins, polymers, or drugs for studies in the fields of biomineralization and biomaterials) in large volumes, is an important economic limiting factor. For that reason, smaller reaction volumes (micro-methods) are strongly recommended. However, the use of citrate as a complexing agent in smaller volumes, such as microdroplets, deals with the problem of solution evaporation, due to the high temperature, necessary for triggering the Ca^{2+} release, and therefore to generate supersaturation.

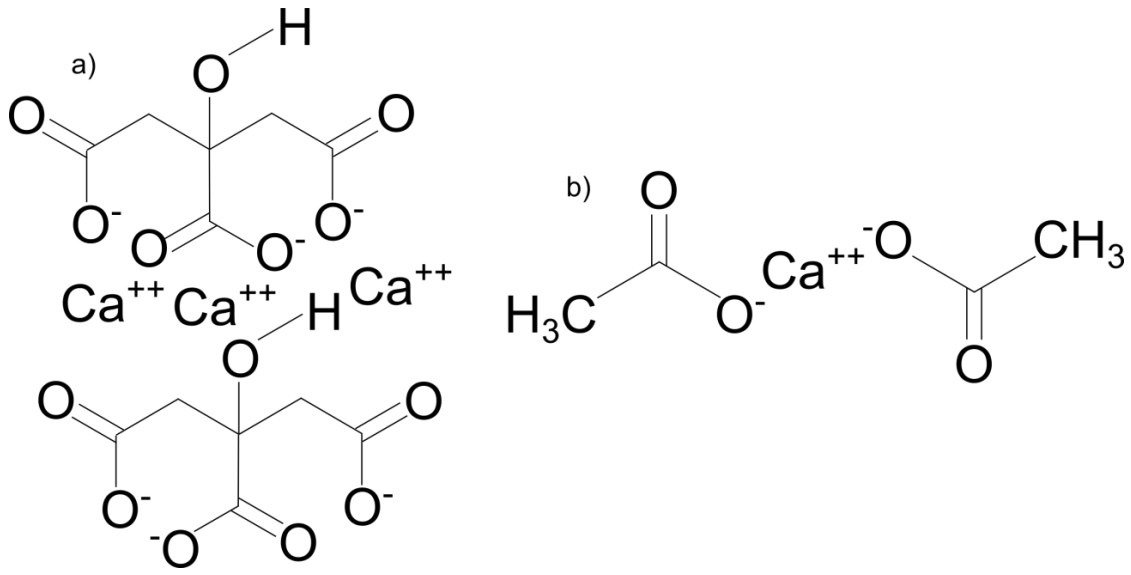

Figure 2. a) Structural formula of Ca-citrate ligand ($Ca_3[C_3H_5O(COO)_3]_2$); b) Structural formula of Ca-acetate ligand ($Ca(CH_3COO)_2$).

Recently, Iafisco et al. reported in 2010 a new methodology to precipitate carbonate-substituted apatite nanoparticles based on the study of small volumes. It consists on a pH-responsive decomplexation method, by means of the well known vapour diffusion sitting drop technique, using acetate (CH_3COO^-) as a Ca^{2+}-complexing agent [63]. The structural formula of the Ca-acetate ligand is shown in figure 2b. The method was developed by using an innovative device called the *"crystallization mushroom"* [64]. The advantages that this set up offers, compared to other crystallization devices, are the following: a reduced consumption of reagents during the crystallization process, since the volume of micro-droplets is around 40 μL and a high reproducibility due to the possibility of performing 12 batch experiments for each run. Therefore, this set up may be suitable to evaluate interactions and/or the co-crystallization of apatites with small amounts of proteins, polymers or drugs for studies in the fields of biomineralization and biomaterials.

Previously, by using this methodology in our laboratory, it was found that mixtures containing 50 mM $Ca(CH_3COO)_2$ and 30 mM $(NH_4)_2HPO_4$ in the micro-droplets and 3 mL of a 40 mM NH_4HCO_3 solution in the gas generation chamber of the *"crystallization*

mushroom" (described in chapter 2) were the optimal concentrations to precipitate carbonate–Ap nanocrystals after 7 days of reaction [63]. The nanocrystals were produced by solvent mediated phase transformation of octacalcium phosphate (OCP) to apatite, with OCP most probably acting as a temporal template for the heterogeneous nucleation of apatite nuclei [63]. The obtained crystals displayed nanometric dimensions, carbonate ions in the crystal lattice, plate-like morphology, and low crystallinity degree, closely resembling the inorganic phase of bones. Contemporarily to these experiments, Nassif et al. [65] precipitated carbonate-Ap by the vapour diffusion method using as reactor a dessicator. They used $CaCl_2$-NaH_2PO_4 mixed solutions in the volume range of milliliters (macro-method) and either a NH_4OH and $NaHCO_3$ solution or solid $(NH_4)_2CO_3$ to generate the gas phase, which led respectively to the precipitation of B- or A-type carbonate-apatite phases. They concluded that the best similarity between synthetic and natural apatite was obtained by using an aqueous carbonate precursor [7] which concurs with the results obtained in our previous work [63].

Along this chapter, two precipitation routes of carbonate substituted apatites will be studied and discussed. 1) Sitting drop vapour diffusion crystallization at very high initial Ca^{2+} and HPO_4^{2-} concentration, using acetate as a pH- dependent Ca^{2+}-complexing agent in microdroplets (40 µL), and 2) batch thermal-decomplexing method using citrate as a Ca^{2+}-complexing agent in large solution volumes (200 ml). Therefore we compare two different ways to produce supersaturation (vapour diffusion versus batch method), and two different volumes (small volumes versus large volumes), with the aim of obtaining a comparable but similar product: monodisperse carbonate-Ap nanoparticles.

The aim of this work is to explore the crystallization mechanisms for different calcium phosphates as well as to investigate the possibilities of increasing the production of nanocrystalline carbonate-apatites in micro-droplets compared with the results obtained in a previous paper employing a low Ca^{2+} and HPO_4^{2-} concentration. The significance of this study comes from two main interests: I) the development of new methodologies for synthesizing monodisperse highly biomimetic bone-like apatite nanoparticles materials, to be used as nanocarriers for local targeted drug delivery systems, as well as building

blocks for the preparation of nanostructured scaffolds for cells in bone tissue engineering; II) the possibility of scaling up the reported methods for its synthesis, allowing a potential industrial production. In accordance with these interests, **Appendix I** of the present chapter presents the application of nanoapatites described below as nanocarriers for local drug delivery of doxorubicin, a commonly used chemotherapeutic drug for cancer treatment. This appendix has been recently published in *Langmuir* under the title "pH-Responsive Delivery of Doxorubicin from Citrate-Apatite Nanocrystals with Tailored Carbonate Content [56].

2. Experimental

2.1. Thermal-decomplexing batch experiments

A new batch heating method has been implemented to precipitate CaP, on the basis of the procedure developed by López-Macipe *et al* [52]. Two solutions (1:1 v/v, 200 mL total) of (i) 0.1 M $CaCl_2$ + 0.4 M Na_3(Cit) and (ii) 0.12 M Na_2HPO_4, + x mM Na_2CO_3 (x = 0 or 100) were mixed at 4 °C. In the experiments without Na_2CO_3, the resulting apatite precipitate is referred to as Ap, whereas in the experiments with x=100 mM Na_2CO_3 the resulting material is referred to as cAp due to the presence of a high amount of doping carbonate ions in the lattice. In both cases the pH was adjusted to 8.5 either with NaOH or HCl. Citrate was used as Ca^{2+}-complexing ligand to prepare homogeneous metastable solutions able to avoid the instantaneous calcium carbonate or calcium phosphate nucleation. The mixture was then introduced in a 250 mL round-bottom flask, sealed with a glass stopper and immersed in a water bath at 80 °C. The experiments were performed at different times ranging from 5 minutes to 96 hours. An additional experiment to the set with x=100 mM Na_2CO_3 was carried out by collecting the powder just after immersing the metastable solution in the flask at 80 °C (time 0). After the precipitation, the particles were repeatedly washed with ultrapure water (MilliQ©, Millipore, 0.22 mS, 25 °C) by centrifugation, and then dried at 37 °C. Solutions were

prepared by using high-purity chemical reagents from Sigma-Aldrich and ultrapure water (MilliQ©, Millipore 0.22 mS, 25 ˚C).

A hot line probe (Sentron) was used to measure the pH evolution of the reaction mixture during the precipitation at 80 ˚C. The activity of the species in solution as a function of both the temperature and the pH were calculated by using the Visual MINTEQ 3.0 speciation software [66]. This software establishes a priority order of thermodynamic stabilities of each solid by comparing the appropriate ion activity products (IAP) with the corresponding solubility product after the aqueous phase was equilibrated. The logarithmic ratio of these terms (saturation index, $SI = \log\left(\frac{IAP}{K_{sp}}\right)$) is calculated and used to establish the stability order for precipitation or dissolution of solids. If the saturation index for a particular mineral is negative, the system is undersaturated with respect to that mineral. If the index is positive, the solution is supersaturated and MINTEQ will precipitate the solid until the equilibrium condition is satisfied. MINTEQ estimates ion activity product and speciation from analytical concentrations of reactive and temperature input data. pH values can be fixed, determining the subsequent effect on supersaturation and speciation, or can be also estimated by the program as a function of the free species. Values of log K_{sp} used for the calculation of saturation indexes are shown in table 2.

Table 2. Values of log K_{sp} used for supersaturation calculations.

Solid Phase	- log K_{sp}
Hydroxyapatite	-44.333
OCP	-47.95
α - TCP	-25.5
β - TCP	-28.92
ACP[(a)]	-25.7

[(a)]It cannot be measured precisely. However, the reported value was found at pH 7.40. From [67].

MINTEQA2 incorporates two schemes for adjusting the equilibrium constants for temperature. If the necessary data are available in the thermodynamic database, MINTEQA2 uses a power function of the form

$$\log K_T = A + BT + \frac{C}{T} + D\log T + ET^2 + \frac{F}{T^2} + GT^{1/2} \quad (1)$$

where:

T = temperature (K)

A,B,...,G = empirical constants stored in the thermodynamic database

For any species that does not have the constants needed for equation (1), the equilibrium constant is corrected for temperature variations from 25 °C by the Van't Hoff equation

$$ln\left(\frac{K_2}{K_1}\right) = -\frac{\Delta H^\circ}{R}\left[\frac{1}{T_2} - \frac{1}{T_1}\right] \quad (2)$$

where:

T_1 = reference temperature, 298.16 °K

log K_2 = logarithm of the equilibrium constant at the reference temperature

R = molar gas constant

T_2 = temperature of the system to be modeled (Kelvin)

$\Delta\Delta H^\circ$ = standard enthalpy change of the reaction

Transmission electron microscopy (TEM) observations as well as selected area electron diffraction (SAED) and energy-dispersive X-ray spectroscopy (EDS) analysis were performed with a STEM Philips CM 20 microscope operating at 80 kV. The powder samples were ultrasonically dispersed in ultrapure water and then few droplets of the slurry were deposited on conventional copper microgrids. The Ca/P ratio was determined by inductively coupled plasma-optical emission spectrometry (ICP-OES, Liberty 200, Varian, Clayton South, Australia). Samples were dissolved in 1% wt. ultrapure nitric acid. The following analytical wavelengths were chosen: Ca 422 nm, P 213 nm. The analyses were carried out 3 times on 3 different synthesis products. Thermogravimetric analysis (TGA) was carried out using a Thermal Analysis SDT Q 600 (TA Instruments, New Castle, DE, USA). Heating was performed in a nitrogen flow (100 mL min^{-1}) using

an alumina sample holder. Temperature was increased from room temperature to 1200 °C with a heating rate of 10 °C min^{-1}. Samples weighted approximately 5 mg. The analyses were carried out 3 times for the same precipitates. Data from ICP and TGA are presented as mean value ± Standard Deviation. Data obtained from experiments were compared by a two-tailed test. Significance level was considered for $p < 0.05$. X-Ray Powder diffraction (XRPD) patterns were collected using a Cu Kα radiation (λ=1.5418Å) on a PANalytical X'Pert PRO diffractometer equipped with a PIXcel detector operating at 45 kV and 40 mA. For the diffracted beam an automatic-variable anti-scatter slit with an irradiated length of 10 mm was used. The 2ϑ range was from 5° to 80° with a step size of (2ϑ) 0.039°. The average size of crystal domains along the apatite axis directions ($D_{[002]}$) and ($D_{[310]}$) were calculated applying the Scherrer equation [68] (3):

$$D_{[hkl]} = \frac{0.9\lambda}{\cos\theta\sqrt{(\Delta_r^2)-(\Delta_0^2)}} \quad (3)$$

where θ is the diffraction angle for plane (hkl), Δ_r and Δ_0 the widths in radians of reflection *hkl* at half height for the synthesized and pure inorganic hydroxyapatite (standard reference material, calcium hydroxyapatite, National Institute of Standards & Technology), respectively, and λ=1.5405 Å. The XRPD patterns were background corrected before the Scherrer analysis. Fourier Transform Infrared (FTIR) spectra were recorded on a Thermo Nicolet 380 FTIR spectrometer. Each powdered sample (~ 1 mg) was mixed with about 200 mg of anhydrous KBr and pressed into 7 mm diameter discs. Pure KBr discs were used as background. The infrared spectra were registered from 4000 cm^{-1} to 400 cm^{-1} with a resolution of 4 cm^{-1}. Raman spectra were collected with a LabRAM-HR spectrometer (Jobin-Yvon, Horiba, Japan). The excitation line was provided by a diode laser emitting at a wavelength of 785.4 nm. A Peltier cooled charge-couple device (CCD) (1064 x 256 pixels) were used as detector. Spectrometer resolution was higher than 3 cm^{-1}. For each acquisition and depending on the quality of the spectra, signal averaging of two or three spectra and acquisition time between 40 and 400 s was performed. The intensity of Raman peaks was represented as counts per seconds (cps).

2.2. pH-decomplexing vapour diffusion sitting drop experiments

The vapour diffusion experiments were carried out in 2 "*crystallization mushrooms*" (Triana Science & Technology, S.L.) at 20 ± 2 °C. Each *crystallization mushroom* is an environmental chamber consisting of a glass Petri dish (2 × 10 cm diameter) placed on top of a cylindrical vessel 5 cm in diameter and 3 cm in height, connected to the Petri dish by a hole and contains 12 micro-bridges (Hampton Research, Inc) placed concentrically in the crystallization chamber. A whole description of the setup is given in chapter 2. Each micro-bridge held 40 μL of a solution whose composition was 500 mM $Ca(CH_3COO)_2$ and 300 mM $(NH_4)_2HPO_4$ (Ca/P=5/3). A 3 mL aliquot of a 40 mM NH_4HCO_3 solution was placed inside the gas generation chamber (lowest reservoir of this device). Solutions of either $Ca(CH_3COO)_2$, $(NH_4)_2HPO_4$ and NH_4HCO_3 were prepared by using high-purity chemical reagents from Sigma-Aldrich and ultrapure water (0.22 mS, 25 °C). The glass cover and the precipitation chamber were sealed with silicon grease. Once each "*mushroom*" was closed and sealed, the underlying NH_4HCO_3 solution started to release NH_3 and CO_2 gasses into the free space of this device (0.112 L). Both CO_2 and NH_3 gases diffused and re-dissolved into the aqueous droplets increasing their pH until it reached an asymptotic value.

The pH was measured by using an electrode (Titan model, Sentron) placed on a hole located on a side wall of the upper chamber (as illustrated in Figure 1), which allows for the measurement of the pH in droplets. The experiments were performed in triplicate and the "crystallization mushrooms" were opened after 1 day, 3 days and 7 days. Consecutively, the precipitates obtained in every twenty-four droplets prepared under the same conditions were removed from the micro-bridges and repeatedly washed with ultrapure water, freeze-dried for 12 h and stored until further characterizations.

Powder X-ray diffraction (XRPD) patterns of the crystals were collected with a Panalytical X'Pert Pro powder diffractometer equipped with X'Celerator detector, using Cu Ka radiation generated at 40 kV and 40 mA. The instrument was configured with ½ ° in both divergence and receiving slits. A quartz sample holder was used. The 2θ

range explored was from 1 ° to 60 °, with a step size of 0.028 ° and a time per step of 104 s. Fourier transform infrared spectroscopy (FTIR) spectra were recorded on a Thermo Nicolet 380 FTIR spectrometer. Each powdered sample (~1 mg) was mixed with about 100 mg of anhydrous KBr. The mixtures were pressed into 7 mm diameter discs. Pure KBr discs were used as background. FTIR spectra were recorded within the wavelength range from 4000 to 400 cm^{-1} at a 2 cm^{-1} resolution. Scanning electron microscopy (SEM) observations were done with a Phenom SEM (Phenom-World B.V, Eindhoven, The Netherlands) while transmission electron microscopy (TEM) inspections were carried out with a Philips CM 100 instrument (80 kV). For the TEM inspections the powdered samples were ultrasonically dispersed in ultrapure water and then a few droplets of the slurry deposited on holey-carbon foils supported on conventional copper microgrids. Finally, thermogravimetric analyses (TGA) were carried out on dried samples using Thermal analysis SDT Q600 (TA Instruments, New Castle, DE, USA) under nitrogen flow (100 mL/min). The temperature was increased to 120 °C using a heating rate of 10 K/min, followed by an annealing of the sample at 120 °C for 30 min and then the temperature was increased further to 1200 °C with the same temperature gradient. The weight of the samples was about 2.5 mg.

Speciation for the reactant solution in equilibrium with a gas phase in which partial pressures of NH_3 and CO_2 (in equilibrium with a 40 mM NH_4HCO_3 solution in the "*crystallization mushroom*") were considered, was also calculated by means of Visual MINTEQA2 software.

3. Results

The activities of the Ca-citrate complex as well as those of main calcium, citrate and phosphate ion pairs for batch experiments (with and without added sodium carbonate), as a function of the temperature are plotted in Figure 3a. Figure 3b shows speciation as a function of pH for sitting drop vapour diffusion experiments containing $Ca(CH_3COO)_2$ and $(NH_4)_2HPO_4$ in the droplets and NH_4HCO_3 40 mM in the reservoir chamber. The

activities of the other Ca-complexes such as $CaCl^{+}$, CaH(Cit) or CaH(Ace) were negligible and for the sake of simplicity were not plotted. Figure 3a clearly shows that the Ca-Citrate complex ($[Ca(Cit)]^{-}$) is destabilized by the temperature increase both with and without sodium carbonate. Same effect can be observed in figure 3b for the Ca-Acetate complex ($[Ca(Ace)]^{+}$) when increasing pH. This fact allows a gradual and homogeneous release of Ca^{2+} ions into the solution, which in the presence of phosphate groups leads to the formation of calcium phosphate aqueous species such as $[CaPO_4]^{-}$ and $[CaHPO_4]^{0}$ and then to the formation of a calcium phosphate precipitate. The above species were proposed two decades ago as growth units for hydroxyapatite [69]. It is worth noting that the activity of $[CaHPO_4]^{0}$ specie is not favored when increasing pH, being enhanced the activity of $[CaPO_4]^{-}$, in accordance with literature [70]. Very recently Habraken *et al.* [71], have proposed that under conditions in which apatite forms from an amorphous calcium phosphate precursor, the $[CaHPO_4]^{0}$ complexes aggregate and take up an extra calcium ion to form ACP, which is a fractal of $Ca_2(HPO_4)_3^{2-}$ clusters. The calcium triphosphate complex also forms the basis of the crystal structure of OCP and apatite. These authors have suggested that this ion-association complex unites both the classical and non-classical theories of nucleation of biomimetic calcium phosphates.

Figure 3a also shows the increase in the activity of the carbonate species $[CaCO_3]^{0}$ with the temperature for experiments in presence of doping carbonate (cAp) indicating that $CaCO_3$ could also precipitate in these experiments. However, we did not find evidences of the $CaCO_3$ precipitation since the solubility product of any $CaCO_3$ phase is much higher than the solubility product of hydroxyapatite. A similar behavior is observed for the carbonate species $[CaCO_3]^{0}$ coming from CO_2 dissolution in figure 3b, for the droplet experiments. Nevertheless, the speciation is calculated in equilibrium state, while the partial pressure of reactant gases in the crystallization chamber increases slowly with time, and the different diffusivity of CO_2 and NH_3 is probably increasing pH levels favoring phosphate precipitation before calcite (calcium carbonate less soluble phase) solubility product is reached. In previous experiments at high concentration of NH_4HCO_3, the partial pressures of released gases NH_3 and CO_2 were higher and therefore

the diffusion rates into the aqueous droplets. Under these circumstances the ionic activity product of calcium carbonate $[(aCa^{2+}) \cdot (aCO_3^{2-})]$ increased rapidly and overpassed the solubility product of calcite ($\log K_{sp}^{calcite} = -8.453$). This process was produced at a rate higher than the one at which the ionic activity product of calcium phosphate $[(aCa^{2+})^5 \cdot (aPO_4^{3-})^3 \cdot (aOH^-)]$ would exceed the solubility product of the apatite phase. This fact led to the precipitation of calcite instead of apatites for those experiments [63]. Thus, the kinetic control would be responsible for the different calcium phosphate/calcium carbonate precipitation by this vapour diffusion method.

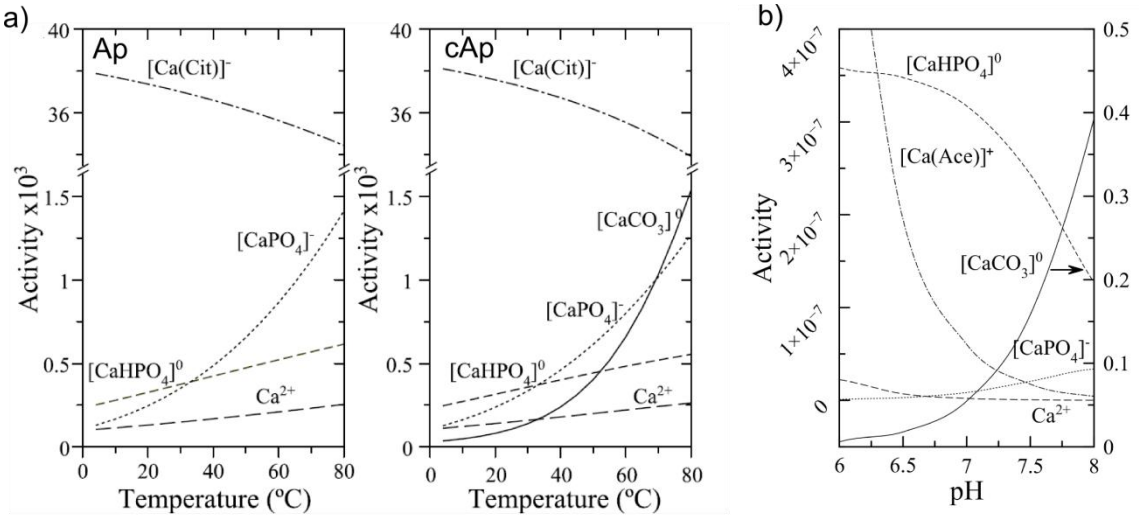

Figure 3. a) Calculated activities as a function of the temperature, of the main ionic and neutral species in the mother solution (pH=8.5) without Na_2CO_3 (Ap) and with 50 mM Na_2CO_3 (cAp) for batch precipitation experiments. Note: Cit=$C_6H_5O_7$; b) Calculated activities as a function of pH, for the main ionic and neutral species for sitting drop vapour diffusion precipitation experiments.

The pH evolution for the experiments is shown in figure 4 for both, batch experiments (figure 4a) and sitting droplets in the "*crystallization mushroom*" (Figure 4b). An initial decrease and a later slow increase of the pH value is observed in both experiments during the first 24 h, being more noticeable for experiments in which the presence of carbonate is more important (cAp and vapour diffusion experiments). In batch experiments, the pH drop corresponds to a single nucleation event when Ca-citrate complexes rapidly

decomplexes, releasing free Ca^{2+} ions which react to precipitate calcium phosphates. For sitting drop vapour diffusion experiments, the initial decrease of pH is due to the diffusion of CO_2 whereas the later increase is ascribed to the diffusion of NH_3. This different pH behavior was the consequence of the faster diffusion rate of CO_2 than NH_3 through the droplets. In addition, after 96 hours the pH stabilized at around 8.8, whereas this value was achieved after 48 h when using lower calcium and phosphate concentrations [5]. This finding in conjunction with the smoother slope of the pH profile measured for experiments with higher concentrated solutions reflects different chemical pathways in the precipitation process, as a consequence of the precipitation of a more acidic calcium phosphate phase.

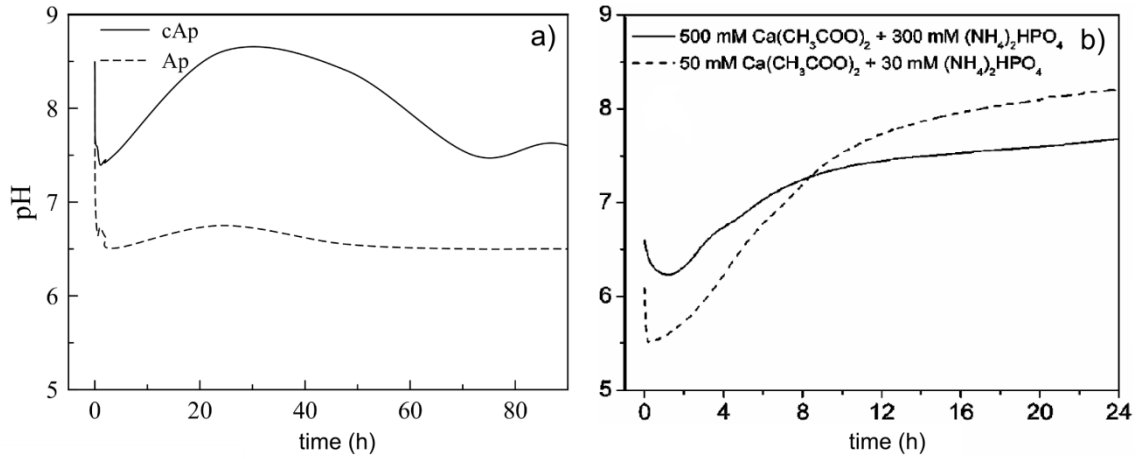

Figure 4. pH-evolution of: a) thermal-decomplexing batch experiments for carbonated (cAp) and non carbonated (Ap) solutions; b) sitting drop vapour diffusion experiments containing $Ca(CH_3COO)_2$ and $(NH_4)_2HPO_4$ at two different concentrations induced by vapours of NH_4HCO_3 40 mM.

3.1. Morphological characterization

Thermal decomplexing batch method

Figure 2 shows TEM micrographs of the Ap (a, c and e) and cAp (b, d, f) particles precipitated by batch method at different times. Apatite crystals grew with their longest axis parallel to the *c* crystallographic axis similarly to the ones crystallized by other

methods [57, 63, 72]. The particles precipitated after 5 minutes show diffuse borders and poor crystallinity degree as pointed out by the SAED patterns (insets in Figures 2a) and 2b). On the contrary, thin needle-like nanoparticles with progressively better-defined border were found when increasing the precipitation time. The SAED patterns collected for the particles crystallized after 96 hours (insets in Figure 2e and 2f) were similar to those reported for crystalline hydroxyapatite [73, 74]. They show the typical reflections 002, 112 and 004 at *d*-spacing equal to 3.44 Å, 2.75 Å and 1.72 Å, respectively (ASTM Card file No. 9-432). The nanoparticles precipitated at short crystallization times are probably composed of a well-ordered apatitic core embedded in a "non-apatitic hydrated layer" as suggested by Rey *et al.* [75, 76]. Actually, one of the most interesting characteristics of biomimetic apatite nanocrystals is the existence of a hydrated surface layer, composed of calcium, phosphate and carbonate species [75, 76] and, in our experiments, also citrate. This surface layer is well developed in freshly formed precipitates and becomes progressively transformed into a more stable apatitic lattice upon maturation in aqueous media [75, 76]. Occasionally, at shorter precipitation times, few platelets (ranging from 1 to 10 µm, not shown) of octacalcium phosphate (OCP) were detected [77].

The average length (L) along the longest axis, the average width (W) and the average aspect ratio (R, i.e., the ratio between L and W) of Ap and cAp nanoparticles crystallized at different times were estimated from TEM observations (table 3). The L values of Ap nanoparticles decreased from 100 nm to 45 nm in the first hour and then gradually increased up to 105 nm after 96 hours. The same trend was observed for the width (from 21 to 12 nm and then to 15 nm). On the contrary, L of the cAp nanocrystals strongly reduced during the first hour; then slightly increased up to 60 nm and after that underwent a slight reduction with the time. In contrast to Ap, R values for cAp become lower with the time. Therefore, the presence of sodium carbonate in the solution leads to the formation of smaller nanoparticles with lower aspect ratio (*i.e.* more isometric particles), in comparison with the Ap, irrespective of the precipitation time. It has to be considered that the uncertainties in the determination of accurate dimensions

of apatites nanoparticles from TEM observations (table 3) is mainly due to an agglomeration process which makes it difficult to observe individual particles. Nonetheless, we have detected that the aggregation trend decreases when increasing the precipitation time as depicted in Figure 5. However, to determine the L and W distributions only non-aggregated nanoparticles were considered.

Table 3. Average length (L), average width (W) and average aspect ratio (R) of Ap and cAp nanoparticles at different precipitation times. Average size of crystal domains (D) along the [0,0,2] and [3,1,0] directions of Ap and cAp at different precipitation times, calculated applying the Scherrer equation.

Precipitation time	L[a] [nm]	W[a] [nm]	R[a]	$D_{[002]}$[nm]	$D_{[310]}$[nm]	$D_{[002]}$/ $D_{[310]}$
Ap 5 minutes	98.6±29.5	21.2±4.6	4.7±1.2	19.4	4.0	4.8
Ap 1 hour	44.7±24.5	11.7±6.6	4.0±1.3	37.1	5.9	6.3
Ap 2 hours	74.6±26.5	14.8±5.6	5.5±2.4	48.0	6.3	7.6
Ap 4 hours	84.8±16.2	15.7±3.8	5.6±1.3	45.3	6.5	7.0
Ap 24 hours	83.6±32.0	13.7±6.1	6.9±3.0	48.0	8.6	5.6
Ap 96 hours	104±43.2	14.8±5.8	7.6±3.2	90.6	9.6	9.4
cAp 5 minutes	108.7±15.7	26.6±5.3	4.3±1.3	17.0	5.2	3.3
cAp 1 hour	48.5±18.4	9.9±5.2	5.4±1.9	22.6	5.9	3.8
cAp 2 hours	59.9±23.7	16.8±6.2	3.7±1.3	30.2	5.6	5.4
cAp 4 hours	54.8±10.1	17.5±3.3	3.2±0.9	35.4	6.1	5.8
cAp 24 hours	40.4±15.1	11.6±3.0	3.7±1.5	31.3	5.7	5.5
cAp 96 hours	29.2±10.7	12.3±2.8	2.5±1.0	45.3	8.0	5.7

[a] Measured from TEM micrographs. The average value and the standard deviations in each one of the experiments were calculated by measuring the dimensions of 100 particles from different experiments

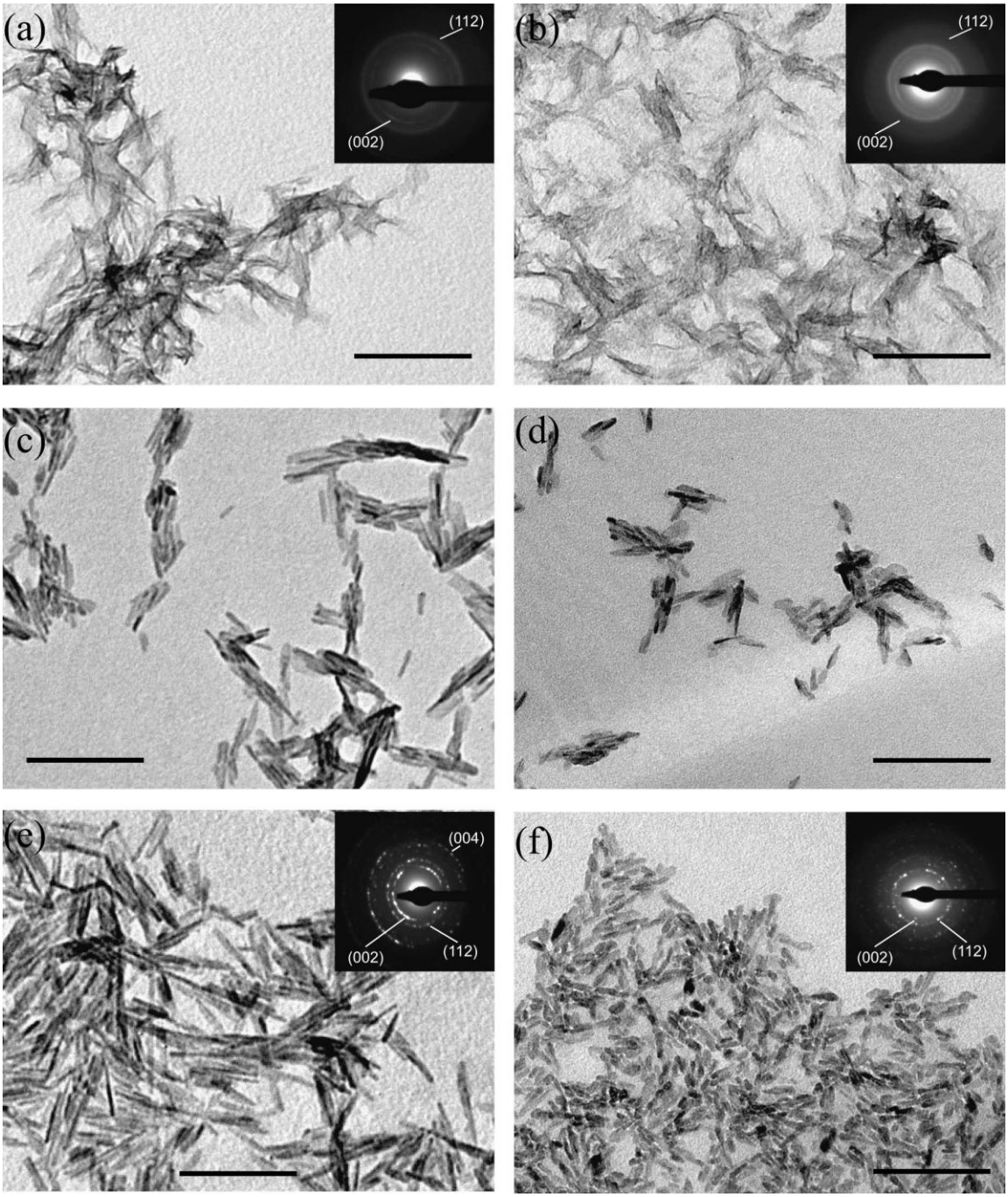

Figure 5. TEM micrographs of Ap crystallized after 5 minutes (a), 2 hours (c) and 96 hours (e) and cAp crystallized after 5 minutes (b), 2 hours (d) and 96 hours (f). Insets show the SAED pattern collected for each sample. The scale bars are 200 nm.

pH-decomplexing vapour diffusion droplet method

The morphological characterization of the crystals precipitated in the *"crystallization mushroom"* was carried out by SEM and TEM microscopies. Figures 6a and 6b show the SEM images of the precipitates after 1 day and 3 days, respectively. After 1 day the crystals were composed of aggregated carbonate-Ap and plate-like shaped DCPD crystals of about 120 μm in length. DCPD crystals precipitated after 3 days appeared elongated along the *b* axis. After 7 days (image not shown), the number of DCPD crystals strongly decreased being apatite the main phase. The most interesting results were obtained from TEM analysis of the crystals collected after 7 days from the zone previously occupied by hydrolyzed DCPD crystals (Fig. 6c). It clearly shows crystals with two different morphologies: needle-like shaped crystals of about 100 nm in length very similar to nanocrystalline apatite [63] and nanoribbons ranging from 1 μm to 2.5 μm in length and from 50 nm to 120 nm in width. The synthesis of ribbon-like calcium phosphate crystals has been previously reported by other authors and the nature of these crystals strongly depends on the crystallization method [78-80]. Actually, it has been reported that the formation of OCP nanoribbons [78, 79] and monoclinic apatite nanoribbons [80] originated from the hydrolysis of DCPD. SAED pattern collected from the nanoribbons is represented in Figure 3f. However, it is practically impossible to discriminate between apatite and OCP because both phases originate the same pattern within the (110) zone axis [79, 80]. However, Figures 3d and 3e point out that the surface of the nanoribbons analyzed by electron diffraction changed after the irradiation with the electron beam. The new bubble-like features formed during the irradiation process (the so-called blistering process) are produced by compounds containing structural water molecules like OCP [78].

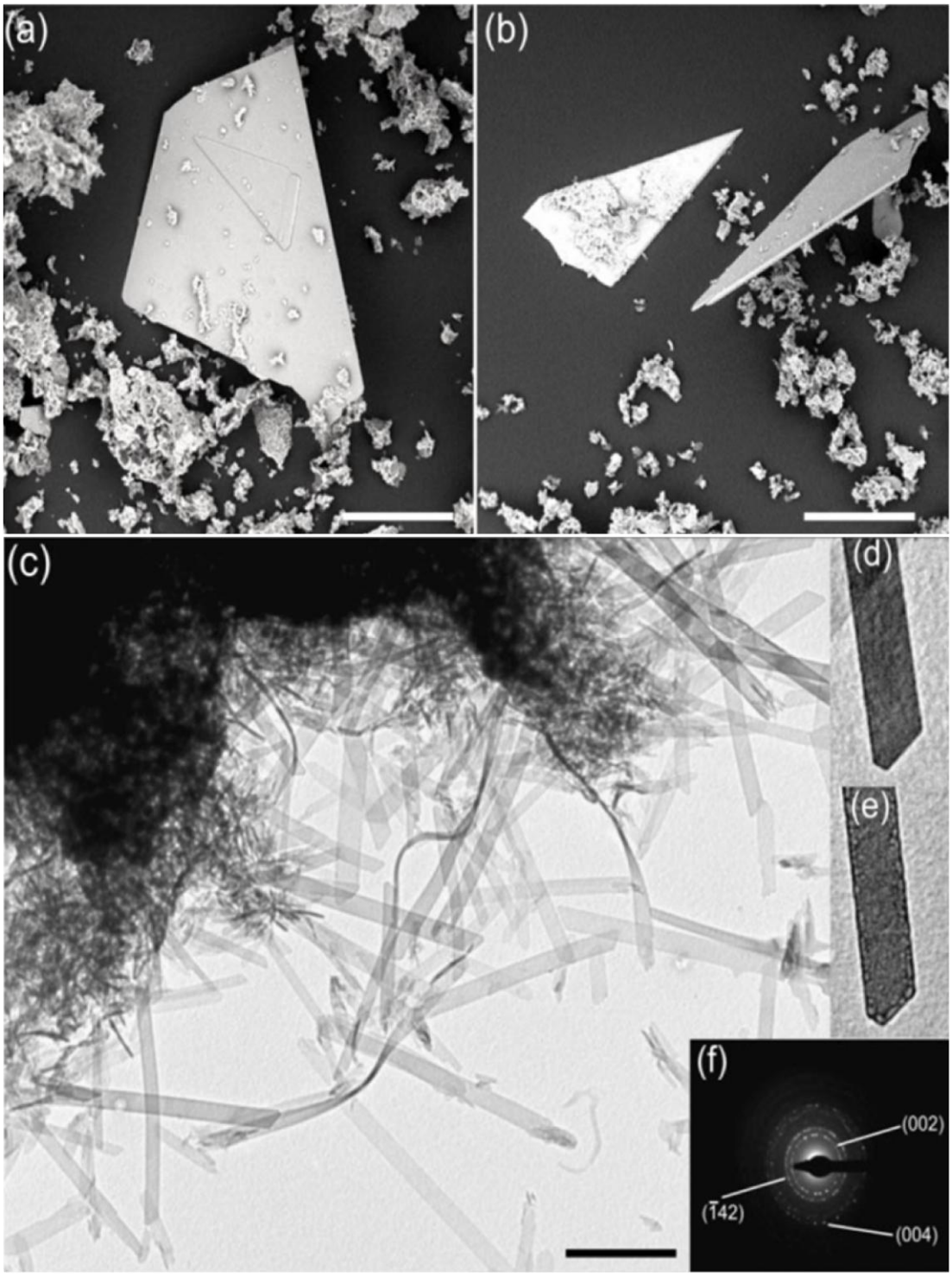

Figure 6. SEM images of the powders crystallized after 1 day (a) and 3 days (b) showing big DCPD crystals. TEM image of the powders crystallized after 7 days (c) showing apatite and OCP crystals. Scale bars correspond to 60, 100 and 0.6 μm, respectively. Insets (d) and (e) show TEM images of an OCP ribbon crystal recorded before and after electron diffraction collection, respectively. Note that electron beam exposition induced the formation of bubble-like features in the OCP ribbons (inset e). Inset (f) shows the selected area electron diffraction (SAED) pattern collected from the OCP ribbon crystals.

3.2. Crystallographic characterization by X-ray Diffraction

Thermal decomplexing batch method

Figures 7a and 7b show the X-ray diffraction patterns of Ap and cAp, respectively, precipitated with the batch method after 5 minutes and 96 hours. They display the characteristic diffraction reflections of hydroxyapatite single phase (ASTM Card file No. 9-432). Any peak assignable to OCP phase (ASTM Card file No. 26-1056) at low diffraction angles was found (data not shown) even at earlier precipitation times. The most intense peaks appear at 25.88°, related with the 002 planes, and around 32° (broad band due to the triplet 211, 112 and 300). The diffraction peaks are broad and poorly defined. This broadness is more evident at shorter crystallization times suggesting a relatively lower degree of crystallinity and nano-dimensions [76] in accordance with the above described SAED results. The diffraction pattern of the powders precipitated at time 0 in the presence of Na_2CO_3 were characterized by the absence of reflections, revealing the amorphous nature of the precipitate.

The average size of crystal domains along the *c*-axis ($D_{[002]}$) and the *a*-*b* plane (orthogonal to the *c*-axis, $D_{[310]}$), calculated by the Scherrer's equation using the width at half height for the respective reflections 002 and non-overlapped 310, are shown in table 1. For both type of apatites, the values of $D_{[002]}$ at short times were close to those of bone apatite (around 20 nm) [81]. $D_{[002]}$ strongly increased with time whereas $D_{[310]}$ slightly raised according to a preferential growth along the *c*-axis. Additionally, the $D_{[002]}$ values as well as the $D_{[002]}/ D_{[310]}$ ratio were lower for cAp in agreement with the TEM observations. This finding is explained by the incorporation of carbonate ions into the lattice, as previously reported by other authors [82-84]. It has to be highlighted that $D_{[002]}$ and $D_{[310]}$ values correspond to dimensions of crystallite domains. In contrast, L and W measurements refer to the dimensions of projected images of nanoparticles as observed by TEM.

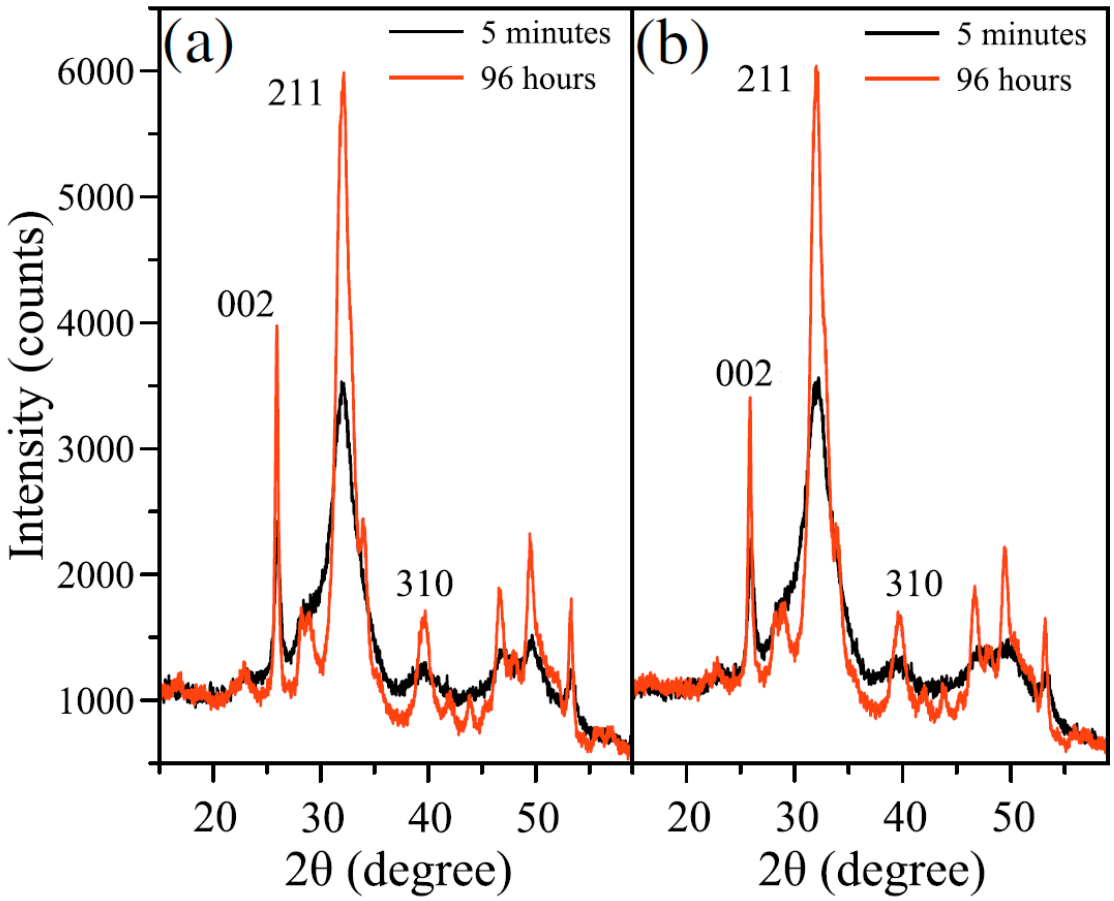

Figure 7. XRPD patterns of (a) Ap crystallized after 5 minutes (black line) and 96 hours (red line) and (b) cAp crystallized after 5 minutes (black line) and 96 hours (red line).

pH-decomplexing vapour diffusion droplet method

Figure 8 shows the XRPD patterns of the crystalline phases obtained after 1, 3 and 7 days by vapour diffusion in the *"crystallization mushroom"*. In all of them, apatite, octacalcium phosphate (OCP) and dicalcium phosphate dihydrate (DCPD, brushite) crystals have been identified. Apatites has a hexagonal crystalline structure with space group P63/m, consisting of tetrahedral and octahedral sites, while OCP has a triclinic structure with the same octahedral sites as those of the apatitic structure [85]. The structural similarity between OCP and apatite is the reason why the two phases share most of the powder XRD reflections. The characteristic diffraction peaks of apatite were the 002 reflection which appears at 25.90° as well as the triple peak placed around 31°

due to 211, 112 and 300 reflections (ASTM card no. 9-432) marked with squares in figure 8. The broadness of these reflections suggests that the apatite crystals were nano-sized and with low crystallinity degree. The formation of OCP was demonstrated by the reflections at 4.72°, (overlapped with the background) which corresponds to the (010) plane, and at 9.44° and 16.04° (marked with asterisks in figure 8), corresponding to the (020) and (101) planes (ASTM card no. 26-1056), respectively. The other reflections were shared with those of the apatite phase. The more acidic crystalline phase DCPD produced reflections at 11.68°, 20.92°, 23.40°, 29.28° and 47.88° (ASTM card no. 9-77) (marked with circles in figure 8). DCPD mainly grew along the *b* axis, as shown in Figure 6. In fact, the peaks that increased their intensity from 1 to 3 days were the reflections at 11.68°, 23.39°, 35.42° and 47.86° corresponding to (020), (040), (060) and (080) planes, respectively, whereas all the peaks corresponding to the other planes decreased their intensity from 1 to 7 days, in agreement with SEM observations. DCPD is a CaP phase stable in weakly acidic environments (pH between 4 and 6) and known to be a precursor of apatite [86]. Pure DCPD transforms to apatite at pH higher than 7-7.5 [86]. In our system, the precipitation of DCPD probably took place because the high concentration of Ca^{2+} and HPO_4^{2-} ions did not allow a fast increase of pH in comparison with that found when using the experimental conditions of Iafisco et al. [5]. Indeed, DCPD grew for up to 3 days and then started to hydrolyze and to convert to apatite and OCP. A complete transformation of DCPD to apatite in a solution of Ca^{2+} ions at basic pH has been also previously suggested by other authors [87].

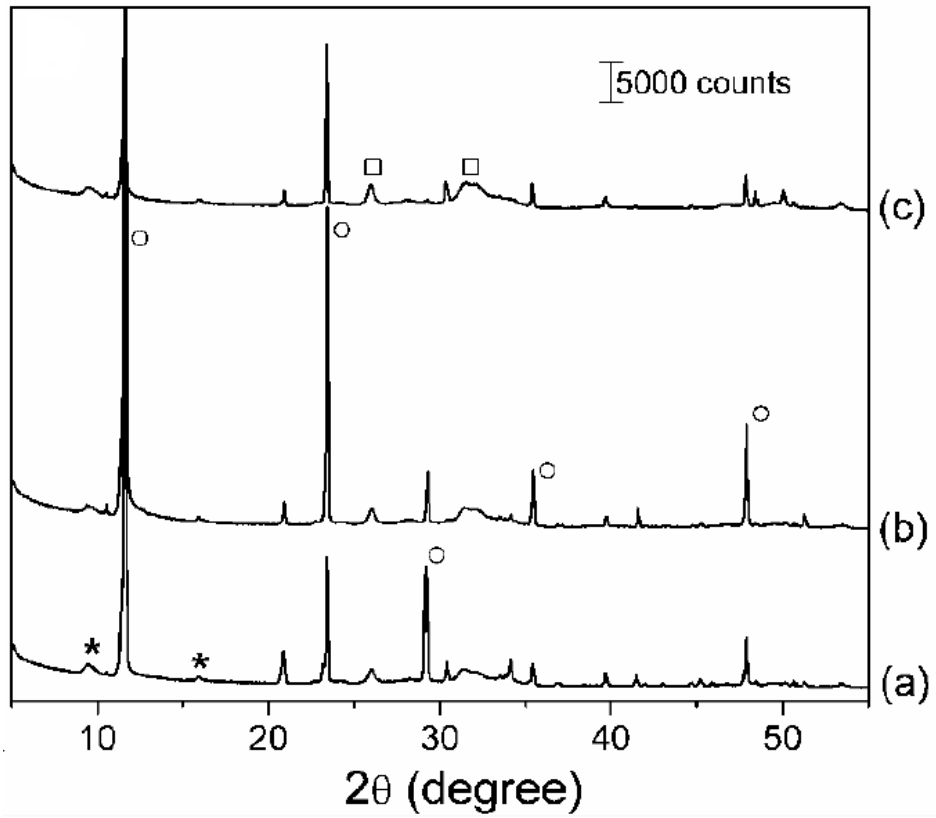

Figure 8. X-Ray powder diffraction (XRPD) patterns of calcium phosphates crystallized by vapour diffusion after 1 (a), 3 (b) and 7 days (c). Symbols represent different calcium phosphate: apatite (□), OCP(*) and DCPD (◯)

3.3. Spectroscopic characterization

Thermal decomplexing batch method

Batch synthesized nanocrystals were characterized by FTIR and Raman spectroscopies. Figure 9a represents the FTIR spectra of cAp crystallized at 5 minutes and 48 hours. They displayed a main broad band at *ca.* 1030 cm^{-1} with shoulders at *ca.* 1046 and 1075 cm^{-1} due to the triply degenerated asymmetric stretching mode of the apatitic PO_4 groups (ν_3PO_4). This band is slightly red-shifted with respect to that of stoichiometric hydroxyapatite, most likely due to the presence of CO_3^{2-}, and/or HPO_4^{2-} ions incorporated into the crystal lattice [88, 89]. Other features emerge at *ca.* 961 cm^{-1} (symmetric stretching mode of the apatitic PO_4 groups, ν_1PO_4) and at *ca.* 603, 576 (as a shoulder) and 565 cm^{-1} (triply degenerated bending mode of the same groups, ν_4PO_4) [88, 89]. FTIR spectra confirm the absence of OCP in agreement with the XRPD data. The

spectrum of the particles after 5 minutes in Figure 6a shows a shoulder at 534 cm^{-1} in the ν_4PO_4 domain. Rey *et al.* [75] assigned this feature to phosphate and/or hydrogenphosphate ions in a non-apatitic environment. The intensity of this shoulder was maximal at 5 minutes and afterwards it strongly decayed with the time. This shoulder disappeared in the spectra of Ap precipitated after 4 hours whereas in the cAp samples, it only disappears for the particles collected after 48 hours. The width of the ν_4PO_4 band at 603 cm^{-1} was directly correlated to the crystallinity degree of the particles, *i.e.* the lower this value the higher the crystallinity [90].

Table 4. Full width at half maximum (FWHM) of the ν4PO4 peak (603 cm^{-1}) of Ap and cAp at different precipitation times.

Precipitation time	FWHM (cm^{-1})	
	Ap	cAp
5 minutes	14.3	14.9
1 hour	12.9	13.6
4 hours	12.5	12.9
24 hours	11.2	13.3
48 hours	10.9	11.9
96 hours	9.6	10.5

Table 4 summarizes the full width at half maximum (FWHM) of this band for the Ap and cAp nanoparticles. According to this parameter, particles increased their crystallinity degree with the precipitation time, Ap being more crystalline than cAp. This trend is in good agreement with the XRPD data (table 2).

The ν_2CO_3 band (at *ca.* 875 cm^{-1}) has been deconvoluted by non-linear fitting (fig. 9b) in order to estimate the intensities of the A-type (880 cm^{-1}) [91], B-type (873 cm^{-1}) [91] and labile (868 cm^{-1}) carbonate bands, *i.e.*, in a non-apatitic environment [75]. The band at 845 cm^{-1} is assignable to the δCOO [92] of the citrate ions. The ratio between the integrated intensities of the different carbonate bands (A-type, B-type and labile) to the total carbonate is plotted in Figure 6c. Carbonate in B positions was noticeably the most favored situation. A-type substitutions, which were practically negligible at short times, increased progressively with time. The nanoparticles with the highest A-type carbonate

content were precipitated at 48 hours. The intensity of the labile carbonate band strongly decreased after 5 minutes being nearly negligible after 48 hours.

Figure 9d shows the Raman spectra of Ap and cAp precipitated at 48 hours. The most intense peak appears at *ca.* 960 cm^{-1} which corresponds to ν_1PO_4 mode. It was red-shifted (957 cm^{-1}) in the cAp spectrum due to the carbonate incorporation [93]. In the spectrum of cAp nanoparticles, B-type carbonate band appeared at *ca.* 1070 cm^{-1} (ν_1CO_3) with a shoulder at *ca.* 1103 cm^{-1} due to A-type substitutions [91]. It confirmed that B-type substitutions are the predominant ones in cAp nanoparticles. Moreover, in the Raman spectrum of Ap an intense peak at *ca.* 3570 cm^{-1} corresponding to the apatitic νOH mode can be clearly observed (inset of the Figure 9d). On the contrary, this band was less intense in the spectrum collected for the cAp nanoparticles because OH ions were replaced by carbonate groups (A-type substitution). The bands at *ca.* 2930 and 845 cm^{-1} are related to the νCH_2 and the δCOO modes [92], respectively, of citrate anions.

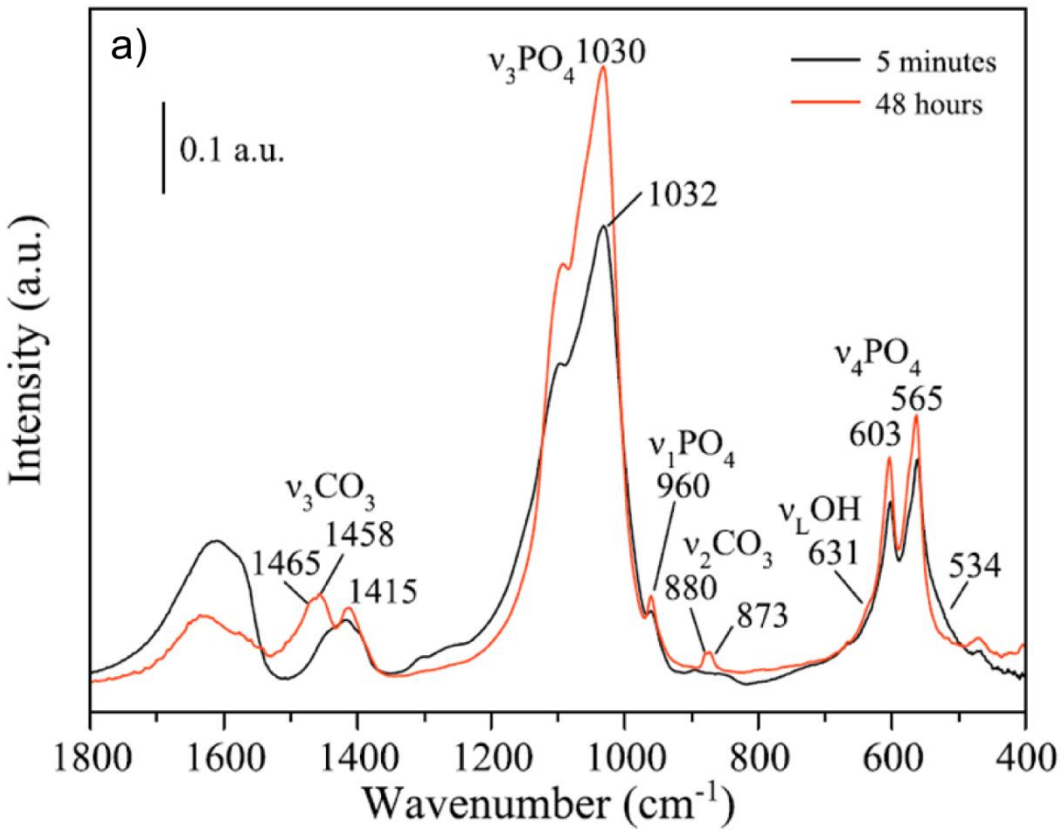

Figure 9. a) FTIR spectra of cAp crystallized after 5 minutes (black line) and 48 hours (red line).

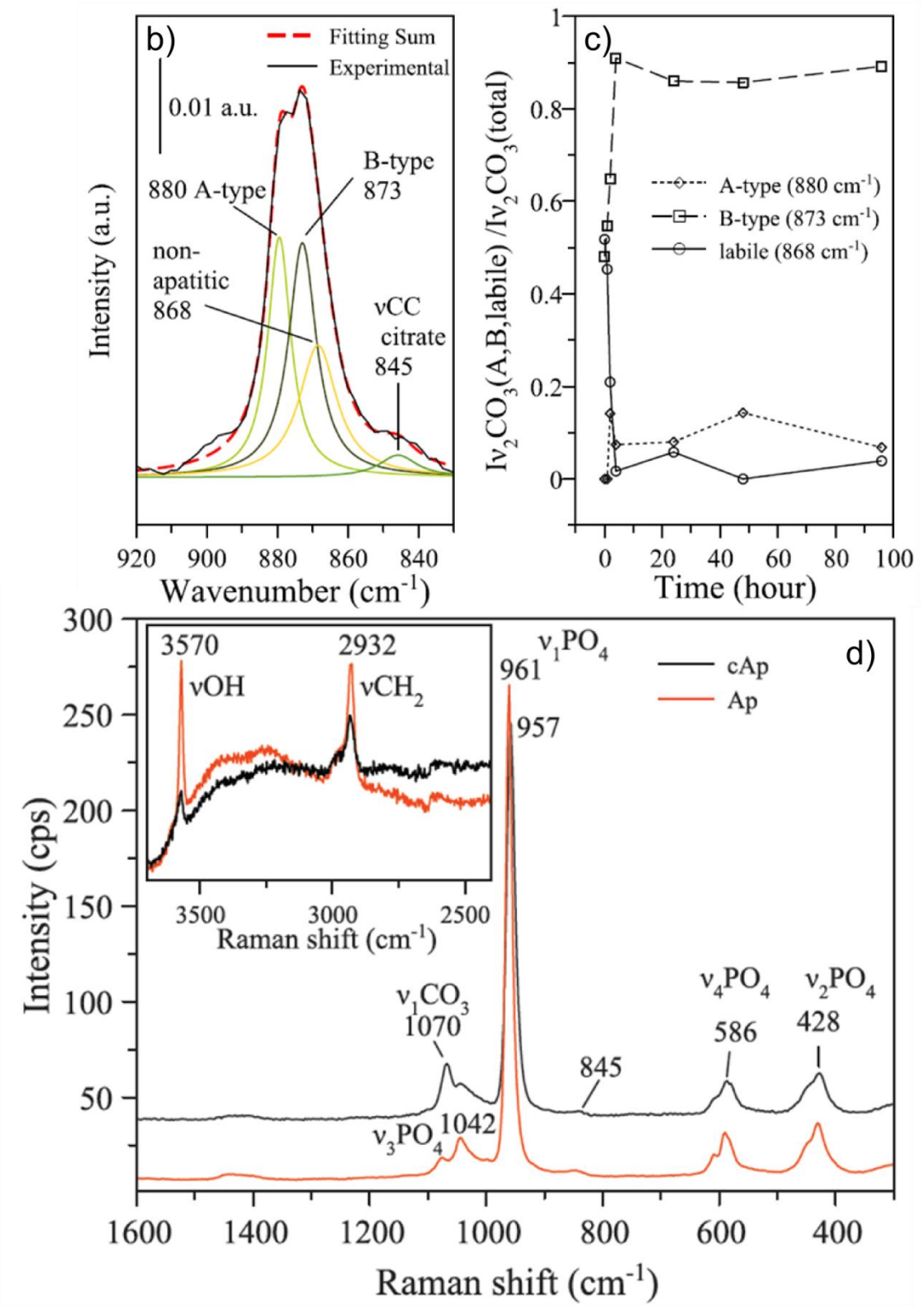

Figure 9. b) Non-linear curve fitting of the cAp bands in the ν_2CO_3 spectral region; c) Plot of the ratio between the integrated intensities of the A-type, B-type and labile carbonate bands to the total intensity of the ν_2CO_3 band as *vs* the precipitation time; d) Raman spectra of cAp (black line) and Ap (red line) crystallized at 48 hours. The inset shows an enlarge view of the typical OH and CH stretching modes spectral region.

pH-decomplexing vapour diffusion droplet method

Figure 10 shows the FTIR spectra collected for the particles grown in the "*crystallization mushroom*" at different times. They show a broad band centered at 1030 cm^{-1} ascribed to the asymmetric stretching mode (ν3) of the phosphate groups [89] and bands at 562 and 603 cm^{-1} corresponding to the bending mode (ν4) of the phosphate groups [89]. These vibrational modes are related to both apatite and OCP phases. The presence of OCP was demonstrated by the appearance of typical bands at ca. 527 and 915 cm^{-1} corresponding to the bending and stretching modes of HPO_4^{2-} groups in OCP, respectively [89]. The presence of DCPD was also confirmed by the appearance of bands at ca. 873, and 1647 cm^{-1} [89]. On the other hand, the bands at ca. 1556, 1450, 1420, and 873 cm^{-1} confirmed that both A- and B- type carbonate substituted apatite (carbonate replacing hydroxyl and phosphate positions in the apatite crystal lattice, respectively) [94, 95] were taking place. However, the intensity of the main band corresponding to A-type carbonation (at ca. 1556 cm^{-1}) strongly increased in the crystals precipitated after seven days, whereas the intensity of the B-type bands decreased during this period. The increase of A-type carbonation and the decrease of the B-type are reasonable due to the more labile OH- ion compared with the PO_4^{3-} ion in the crystalline apatite structure. These findings, which are similar to those reported by Nassif *et al.* [65], confirm the role that the employed source for the gases' generation has on the selectivity of the carbonate substitution.

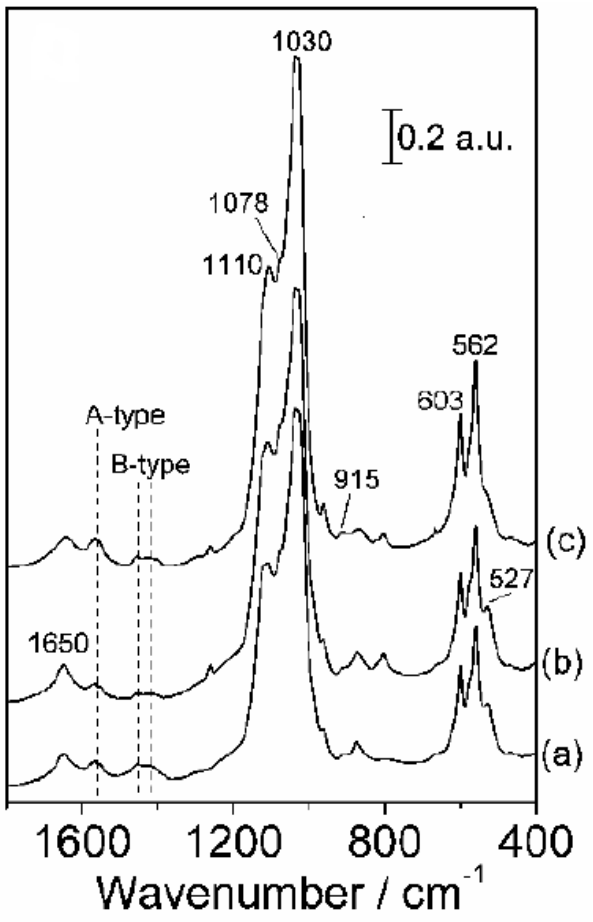

Figure 10. FTIR spectra of calcium phosphates crystallized after 1 (a), 3 (b) and 7 days (c).

3.4. Chemical analysis

Thermal decomplexing batch method

The chemical composition of nanocrystals obtained by batch method was analyzed by ICP and TGA (table 5). The Ca/P ratios estimated by ICP for the Ap and cAp nanocrystals were slightly lower than the stoichiometric value (1.67) irrespective of the precipitation time. They were slightly higher for the cAp since carbonate was replacing phosphates groups [84]. Therefore, this method yields Ca-deficient apatites with Ca/P ratio close to the biological ones (1.5) [43, 44].

TGA analysis mainly showed four weight losses (see figure 11a): i) from room temperature to 200 °C due to the adsorbed water, ii) from 200 °C to 400 °C related to structural water, iii) from 400 to 600 °C due to the citrate as well as the small amount of non-apatitic HPO_4^{2-} ions and iv) from 600 to 1000 °C corresponding to the carbonate ions [96]. These assignments are well supported by the FTIR spectra collected after sample annealing at 400 °C and 600 °C losses (see [62] for more information). The amount of structural water as well as of the adsorbed citrate decreased with the precipitation time in both samples, probably because of a progressive modification from non-apatitic chemical environments to apatitic ones and a gradual dissolution of the hydrated layer with the time. The citrate content is close to the one recently measured in bone apatite surface [46]. The presence of carbonate in the Ap (around 1%) was mainly due to dissolved CO_2 in the mother solution and to CO_2 adsorbed onto the surface materials during the storage. The highest carbonate content in the cAp was obtained after 24 hours which is explained by a higher activity of carbonated species in the solution at that time.

Table 5. Compositional features and bulk Ca/P of Ap and cAp at different precipitation times.

Precipitation time	Structural water[a] (%wt.)	Citrate[a] (%wt.)	Carbonate[a] (%wt.)	Ca/P[b]
Ap 5 minutes	5.8±0.2	5.0±0.2	1.5±0.2	1.53±0.02
Ap 4 hours	3.9±0.1	2.4±0.1	1.1±0.1	1.51±0.02
Ap 24hours	3.3±0.1	1.9±0.1	1.0±0.1	1.52±0.03
Ap 48 hours	2.9±0.2	2.1±0.2	1.3±0.2	1.53±0.01
Ap 96 hours	2.6±0.2	2.0±0.1	1.0±0.1	1.54±0.02
cAp 5 minutes	6.3±0.3	5.9±0.2	1.5±0.1	1.60±0.02
cAp 4 hours	3.8±0.3	3.3±0.2	1.5±0.1	1.60±0.02
cAp 24hours	3.6±0.2	3.5±0.2	3.1±0.2	1.59±0.02
cAp 48 hours	2.6±0.2	2.1±0.1	2.6±0.3	1.59±0.01
cAp 96 hours	2.5±0.1	2.1±0.1	2.9±0.2	1.58±0.01

[a] Calculated by TGA, [b] Calculated by ICP-OES.

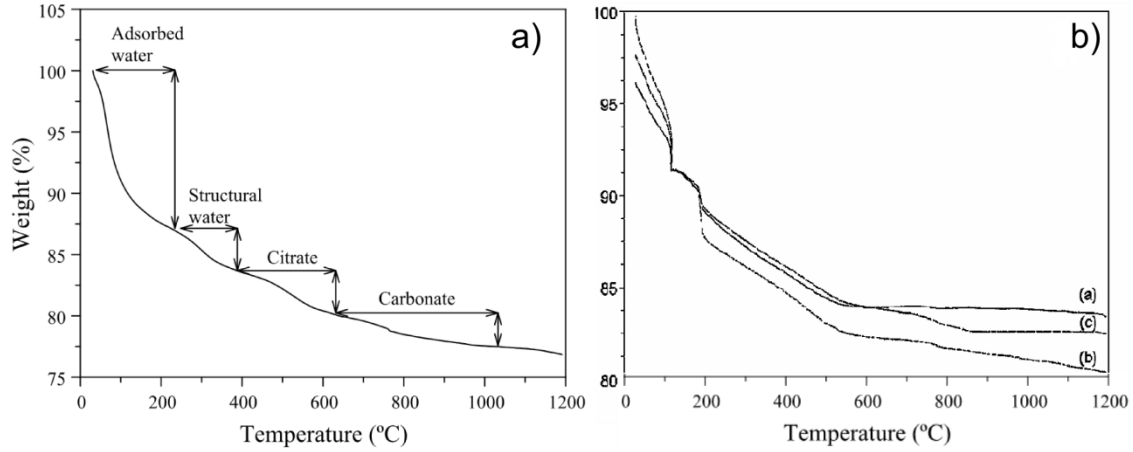

Figure 11. TGA curves of calcium phosphates: a) crystallized by thermal-decomplexing batch method after 96 h. Steps of weight loss are showed with arrows; b) crystallized by vapour diffusion method after 1 (a), 3 (b) and 7 days (c).

pH-decomplexing vapour diffusion droplet method

TGA analysis of precipitates obtained by vapour diffusion in droplets (Figure 11b) also confirm the presence of calcium phosphate compounds with structural water molecules (DCPD and /or OCP) in all samples and the increase of carbonate content with the crystallization time. In accordance with particles precipitated by batch method, four main weight losses were detected in the three analyzed samples. The weight loss from room temperature to 120 ˚C corresponds to the loss of adsorbed water, the sharp weight loss at 180 ˚C is due to the dehydration of brushite to monetite (DCP, $CaHPO_4$) and the weight loss from 200 ˚C to 550 ˚C is attributed to the loss of OCP lattice water molecules [97]. Finally, the weight loss from 550 ˚C to 950 ˚C is due to the CO2 released from the carbonate-substituted apatite [98]. The second and fourth weight losses confirm that the DCPD amount increased from 1 to 3 days and then decreased from 3 to 7 days. Moreover, the carbonate content clearly increases from 1 to 7 days. This finding together with FTIR data commented above suggest that A-type carbonate-apatite is favoured when increasing precipitation time, which is most probably due to the use of NH_4HCO_3 as a carbonation source [65].

4. Discussion

Important differences have been observed in the CaP precipitates obtained by the two different precipitation methods. When CaP was precipitated by pH-decomplexing vapour diffusion droplet method three different phases were obtained: DCPD plates, OCP ribbons and carbonate apatite nanocrystals. From these phases the OCP fulfils the criteria to be a precursor of apatite similar to that found in enamel, because under physiological conditions it crystallizes faster than apatite. OCP is thermodynamically less stable than apatite and therefore it can spontaneously transform to apatite, keeping the plate-like morphology and maintaining c- axes of the original OCP crystals. Experimental evidences strongly support a mechanism of enamel crystal formation through the OCP precursor phase [99]. Iijima et al. [100], by using a dual membrane device, consistent with the results of this work, found that the elongation of OCP crystals into a ribbon-like morphology was enhanced with the increase in concentration of Ca^{2+} or HPO_4^{2-}. Indeed, L increased while W decreased when the concentration of the solutions rose. However, our results show that when a high ionic concentration of Ca^{2+} and HPO_4^{2-} and a low concentration of NH_4HCO_3 are used this method does not allow a kinetic control of the precipitation of the CaP phases but only a thermodynamic control. Thus, the more stable carbonate-Ap phase is expected to be the unique crystalline phase in the precipitate after 7 days.

In contrast, when CaP were precipitated by thermal-decomplexing batch method, only presence of ACP was found in the first moments for both cAp and Ap reactions, transforming in time to carbonate-Ap, with a higher crystallinity degree for longer reaction periods. Both results have interesting implications in industrial calcium phosphate synthesis, as the desired precipitating phase would depend on the potential application of the material, with main applications in the biomedical science field.

In addition, it has been found that the presence of doping carbonate ions takes place through B-Type (phosphate) carbonate substitution. While, in both precipitation methods an increase of A-type (hydroxyl) carbonation have been observed with

precipitation time, B-type carbonation has been found to be predominant in doped cAp nanocrystals.

Apatites precipitated by batch method were found to be formed by a well-ordered carbonate-apatitic core coated by a non-apatitic layer composed of calcium, phosphate and carbonate species, citrate and structural water. The carbonate-substituted apatite core preferentially grew along the *c*-axis, although the two types of apatite displayed a different shape and size, which can be ascribed to the absence or presence of carbonate during the precipitation process [82, 101]. In the (10$\underline{1}$0) plane the spacing between Ca ions matches with either the spacing between the centers of two neighbor COO^- citrate groups (0.32 nm) or the distance between the two terminal carboxylates of citrate (0.688 nm) [46]. Consequently, citrate strongly bound to the (10$\underline{1}$0) face inhibiting their further growth. Nevertheless, the citrate adsorption on other crystal faces is less favored since Ca distances do not match well with the carboxylate distances of the citrate. Accordingly, after crystal growth, the (10$\underline{1}$0) face became predominant, resulting in thin nanocrystals with plate-like morphology. Rey *et al.* [75, 76] have reported the existence of a non-apatitic hydrated surface layer, which was well developed in freshly formed precipitates. They suggested that upon drying a partial restructuration of the surface hydrated layer occurs, but part of the non-apatitic environments still remains [75, 76].

By using both methods, the precipitation of nanocrystalline apatites is suggested to be formed by heterogeneous nucleation on a precursor phase that acts as a temporal template. The precipitation of a temporal substrate prior to the formation of nanosized apatites was previously demonstrated during the precipitation of this material from a calcium/citrate/phosphate solution at pH=8.3 using microwave or conventional heating [102]. In this system, the precipitation of a calcium citrate precipitate of composition $Na_3(Cit) \cdot 2H_2O$ during the first minutes of the experiment acted as temporal template for the formation of apatites with nanometric size. In the absence of this template, crystals grew until submicrometric or micrometric sizes. In the case of pH decomplexing vapour diffusion experiments, not acetate species but the OCP phase was found prior to nanoapatite, so this phase was suggested to act as a temporal template, as previously

reported [63]. The role of the template basically consists on the stabilization of the newly heterogeneously nucleated crystals within the nanometric sizes range. Indeed, the precipitation of apatites, or other calcium phosphates, usually takes place at very high values of the thermodynamic supersaturation, which leads to the formation of critical nuclei of extremely small sizes. The decrease of free energy in that system can be produced not only by growth but also by primary aggregation of the nascent particles with nanometer size. The presence of a template might interact with the primary particles formed by heterogeneous nucleation stabilizing them and, thus, minimizing their tendency to grow by aggregation [103]. By doing so, particles reach smaller sizes than those obtained in absence of citrate or presence of other Ca-complexing agent such as EDTA.

The nucleation process in both precipitation techniques is accompanied by a pH drop. As a consequence, the stabilization of OCP is firstly favored in the vapour diffusion experiments, as it is more stable than apatite at lower pH [1]. Subsequently, when NH_3 diffuses in the droplets and pH is increased, the thermodynamically more stable apatite epitaxially grows into OCP surface, which acts as a template while transforming to apatite by a solvent mediated transition [63]. In the batch method, due to the pH drop, the dissolution of the $Na_3(Cit) \cdot 2H_2O$ template occurs. Figure 12 represent a schematic model for the template nanoapatite formation in both systems, in order to illustrate the above mentioned processes.

Our results suggest that ACP is the first precipitated phase that directly and gradually, from the inner toward the outer surface, transforms to apatite [104], and that this transformation is promoted by the adsorption of free citrate ions on the particle surface, which results in the formation of nanoparticles composed of a carbonate-substituted apatitic core embedded on a non-apatitic hydrated layer (Figure 8). Moreover, it is noteworthy that the amount of citrate found on the nanoparticles is curiously very similar to that recently measured in bone apatite by Hu et al. [46]. From our current experimental data it is not possible to determine the nature, crystalline or amorphous, of the outermost hydrated layer. It could be either a well-structured non-

apatitic layer as proposed by Rey *et al.* or, on the other hand, it could be the remaining non-transformed ACP. Indeed, a non-structured surface layer has been previously detected in synthetic apatite by HREM and Solid-State MNR [65, 105-108]. Additionally, recent studies proposed a model of apatitic crystallites embedded in an amorphous matrix to explain the formation of nanocrystalline apatites in dentin of rats [109, 110] and human molars [111]. This amorphous surface layer is not a particularity of calcium phosphates, and has been also found in synthetic [112] and biological [113] aragonite.

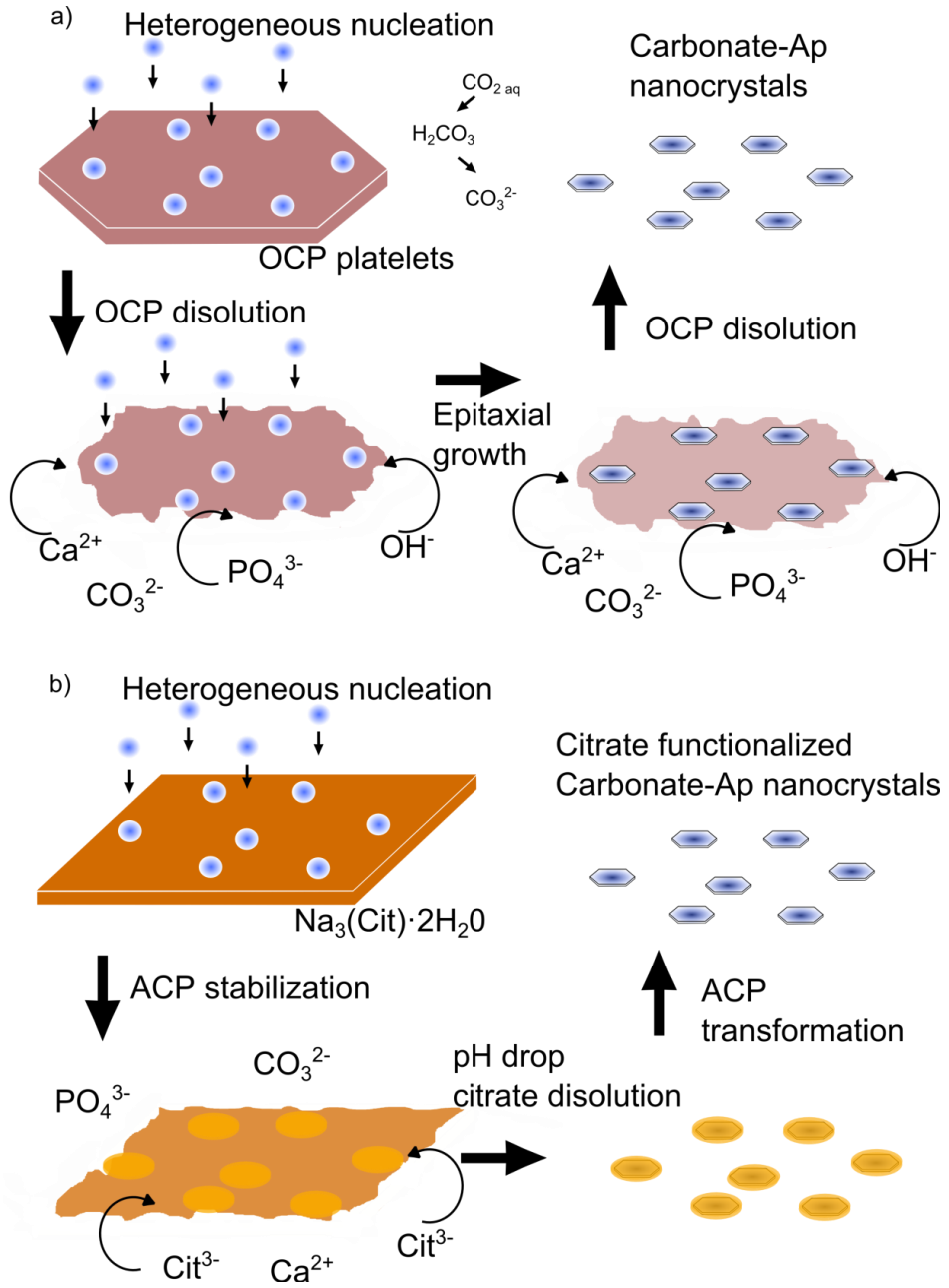

Figure 12. Schematic model for the template carbonate-Ap nanocrystals formation in a)vapour diffusion droplet method; b) thermal-decomplexing batch method

5. Conclusions

Two different precipitation techniques using Ca^{2+}complexing agents for the production of monodisperse carbonate-Ap nanoparticles have been studied along this chapter. The possibilities that offer these two routes and the scaling down process for investigating calcium phosphate nucleation and phase transformation have been evaluated.

- The sitting drop vapour diffusion technique, employing the "*crystallization mushroom*" was used to study CaP crystallization in micro-droplets containing high initial concentrations of $Ca(CH_3COO)_2$ and $(NH_4)_2HPO_4$, The method consists in diffusing vapours of NH_3 and CO_2 resulting from decomposition of NH_4HCO_3 solutions through droplets containing an aqueous solution of $Ca(CH_3COO)_2$ and $(NH_4)_2HPO_4$. The result is the increase in pH of the drops by means of the diffusion of NH_3 gas and the doping of the apatite precipitate with CO_3^{2-} ions by means of the diffusion of CO_2 gas. In a previous work, Iafisco et al. [63] have synthesized carbonate-Ap via OCP, which display nanometric dimensions, plate-like morphology, and low crystallinity degree. In this work we have investigated the same methodology of synthesis, but using a higher concentrated solution of Ca^{2+} and HPO_4^{2-} to increase the production of carbonate-Ap crystals and to explore the production of calcium phosphate by vapour diffusion technique in high ionic strength solutions. The evolution of the precipitates was monitored for one week and fully characterized. After one day, three calcium phosphate phases appeared: carbonate-Ap, DCPD and OCP. DCPD and OCP are well known to be the precursor phases for the crystallization of apatites. As suggested by SEM and XRD experiments, the relative amount of DCPD, which mainly grew along the *b* axis, increased from 0 to 3 days and then decreased up to 7 days. The OCP phase is found in a smaller weight percentage, whereas the amount of carbonate-Ap gradually increased with the precipitation time up to 7 days. Moreover, TEM images of precipitates obtained after 7 days showed crystals with two different morphologies: needle-like shaped apatite nanocrystals whose dimensions varied from 50-100 nm, closely resembling the

inorganic phase of bones, and OCP nanoribbons ranging from 1 μm to 2.5 μm in length and from 50 nm to 100 nm in width. The precipitation of disperse apatite nanocrystals has been explained by the template effect of OCP phase, which stabilizes the growing apatite nuclei, avoiding its aggregation while growing.

- The thermal decomplexing batch method applied to calcium/citrate/phosphate/carbonate metastable solutions was carried out with the aim of comparing small versus big precipitation volumes. Na_2CO_3 was added to the batch in order to crystallize bone-like carbonate-apatite nanoparticles with controlled carbonation degree, size and crystallinity. Non-stoichiometric poorly crystalline nanoparticles with sizes ranging from 20 to 200 nm and carbonation degree close to the one observed in bone-like apatites were precipitated. They contain a non-apatitic surface hydrated layer stabilized by citrate ions. In the absence of carbonate in the initial solution, we obtained larger and more crystalline nanoparticles whereas in the presence of carbonate we found smaller and more isometric nanoparticles. Furthermore, in the latter case, the presence of carbonate in the solution promoted the incorporation of these ions in A and B type positions on the apatitic structure, i.e., replacing OH^- and PO_4^{3-} groups, respectively.

Hence, we have demonstrated, with the help of small volumes for creating different precipitation environments, that experimental conditions (i.e. the way supersaturation is achieved, as well as physicochemical composition of the media) play an important role in tailoring both the physicochemical and the morphological properties of nanoapatites such as nucleating phase, size, solubility and carbonate content. All of them are quite important to obtain bone-like apatite with potential biomedical applications. The possible techniques for studying apatite crystallization in droplets are restricted by the special limitations of working with small volumes. The vapour diffusion technique, carried out in a *"crystallization mushroom"* permitted us to synthesize carbonate-Ap nanoparticles via heterogeneous nucleation on metastable OCP acting as temporal

template. On the other hand, the study of apatite crystallization in large volumes, performed by thermal-decomplexing batch method, led us to obtain carbonate-Ap nanoparticles via heterogeneous nucleation on $Na_3(Cit) \cdot 2H_2O$ acting also as a temporal template.

We should mention two noteworthy highlights that can be extracted from the characterization of both precipitation methods:

- The presence of ACP nanoparticles in the first instants of precipitation process of thermal-decomplexing batch reactions, while big sized crystalline particles of DCPD and OCP were obtained by vapour diffusion method. This observation can be explained by two combined effects: the speed by which supersaturation is created by thermal-decomplexing method, which is much faster than by vapour diffusion, allowing to reach more unstable calcium phosphate phases, as it has been observed for other different substances [114-116]; and the template effect of $Na_3(Cit) \cdot 2H_2O$ crystals, acting as a temporal substrate for heterogeneous nucleation, thus lowering the energy barrier for ACP formation.
- The precipitation of disperse apatite nanoparticles by vapour diffusion method, due to an analog template effect, established by the precursor OCP phase. Morphological differences between apatite nanoparticles synthesized by both methods were conditioned by the first nucleating phase, as well as by the presence of additives, that strongly affected crystal growth in given growth directions and its crystallinity degree.

As a concluding remark, it is well known that the biological properties, as well as the behavior of drug-functionalized nanoparticles (mainly load and release properties), are basically controlled by the physic-chemical properties of the nanoparticles such as size, charge and surface chemistry [117]. These properties were found to be easily tailored by the proposed batch crystallization method. For that reason cytotoxicity tests were carried out for the precipitated particles, and reported at [62], finding them to be fully biocompatible. These results are not presented in this chapter, as the direct applications

of the particles are not strictly related to the subject of this chapter. Nevertheless, the synthesized nanoparticles can be used as nanocarriers for local targeted drug delivery as well as biomimetic scaffold based materials in bone replacement [55]. **Appendix I** of the present chapter is attached in order to demonstrate its applicability, as the enclosed article has also been carried out within the framework of the same project.

The results of this chapter have been recently published:

- M. Iafisco, J. M. Delgado-López, J. Gómez-Morales, M. A. Hernández-Hernández, I. Rodríguez-Ruiz, N. Roveri. Formation of calcium phosphates by vapour diffusion in highly concentrated ionic micro-droplets, *Crystal Research Technology* 2011, 46(8), 841 – 846

- J. M. Delgado-Lopez, M. Iafisco, I. Rodríguez-Ruiz, A. Tampieri, M. Prat, J. Gomez-Morales. Crystallization of bioinspired citrate-functionalized nanoapatite with tailored carbonate content. *Acta Biomaterialia* 2012, 8(9), 3491-3499

- I. Rodríguez-Ruiz, J. M. Delgado-Lopez, M. A. Durán-Olivencia, M. Iafisco, A. Tampieri, D. Colangelo, M. Prat, J. Gomez-Morales. pH-Responsive Delivery of Doxorubicin from Citrate-Apatite Nanocrystals with Tailored Carbonate Content. *Langmuir* 2013. 29, 8213−8221

References

1. Dorozhkin S. Calcium Orthophosphates in Nature, Biology and Medicine. Materials. 2009;2(2):399-498.

2. LeGeros RZ. Calcium phosphates in oral biology and medicine. Monographs in oral science. 1991;15:1-201.

3. Elliot JC. Structure and Chemistry of the Apatites and Other Calcium Phosphates1994.

4. Amjad Z. Calcium phosphates in biological and industrial systems: Kluwer Academic Publishers Boston; 1998.

5. Johnsson MS-A, Nancollas GH. The Role of Brushite and Octacalcium Phosphate in Apatite Formation. Critical Reviews in Oral Biology & Medicine. 1992;3(1):61-82.

6. O'Neill W. The fallacy of the calcium-phosphorus product. Kidney International. 2007;72(7):792-6.

7. LeGeros R. Formation and transformation of calcium phosphates: relevance to vascular calcification. Zeitschrift für Kardiologie. 2001;90(3):116-24.

8. Becker A, Epple M, Müller K, Schmitz I. A comparative study of clinically well-characterized human atherosclerotic plaques with histological, chemical, and ultrastructural methods. Journal of Inorganic Biochemistry. 2004;98(12):2032-8.

9. Young RA, Brown WE, Nancollas GH. Biological Mineralization and Demineralization1982. 101 p.

10. Bermudez O, Boltong M, Driessens F, Planell J. Development of some calcium phosphate cements from combinations of α-TCP, MCPM and CaO. Journal of Materials Science: Materials in Medicine. 1994;5(3):160-3.

11. Kurashina K, Kurita H, Hirano M, Kotani A, Klein C, De Groot K. *In vivo* study of calcium phosphate cements: implantation of an α-tricalcium phosphate/dicalcium phosphate dibasic/tetracalcium phosphate monoxide cement paste. Biomaterials. 1997;18(7):539-43.

12. Driessens FC, Planell J, Boltong M, Khairoun I, Ginebra M. Osteotransductive bone cements. Proceedings of the Institution of Mechanical Engineers, Part H: Journal of Engineering in Medicine. 1998;212(6):427-35.

13. Eanes E, Termine J, Nylen M. An electron microscopic study of the formation of amorphous calcium phosphate and its transformation to crystalline apatite. Calcified Tissue Research. 1973;12(1):143-58.

14. Meyer J, Eanes E. A thermodynamic analysis of the amorphous to crystalline calcium phosphate transformation. Calcified Tissue Research. 1978;25(1):59-68.

15. Wuthier RE, Rice GS, Wallace Jr JE, Weaver RL, LeGeros RZ, Eanes ED. In vitro precipitation of calcium phosphate under intracellular conditions: formation of brushite from an amorphous precursor in the absence of ATP. Calcified Tissue International. 1985;37(4):401-10.

16. Sinyaev V, Shustikova E, Levchenko L, Sedunov A. Synthesis and dehydration of amorphous calcium phosphate. Inorganic Materials. 2001;37(6):619-22.

17. Termine J, Peckauskas R, Posner A. Calcium phosphate formation *in vitro*: II. Effects of environment on amorphous-crystalline transformation. Archives of Biochemistry and Biophysics. 1970;140(2):318-25.

18. Harries J, Hukins D, Holt C, Hasnain S. Conversion of amorphous calcium phosphate into hydroxyapatite investigated by EXAFS spectroscopy. J Cryst Growth. 1987;84(4):563-70.

19. Harries J, Hukins DW. Analysis of the EXAFS spectrum of hydroxyapatite. Journal of Physics C: Solid State Physics. 1986;19(34):6859.

20. Peters F, Schwarz K, Epple M. The structure of bone studied with synchrotron X-ray diffraction, X-ray absorption spectroscopy and thermal analysis. Thermochimica Acta. 2000;361(1):131-8.

21. Takagi S, Chow L, Ishikawa K. Formation of hydroxyapatite in new calcium phosphate cements. Biomaterials. 1998;19(17):1593-9.

22. Skrtic D, Antonucci JM, Eanes ED. Improved properties of amorphous calcium phosphate fillers in remineralizing resin composites. Dental Materials. 1996;12(5):295-301.

23. Skrtic D, Antonucci J, Eanes E. Amorphous calcium phosphate-based bioactive polymeric composites for mineralized tissue regeneration. Journal of Research - National Institute of Standards and Technology. 2003;108(3):167-82.

24. Linhart W, Peters F, Lehmann W, Schwarz K, Schilling AF, Amling M, et al. Biologically and chemically optimized composites of carbonated apatite and polyglycolide as bone substitution materials. Journal of Biomedical Materials Research. 2001;54(2):162-71.

25. Tadic D, Epple M. Amorphous calcium phosphates as bone substitution materials. Eur J Trauma. 2002;28:136-7.

26. Brown W, Mathew M, Tung M. Crystal chemistry of octacalcium phosphate. Progress in crystal growth and characterization. 1981;4(1):59-87.

27. LeGeros RZ. Variations in the crystalline components of human dental calculus: I. Crystallographic and spectroscopic methods of analysis. Journal of Dental Research. 1974;53(1):45-50.

28. Schroeder HE, Shanley D. Formation and inhibition of dental calculus. Journal of Periodontology. 1969;40(11):643-6.

29. Brown WE. Octacalcium Phosphate and Hydroxyapatite: Crystal Structure of Octacalcium Phosphate. Nature. 1962;196:1048-50.

30. Brown WE. Crystal growth of bone mineral. Clinical Orthopaedics and Related Research. 1966;44:205-20.

31. Tomazic B, Brown W, Schoen F. Physicochemical properties of calcific deposits isolated from porcine bioprosthetic heart valves removed from patients following 2–13 years function. Journal of Biomedical Materials Research. 1994;28(1):35-47.

32. Nancollas GH, Wu W. Biomineralization mechanisms: a kinetics and interfacial energy approach. J Cryst Growth. 2000;211(1):137-42.

33. Kamakura S, Sasano Y, Homma H, Suzuki O, Kagayama M, Motegi K. Implantation of octacalcium phosphate (OCP) in rat skull defects enhances bone repair. Journal of Dental Research. 1999;78(11):1682-7.

34. Suzuki O, Imaizumi H, Kamakura S, Katagiri T. Bone regeneration by synthetic octacalcium phosphate and its role in biological mineralization. Current medicinal chemistry. 2008;15(3):305-13.

35. Jensen AT, Rowles S. Magnesian whitlockite, a major constituent of dental calculus. Acta Odontologica. 1957;15(2):121-39.

36. Frondel C. Whitlockite: a new calcium phosphate Ca3 (PO4) 2. Am Miner. 1941;26:145-52.

37. Kodaka T, Debari K, Higashi S. Magnesium-containing crystals in human dental calculus. Journal of electron microscopy. 1988;37(2):73.

38. Mirtchi AA, Lemaître J, Munting E. Calcium phosphate cements: study of the β-tricalcium phosphate—dicalcium phosphate—calcite cements. Biomaterials. 1990;11(2):83-8.

39. Ohura K, Bohner M, Hardouin P, Lemaître J, Pasquier G, Flautre B. Resorption of, and bone formation from, new β-tricalcium phosphate-monocalcium phosphate cements: An in vivo study. Journal of Biomedical Materials Research. 1996;30(2):193-200.

40. Yin X, Stott M, Rubio A. α-and β-tricalcium phosphate: a density functional study. Physical Review B. 2003;68(20):205205.

41. Fernandez E, Ginebra M, Boltong M, Driessens F, Planell J, Ginebra J, et al. Kinetic study of the setting reaction of a calcium phosphate bone cement. Journal of Biomedical Materials Research. 1996;32(3):367-74.

42. Oda M, Takeuchi A, Lin X, Matsuya S, Ishikawa K. Effects of liquid phase on basic properties of alpha-tricalcium phosphate-based apatite cement. Dental Materials Journal. 2008;27(5):672.

43. Mann S. Biomineralization: principles and concepts in bioinorganic materials chemistry. Oxford: University Press; 2001.

44. Lowenstam HA, Weiner S. On Biomineralization. Oxford: University Press; 1989.

45. Eichert C, Drouet C, Sfihi H, Rey C, Combes C. Nanocrystalline apatite-based biomaterials: synthesis, processing and characterization. In: Kendall JB, editor. Biomaterials Research Advances: Nova Science Publishers; 2007. p. 93–143.

46. Hu YY, Rawal A, Schmidt-Rohr K. Strongly bound citrate stabilizes the apatite nanocrystals in bone. PNAS. 2010;107(52):22425-9.

47. Wang L, Nancollas GH. Calcium Orthophosphates: Crystallization and Dissolution. Chemical Reviews. 2008;108(11):4628-69.

48. Roveri N, Palazzo B. Hydroxyapatite Nanocrystals as Bone Tissue Substitute. Nanotechnologies for the Life Sciences: Wiley-VCH Verlag GmbH & Co. KGaA; 2007.

49. Gómez-Morales J, Iafisco M, Delgado-López JM, Sarda S, Drouet C. Progress on the preparation of nanocrystalline apatites and surface characterization: Overview of fundamental and applied aspects. Progress in Crystal Growth and Characterization of Materials. 2013;59(1):1-46.

50. Legros R, Balmain N, Bonel G. Age-related changes in mineral of rat and bovine cortical bone. Calcified Tissue International. 1987;41(3):137-44.

51. Iafisco M, Palazzo B, Marchetti M, Margiotta N, Ostuni R, Natile G, et al. Smart delivery of antitumoral platinum complexes from biomimetic hydroxyapatite nanocrystals. Journal of Materials Chemistry. 2009;19(44):8385-92.

52. López-Macipe A, Gómez-Morales J, Rodríguez-Clemente R. Nanosized Hydroxyapatite Precipitation from Homogeneous Calcium/Citrate/Phosphate Solutions Using Microwave and Conventional Heating. Adv Mater. 1998;10(1):49-53.

53. Iafisco M, Palazzo B, Falini G, Foggia MD, Bonora S, Nicolis S, et al. Adsorption and conformational change of myoglobin on biomimetic hydroxyapatite nanocrystals functionalized with alendronate. Langmuir. 2008;24(9):4924-30.

54. Palazzo B, Iafisco M, Laforgia M, Margiotta N, Natile G, Bianchi CL, et al. Biomimetic Hydroxyapatite–Drug Nanocrystals as Potential Bone Substitutes with Antitumor Drug Delivery Properties. Adv Funct Mater. 2007;17(13):2180-8.

55. Delgado-López JM, Iafisco M, Rodríguez-Ruiz I, Gómez-Morales J. Bio-inspired citrate-functionalized apatite thin films crystallized on Ti-6Al-4 V implants pre-coated with corrosion resistant layers. Journal of Inorganic Biochemistry. (0).

56. Rodríguez-Ruiz I, Delgado-López JM, Durán-Olivencia MA, Iafisco M, Tampieri A, Conagelo D, et al. pH-Responsive Delivery of Doxorubicin from Citrate-Apatite Nanocrystals with Tailored Carbonate Content. Langmuir. 2013;29:8213−21.

57. Dorozhkin SV. Nanosized and nanocrystalline calcium orthophosphates. Acta Biomaterialia. 2010;6(3):715-34.

58. Dorozhkin SV. Nanosized and nanocrystalline calcium orthophosphates. Acta Biomater. 2010;6(3):715-34.

59. Padilla S, Izquierdo-Barba I, Vallet-Regí M. High Specific Surface Area in Nanometric Carbonated Hydroxyapatite. Chemistry of Materials. 2008;20(19):5942-4.

60. Sanchez C, Arribart H, Giraud Guille MM. Biomimetism and bioinspiration as tools for the design of innovative materials and systems. Nat Mater. 2005;4(4):277-88.

61. Sugimoto T. Preparation and characterization of monodispersed colloidal particles. MRS Bull. 1989;14(12):23-8.

62. Delgado-Lopez JM, Iafisco M, Rodriguez I, Tampieri A, Prat M, Gomez-Morales J. Crystallization of bioinspired citrate-functionalized nanoapatite with tailored carbonate content. Acta Biomaterialia. 2012;8(9):3491-9.

63. Iafisco M, Morales JG, Hernández-Hernández MA, García-Ruiz JM, Roveri N. Biomimetic Carbonate–Hydroxyapatite Nanocrystals Prepared by Vapor Diffusion. Advanced Engineering Materials. 2010;12(7):B218-B23.

64. Hernández-Hernández A, Rodríguez-Navarro AB, Gómez-Morales J, Jiménez-Lopez C, Nys Y, García-Ruiz JM. Influence of Model Globular Proteins with Different Isoelectric Points on the Precipitation of Calcium Carbonate. Cryst Growth Des. 2008;8(5):1495-502.

65. Nassif N, Martineau F, Syzgantseva O, Gobeaux F, Willinger M, Coradin T, et al. In Vivo Inspired Conditions to Synthesize Biomimetic Hydroxyapatite. Chemistry of Materials. 2010;22(12):3653-63.

66. Gustafsson JP.Visual MINTEQ 3.0, Computer Program for Calculating Aqueous Geochemical Equilibria; 2011. Adapted from MINTEQA2 (CEAM, EPA, 1999).

67. Dorozhkin SV. Amorphous calcium (ortho)phosphates. Acta Biomaterialia. 2010;6(12):4457-75.

68. Klug HP, Alexander LE. X-Ray Diffraction Procedures: For Polycrystalline and Amorphous Materials. 2nd ed. New York: Wiley-VCH; 1974.

69. Lazic S. Microcrystalline hydroxyapatite formation from alkaline solutions. J Cryst Growth. 1995;147(1-2):147-54.

70. Lynn A, Bonfield W. A novel method for the simultaneous, titrant-free control of pH and calcium phosphate mass yield. Accounts of Chemical Research. 2005;38(3):202-7.

71. Habraken WJEM, Tao J, Brylka LJ, Friedrich H, Bertinetti L, Schenk AS, et al. Ion-association complexes unite classical and non-classical theories for the biomimetic nucleation of calcium phosphate. Nat Commun. 2013;4:1507.

72. Gómez-Morales J, Delgado-López JM, Iafisco M, Hernández-Hernández A, Prat M. Amino Acidic Control of Calcium Phosphate Precipitation by Using the Vapor Diffusion Method in Microdroplets. Cryst Growth Des. 2011;11(11):4802-9.

73. Pan HB, Darvell BW. Effect of Carbonate on Hydroxyapatite Solubility. Cryst Growth Des. 2010;10(2):845-50.

74. Zhang C, Yang J, Quan Z, Yang P, Li C, Hou Z, et al. Hydroxyapatite Nano- and Microcrystals with Multiform Morphologies: Controllable Synthesis and Luminescence Properties. Cryst Growth Des. 2009;9(6):2725-33.

75. Rey C, Combes C, Drouet C, Sfihi H, Barroug A. Physico-chemical properties of nanocrystalline apatites: Implications for biominerals and biomaterials. Materials Science & Engineering C: Biomimetic and Supramolecular Systems. 2007;27(2):198-205.

76. Rey C, Combes C, Drouet C, Glimcher MJ. Bone mineral: update on chemical composition and structure. Osteoporosis International. 2009;20(6):1013-21.

77. Arellano-Jiménez MJ, García-García R, Reyes-Gasga J. Synthesis and hydrolysis of octacalcium phosphate and its characterization by electron microscopy and X-ray diffraction. Journal of Physics and Chemistry of Solids. 2009;70(2):390-5.

78. Xin R, Leng Y, Wang N. In situ TEM examinations of octacalcium phosphate to hydroxyapatite transformation. J Cryst Growth. 2006;289(1):339-44.

79. Ma G, Liu XY. Hydroxyapatite: Hexagonal or Monoclinic? Cryst Growth Des. 2009;9(7):2991-4.

80. Yang X, Gao X, Gan Y, Gao C, Zhang X, Ting K, et al. Facile Synthesis of Octacalcium Phosphate Nanobelts: Growth Mechanism and Surface Adsorption Properties. The Journal of Physical Chemistry C. 2010;114(14):6265-71.

81. Roveri N, Palazzo B, Iafisco M. The role of biomimetism in developing nanostructured inorganic matrices for drug delivery. Expert Opinion on Drug Delivery. 2008;5(8):861-77.

82. Legeros RZ, Trautz OR, Legeros JP, Klein E, Shirra WP. Apatite Crystallites: Effects of Carbonate on Morphology. Science. 1967;155(3768):1409-11.

83. Baig AA, Fox JL, Hsu J, Wang Z, Otsuka M, Higuchi WI, et al. Effect of carbonate content and crystallinity on the metastable equilibrium solubility behavior of carbonated apatites. Journal of Colloid and Interface Science. 1996;179(2):608-17.

84. Yao F, LeGeros JP, LeGeros RZ. Simultaneous incorporation of carbonate and fluoride in synthetic apatites: Effect on crystallographic and physico-chemical properties. Acta Biomaterialia. 2009;5(6):2169-77.

85. Bigi A, Boanini E, Cojazzi G, Falini G, Panzavolta S. Morphological and Structural Investigation of Octacalcium Phosphate Hydrolysis in the Presence of Polyacrylic Acids: Effect of Relative Molecular Weights. Cryst Growth Des. 2001;1(3):239-44.

86. Kumta PN, Sfeir C, Lee DH, Olton D, Choi D. Nanostructured calcium phosphates for biomedical applications: novel synthesis and characterization. Acta Biomater. 2005;1(1):65-83.

87. Štulajterová R, Medvecký Ľ. Effect of calcium ions on transformation brushite to hydroxyapatite in aqueous solutions. Colloids and Surfaces A: Physicochemical and Engineering Aspects. 2008;316(1–3):104-9.

88. Liou SC, Chen SY, Lee HY, Bow JS. Structural characterization of nano-sized calcium deficient apatite powders. Biomaterials. 2004;25(2):189-96.

89. Koutsopoulos S. Synthesis and characterization of hydroxyapatite crystals: A review study on the analytical methods. Journal of Biomedical Materials Research. 2002;62(4):600-12.

90. Bala Y, Farlay D, Delmas PD, Meunier PJ, Boivin G. Time sequence of secondary mineralization and microhardness in cortical and cancellous bone from ewes. Bone. 2010;46(4):1204-12.

91. Antonakos A, Liarokapis E, Leventouri T. Micro-Raman and FTIR studies of synthetic and natural apatites. Biomaterials. 2007;28(19):3043-54.

92. Socrates G. Infrared and Raman Characteristic Group Frequencies. Chichester: John Wiley & Sons; 2001.

93. Awonusi A, Morris M, Tecklenburg M. Carbonate assignment and calibration in the raman spectrum of apatite. Calcified Tissue International. 2007;81(1):46-52.

94. Fowler BO, Markovic M, Brown WE. Octacalcium phosphate. 3. Infrared and Raman vibrational spectra. Chemistry of Materials. 1993;5(10):1417-23.

95. Xu G, Aksay IA, Groves JT. Continuous crystalline carbonate apatite thin films. A biomimetic approach. J Am Chem Soc. 2001;123(10):2196-203.

96. Tõnsuaadu K, Gross K, Plũduma L, Veiderma M. A review on the thermal stability of calcium apatites. Journal of Thermal Analysis and Calorimetry. 2011;DOI: 10.1007/s10973-011-1877-y.

97. Jinlong N, Zhenxi Z, Dazong J. Investigation of Phase Evolution During the Thermochemical Synthesis of Tricalcium Phosphate. Journal of Materials Synthesis and Processing. 2001;9(5):235-40.

98. Yusufoglu Y, Akinc M. Effect of pH on the Carbonate Incorporation into the Hydroxyapatite Prepared by an Oxidative Decomposition of Calcium–EDTA Chelate. Journal of the American Ceramic Society. 2008;91(1):77-82.

99. Iijima M, Moradian-Oldak J. Control of octacalcium phosphate and apatite crystal growth by amelogenin matrices. Journal of Materials Chemistry. 2004;14(14):2189-99.

100. Iijima M, Hayashi K, Moriwaki Y. Effects of the Ca2+ and PO43− ion flow on the lengthwise growth of octacalcium phosphate in a model system of enamel crystal formation with controlled ionic diffusion. J Cryst Growth. 2002;234(2–3):539-44.

101. LeGeros RZ. Apatites in biological systems. Prog Cryst Growth Charact. 1981;4(1-2):1-45.

102. López-Macipe A, Gómez-Morales J, Rodríguez-Clemente R. Nanosized hydroxyapatite precipitation from homogeneous calcium/citrate/phosphate solutions using microwave and conventional heating. Adv Mater. 1998;10(1):49.

103. Rodríguez-Clemente R, López-Macipe A, Gómez-Morales J, Torrent-Burgués J, Castaño VM. Hydroxyapatite precipitation: A case of nucleation-aggregation-agglomeration-growth mechanism. J Eur Ceram Soc. 1998;18(9):1351-6.

104. Tsuji T, Onuma K, Yamamoto A, Iijima M, Shiba K. Direct transformation from amorphous to crystalline calcium phosphate facilitated by motif-programmed artificial proteins. PNAS. 2008;105(44):16866-70.

105. Sakhno Y, Bertinetti L, Iafisco M, Tampieri A, Roveri N, Martra G. Surface Hydration and Cationic Sites of Nanohydroxyapatites with Amorphous or Crystalline Surfaces: A Comparative Study. The Journal of Physical Chemistry C. 2010;114(39):16640-8.

106. Isobe T, Nakamura S, Nemoto R, Senna M, Sfihi H. Solid-State Double Nuclear Magnetic Resonance Study of the Local Structure of Calcium Phosphate Nanoparticles Synthesized by a Wet-Mechanochemical Reaction. The Journal of Physical Chemistry B. 2002;106(20):5169-76.

107. Jäger C, Welzel T, Meyer-Zaika W, Epple M. A solid-state NMR investigation of the structure of nanocrystalline hydroxyapatite. Magnetic Resonance in Chemistry. 2006;44(6):573-80.

108. Bertinetti L, Tampieri A, Landi E, Ducati C, Midgley PA, Coluccia S, et al. Surface Structure, Hydration, and Cationic Sites of Nanohydroxyapatite:,Äâ UHR-TEM,

IR, and Microgravimetric Studies. The Journal of Physical Chemistry C. 2007;111(10):4027-35.

109. Tseng Y-H, Tsai Y-L, Tsai TWT, Chao JCH, Lin C-P, Huang S-H, et al. Characterization of the Phosphate Units in Rat Dentin by Solid-State NMR Spectroscopy. Chemistry of Materials. 2007;19(25):6088-94.

110. Huang S-J, Tsai Y-L, Lee Y-L, Lin C-P, Chan JCC. Structural Model of Rat Dentin Revisited. Chemistry of Materials. 2009;21(13):2583-5.

111. Porter AE, Nalla RK, Minor A, Jinschek JR, Kisielowski C, Radmilovic V, et al. A transmission electron microscopy study of mineralization in age-induced transparent dentin. Biomaterials. 2005;26(36):7650-60.

112. Nassif N, Gehrke N, Pinna N, Shirshova N, Tauer K, Antonietti M, et al. Synthesis of Stable Aragonite Superstructures by a Biomimetic Crystallization Pathway. Angewandte Chemie. 2005;117(37):6158-63.

113. Nassif N, Pinna N, Gehrke N, Antonietti M, Jäger C, Cölfen H. Amorphous layer around aragonite platelets in nacre. PNAS. 2005;102(36):12653-5.

114. Lee I, Lee A, Myerson A. Concomitant Polymorphism in Confined Environment. Pharm Res. 2008;25(4):960-8.

115. Lee AY, Lee IS, Myerson AS. Factors Affecting the Polymorphic Outcome of Glycine Crystals Constrained on Patterned Substrates. Chem Eng Technol. 2006;29(2):281-5.

116. Lee IS, Kim KT, Lee AY, Myerson AS. Concomitant Crystallization of Glycine on Patterned Substrates: The Effect of pH on the Polymorphic Outcome. Cryst Growth Des. 2008;8(1):108-13.

117. Li S-D, Huang L. Pharmacokinetics and Biodistribution of Nanoparticles. Molecular Pharmaceutics. 2008;5(4):496-504.

CHAPTER 5

Effects of confinement in nucleation

Controlled water diffusion and effects of confinement in NaCl solution micro-droplets

1. State of the art

Droplet evaporation is a phenomenon involved in many domains such as : drying of colloidal suspension [1], drying of human blood drops for diagnostic purposes [2], coffee ring deposition on solid surfaces [3], efficacy and efficiency of pesticide applications [4], meteorology and air-conditioning [5], nanoscale pipetting for confined chemistry [6], detection of molecules and biomarkers below picomolar concentration [7], inked-based direct writing technology [8], crystallization of protein by the vapor diffusion method [9], crystallization in confined environments [10, 11] and in a close relation with this latter domain, deterioration of building materials and porous stones [12, 13] due to salt weathering.

Salt weathering is a common mechanism of degradation for porous natural systems and is one of the main weathering processes causing the loss of sculptural and architectural heritage [13]. This degradation mechanism consists on the disruptive pressure exerted by a crystallizing salt when it grows in a confined space [14], that is to say deep in the stone pores [13, 15, 16], often resulting in significant damage [17]. The pressure generated by the crystal growth against the pore walls is frequently high enough to overcome the tensile strength of the porous material, leading to their gradual disintegration[18]. On this sense, many studies have been performed on the effects that crystal growth exerts on porous materials of interest. It has been shown that the crystallographic characteristics of the salt may control the pattern and significance of damage in porous stones when crystallization occurs [19], being crystal shape and morphology dependent on the achieved supersaturation for the nucleation of crystals. This supersaturation would depend in the last term of solution flow and water evaporation rate within the stone, and it is directly related to the extent of salt damage [13], i.e. the higher supersaturation, the higher weathering effect.

Recently, a simply-constructed and easy-to-use fluidic device was reported for generating arrayed aqueous phase microdroplets under oil (sessile geometry), in volumes ranging from nanoliter to femtoliters, without surfactant required [20]. In subnanoliter crystallization experiments performed with this fluidic device, the evaporation of the droplets was observed [21] due to selective diffusion of water into oil [22]. This process generates an increment of solute concentration and thus supersaturation, leading to crystallization. Microdroplets were observed under an inverted optical microscope and the solute concentration was qualitatively monitored through the evolution of the optical contrast between the droplet and the continuous phase. Nevertheless, it is possible to implement a precise and quantitative determination of the solute concentration during the diffusion process by monitoring the droplet volume. To date, this was performed, for instance, by image analysis of dispersed aqueous salt solutions in silicone oil [22] but not for sessile microdroplets in oil. Microdroplet evaporation due to diffusion of water in oil is equivalent to their evaporation in air, but the lower evaporation rates and small volumes, somewhat resembling the evaporation conditions during the processes of salt weathering, makes this technique very interesting for studying nucleation phenomena in porous systems.

In this section, with a view to give insights in crystallization phenomena causing weathering processes, we present experiments in which the contraction/evaporation of sessile microdroplets of aqueous phase into oil is observed using an optical microscope. A full characterization of the evaporation process and droplet evolution has been carried out, considering that there are not so many studies reported on contact angle measurement on picoliter droplets [23, 24], mainly due to the rapid evaporation of such small volumes, rendering quantitative measurements difficult to be performed. Contact angle of the microdroplet with the substrate, microdroplet height and contact diameter are monitored during diffusion of water into oil and, using simple trigonometry, already presented in **chapter 2** of the present manuscript, microdroplet volumes are computed and time evolution of concentration in the droplets is calculated.

2. Experimental

Reagents and solutions

Sodium Chloride (NaCl, ACS reagent, ≥ 99,0 % purity), was supplied by Sigma-Aldrich. Paraffin oil was supplied by Hampton Research. Ultrapure water (0.22 µS, 25 °C, MilliQ©, Millipore) was used to prepare all the solutions. NaCl solutions were filtered by using 0.22 µm Millipore filters.

Microdroplet water diffusion experiments (subnano to picovolumes)

Experiments were carried out using a Femtojet microinjector (Eppendorf), introducing a 2.71M NaCl solution in a femtotip (Eppendorf), and subsequently injecting it on a plastic coverslip (22x22mm SPI) under 100 µL of paraffin oil inside a homemade plastic-cell with vertical walls for side observation using an optical microscope. Arrays of microdroplets of NaCl solution were deposited over the cover slip under a Zeiss Axio Observer D1 inverted microscope, and subsequently the cell was transferred to a side-view microscope (BXFM focusing module, Olympus equipped of an homemade holder) and observed (figure 1). The description of the microinjection technique and the experimental set-up is detailed in chapter 2 of this manuscript. Femtotips, attached to a capillary holder, were controlled by a home-made micromanipulator consisting of three miniature translation stages (piezo electric, MS30 mechonics) in X, Y and Z with a displacement of 18 mm in the 3 directions by steps of 16 nm [25]. Initial microdroplet volumes were determined through image analysis, following the model described in section 2 of chapter 2 of this manuscript. The principle of the experiments is to let water slowly diffuse from the crystallization drops through the layer of parffin oil, which results in an increase in the concentration of solute, establishing supersaturation [25]. Figure 2 presents top- and side-views of a part of an array of 2.71M NaCl microdroplets in oil. In a previous paper, the monodispersity of the droplet size at the pixel resolution was shown [20]. For instance, the volume of the 4 microdroplets of figure 2b is 151±7pL (details of

the calculation are given in chapter 2). *In situ* observation of the evaporation and precipitation process was carried out from the time of initial droplets generation until crystallization events took place (from 15 to 120 hours).

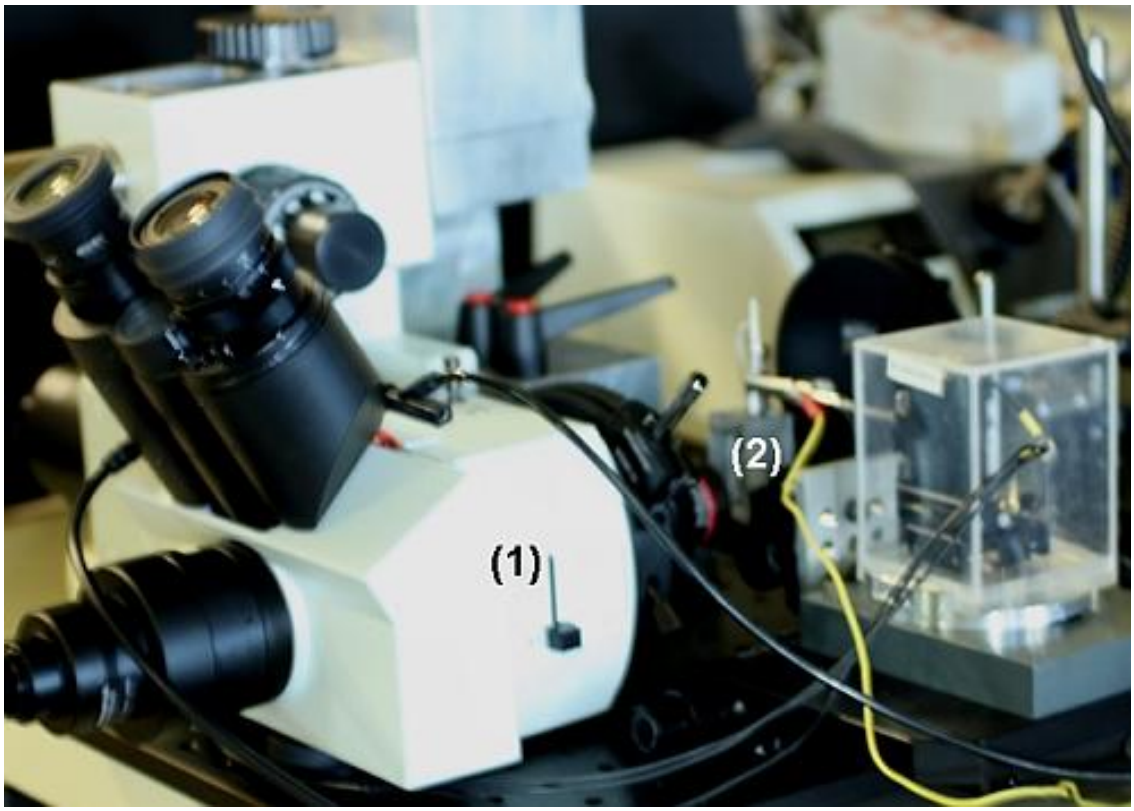

Figure 1. Image of the experimental setup for side observation**,** (1) microscope and (2) plastic cell.

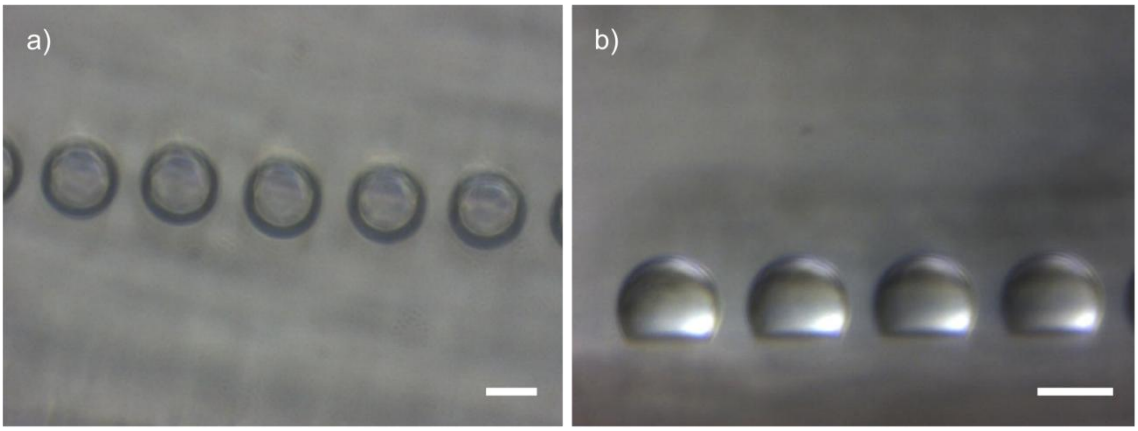

Figure 2. a) Top-view and b) side-view of 2.71M NaCl microdroplets (151pL) in oil. The scale bar represents 50µm.

3. Results and discussion

The sequence of figure 3 presents the 2.71M NaCl microdroplet contraction by diffusion of water into oil. During contraction, the solution becomes more and more concentrated. At the end of the process, when the concentration reach condition of instability, the microdroplets collapse due to the nucleation and growth of one single crystal by microdroplet in accordance with previous theoretical predictions [26]. For instance, this phenomena was used to deposit a solute in a confined region, which is of high interest for detection of molecules in highly diluted solutions in biomedicine, safety and eco-pollution in relation to rare and dangerous chemicals [7].

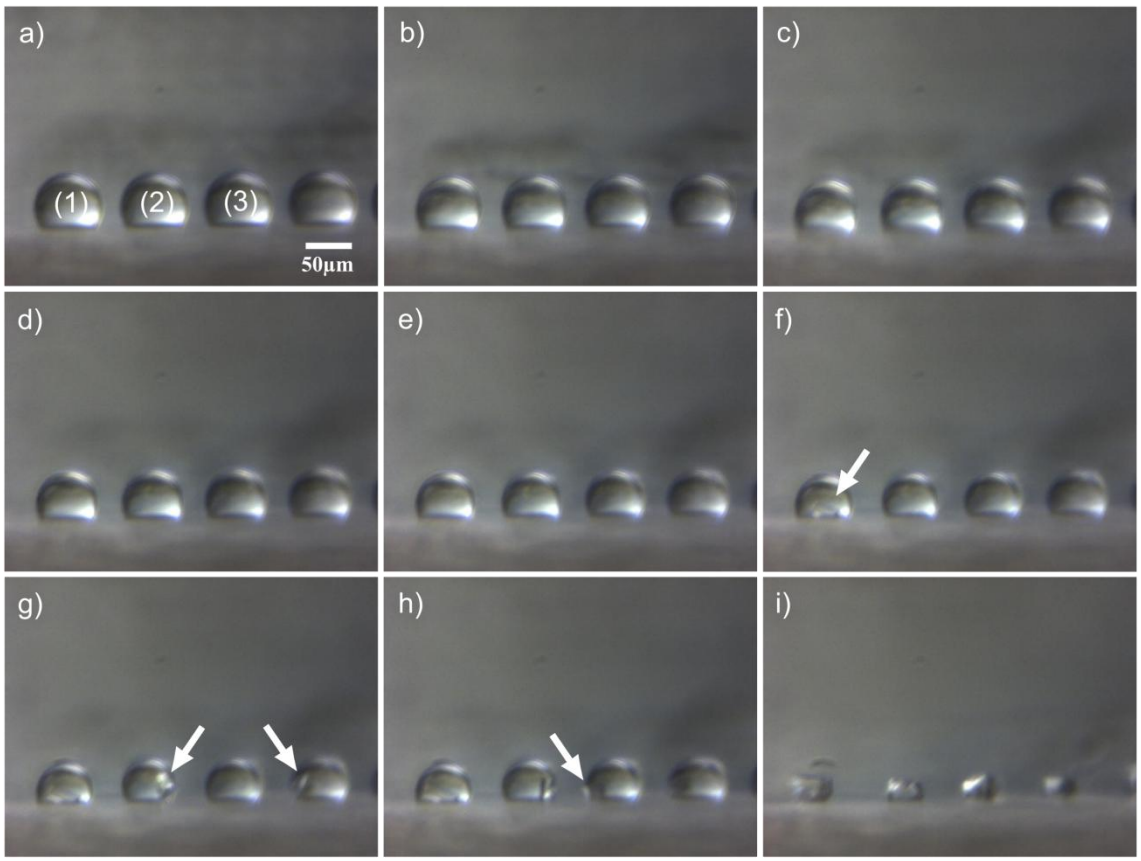

Figure 3. Time sequence showing the side-view of 2.71M NaCl microdroplets (151pL) contraction in oil, a) t=0min, b) t=60.05min, c) t=130.12min, d) t=190.18min, e) t=260.25min, f) t=330.32min g) t=360.32min, h) t=380.32min and i) t=740.31min. Arrows in (f), g) and h) show the appearance of crystals.

In practice, because of the microdroplet size, we can assume there is no shape distortion due to gravity; thus microdroplet profiles can be fitted to a segment of a circle [23, 27]. Thus contact angle of the microdroplet with the substrate, microdroplet height and contact diameter can be easily extracted from this experiment, as it will be shown below.

Evolution of contact angle and contact diameter

Evaporation of a sessile droplet is known to proceed via different stages: constant contact angle, constant contact area and mixed mode depending on the surface roughness and chemical nature, atmospheric conditions and to the droplet size [23, 24, 28]. Figure 4a shows a continuous decrease of the contact angle, θ, for our experiments. The initial contact angle can be identified as an advancing angle, θ_A, and the decrease of the contact angle corresponds to a bracketing by the receding angle, θ_R:

$$\theta_A > \theta > \theta_R \quad (1)$$

This decrease corresponds to the stage II described by Bourgès-Monnier and Shanahan [28], where the height and the contact angle decrease, while the contact diameter remains constant. At the end of the stage II, the contact angle is θ_R and should remain constant, although it is not observed here because nucleation occurred before, as we saw in fig.3f-i. The evolution of height and contact diameter also confirms the process to be in stage II. An initial pinning of the perimeter leads to a nearly constant contact diameter (respectively area), thus contraction proceeds via microdroplet height and contact angle diminutions [23]. These results confirm that evaporation of picoliter microdroplets is comparable to microliter droplets. Moreover, the rapid decrease of θ in the first stage due to rapid evaporation observed by Taylor *et al.* [23] is not observed due to the presence of oil which act as a buffer slowing down the diffusion rate. For instance, in previous experiments presented by Furuta *et al.* [24] evaporation of a 800 pL droplet takes about 8 s, whereas in the experimental approach presented in this letter, evaporation takes several hours.

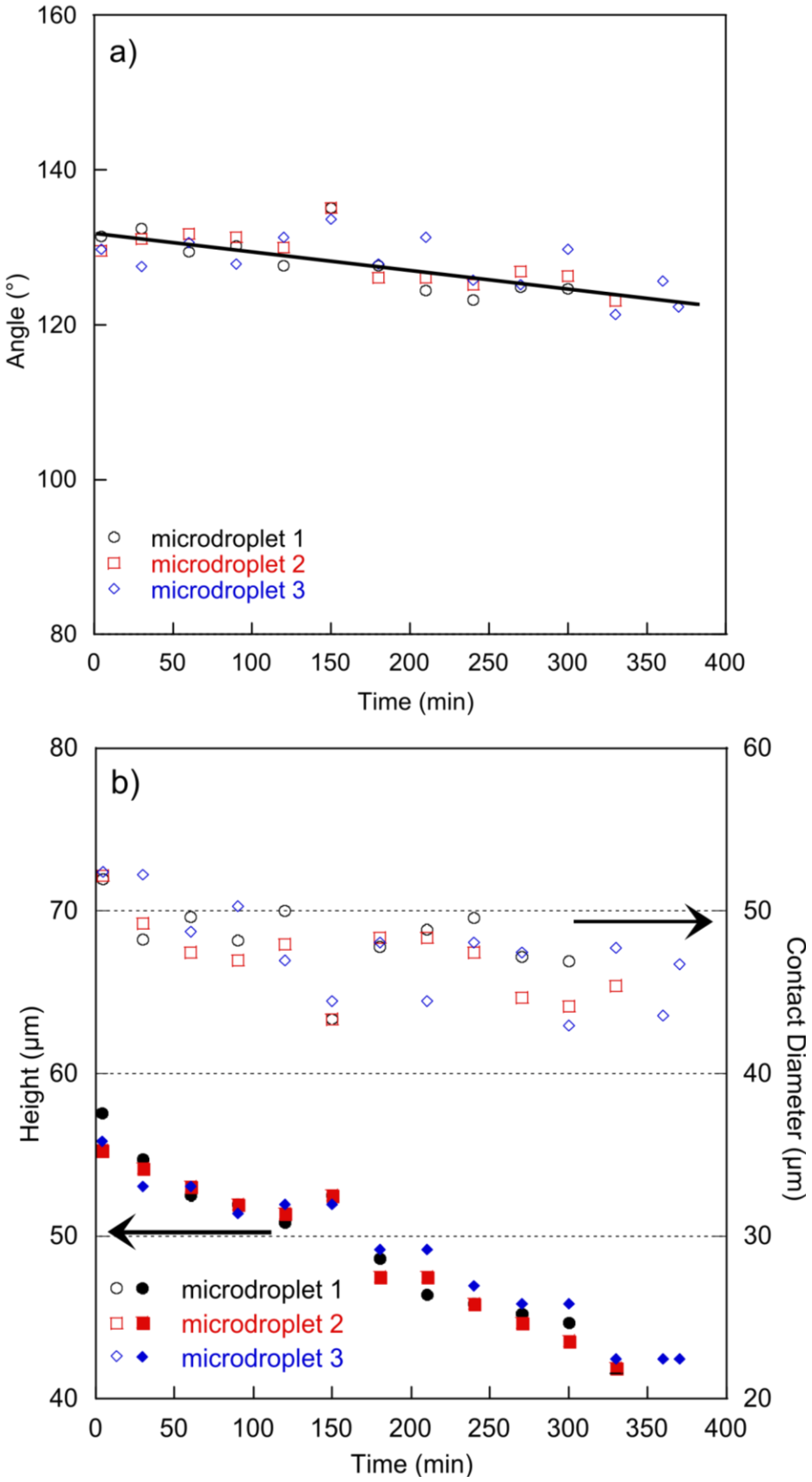

Figure 4. a) Contact angle of the microdroplets of figure 3 with the substrate and b) microdroplet height and contact diameter. The line is a guide to the eyes and microdroplet numbers correspond to the microdroplets of figure 3a.

Evolution of volume

Figure 5 presents the evolution of NaCl, water, Na_2CO_3 and $CaCl_2$ microdroplet volumes with time; lines in the figure are linear fits of the data corresponding to a constant evaporation rate of the microdroplet, α, according to:

$$\frac{V}{V_0} = (1 - \alpha t) \quad (2)$$

with V_0 and V the initial and actual microdroplet volumes respectively and α the normalized evaporation rate, which is a linear function of the saturation fraction of water into oil [29]. A semi-log plot is used to traduce the apparent final acceleration in the evaporation which is not due to an increase of the evaporation rate but to the fact there is less matter to evaporate to decrease the microdroplet volume.

The evaporation rate of a water microdroplet into an infinite medium is constant. In our experiments, water microdroplets of 64.6 ± 1.2 pL are formed in an immiscible medium having a volume of ~100 µL (6 orders of magnitude larger than the microdroplets) which means that the water droplet is in effectively infinite dilution regime, as confirmed by the constant value of α obtained in our experiments in pure water (fig.5a). Moreover, when a salt is added to water the rate of solvent evaporation would be constant for a dilute solution if the activity of water is not greatly affected by the presence of salt. In their paper, Talreja *et al.* [30] assumed a constant evaporation rate for protein and salt solutions until $\frac{V}{V_0} = 0.15$. In our experiments with 2.71 M NaCl solutions (fig.5a) the evaporation rate is constant until nucleation occurred for $\frac{V}{V_0} > 0.4$ in agreement with Talreja *et al.* Moreover, the evaporation rate is also constant for Na_2CO_3 and $CaCl_2$ microdroplets evaporation.

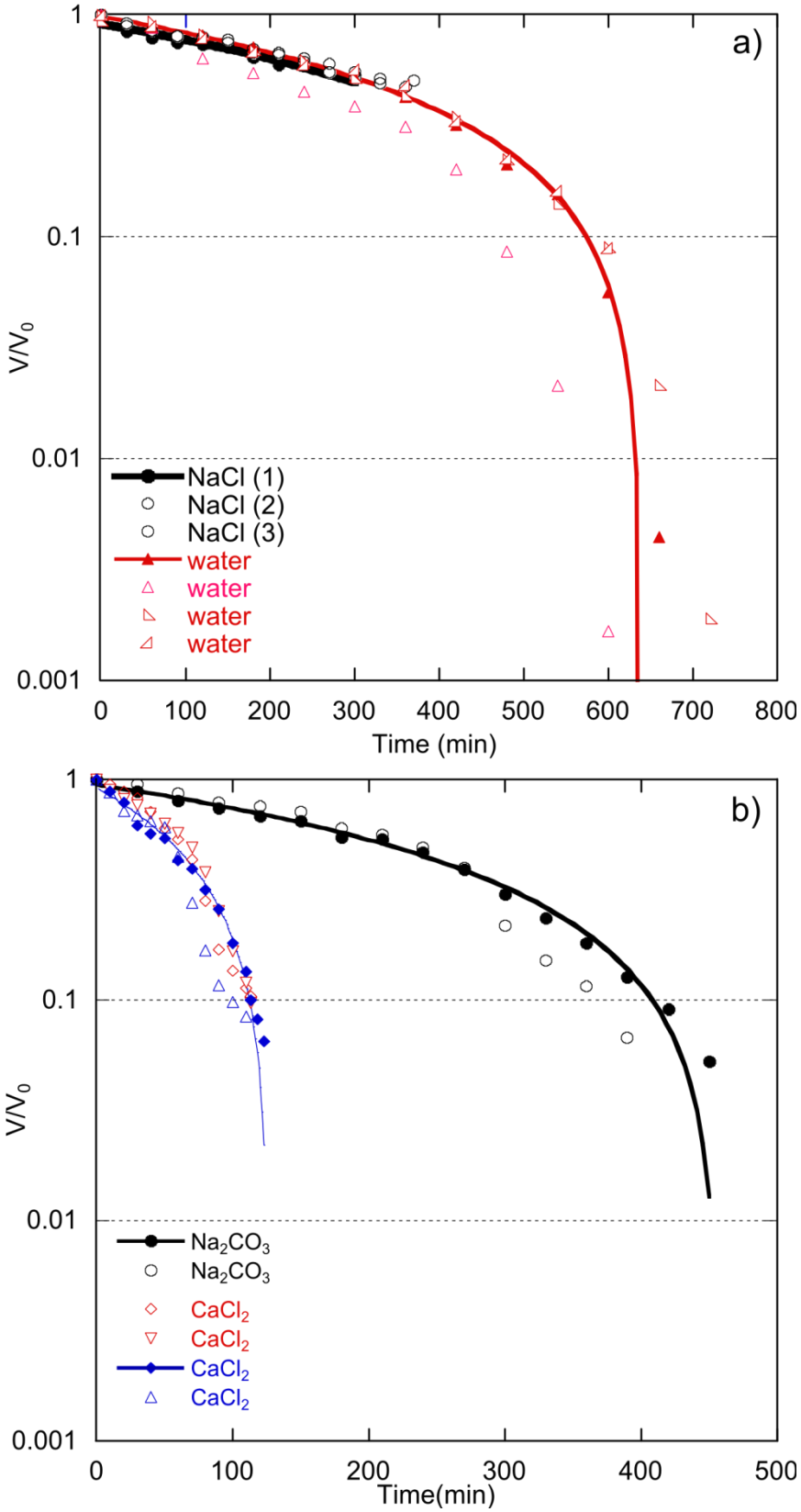

Figure 5. Volume contraction in semi-log plot (a) for the 2.71M NaCl and water microdroplets of initial volume of 151 ± 7 pL and 64.6 ± 1.2 pL respectively and (b) for 60 mM Na_2CO_3 and $CaCl_2$ microdroplets of initial volume of 655 ± 24 pL and 42.2 ± 5.5 pL respectively. The underscores for NaCl captions correspond to the microdroplets of figure 3; lines are linear fits of the data.

Evolution of concentration

Concentration was followed as a function of volume reduction for two ranges of volumes. Figure 6a shows the evaporation sequence of a single droplet with an initial volume of 2.7 nL. This droplet was generated reclusively, instead of in an array. For that reason the initial contact angle is slightly higher than for droplets generated in arrays, in which contact area becomes larger due to de dynamic forces produced with the tip during the injection. Sodium chloride crystal appears after 57.5 h, at a determined concentration of ~ 7.2 M, value significantly above saturation concentration (5.4 M at 25 °C, which is reached at approximately 35 h). Figure 6b shows the evolution of the concentration of this droplet with time, as well as the saturation concentration for NaCl at the experiment temperature. Similar behavior was observed for 7 droplets with an initial volume of 356.7 ± 17.6 pL, reaching concentration values between 6.1 and 7 M. (fig. 7), also clearly above saturation concentration for NaCl. If we express these concentration values in terms of supersaturation, S, (eq. 1.3 of introductory chapter 1)

$$S = \frac{C}{C^*} \tag{1.3}$$

we determine a value of S between 1.13 and 1.32 for these experiments before nucleation occurs. It is noteworthy that these achieved high supersaturation values prior to nucleation events are not caused by a quick variation of supersaturation conditions, as concentration in the droplets is a function of evaporation rate, and this evaporation rate is very low. The stabilization of the supersaturated NaCl solutions is explained through the Classical Nucleation Theory by the reduced number of nucleation evens expected in a smaller volume, for a given nucleation frequency. Therefore, for our experiments, induction periods should be expected to be longer than those for analog experiments in larger volumes. In this context, as evaporation of the water molecules is constant in time, the longer induction periods maintain the droplets in a metastable state while supersaturation is being increased in time by water evaporation. This observation becomes especially interesting for the salt weathering processes. A higher supersaturation achieved in the pores of stones, due to confinement effects, would cause a major

degradation and disintegration of the material due to a higher disruptive pressure exerted for the growing crystals.

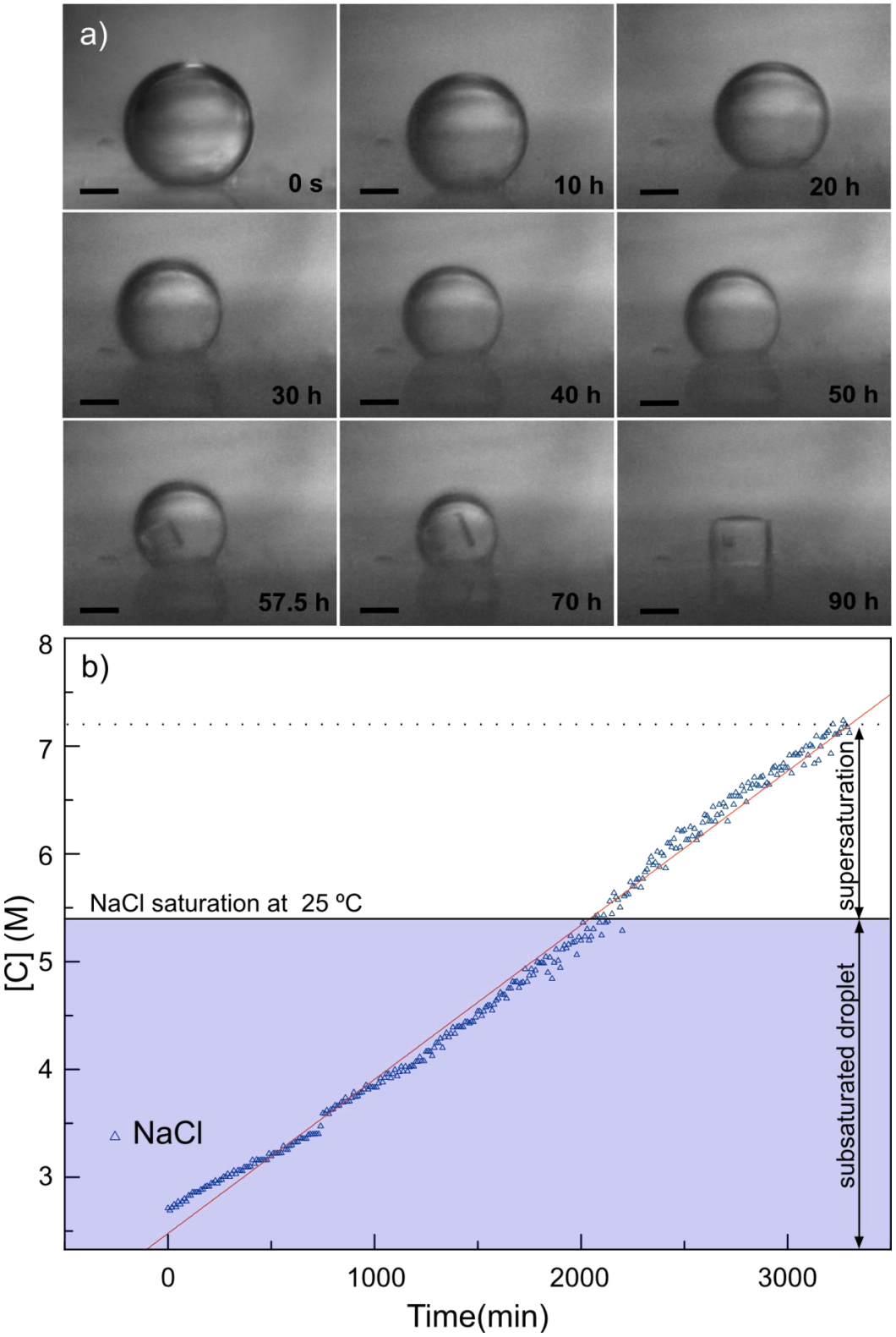

Figure 6. a) Time sequence showing the side-view of 2.71M NaCl microdroplets (2.7 nL) contraction in oil. b) Evolution of the concentration with time in the same microdroplet, overcoming NaCl saturation concentration for the experiment and reaching a value of 7.2 M for nucleation concentration several hours later.

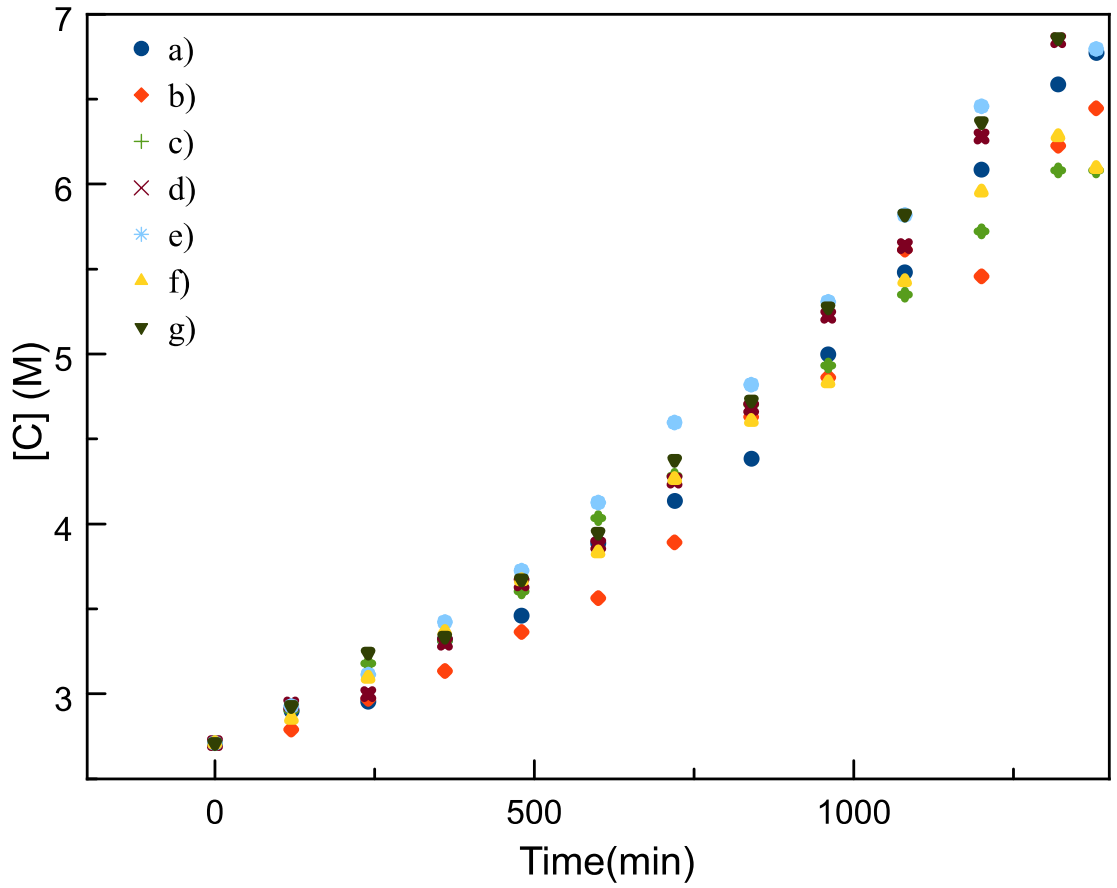

Figure 7. Evolution of the concentration of 7 different NaCl microdroplets (a) to g) V= 356.7 pL) with time.

4. Conclusions

We have presented experiments in which the evaporation of sessile microdroplets of aqueous phase into oil are observed and characterized using a recently developed [20] fluidic device that generates arrayed aqueous phase microdroplets in oil. An initial pinning of the microdroplet perimeter leads to a nearly constant contact diameter, thus contraction proceeds via microdroplet height and contact angle diminutions confirming the process to be the stage II described by Bourgès-Monnier and Shanahan [28] for evaporation of a sessile droplet. We evidenced a constant evaporation rate of the microdroplet for different microdroplet composition, from pure water to different salts. The application of this simple model to crystallization experiments in confined volume driven by solvent diffusion, has allowed us to precisely know the value of the

concentration in the microdroplets during the experiments and particularly at the moment of nucleation. The determined supersaturation values in the microdroplets prior to nucleation revealed that confinement of the solution in nano- to pico-volumes exerts an effect of temporary stabilization of supersaturated solutions, reaching higher supersaturation values at the moment of nucleation. This observation is of special interest in the context of salt weathering processes, where a higher supersaturation achieved in the pores of stones leads to higher disruptive pressure values, exerted for the growing crystals, and therefore to a major degradation and disintegration of the porous stones.

Transient calcium carbonate hexahydrate (ikaite) temporarily stabilized in confined nano- and picovolumes

1. State of the art

Important efforts have been done during the last decades towards a better comprehension of the mechanisms by which nucleation and crystal growth occur. In this direction, the use of confinement in small volumes has been identified as a really powerful tool for the study of nucleation. Since the probability of observing the formation of a crystal during a nucleation process is very low due to its stochastic nature [31], confinement permits the location of nucleation events in space and thus, it makes their observation possible. Moreover, confinement is also of great interest in controlled biomineralization when the mineral deposition occurs in compartmented well defined volumes such as intracellular vesicles [32]. This natural process of nucleation control, of great importance, is the critical key point in the formation of biological mineral structures, and it is not yet completely understood, requiring thus a better consideration and study. Related with biomineralization, $CaCO_3$ is a protagonist in this process, and one of the main inorganic biominerals in nature, as well as being of interest for its industrial applications as a filler in plastics, rubber, paper, paints and pigments, food and pharmaceutical industry, in addition to plastisol industry for car underbody paints, among many others [33-35]. For both, natural and industrial processes, the control of either the calcium carbonate nucleating phase or its transformation in other more stable one and its growth is essential for determining not only the necessary or desired polymorph, size distribution and morphology of the crystals (which finally determine its physical-chemical and optical properties, such as solubility, hardness, opacity or brightness, directly related with its functionality) but also the properties of the natural (biomaterials) or manufactured composite materials.

Nowadays The use of confinement for nucleation and polymorphism studies is attracting an increasing scientific interest [31]. Controlled-pore glasses, membranes and other nanoporous materials have been used as confining environments. These materials are generally in contact with the bulk solution, limiting the availability of reactants and generating the depletion of free molecules when the nucleation events take place [36-38]. Microemulsions have also been used to produce confinement in isolated volumes, in order to measure critical nucleus size via a thermal behavior [39]. Generation of small droplets, with the help of different techniques [40-43], offers the possibility of a volumetric isolation and a spatial confinement that differs from all the previously mentioned methods and permits the control of nucleation events in a particular space that can be directly observed and monitored. To this end, regular arrays of microdroplets have been generated on patterned self-assembled monolayers as substrate, to investigate the polymorphism of some organic compounds [42, 44, 45], reaching supersaturation through controlled evaporation of subsaturated droplets and finding the access to different polymorphs by generating high supersaturation by very high evaporation rates. Same kind of substrate has also been used to study the nucleation and growth of $CaCO_3$ in controlled heterogeneous conditions and low supersaturation [46]. Other microdevices like the crystallization mushroom also permitted to study the nucleation and polymorphism of calcium carbonate in a previous work [43], generating supersaturation by slow diffusion of NH_3 and CO_2 gasses in $CaCl_2$ microdroplet solutions at different supersaturations. The order of appearance of the polymorphs in the droplets was controlled by the intrinsic features of the crystallization mushroom, that is, the slow increase in the ionic activity product caused by slow diffusion of NH3 and CO2 gases, which favors the least soluble phase calcite to crystallize before other more soluble polymorphs. In a closer relation with this manuscript, a droplet based microfluidic reactor was used to precipitate $CaCO_3$ generating supersaturation by direct mixing of equal volumes of equimolar aqueous solutions of $CaCl_2$ and Na_2CO_3, with the aim of control crystal size and size distribution, as well as the nucleating phase, as a function of supersaturation [47].

Nucleation of $CaCO_3$, and the possible effects that confinement exerts on it, is also nowadays of increasing scientific, enviromental and social interest. Increasing environmental pollution in urban areas has been endangering the survival of carbonate stones in monuments and statuary for many decades, seriously affecting cultural heritage. New methodologies for restoring the carbonate materials have been developed by the use of bacterially induced carbonate mineralization [48]. The calcite biominerals grains acts as a cement by deposition on the walls of the stone pores increasing its stress ressisstence. Variations in the composition of the culture medium directly affect the nucleation of different polymorphs (vaterite or calcite), therefore modifying the cementing properties [49, 50]. CaCO3 has also direct and obvious implications the injection of supercritical CO_2 for geological storage under deep permeable formations. Indeed, when injecting supercritical CO2, the capture of this gas takes place in the small pores and cracks of deep permeable geological formations. Then it transforms to calcium carbonate and other carbonates by reaction with free earth alkali ions found in solution. Therefore the precipitation of calcium carbonate may have an important impact in the permeability of the geological formation, as well as in its long-term storage capability.

Previous efforts have been done with the purpose of enlightening the obscuracy surrounding the structure formation during precipitation of CaCO3 towards a better understanding of the process. On one hand, when CaCO3 precipitates from highly supersaturated solutions, it is known that a first metastable phase nucleates and transforms to more stable phases according to the Ostwald's step rule. Precipitation and aggregation of precursor nanoparticles to form vaterite and thermodynamically stable calcite crystals was observed by Ogino et al. by initial time-resolved studies [51]. These nanoparticles were further characterized using in situ small angle X-ray scattering by Bolze et. al, revealing the amorphous and hydrated nature of this monodisperse nanoparticles, which subsequently dissolve to crystallize in a more thermodynamically stable form [52]. The initial formation of an amorphous phase has been explained through both classical and non-classical approaches. The classical approach assumes a decreasing in the interfacial energy of the nucleating phase as it becomes more

metastable, expecting thus a lower nucleation barrier for amorphous than for crystalline phase, and therefore kinetically favoring the formation of the metastable phase [53]. A non-classical approach was recently reported by Gebauer et. al [54], suggesting that nucleation takes place through precritical cluster aggregation. Evidences of structural preformation and the nucleation of different ACC species which later transform into the particular crystalline polymorph were found at different pH conditions. In addition, overtaking of the solubility product and generation of supersaturation with respect to a given polymorph are necessary conditions for its formation from a solution. It was shown that within narrow supersaturation conditions in which ACC solubility is not reached, it is possible for other hydrated metastable $CaCO_3$ phases to precipitate [55]. $CaCO_3$ hydrated phases are ikaite (IK, $CaCO_3 \cdot 6H_2O$) and monohydrocalcite (MHC, $CaCO_3 \cdot H_2O$). IK is known to precipitate steadily at low temperatures or high pressures [56, 57]. In nature and in the laboratory, the mineral readily crystallizes from solution at temperatures near 0 $^\circ$C, although it rapidly decomposes at warmer temperatures. On the other hand the stability of MHC has long been debated [58]. Generally MHC is formed from ACC and transforms to calcite and/or aragonite [58-60], although it was found stable for centuries in natural ancient sediments [61, 62].

In this section we present experiments in which ikaite (not ACC) is the first nucleating polymorph at laboratory temperature. The IK phase is temporarily stabilized in confinement at medium to high supersaturations. Its stability increases when reducing the volume of the droplets from nano- to picoliter scale and transforms to calcite (in certain experiments to vaterite) by a solvent mediated transformation. These findings are relevant for the aforementioned fields, but particularly for biomineralization since there are biomineralization processes involving calcium carbonate that occur in the confined volume of intracellular vesicles [32], at relatively high supersaturations [63-65].

2. Experimental

Reagents and solutions

Sodium chloride (NaCl, ACS reagent, ≥ 99,0 % purity), calcium chloride dihydrate ($CaCl_2 \cdot 2H_2O$, Bioxtra, ≥ 99,0 % purity) and sodium carbonate monohydrate ($Na_2CO_3 \cdot H_2O$, ACS reagent, 99.5% purity) were supplied by Sigma-Aldrich. FC-70 fluorinated oil and paraffin oil were supplied by Hampton Research. Ultrapure water (0.22 µS, 25 °C, MilliQ©, Millipore) was used to prepare all the solutions. Na_2CO_3 and $CaCl_2$ solutions of concentrations ranging from 10 to 200 mM were prepared by dilution of corresponding 1 M stock solutions, and filtered by using 0.22 µm Millipore filters. Ionic strength was equilibrated by adding the necessary amount of NaCl (after which solutions were re-filtered). Speciation, nominal ion activity product (IAP) and saturation index (SI=log (IAP/Ks)) with respect to calcite phase of solutions were obtained by mixing equimolar volumes of Na_2CO_3 and $CaCl_2$ were determined by using PHREEQ-C software package [66] considering chloride mean-salt ionic activity-coefficient data [67] in the Debye-Hückel equation and equilibration of all solutions with atmospheric CO_2.

Droplet based microfluidic experiments (nanovolumes)

Experiments in nanoliter droplets (2-3 nL) whose nominal IAPs range from 2.82×10^{-8} to 5.25×10^{-6} $mol^2.L^{-2}$ (SI from 0.9 to 3.18), were performed in HPFA (Teflon polymer) capillaries of 150 µm internal diameter. Equimolar solution volumes of Na_2CO_3 and $CaCl_2$ were pumped through a PEEK T-junction and mixed in a capillary (2.8 cm long). This capillary is connected to a second T-junction [41, 68]. The second T-junction is connected to an oil reservoir, which is used as the carrier fluid to generate the droplets (for a more detailed description see Figure 5 of chapter 2). In each experiment an array of nanoliter droplets was generated inside a teflon capillary (as shown in figure 5b of chapter 2). After mixing of the two reagent solutions an initial precipitate was formed almost instantaneously in the capillary before the T-junction with oil. Then, this precipitate experienced a phase transition. We, thus, optimized the flow rates of both, reagent solutions and oil in order to observe this transition within the generated droplets and not

inside the capillary connecting the first T-junction. The total mixing flow rate for the experiments was 6 mL/h, representing a residence time of 0.5 s in the connecting capillary. Monitoring was carried out through direct observation with a Wild Heerbrugg M420 Makroskop and a Nikon Diaphot inverted microscope at room temperature (20 ± 2 °C). *In situ* observations were performed from the moment of mixing the initial solutions up to the end of the experiments (lasting from several hours to several days).

Microinjection experiments (picovolumes)

Experiments in subnanoliter and picoliter volumes (hundreds of picoliters and tens of picoliters, respectively) with $CaCl_2/Na_2CO_3$ molar ratios between 0.25 and 3.0, whose IAPs range from $6.16x10^{-9}$ to $3.09x10^{-7}$ $mol^2.L^{-2}$ (SI from 0.27 to 1.97 with respect to calcite phase), were carried out using a Femtojet microinjector (Eppendorf). Solutions were first introduced on different femtotips (Eppendorf), and then injected under a 30 µL droplet of paraffin oil. The description of this technique and the experimental set-up is detailed in chapter 2 of this manuscript. Arrays of microdroplets of $CaCl_2$ solutions were deposited over a plastic cover slip. Subsequently, Na_2CO_3 equimolar solutions were added with a second tip to the first droplets in different volume ratios, thus generating droplet mixtures with different molar ratios, directly in a confined space. Femtotips, attached to a capillary holder, were controlled by a home-made micromanipulator consisting of three miniature translation stages (piezo electric, MS30 mechonics) in X, Y and Z with a displacement of 18 mm in the 3 directions by steps of 16 nm [25]. Experiments were monitored with a Zeiss Axio Observer D1 inverted microscope, and initial and mixing volumes were determined through image analysis of the microdroplets, following the model described in section 2 of chapter 2 of this manuscript. The principle of the experiments is to mix picoliter volumes of the reactant solutions under oil, generating an initial supersaturation. Lately water slowly diffuses from the crystallization drops through the layer of parffin oil, resulting in an increase in the concentration of solute. *In situ* observation of the precipitation process was carried out from the time of initial droplets mixture until complete crystallization of the droplets (which lasted from 15 to 24 hours).

Characterization

High resolution transmission electron microscopy (HRTEM), and selected area electron diffraction (SAED) experiments were performed with a JEOL 3010 instrument and a JEOL JEM-2010 operating at 200 kV. The samples were prepared recovering the precipitates from the droplets under oil with the help of a capillary and depositing them over copper-carbon TEM grids lying on an adsorbent tissue. A droplet of hexane was immediately added over the grids to dissolve and remove the remaining mineral oil. SAED patterns analyses were performed by comparing measured distances and related measured angles between them with the help of CaRIne 3.1 crystallography software [69]. d-spacings were assigned to their corresponding reflections under the criteria of the best fit with respect to reported d-spacings and related angles for calcium carbonate phases, i.e. IK (Cystallography Open Ddatabase (COD) ID: 9008306), MHC (COD ID: 9010479), aragonite (COD ID: 9000229), vaterite (COD ID: 9007475) and calcite (COD ID: 9009667). Field emission scanning electron microscopy (FESEM) and energy-dispersive X-ray spectroscopy (EDS) analyses were performed with a JEOL 6320F over the same grids after HRTEM analysis.

X-Ray diffraction (XRD) patterns of precipitates obtained in nanoliters droplets were collected on a Mar Research single crystal rotating anode diffractometer (CuKα, λ=1.5418Å) equipped with a mar345 Image Plate Detector. Precipitates were fished from the droplets with the help of a nylon loop. XRD patterns of precipitates were collected in different images with an exposition time of 60 s/image in a total rotating angle of 360°. Additionally, XRD patterns of precipitates obtained in picoliter droplets (microinjection technique) were collected on a Bruker D8 Venture single crystal diffractometer equipped with a high brilliance in-coatec micro source (CuKα, λ=1.5418Å) and a Photon100 detector at 2θ = 0, 10, 20 and 30°. The frames were added and integrated with the Bruker APEX2 suite and the help of XRD2EVAL plug-in.

A Mach-Zehnder interferometer was used to characterize the mixing of droplets containing the reactant solutions. The experiment was performed in a Hele-Shaw [70]

type cell composed by two parallel glass plates separated by a 200 µm gap. A laser diode beam (20 mW, 633 nm) was first passed through a Faraday isolator, so as to avoid any back-reflection toward the semiconductor laser cavity. A movable short focal length lens and a rotating ground glass diffuser allowed tuning the spatial coherence of the beam. Beam was subsequiently divided in the reference and the sample (test) beams by means of a beamsplitter. The sample beam propagated through the experimental volume before being recombined with the reference beam. The result of the recombination is the generation of interference fringes (interferogram) at imaging plane. The interferogram carries the information of the variation of the optical path between the object and the reference beam. The Laser diode controller, CCD, and a temperature sensor for gathering the room temperature during the experiments were all controlled by means of a Labview based scripts developed ad hoc for the application. More information about the interferometer can be found in section 5 of chapter 2 in the present manuscript. For a qualitative description of the mixing, the concentration profiles for Ca^{2+} and CO^{3-} ions was simulated for the first instants of mixing, in a first approach, applying Fick's law of diffusion [71]. For diffusion coefficient calculations ionic radii of 0.99 Å and 1.73 Å were respectively considered for Ca^{2+} and CO^{3-} ions [72].

3. Results

3.1. Calcium carbonate precipitation in nanoliter droplets (microfluidic setup)

3.1.1. Optical microscopy monitoring

Figure 2a shows images of time resolved precipitation in a 3 nL droplet at SI = 3.18 and 1:1 ($CaCl_2$:Na_2CO_3) mixing ratio. It is observed the formation of a first precipitate and its dissolution while a second crystalline precipitate appears and grows. In the initial moments (from 30 s to 2 min) a sol composed of ultrafine particles describing a brownian motion appears in the droplets (red circle at t = 2 min). At 2 min 2 small crystals (lately morphologically characterized as calcite) appeared (red arrows at t = 2 min) and merged into an aggregate (t = 7 min) that grew while the first precipitate dissolved (from 9 to 11min, red circles at t = 9, 10 and 11 min). The period for this transition was increased from few minutes to several hours as the initial SI with respect to calcite phase was

decreasing from 3.18 to 0.9. Figure 2b shows an array of 2 nL droplets of different chemical composition (SI 2.74, fig2b shows 3 droplets of a total of more than 50 droplets experiment). First, precipitation occurred instantaneously after mixing in all the droplets. Precipitates showed birefringence under crossed polarisers since the very beginning of the experiment, increasing its intensity during the first instants. Second, from 35 min the precipitate transformed in some droplets into faceted calcite crystals, clearly identified by its morphology. Finally, after 5.6 h precipitates in all droplets were transformed in facetted calcite crystals. The transformation to calcite occurred in most of the observed droplets (~95% of the total). In few droplets (~5% of the total), in addition to the faceted calcite crystals, polycrystalline spherulitic aggregates of different sizes, morphologically assigned to vaterite, were also found. This appreciation is shown in figure 3.

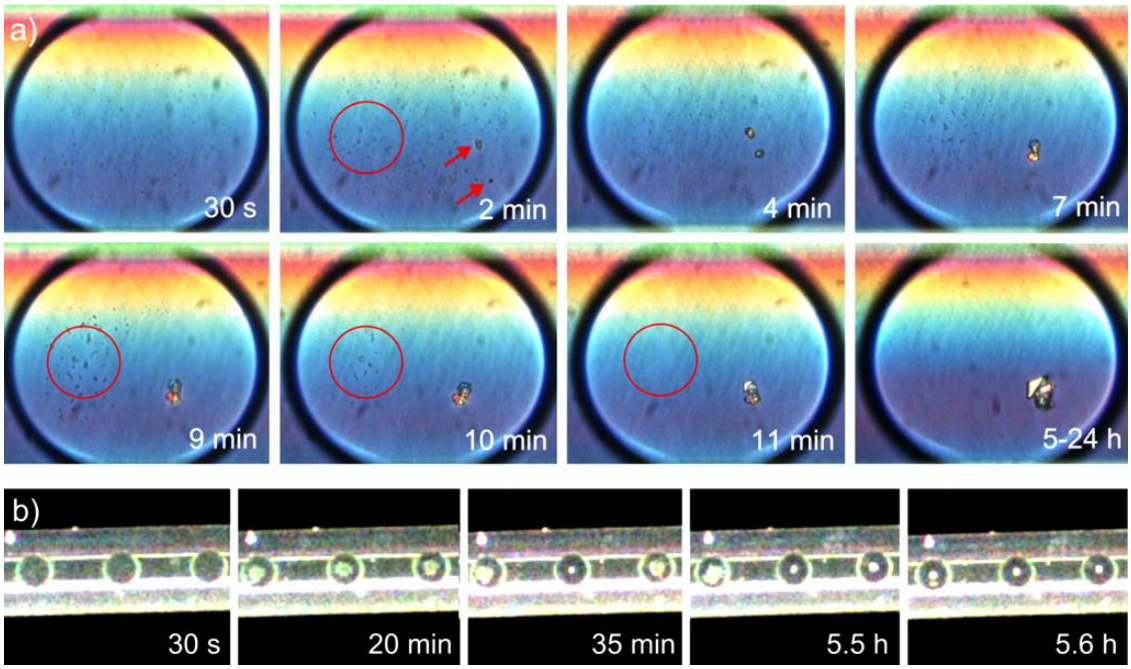

Figure 2. Time sequences showing calcite nucleation in microfluidic droplets: **a)** Precipitation of a 50 mM $CaCO_3$ solution (IAP $5.25x10^{-6}$ $mol^2.L^{-2}$, SI = 3.18 with respect to calcite phase) in a ≈ 3 nanoliter droplet in a teflon capillary internal diameter of 150 µm. and its evolution in time. Red arrows show the appearance of two calcite crystals. Marked with a red circle the presence of particles/aggregates of few micrometers and its dissolution while the calcite crystals grow. b) Precipitation of a $CaCO_3$ solution (IAP $1.95x10^{-6}$ $mol^2.L^{-2}$, SI = 2.74 with respect to calcite phase) in 2 nL droplets and its evolution in time under crossed polarisers.

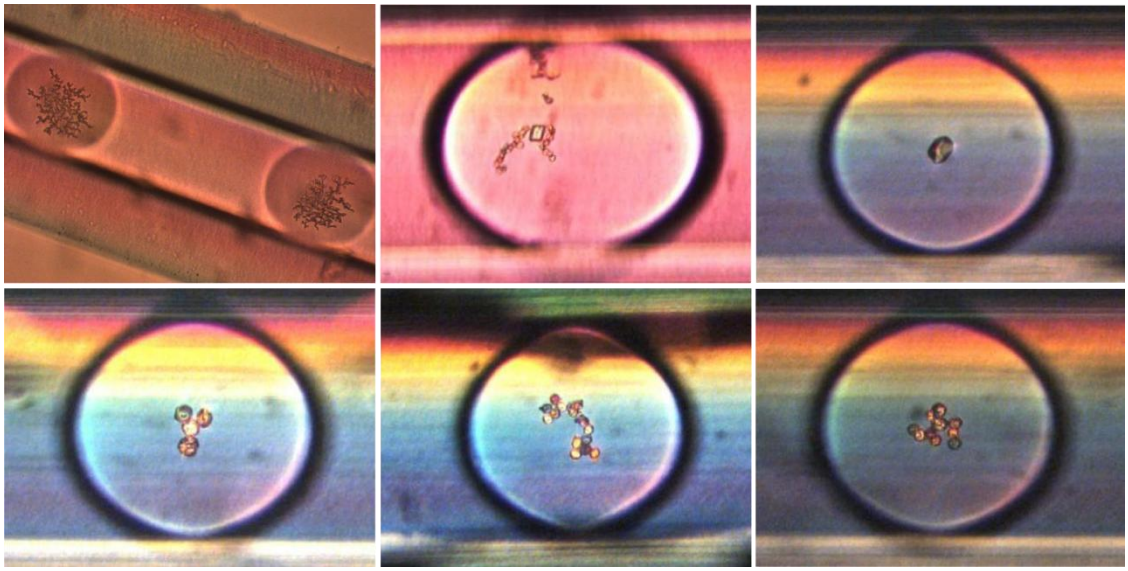

Figure 3. Different precipitate morphologies observed in ≈ 2 nanoliter droplets. Teflon capillary internal diameter: 150 µm. a) and b): 50 mM $CaCO_3$ solution (IAP 5.25 x 10^{-6}, SI = 3.18) after 12 h observation. c) to f) 40 mM $CaCO_3$ solution (IAP 3.80 x 10^{-6}, SI = 2.74), after 12 days.

3.1.2. Identification of the precipitates

SEM micrographs of precipitates withdrawn after the first minutes show hollow hemispheres formed at the solution-oil interface by aggregation of ~200 nm spherulites (figure 4) as well as calcite crystals displaying the typical (104) and (110) faces. EDS analysis of hemispheres confirms they contain Ca and C. Moreover, measured d-spacings and SAED patterns over similar spherulites (figure 5d) identified them as $CaCO_3 \cdot 6H_2O$ (IK). For precipitates obtained in identical nanoliters droplets (IAP 5.25x10^{-6} $mol^2 \cdot L^{-2}$) the collected XRD patterns were analyzed, d-spacings are measured and assigned to different phases. The data are presented in table I. It is noteworthy that in these precipitates there were no SEM and optical microscopy evidences of the presence of vaterite or aragonite [73, 74], so these phases were not considered for the assignment. We clearly identified the reflections 0 0 6 of calcite, 2 1 1 of MHC and -3 1 2 of IK. Other reflections were also found but are shared by more than one calcium carbonate phase (see table 1). Finally, for experiments lasting more than 30 days, XRD patterns of the precipitates revealed the presence of only calcite.

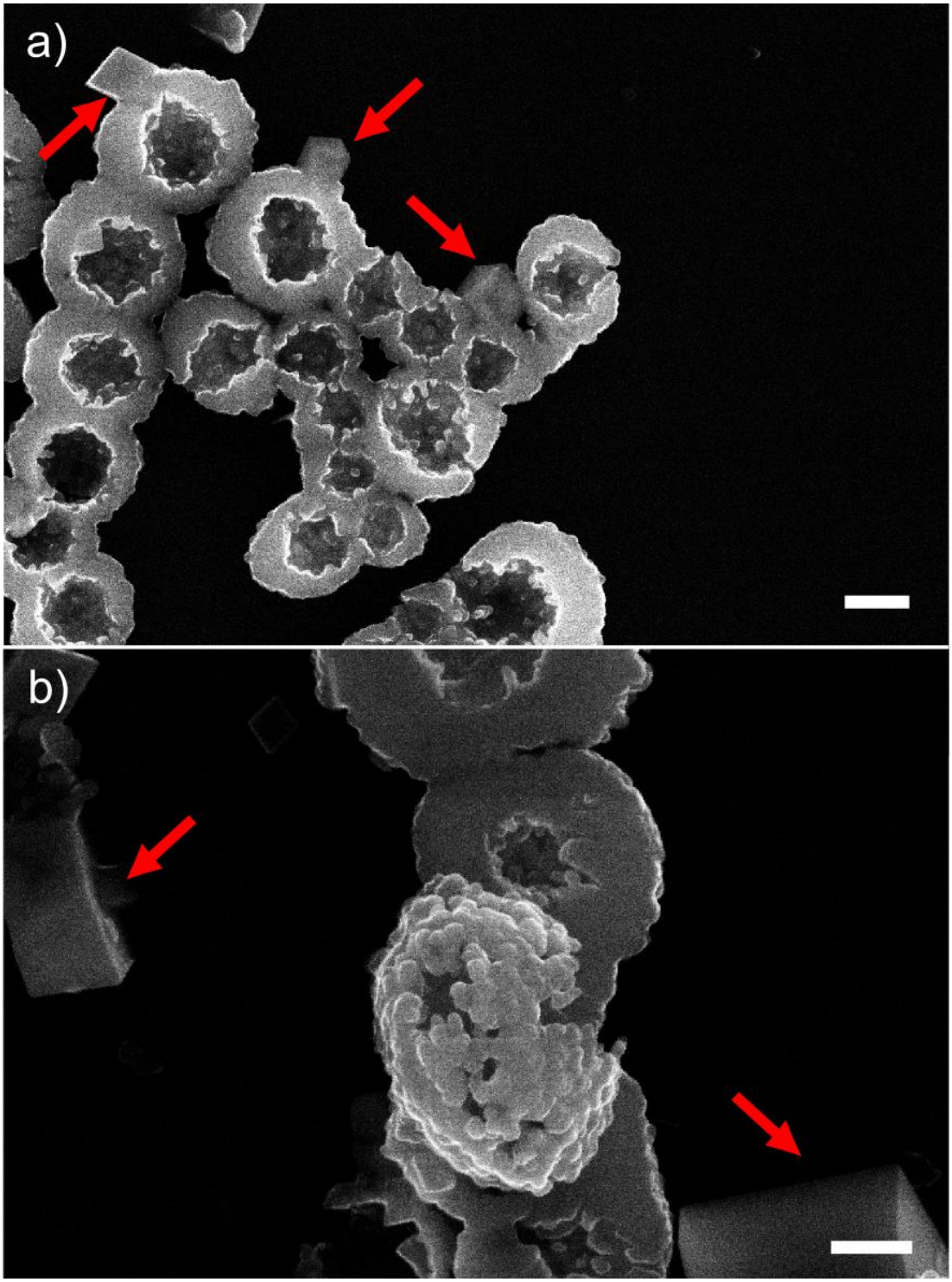

Figure 4. SEM micrographs of precipitates obtained after the first minutes in a 3 nL droplet containing 50 mM $CaCl_2$ and 50 mM Na_2CO_3 (nominal IAP 5.25×10^{-6} $mol^2 \cdot L^{-2}$, SI=3.18). Micrographs show hollow hemispheres (1-3 µm) composed of 200 nm spherulites and rhombohedral calcite (red arrows). Scale bars = 1 µm.

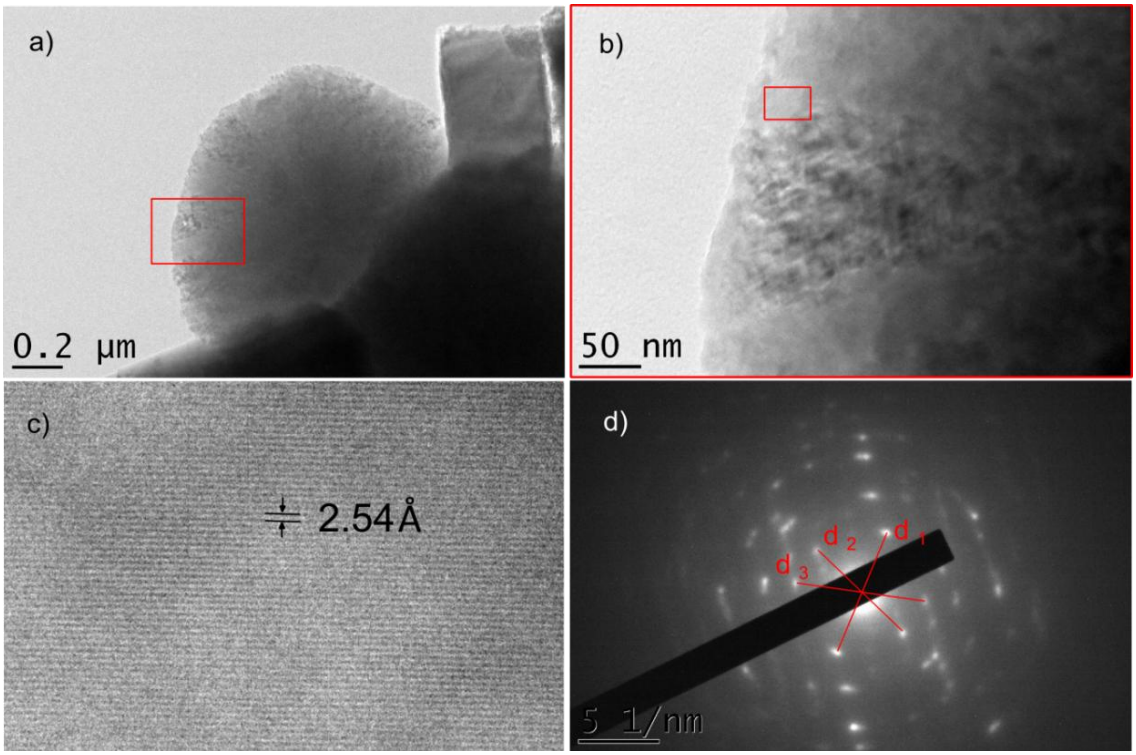

Figure 5. TEM images of a precipitate obtained from a 50 mM $CaCO_3$ solution (IAP 5.25 x 10^{-6} $mol^2.L^{-2}$, SI = 3.18 with respect to calcite phase) in a 2 nL droplet. a), b) and c) Zoom of a spherulitic particle and measured d-spacing (2.54 Å corresponding to (-2 2 3) ikaite crystallographic plane). D) SAED pattern obtained from the particle, and measured d-spacings d1 = 2.498 Å, d2 = 2.691 Å and d3 = 2.465 Å, corresponding to ikaite (0 1 4), (1 3 0) and (3 2 -1) crystallographic planes respectively.

Table 1. Obtained XRD d-spacings, averaged over 10 measurements, and possible assignations to calcium carbonate phases

d(Å)	Calcite[a]	Monohydrocalcite[b]	Ikaite[c]
3.17 ± 0.02		(2 1 1) = 3.15	
3.04 ± 0.02	(1 0 4) =3.035	(3 0 0) = 3.05	
2.845 ± 0.005	(0 0 6) = 2.845		
2.74 ± 0.02			(-3 1 2) = 2.733
2.17 ± 0.02		(4 0 1) = 2.1899	(1 1 4) = 2.178
		(2 2 2) = 2.1665	
1.99 ± 0.02		(4 1 0) = 1.9968	(-3 3 2) = 1.992
			(-4 0 4) = 1.992
			(2 2 3) = 2.004
1.94 ± 0.02	(0 2 4) = 1.927	(3 0 3) = 1.9447	(3 3 0) = 1.9509
		(4 1 1) = 1.9308	(-4 0 4) = 1.9509
			(-1 3 4) = 1.9433
			(-4 2 1) = 1.9345
			(-2 2 5) = 1.9235
1.79 ± 0.02		(1 1 4) = 1,7823	(-4 2 4) = 1.7926

d-spacings assigned according to PDF card files: [a] 050586, [b] 290306, [c] 370416

3.2. Calcium carbonate precipitation in picoliter droplets (microinjector setup)

3.2.1. Optical microscopy monitoring

We found the following results: first, in all droplets, irrespective of the initial nominal IAP, the nucleation of thou-sands of ultrafine particles undergoing brownian motions (a viscous sol) occurred during the first few minutes of the experiment (fig. 6a-d). This precipitate remained stable in many of the droplets until their complete evaporation (~ 2/3 from a total of ~ 120 experiments). Second, in ~1/3 of the droplets precipitates were stable for several minutes/hours until the appearance of few rhombohedral calcite crystals (or vaterite in few droplets at the lowest IAPs). These phases grew by forming a radial area of depletion of the first precipitate (fig.6e-h), thus suggesting a solvent-mediated phase transition, as previously reported [75]. Third, once the second and more stable phase appeared, the sol completely disappeared in a short period, from a few seconds to a few minutes. No direct relationship between time to complete the phase transition and initial nominal IAP was observed but, in general, longer transition periods occur for mixing $CaCl_2$:Na_2CO_3 ratios closer to 1. This is related with the number of crystals per droplet (fig.7c): the lower the crystals number the longer the phase transition. For instance, we observed a lower tendency for the transformation of precipitate at molar ratio 1 (24 of 38 droplets do not evolve after precipitation (fig.7a)) whereas a higher tendency is observed for molar ratio of 0.5 (31 of 43 droplets undergo phase transition (fig.7b)). These observations indicate lower nucleation frequencies of the stable phase for molar ratio 1 than for molar ratio 0.5. The influence of stoichiometry on nucleation was previously observed for calcium phosphate [76].

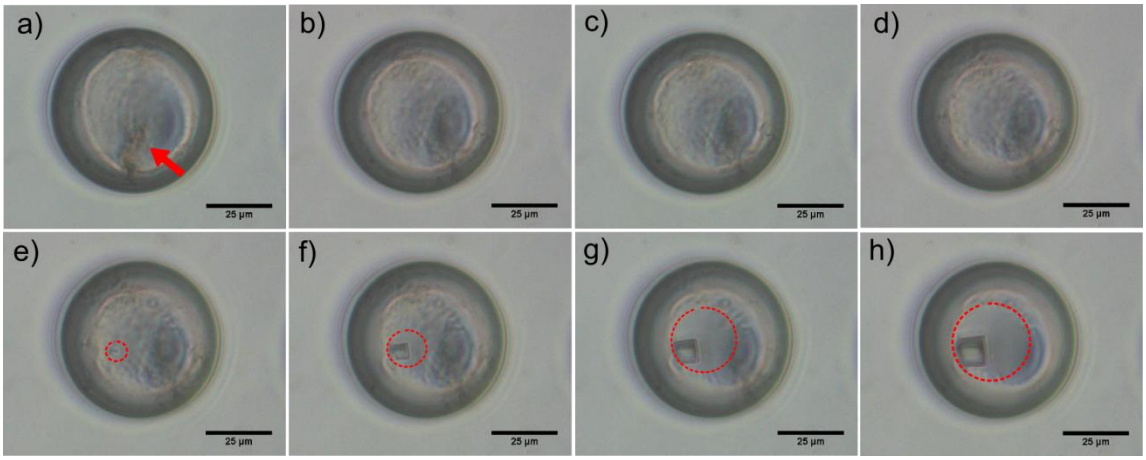

Figure 6. Time sequence of micrographs showing the course of precipitation in a 400 pL droplet containing 100 mM $CaCl_2$ and 100 mM Na_2CO_3 (nominal IAP=3.16x10-7 $mol^2 \cdot L^{-2}$, SI 1.98): a) t = 0 s, a viscous sol is firstly formed (red arrow); b) t = 10 min; c) t = 20 min; d) t = 80 min; e) t = 112 min; a calcite crystal nucleates; f) t = 115 min, the depletion area surrounding the crystal starts to increase; g) t = 118 min, growth of calcite crystal consumes most of the solute becoming from the dissolution of the fine particles composing the sol; h) t = 120 min, the growth of calcite stops few seconds after complete dissolution of the sol particles.

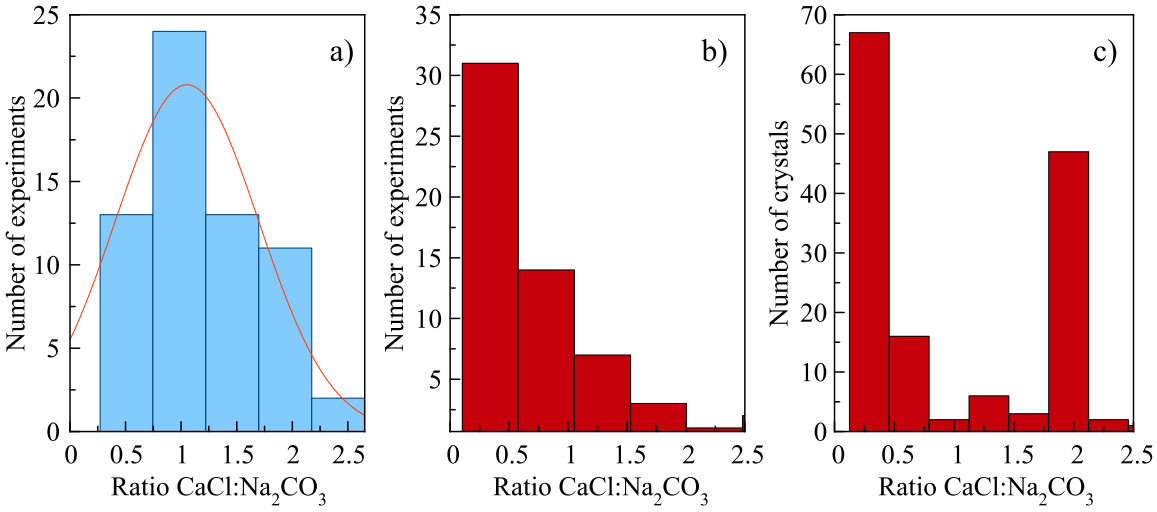

Figure 7. For the same molar ratio, the Y-axis represent: a) number of droplets where the first precipitate remained stable (2/3 of the total) and Gaussian fitting of the distribution centred at a molar ratio of 1.053 ± 0.096; b) number of droplets in which a phase transition is observed (1/3 of the total); c) Average number of crystals precipitated after the phase transition. No significant number of experiments were performed at molar ratios higher than 2.0.

In order to confirm that the stability of the firstly precipitated sol is related to the absence of nucleation of a stable phase (and not to an unlikely inhibition of the precipitate dissolution), calcite single crystals were seeded in droplets with a micropipette where the sol remained stable for several hours. Micrographs of the process are shown in Figure 8. Once the crystal gets in contact with the solution inside the droplet, dissolution of the precipitate and growth of the calcite crystal take place concomitantly generating a depletion area surrounding the crystal (fig. 8c-e). Finally the particles composing the sol completely dissolved (fig. 8f).

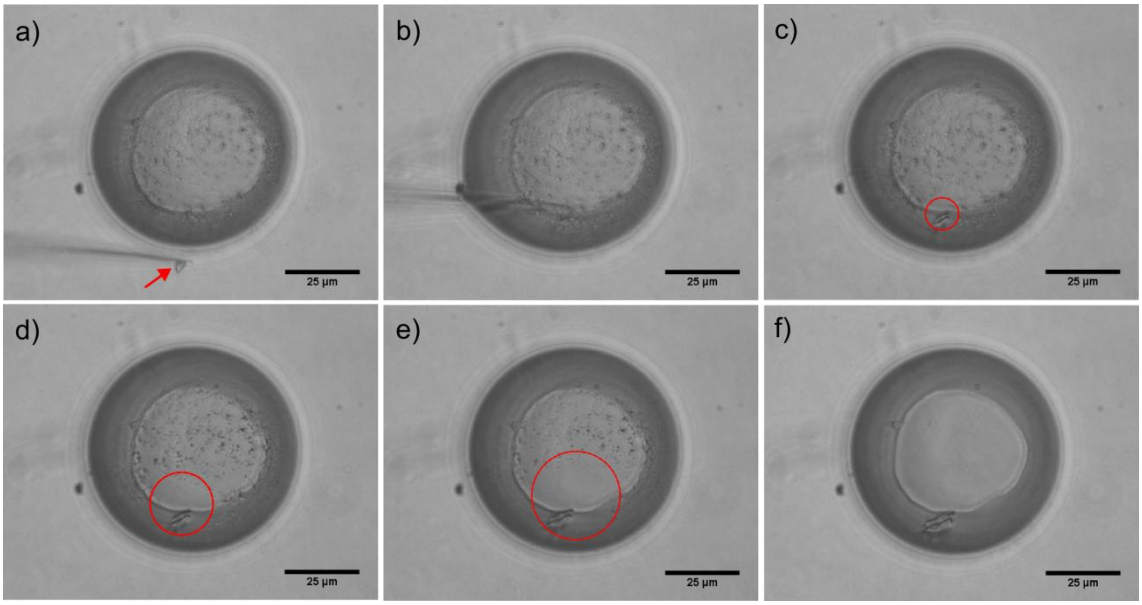

Figure 8. Micrographs represent a time sequence showing the dissolution of the first precipitate and the growth of a calcite seed. A calcite single crystal, marked with a red arrow in image a), was seeded in the droplet with a micropipette, as shown in b). Subsequently, dissolution of the precipitate and growth of the calcite crystal take place concomitantly generating a depletion area surrounding the crystal, as shown in figures c) to f).The droplet contained 20 mM $CaCl_2$ and 20 mM Na_2CO_3 solution. The whole sequence lasted 5 minutes.

3.2.2. Characterization of solution

With a view to understand the mixing process, Mach-Zehnder interferometric experiments were performed in 2 µL droplets. No interferences were observed in experiments performed with $CaCl_2$ and Na_2CO_3 solutions due to their similar density. Nevertheless, a clear mixing front (depicted in Figure 9a -1s by arrows) was drawn in the interface generated between the two reactant solutions due to precipitation of a $CaCO_3$ metastable phase. This front, clearly defined by the opacity of a first precipitate, appeared spontaneously and subsequently disappeared when the metastable precipitate completely transformed into the more stable phase, while the density of this phase increased forming a cloud around the interface (depicted by an oval in Figure 9-a 25 min, and also present in the subsequent frames). As the diffusivity of both reactants in water is similar, a supersaturation gradient is formed symmetrically around the mixing front in both directions generating, as a result, the nucleation of a metastable phase in the supersaturation maxima front, as well as crystals of the stable phase (characterized by optical microscopy as calcite) in the lower supersaturated areas. It is worth noting that nucleation is taking place at the interface of the two solutions, therefore at a higher IAP than the nominal one calculated for an ideal mixing of the two reactants. This initial IAP value is very close to the one given by the sum of reactant concentrations of the two droplets. For a qualitative description, figure 9c depicts simulated concentration profiles of Ca^{2+} and CO_3^- ions during first instants of mixing. It can be appreciated that for a mixing time of only 10 milliseconds concentration in the mixing front (around ±1µm thickness) is 90 % of the initial ion concentration of each droplet.

In order to illustrate the diffusive regime of the mixing, two solutions of different densities were mixed to obtain clear interferometric bands (mixing 1:1 0.5 M sodium citrate:pure H_2O). A higher number of interferometric bands along the mixing interface during first moments (figure 9b) reveals a maximum concentration gradient, and a diffusion of the more concentrated droplet to the less concentrated one.

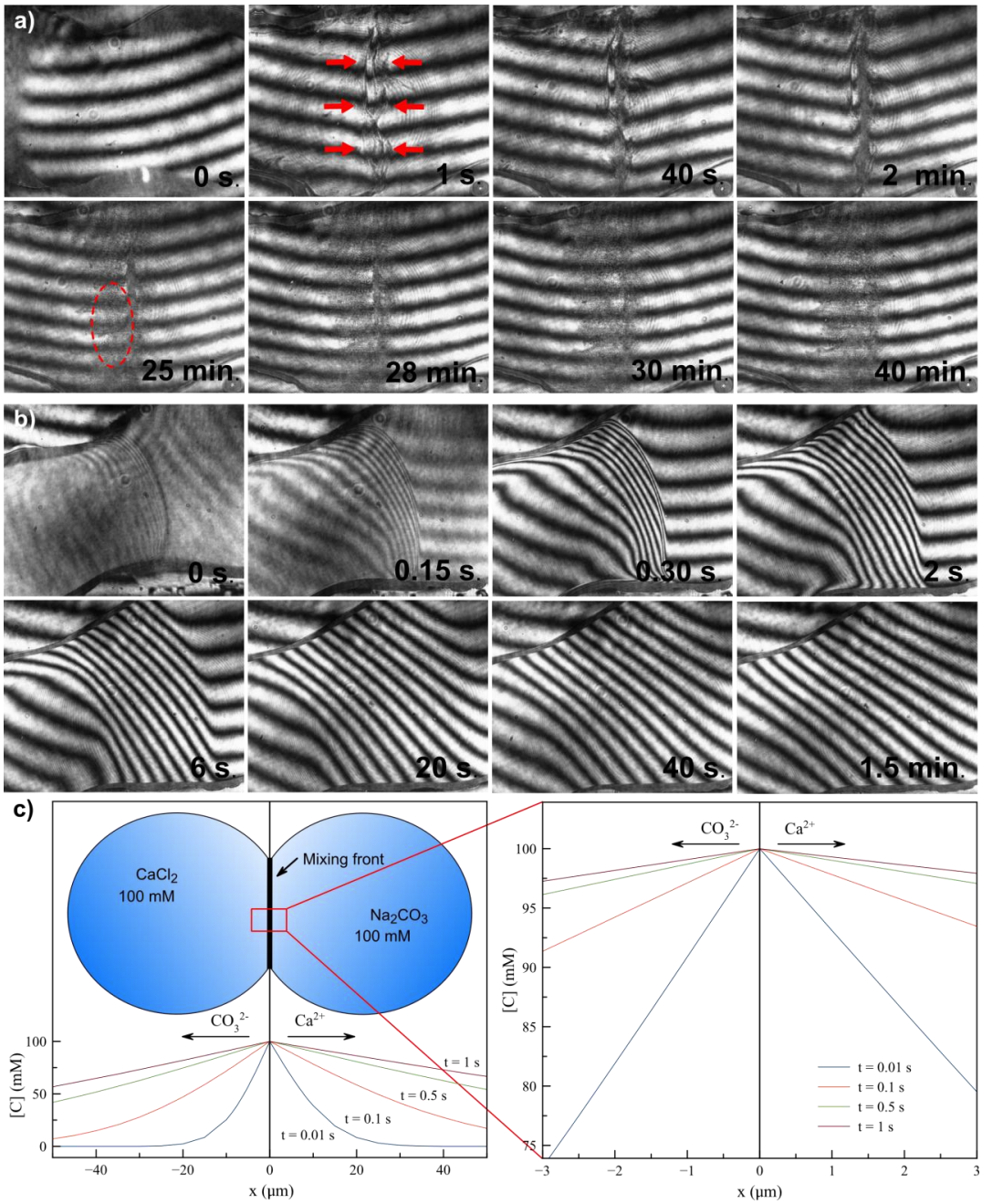

Figure 9. Series of frames selected from interferometric experiments corresponding to a) the mixing a 1 uL droplet 100 mM $CaCl_2$ with 1 uL droplet 100 mM Na_2CO_3. b) the dilution of a 1µL droplet 0.5 M Na_3Cit in a 1 µL water droplet. c) Simulation of concentration profiles for Ca^{2+} and CO_3^{2-}ions corresponding to the mixing of micron-sized droplets with the same concentration of experiment in figure 9a.

3.2.3. Identification of the precipitates

XRD patterns collected from initial precipitates after mixing the reactant solutions in ~200 pL droplets with SI≈1.4, are shown in figure 10. Figure 10d shows in green a pattern collected at room temperature in which 2 0 2/-3 1 1 and -3 1 5 IK (PDF card file 370416) reflections are well observed. Particles from 3 different experiments were independently diffracted showing the same pattern. In order to increase the number of reflections by diffracting a higher number of particles, whole droplets were fished from underneath the oil and instantaneously quenched to 100 K under N_2. This prevented the droplets from slipping down when locating them vertically in the diffractometer, and avoided their fast evaporation. Three other independent experiments were also had samples fished, quenched and placed on the diffractometer, and showed similar patterns among them. Diffractograms are shown and compared in figures 10a (red), 10b (purple) and 10c (blue) in order to provide a higher number of reflections. An important number of the characteristic IK reflections are displayed in the patterns (PDF card file 370416).

HRTEM analysis of first precipitates in pL droplets show the presence of a crystalline $CaCO_3$ phase displaying similar spherulitic morphology and size to those particles found in the experiments performed in nL droplets. These particles collapse under the electron beam when high energy electrons are applied (200 keV) and transform to a polycrystalline particle (figure 11). This transformation has been found to happen with other materials and can be explained by the loss of structural H_2O molecules due to the energy applied [77]. A detail of the transformation of one of these particles close to a calcite crystal, which does not undergo obvious degradation under the electron beam is show in figure 11 a. Insets in figure 11a show the corresponding SAED patterns which are also in agreement with our previous measurements of samples from nL experiments, revealing the presence of IK, as it is shown in figure 11b. It is worth noting that SAED diffractograms are not perfectly oriented, as the intensity of equivalent spots is not the same. Since the lifetime of the crystallite under the beam is very short, this does not allow us to reorient the sample before the crystallite is completely transformed.

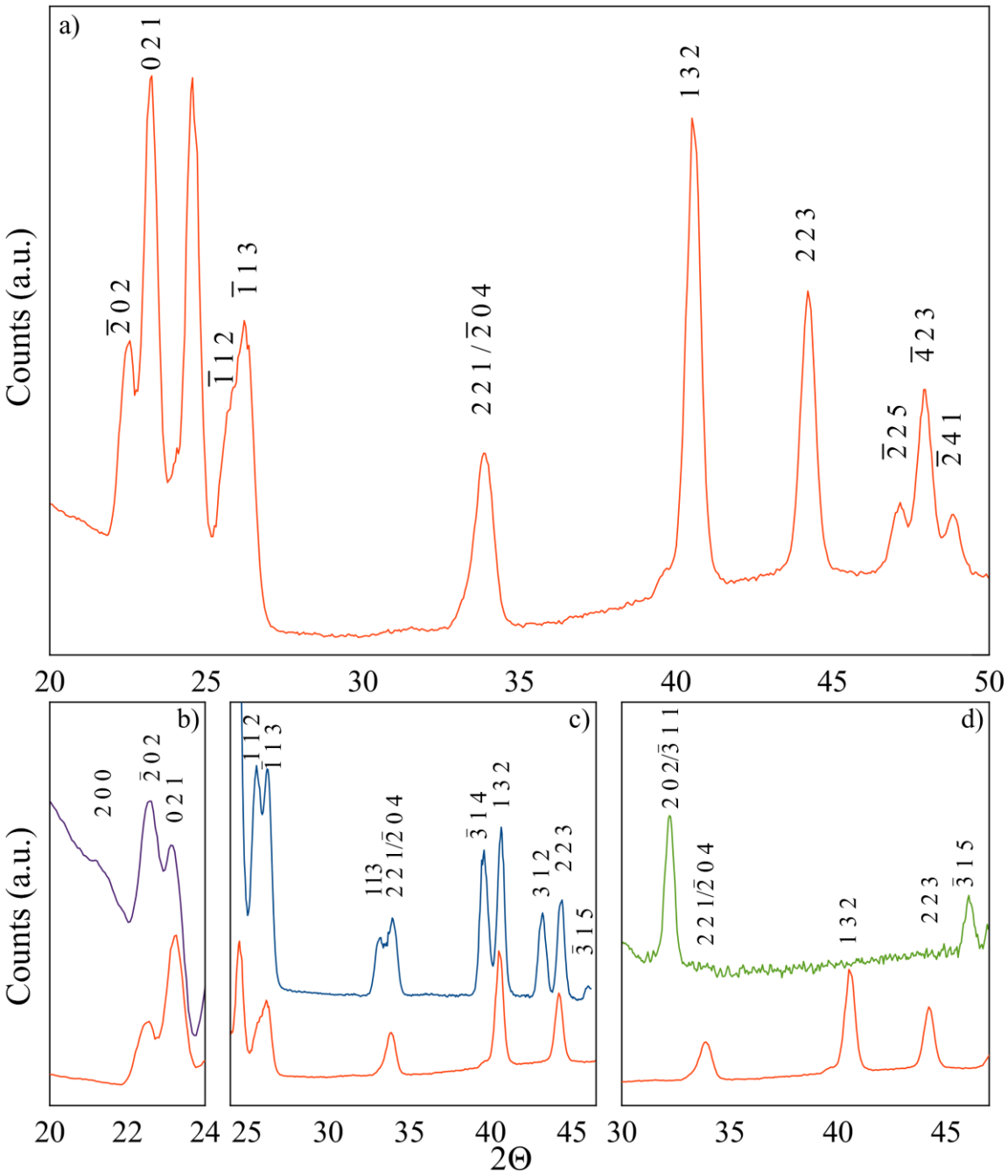

Figure 10. XRD patterns collected from precipitates obtained just after mixing reactants in ~200 pL droplets (SI ≃ 1.4). All the peaks correspond to ikaite reflections (PDF card file 370416). Red spectra in a) to d) shows a representative diffraction pattern. Figures b, c and d are a zoom of spectrum a) compared with other 3 different XRD patterns in which other reflections appear providing complementary information. Differences in intensity, broadening and lack of some peaks are due to the small quantity of diffracted material.

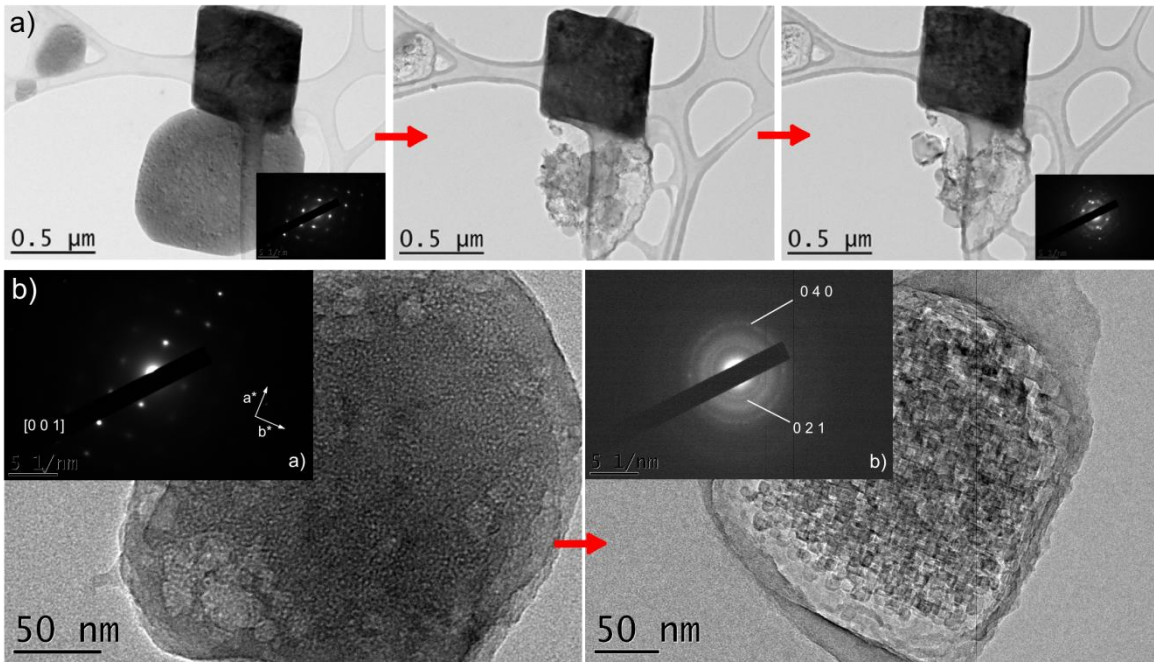

Figure 11. a) Transformation of a crystalline particle under the electron beam and collected SAED patterns at the first instants of the experiments and during its transformation. It is worth noting that SAED patterns are not perfectly oriented, as the intensity of equivalent spots is not the same. Since the lifetime of the crystallite under the beam is very short, this does not allow us to reorient the sample before the crystallite is completely transformed. The pattern in the first instants is collected along [0 0 1] direction, showing the orientation of axis a* and b* in the reciprocal lattice, corresponding to the lattice parameters of IK (a = 8.79 Å, b = 8.31 Å, c = 11.02 Å, α = 90 °, β = 110.5 °, γ = 90 °). SAED pattern in b) is representative of a polycrystalline material, due to the decomposition of the single crystal into smaller crystallites, under the electron beam. Measured d-spacings correspond to 0 4 0 and 0 2 1 ikaite reflections, equal to 2.06 Å and 3.82 Å respectively.

4. Discussion

In this section, the effects of confinement on the nucleation of calcium carbonate in the volume range from nanoliters to picoliters with two different set ups for droplet generation have been studied. The $CaCl_2$:Na_2CO_3 ratio of the mixed droplets is controlled by changing the ratio of the volumes of the two reactant droplets in the pL set up. In each set up the micromixing proces exerts a crucial role in how supersaturation is generated. Indeed, by using the nanoliter microfluidic set up micromixing can be seen to take place at the contact between two solutions flowing in a laminar regime, while in the

picoliter microinjector set up micromixing takes place by diffusion of the reagents through the mixing plane. In both cases, at the contact plane the local IAP is higher than the nominal one, and as a consequence the K_s of the metastable phases is overtaken (supersaturation is generated), leading to its precipitation.

The characterization by SAED and XRD confirm that the precipitates formed consist of crystalline hydrated forms of $CaCO_3$ such as IK and in few cases MHC. Moreover, no evidence of the initial precipitation of ACC has been found. The hydrated phase remains stable for different periods of time: in most of the picoliter droplets it remains stable until complete droplet evaporation. However for some droplets the stabilization time depends on the initial $CaCl_2$:Na_2CO_3 ratio, becoming maximal as this ratio approaches 1. Afterwards, calcite (sometimes vaterite) nucleates and grows at the expenses of the hydrated phase. This solution-mediated phase transformation (SMPT) leads to 1 or 2 calcite crystals at molar ratio 1.

The nucleation and stabilization of the first metastable phase seems to be promoted by the combined effect of three parameters which has been previously reported and studied. These are (high) supersaturation [42, 44, 45, 78], stoichiometry [79-84], and (reduction of) volume [11, 85]. These three aspects are considered and discussed below.

4.1. Effect of mixing of reactants on nucleation of metastable phases

XRD and SAED confirm the SMPT process (figure 6). Nucleation of the metastable phase occurs followed by nucleation of the stable phase and its growth at the expense of the dissolution of the first precipitate. Thus, an Ostwald ripening mechanism can be ruled out: the dissolution process is too fast for Ostwald ripening - and the experiment presented in figure 8 confirms that metastability is broken by seeding with a more stable phase. The metastable phase has been identified as a hydrated phase, IK and in few cases MHC. Thus, the solution has to be supersaturated with respect to at least MHC (IAP $>$ $K_{s(MHC)}$). It is noteworthy that when IAP $<$ $K_{s(MHC)}$, the solution remains

metastable and the precipitation does not occur instantaneously [55]. However, as soon as the IAP reaches the $K_{s(MHC)}$ nucleation occurs spontaneously. Nonetheless, in most of the experiments performed, spontaneous nucleation has been observed, despite the initial nominal IAP $< K_{s(MHC)}$. IAP is calculated for an ideal homogeneous reactant solution, that is to say mixing is considered instantaneous. However, as it has been demonstrated, the mixture of the reactant solutions is not instantaneous, and therefore, the chemical conditions in a microliter-sized droplet cannot be considered homogeneous [86]. For the microfluidic experiments in Teflon capillaries the mixing occurs through a micron sized channel in which laminar flow generates a diffusive interface between reactant solutions, in absence of convective forces [40, 87]. On the other hand, in microinjection experiments, mixing takes place when two micron sized droplets containing the reagents come into contact, generating an instantaneous nucleation front, corresponding to the first contact interface between both droplets, and later homogenizing by diffusion, as confirmed by interferometric experiments (fig. 9). The formation of local supersaturation maxima in the mixing front of the solutions explains why nucleation of an hydrated phase occurred in undersaturated solutions: the global IAP $< K_{s(MHC)}$ but the local IAP $> K_{s(MHC)}$. For the same reasons, we found crystals with rounded or lobulated morphologies, corresponding to the vaterite phase, for some droplets where the nominal IAP $< K_s$ for vaterite (1.336×10^{-8}). This occurred in 11 out of 18 experiments after the dissolution of the firstly precipitated metastable phase. To further illustrate these findings, figure 12 shows the initial nominal IAP values as a function of the mixing $CaCl_2$:Na_2CO_3 ratio (fig 12a) for all droplets generated by microinjection in the picoliter range (from 800 to 30 pL) and the initial IAP calculated in the mixing front at t = 0 for the different reactant concentrations. This IAP overcomes $K_{s(MHC)}$ for most of the microinjection experiments.

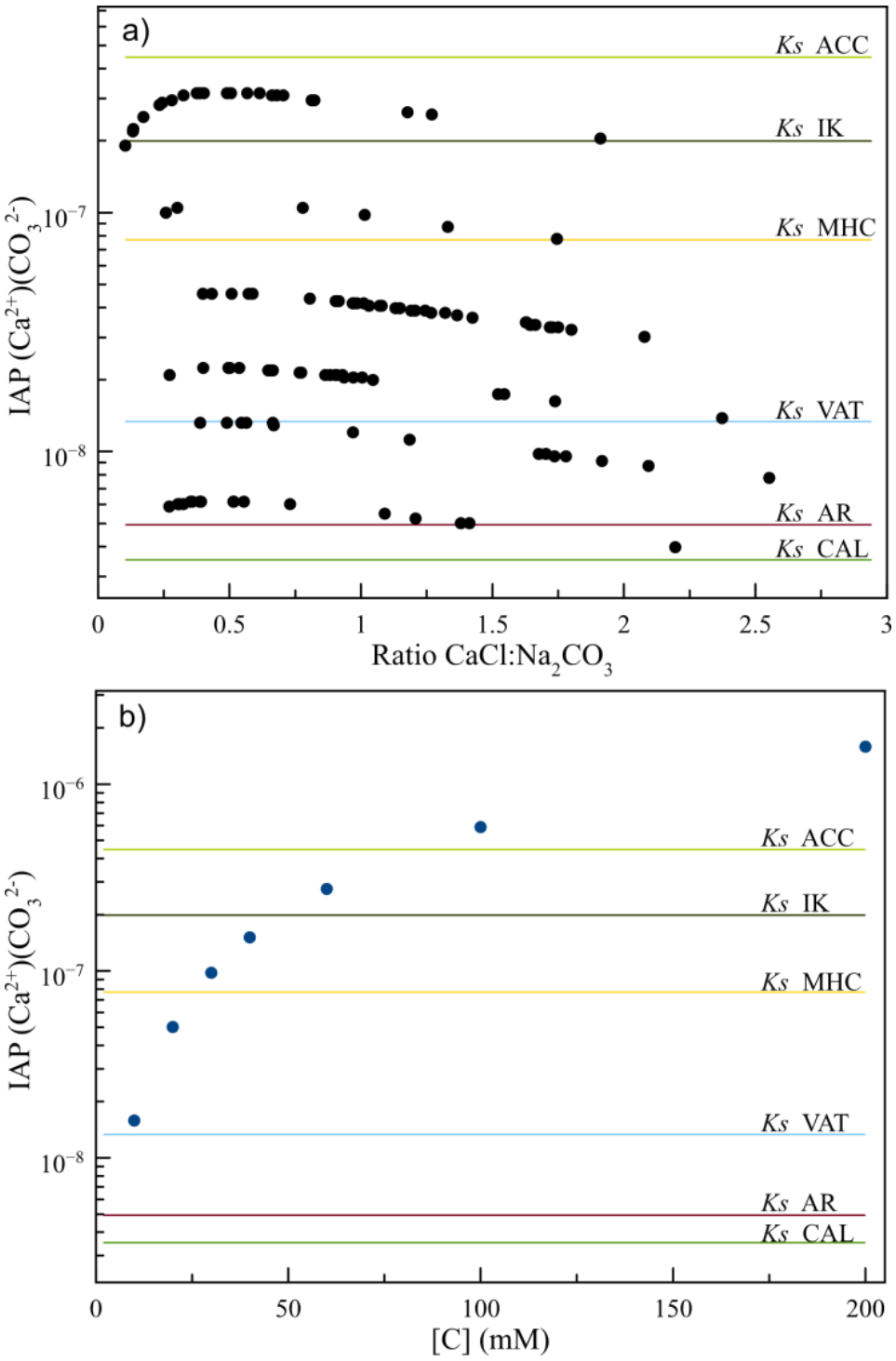

Figure 12. a) Plot of the estimated nominal IAP vs molar ratio of reagent solutions for the whole experimental dataset used in microinjection experiments. b) Plot of the IAP in the mixing front of solution (calculated at mixing time t=0) vs initial reagent concentration. IAP values estimated by PHREEQC [66]. Solubility product constants (K_s) for all calcium carbonate phases were calculated at 20 ˚C using equations reported by Elfil *et al.* [55]

4.2. Ikaite as a transient precursor phase

The phase diagram of $CaCO_3$ is rich: ACC, IK, MHC, vaterite, aragonite and calcite (from the least stable phase to the most stable one). The solid characterization has provided evidence for 3 phases IK or MHC and in some experiments calcite at the end (fig.6). If the first phase to nucleate is metastable, in agreement with the Ostwald's step rule, the final concentration corresponds to the solubility of this phase. But the solution is still supersaturated for more stable phases to nucleate and for SMPT to proceed (growth of the stable phase at the expense of the metastable phase). Hereafter we discuss the possible nucleation of metastable phases. First, if ACC has nucleated, and as no traces of ACC were detected in the first instants, ACC transformation to a more stable (but yet metastable) phase would happen fast. Second, the second metastable $CaCO_3$ phase is IK, known to nucleate at low temperatures and high pressures. It generally transforms to calcite while losing its water molecules, but it has also been reported to transform to MHC during its dehydration [88]. Third, MHC is the next metastable hydrated $CaCO_3$ phase and its stability has long been debated [58]. Laboratory studies indicate that MHC is formed from ACC and transforms to aragonite or calcite in solution within several days [58-60]. However, observations in nature demonstrate that MHC has been preserved in ancient sediments formed more than a thousand years ago [61, 62]. Water temperature does not seem to be an important factor for MHC formation, and its solubility is higher than those of calcite, aragonite and vaterite, but lower than those of IK and ACC at ambient temperature. MHC phase transition has been reported to be solvent mediated, where the nucleation and growth of the stable crystalline phase are the rate-limiting steps of the transformation [89].

We rule out ACC nucleation (at least for the moment), as no traces of ACC were detected in the first instants. Thus, and due to the evidences for its presence in our experiments, IK may be proposed to be the first metastable phase to nucleate. Presence of MHC would be explained both by IK transformation or by MHC direct nucleation in the case of experiments at lower initial supersaturations.

A second point to discuss is the SMPT. This process requires the nucleation of a more stable phase than the hydrated phases. It can be vaterite, aragonite or calcite. When SMPT occurred it is always calcite (and in some cases vaterite) that is finally obtained. We know from literature that it takes several hours for the transformation from vaterite to calcite in solution [90] and several months for that of aragonite to calcite [91] to be completed at room temperature. The possible effect of Na^+ and Cl^- ions, present in the solutions of our experiments, on this transformation has also been studied and discussed [92]. It was shown that the halide anions and most of alkali ions (including Na^+) do not affect the transformation rate. Hence, the hypothesis of a first transition from a hydrated form to vaterite or aragonite, and later a second transformation to calcite is to be ruled out. Thus the transformation should take place from a first instantaneously precipitated hydrated calcium carbonate phase, IK or MHC to calcite. IK is not as yet known to be formed biologically [65], however, the present results of IK nucleation as a stable transient precursor in confinement indicate that this possibility might not be so easily dismissed.

4.3. Effect of volume in the nucleation and stabilization of precipitates

The fact that experiments performed in nanoliter volumes and at 1:1 molar ratio mostly showed a phase transition whilst the first precipitate has been found to remain stable for longer periods at picoliter scale, on equivalent injection experiments, indicates that volume reduction up to picoliter droplets exerts an effect of stabilization in the first nucleating phase. This is to say confinement stabilizes supersaturated solutions [11]. This effect has previously been observed for other metastable $CaCO_3$ phases: Indeed, it was observed for ACC to be stabilized in confinement at micrometer-scale separations [85], and picoliter droplets in our experiments are exerting the same confinement effect [31]. It is known that higher supersaturations increase the probability of nucleating a metastable phase [78] and that confinement can stabilize a metastable phase [44]. Because the nucleated crystal(s) of the metastable phase decrease the supersaturation rapidly, the

rapidly, the probability for a more stable nucleus to appear is reduced and thus the SMPT process is postponed [93]. According to the classical theory of nucleation (CNT), nucleation frequency is directly related to the volume of solution. By reducing the volume, the probability of a nucleation event to occur is decreased. This phenomenon has been observed for a long time in microfluidic experiments and for many different substances [94]. A reduction in the reactive species to support the growing precipitates, together with the reduced probability for a stable cluster to nucleate and grow, explain the observations of mononucleation of a single calcite crystal, whose final size will be determined by the total amount of calcium and carbonate ions in the droplet.

4.4. Effect of stoichiometry in the stabilization of precipitates

After analyzing the stability of the first precipitate for different molar ratios, a very clear tendency was observed for persistence of the metastable phase with time and the absence of any nucleation of the stable calcite phase for the experiments (given molar ratio of 1). In addition the mononucleation of calcite is observed for those experiments that undergo the SMPT process where the molar ratios were also 1. As is described in Figure 7c, unstable precipitates at other different ratios displayed many calcite crystals after phase transition. Many studies confirm that the solution stoichiometry of the reactant ions can affect the rate of calcite precipitation, although how it exactly affects this precipitation varies from publication to publication. An increase of the precipitation rate while decreasing the calcium to total carbonate Ca/C_T ratio was reported by Lin and Singer [79], whereas rate maxima at molar ratio 1 [80-82] and other particular stoichiometries [83, 84] have been also found. In our case, i.e. the confined picoliter droplets and a stoichiometric molar ratio, a maximum nucleation rate of the metastable precipitate is taking place and thus this leads to the fastest consumption of reactant ions and therefore to a minimum remaining IAP, but yet higher than K_s of calcite. At these conditions and according to CNT few calcite nuclei (mononucleation) will form (indicating a low nucleation frequency) and the metastable phase will remain stable for

longer periods. This explains the maximum number of stabilized experiments for the molar ratio of 1, as well as the symmetric behavior observed around this ratio. Indeed, the more the molar ratio differs from one, the slower the nucleation rate (despite of observing instantaneous precipitation) and the higher is the remaining supersaturation in the droplet and therefore the nucleation frequency for calcite, thus providing an environment that favors the nucleation of a higher number calcite crystals, as seen in figure 7c.

5. Conclusions

Calcium Carbonate precipitation at medium to high values of the nominal IAP has been studied in nanoliter and picoliter droplets at constant ionic strength and different molar ratios. Instantaneous precipitation of crystalline calcium carbonate hydrated phases has been confirmed by optical microscopy through birefringence under crossed polarizers, XRD and SAED. No evidence of ACC has been found. Ikaite was found to be a transient metastable phase and its stability was found to increase in time when reducing the volume of the droplets from nano- to picoliter range (in this case until complete solvent evaporation), and for a stoichiometric molar ratio. In these conditions, when a phase transformation was observed, nucleation of few calcite crystals (mononucleation) occurred. Precipitation of the hydrated metastable phase was explained by a local supersaturation higher than the nominal one, generated by micromixing at the contact plane between both mixing solutions. Due to the location in space of the crystallization events in isolated volumes, confinement has been proved to be a good approach for the study of crystalline precipitation. Moreover, the mixing of reagent solutions by the microinjection technique has been demonstrated to provide a useful method for investigating the effect of confinement on precipitation. It has been shown that confinement exerts a clear effect in the temporary stabilization of IK in nano- and picovolumes at room temperature, as the nucleation and stabilization of this metastable phase has only been previously achieved by using low temperatures (near

0 °C) or high pressures. These new *in vitro* findings are particularly relevant for biomineralization processes involving calcium carbonate that occur in the confined volume of intracellular vesicles, at relatively high supersaturations. They suggest that IK could be proposed as an alternative *in vivo* transient precursor for the formation of calcite biominerals.

The results of this chapter have been recently submitted to:

- I. Rodríguez-Ruiz, Z. Hammadi, R. Grossier, J. Gómez-Morales, J. M. García-Ruiz, S. Veesler. Monitoring picoliter sessile microdroplet dynamics shows that size doesn't matter. Accepted in *Langmuir.*

- I. Rodríguez-Ruiz, St. Veesler, J. Gómez-Morales, J. M. Delgado-López, O. Grauby, Z. Hammadi, N. Candoni, J. M. García-Ruiz. Transient calcium carbonate hexahydrate (ikaite) temporarily stabilized in confined nano- and picovolumes. Submitted to *Journal of the American Chemical Society.*

References

1. Parisse F, Allain C. Drying of Colloidal Suspension Droplets: Experimental Study and Profile Renormalization. Langmuir. 1997;13(14):3598-602.

2. Brutin D, Sobac B, Loquet B, Sampol J. Pattern formation in drying drops of blood. Journal of Fluid Mechanics. 2011;667:85-95.

3. Deegan R, D., Bakajin O, Dupont T, F., Huber G, Nagel SR, Witten T, A. Capillary flow as the cause of ring stains from dried liquid drops. Nature. 1997;389:827-9.

4. Yu Y, Zhu H, Frantz JM, Reding ME, Chan KC, Ozkan HE. Evaporation and coverage area of pesticide droplets on hairy and waxy leaves. Biosystems Engineering. 2009;104(3):324-34.

5. Houghton HG. A Study of the Evaporation of Small Water Drops. Physics. 1933;4(12):419-24.

6. Rodolfa KT, Bruckbauer A, Zhou D, Schevchuk AI, Korchev YE, Klenerman D. Nanoscale Pipetting for Controlled Chemistry in Small Arrayed Water Droplets Using a Double-Barrel Pipet. Nano Letters. 2006;6(2):252-7.

7. De Angelis F, GentileF, MecariniF, DasG, MorettiM, CandeloroP, et al. Breaking the diffusion limit with super-hydrophobic delivery of molecules to plasmonic nanofocusing SERS structures. Nat Photon. 2011;5(11):682-7.

8. Hon KKB, Li L, Hutchings IM. Direct writing technology--Advances and developments. CIRP Annals - Manufacturing Technology. 2008;57(2):601-20.

9. Ducruix A, R. Giégé, editors. Crystallization of Nucleic Acids and Proteins

A Practical Approach second ed. Oxford: Oxford University Press; 1999.

10. Lee AY, Lee IS, Dette SS, Boerner J, Myerson AS. Crystallization on Confined Engineered Surfaces: A Method to Control Crystal Size and Generate Different Polymorphs. J Am Chem Soc. 2005;127(43):14982-3.

11. Grossier R, Hammadi Z, Morin R, Veesler S. Predictive Nucleation of Crystals in Small Volumes and Its Consequences. Phys Rev Lett. 2011;107(2):025504.

12. Winkler EM, Singer PC. Crystallization Pressure of Salts in Stone and Concrete. Geological Society of America Bulletin. 1972;83(11):3509-14.

13. Rodriguez-Navarro C, Doehne E. Salt weathering: Influence of evaporation rate, supersaturation and crystallization pattern. Earth Surface Processes and Landforms. 1999;24(2-3):191-209.

14. Rodriguez-Navarro C, Linares-Fernandez L, Doehne E, Sebastian E. Effects of ferrocyanide ions on NaCl crystallization in porous stone. J Cryst Growth. 2002;243(3):503-16.

15. Benavente D, García del Cura MA, Fort R, Ordóñez S. Thermodynamic modelling of changes induced by salt pressure crystallisation in porous media of stone. J Cryst Growth. 1999;204(1–2):168-78.

16. Correns CW. Growth and dissolution of crystals under linear pressure. Discussions of the Faraday Society. 1949;5:267-71.

17. López-Acevedo V, Viedma C, Gonzalez V, La Iglesia A. Salt crystallization in porous construction materials. II. Mass transport and crystallization processes. J Cryst Growth. 1997;182(1–2):103-10.

18. Winkler EM, Singer PC. Crystallization pressure of salts in stone and concrete. Bulletin of the Geological Society of America. 1972;83(11):3509-14.

19. Zehnder K, Arnold A. Crystal growth in salt efflorescence. J Cryst Growth. 1989;97(2):513-21.

20. Grossier R., Hammadi Z., Morin R., Magnaldo A., veesler S. Generating nanoliter to femtoliter microdroplets with ease. Applied Physics Letters. 2011;98(9):091916-3.

21. Grossier R., Magnaldo A., veesler S. Ultra-fast crystallization due to Confinement. J Crystal Growth. 2010;312:487-9.

22. Velazquez J. A., Hileman Jr O.E. Studies on nucleation from solution of some soluble inorganic salts. Can J Chem. 1970;48:2896-9.

23. Taylor M, Urquhart AJ, Zelzer M, Davies MC, Alexander MR. Picoliter Water Contact Angle Measurement on Polymers. Langmuir. 2007;23(13):6875-8.

24. Furuta T, Sakai M, Isobe T, Nakajima A. Evaporation Behavior of Microliter- and Sub-nanoliter-Scale Water Droplets on Two Different Fluoroalkylsilane Coatings. Langmuir. 2009;25(20):11998-2001.

25. Grossier R, Hammadi Z, Morin R, Magnaldo A, Veesler S. Generating nanoliter to femtoliter microdroplets with ease. Appl Phys Lett. 2011;98(9):091916-3.

26. Grossier R., Veesler S. Reaching one single and stable critical cluster through finite sized systems. Cryst Growth Des. 2009;9(4):1917-22.

27. Picknett RG, Bexon R. The evaporation of sessile or pendant drops in still air. Journal of Colloid and Interface Science. 1977;61(2):336-50.

28. Bourges-Monnier C, Shanahan MER. Influence of Evaporation on Contact Angle. Langmuir. 1995;11(7):2820-9.

29. Duncan PB, Needham D. Microdroplet Dissolution into a Second-Phase Solvent Using a Micropipet Technique: Test of the Epstein−Plesset Model for an Aniline−Water System. Langmuir. 2006;22(9):4190-7.

30. Talreja S, Kenis PJA, Zukoski CF. A Kinetic Model To Simulate Protein Crystal Growth in an Evaporation-Based Crystallization Platform. Langmuir. 2007;23(8):4516-22.

31. Grossier R, Veesler Sp. Reaching One Single and Stable Critical Cluster through Finite-Sized Systems. Cryst Growth Des. 2009;9(4):1917-22.

32. Meldrum FC. Calcium carbonate in biomineralisation and biomimetic chemistry. Int Mater Rev. 2003;48(3):187-224.

33. Hostomský J, Jones AG. Crystallization and agglomeration kinetics of calcium carbonate and barium sulphate in the MSMPR crystallizer. Industrial Crystallization '93. 1993:2-055.

34. García-Carmona J, Gómez-Morales J, Rodríguez-Clemente R. J Cryst Growth. 2003;249:561.

35. Plummer LN, Wigley TML, Parkhurst DL. The kinetics of calcite dissolution in CO 2 -water systems at 5 degrees to 60 degrees C and 0.0 to 1.0 atm CO 2. American Journal of Science. 1978;278(2):179-216.

36. Jackson CL, McKenna GB. The melting behavior of organic materials confined in porous solids. J Chem Phys. 1990;93(12):9002-11.

37. Ha J-M, Wolf JH, Hillmyer MA, Ward MD. Polymorph Selectivity under Nanoscopic Confinement. JACS. 2004;126(11):3382-3.

38. Haller W. Chromatography on glass of controlled pore size. Nature. 1965;206(4985):693-6.

39. Liu J, Nicholson CE, Cooper SJ. Direct Measurement of Critical Nucleus Size in Confined Volumes. Langmuir. 2007;23(13):7286-92.

40. Bringer MR, Gerdts CJ, Song H, Tice JD, Ismagilov RF. Microfluidic systems for chemical kinetics that rely on chaotic mixing in droplets. Philos Trans R Soc London, Ser A. 2004;362(1818):1087-104.

41. Ildefonso M, Candoni N, Veesler S. A Cheap, Easy Microfluidic Crystallization Device Ensuring Universal Solvent Compatibility. Org Process Res Dev. 2012;16(4):556-60.

42. Lee I, Lee A, Myerson A. Concomitant Polymorphism in Confined Environment. Pharm Res. 2008;25(4):960-8.

43. Gómez-Morales J, Torrent-Burgués J, Rodríguez-Clemente R. Nucleation of calcium carbonate at different initial pH conditions. J Cryst Growth. 1996;169(2):331-8.

44. Lee AY, Lee IS, Myerson AS. Factors Affecting the Polymorphic Outcome of Glycine Crystals Constrained on Patterned Substrates. Chem Eng Technol. 2006;29(2):281-5.

45. Lee IS, Kim KT, Lee AY, Myerson AS. Concomitant Crystallization of Glycine on Patterned Substrates: The Effect of pH on the Polymorphic Outcome. Cryst Growth Des. 2008;8(1):108-13.

46. Stephens CJ, Kim Y-Y, Evans SD, Meldrum FC, Christenson HK. Early Stages of Crystallization of Calcium Carbonate Revealed in Picoliter Droplets. JACS. 2011;133(14):5210-3.

47. Yashina A, Meldrum F, Demello A. Calcium carbonate polymorph control using droplet-based microfluidics. Biomicrofluidics. 2012;6(2):22001-2200110.

48. Rodriguez-Navarro C, Rodriguez-Gallego M, Ben Chekroun K, Gonzalez-Munoz MT. Conservation of ornamental stone by Myxococcus xanthus-induced carbonate biomineralization. Appl Environ Microbiol. 2003;69(4):2182-93.

49. Rodriguez-Navarro C, Jimenez-Lopez C, Rodriguez-Navarro A, Gonzalez-Muñoz MT, Rodriguez-Gallego M. Bacterially mediated mineralization of vaterite. Geochim Cosmochim Acta. 2007;71(5):1197-213.

50. Chekroun KB, Rodríguez-Navarro C, González-Muñoz MT, Arias JM, Cultrone G, Rodríguez-Gallego M. Precipitation and Growth Morphology of Calcium Carbonate Induced by Myxococcus Xanthus: Implications for Recognition of Bacterial Carbonates. JSR. 2004;74(6):868-76.

51. Ogino T, Suzuki T, Sawada K. The formation and transformation mechanism of calcium carbonate in water. Geochim Cosmochim Acta. 1987;51(10):2757-67.

52. Bolze J, Peng B, Dingenouts N, Panine P, Narayanan T, Ballauff M. Formation and Growth of Amorphous Colloidal CaCO3 Precursor Particles as Detected by Time-Resolved SAXS. Langmuir. 2002;18(22):8364-9.

53. Navrotsky A. Energetic clues to pathways to biomineralization: Precursors, clusters, and nanoparticles. PNAS. 2004;101(33):12096-101.

54. Gebauer D, Völkel A, Cölfen H. Stable Prenucleation Calcium Carbonate Clusters. Science. 2008;322(5909):1819-22.

55. Elfil H, Roques H. Role of hydrate phases of calcium carbonate on the scaling phenomenon. Desalination. 2001;137(1–3):177-86.

56. Marland G. The stability of $CaCO3 \cdot 6H2O$ (ikaite). Geochim Cosmochim Acta. 1975;39(1):83-91.

57. Bischoff JL. The solubility and stabilization of ikaite (CaCO3.6H2O) from 0° to 25°C: environmental and paleoclimatic implications for thinolite tufa. J Geol. 1993;101(1):21-33.

58. Taylor GF. The occurrence of monohydrocalcite in two small lakes in the south-east of South Australia. . Am Mineral. 1975;60(7/8):8.

59. Brooks R, Clark LM, Thurston EF. Calcium Carbonate and Its Hydrates. Philos Trans R Soc London, Ser A. 1950;243(861):145-67.

60. Munemoto T, Fukushi K. Transformation kinetics of monohydrocalcite to aragonite in aqueous solutions. J Mineral Petrol Sci. 2008;103(5):345-9.

61. A.A. Abzaeva, E.V. Bezrukova, V.A. Bychinsky, S.A. Fedenya, K. Fukishi, V.F. Gelety, et al. Sedimentary record from Lake Hovsgol, NW Mongolia: Results from the HDP-04 and HDP-06 drill cores. Quat Int. 2009;205(1–2):21-37.

62. Stoffers P, Fischbeck R. Monohydrocalcite in the sediments of Lake Kivu (East Africa). Sedimentology. 1974;21(1):163-70.

63. Raz S, Testeniere O, Hecker A, Weiner S, Luquet G. Stable amorphous calcium carbonate is the main component of the calcium storage structures of the crustacean Orchestia cavimana. The Biological Bulletin. 2002;203(3):269-74.

64. Nys Y, Hincke M, Hernandez-Hernandez A, Rodriguez-Navarro A, Gomez-Morales J, Jonchére V, et al. Structure, propriétés et minéralisation de la coquille de l'œuf: rôle de la matrice organique dans le contrôle de sa fabrication. Inra Prod Anim. 2010;23(2):143-54.

65. Addadi L, Raz S, Weiner S. Taking Advantage of Disorder: Amorphous Calcium Carbonate and Its Roles in Biomineralization. Adv Mater. 2003;15(12):959-70.

66. Parkhurst DL. User's guide to PHREEQC. US Geol. Surv. Water Resour. Inv. Rep1999.

67. Truesdell AH, Jones BF. WATEQ, a computer program for calculating chemical equilibria in natural waters. J Res US Geol Surv. 1974;2:16.

68. Dombrowski RD, Litster JD, Wagner NJ, He Y. Crystallization of alpha-lactose monohydrate in a drop-based microfluidic crystallizer. Chem Eng Sci. 2007;62(17):4802.

69. Boudias C, Monceau D. CaRIne crystallography 3.1. 17 rue du Moulin du Roy, F-60300 Senlis, France; 1989-1998.

70. Hele-Shaw HS. Nature (London, UK). 1898;58:33.

71. Fick A. Ueber Diffusion. Ann Phys. 1855;170(1):59-86.

72. Kester DR, Pytkowicz RM. Theoretical model for the formation of ion-pairs in seawater. Mar Chem. 1975;3(4):365-74.

73. Gómez-Morales J, Hernández-Hernández An, Sazaki G, García-Ruiz JM. Nucleation and Polymorphism of Calcium Carbonate by a Vapor Diffusion Sitting Drop Crystallization Technique. Cryst Growth Des. 2009;10(2):963-9.

74. Hernández-Hernández A, Rodríguez-Navarro AB, Gómez-Morales J, Jiménez-Lopez C, Nys Y, García-Ruiz JM. Influence of Model Globular Proteins with Different Isoelectric Points on the Precipitation of Calcium Carbonate. Cryst Growth Des. 2008;8(5):1495-502.

75. Kawano J, Shimobayashi N, Kitamura M, Shinoda K, Aikawa N. J Cryst Growth. 2002;237−239:419.

76. Boistelle R, Lopez-Valero I. Growth units and nucleation: the case of calcium phosphates. J Cryst Growth. 1990;102(3):609-17.

77. Xin R, Leng Y, Wang N. In situ TEM examinations of octacalcium phosphate to hydroxyapatite transformation. J Cryst Growth. 2006;289(1):339-44.

78. Mangin D, Puel F, Veesler S. Polymorphism in Processes of Crystallization in Solution: A Practical Review. Org Process Res Dev. 2009;13(6):1241-53.

79. Lin Y, Singer P. Effects of seed material and solution composition on calcite precipitation. Geochim Cosmochim Acta. 2005;69:4495 - 504.

80. Nehrke G, Reichart G, Van Cappellen P, Meile C, Bijma J. Dependence of calcite growth rate and Sr partitioning on solution stoichiometry: non-Kossel crystal growth. Geochim Cosmochim Acta. 2007;71:2240 - 9.

81. Perdikouri C, Putnis C, Kasioptas A, Putnis A. An atomic force microscopy study of the growth of a calcite surface as a function of calcium/carbonate concentration ratio in solution at constant supersaturation. Cryst Growth Des. 2009:9.

82. Gómez-Morales J, Torrent-Burgués J, López-Macipe A, Rodríguez-Clemente R. Precipitation of calcium carbonate from solutions with varying Ca2+carbonate ratios. J Cryst Growth. 1996;166(1–4):1020-6.

83. Tai C, Lu J, Wu J. Crystal growth rate of calcite in a constant composition environment. J Chin Inst Chem Eng. 2005;36:443 - 50.

84. Gebrehiwet T, Redden G, Fujita Y, Beig M, Smith R. The Effect of the CO32- to Ca2+ Ion activity ratio on calcite precipitation kinetics and Sr2+ partitioning. Geochem Trans. 2012;13(1):1.

85. Stephens CJ, Ladden SF, Meldrum FC, Christenson HK. Amorphous Calcium Carbonate is Stabilized in Confinement. Adv Funct Mater. 2010;20(13):2108-15.

86. Howard EI, Fernandez JM, Garcia-Ruiz JM. On the Mixing of Protein Crystallization Cocktails. Cryst Growth Des. 2009;9(6):2707-12.

87. Bird R, Stewart W, Lightfoot E. Transport phenomena. 2nd. New York: John Wiley & Sons; 2002.

88. Krauss F, Schriever W. Die Hydrate des Calciumcarbonats. Z Anorg Allg Chem. 1930;188(1):259-73.

89. Fukushi K, Munemoto T, Sakai M, Yagi S. Monohydrocalcite: A promising remediation material for hazardous anions. Sci Technol Adv Mater. 2011;12(6).

90. Yamaguchi T, Murakawa K. Preparation of spherical CaCO3 (vaterite) powder transition to calcite in water. Zairyo. 1981;30:856-60.

91. Taft WH. Chapter 3 Physical Chemistry of Formation of Carbonates. In: George V. Chilingar HJB, Rhodes WF, editors. Developments in Sedimentology: Elsevier; 1967. p. 151-67.

92. Ogino T, Suzuki T, Sawada K. The rate and mechanism of polymorphic transformation of calcium carbonate in water. J Cryst Growth. 1990;100(1–2):159-67.

93. Ildefonso M, Revalor E, Punniam P, Salmon JB, Candoni N, Veesler S. Nucleation and polymorphism explored via an easy-to-use microfluidic tool. J Cryst Growth. 2012;342(1):9-12.

94. Hammadi Z, Candoni N, Grossier R, Ildefonso M, Morin R, Veesler S. Small-volume nucleation. CR Phys. 2013;14(2–3):192-8.

CHAPTER 6

Development of new techniques and methodologies for the study of nucleation and crystal growth in small volumes

CHAPTER 6

Development of new techniques and methodologies for the study of nucleation and crystal growth in small volumes

Analysis of the structural integrity of SU-8 based optofluidic systems for small molecule crystallization studies

1. State of the art

Microfluidics are of relevant interest in the field of crystallization, due to the low consumption of reactants and the ubiquitous laminar flow (i.e. low Reynolds number) under the most standard flow injection conditions [1]. In addition, droplet based methods [2-5] have been demonstrated to be an extremely powerful high-throughput technique for applications including biological assays [6, 7], production of polymer particles [8, 9], protein crystallization screening [5, 10] or crystallization of pharmaceutical compounds [11, 12]. For microfluidic systems to become widespread, it is required to have low-cost manufacturable methods for the production of fluidic structures. An additional property that should be addressed is their compatibility with organic solvents. Here, it would allow its usability not only with aqueous solutions, but also for small molecule crystallization, organic synthesis or analysis of organic compounds in general (ranging from active pharmaceutical ingredients to novel metal–organic frameworks). Recently, techniques using thermoset materials have been widely used in micromachining. A well-known example is the set of polydimethylsiloxane (PDMS)-based techniques, which has applications in the fabrication of microfluidics [13, 14] and have been extensively used for droplet based crystallization studies in aqueous media [10, 15-21]. Reasons for the success of this polymer can be associated to its outstanding advantages, among which it could be highlighted its technological simplicity [14, 17], its biocompatibility [22] and its high transparency in the UV-NIR range. Albeit, what is one of the major advantages of this

polymer for cell culture applications, namely the permeability to gases, becomes a major drawback when using organic solvents. PDMS microchannels present severe structural integrity failure [23, 24] and/or swelling [25, 26] in the presence of most organic solvents. This swelling causes distortion of the fluidic structure and even channel collapsing if the channel width is not large enough. Additionally, hydrophobic small molecules penetrate and diffuse in the PDMS cured matrix [27]. Partitioning of molecules into PDMS can significantly change solution concentrations and could potentially alter experimental outcomes [27]. Therefore, PDMS cannot be considered as a good candidate for implementing microfluidics if organic solvents were to be used.

Teflon and specially glass capillaries were (and still are) used to perform microfluidic crystallization experiments. Nevertheless, the use of such materials has severe technological limitations, as the possible configuration of the experimental setups is strongly restricted by their special characteristics. Silicon [28] offers a well-known alternative for the fabrication of microfluidics. Silicon is often selected for fabricating microdevices due to the broad technological knowledge regarding its processing, which arises from micromechanization. Here, etching techniques such as Reactive Ion Etching (RIE) [29] and more recently Deep Reactive Ion Etching (DRIE, using the Bosch process) [8], in combination with the silicon-to-silicon [30] and silicon-to-glass [31] bonding, allows obtaining a myriad of microfluidics, from ultrasonic microfluidic separators and mixers [32, 33] to microdevices for biological and protein crystallization studies [28, 34]. Nevertheless, access to specialized equipment is required, strongly compromising the low cost issue.

Glass-based microfluidics are even more common in the literature [35-38], and they have been widely used for crystallization studies and chemical synthesis in general [11, 39, 40]. Optically, they offer better optical properties (for optical monitoring) than silicon in terms of working wavelength range, since most glasses are transparent from ultraviolet (UV) to Infrared (IR) wavelengths, in opposition to silicon, that is only transparent for wavelengths above 1100 nm. Despite the clear advantages of glass technology, it is also limited to the existing patterning processes [41]. Again, the high cost and limited

accessibility of the above mentioned techniques hampers its massive entrance to the market.

Therefore, reduction of fabrication complexity and lowering the fabrication costs brings again to polymer technology. We have already discussed the unsuitability of PDMS against organic solvents. Yet, other polymers have also been reported, using many replication techniques for forming plastics at the microscale like embossing [42], casting [17], injection molding [43] and imprinting [44] . Again, these techniques are very popular for manufacturing water-based microfluidics [18, 45-47]. Unfortunately, most of these plastics have low or no tolerance against organic solvents, being dissolved or damaged by them. An alternative would be using the negative-tone epoxy polymer SU-8, developed by IBM and EPFL [48-50]. Since its appearance, it has been increasingly used in micro- and nanotechnologies. SU-8 has become an alternative material for producing polymeric micro structures through low temperature processes, making the fabrication of such structures accessible to labs with no need of the previously mentioned high-end facilities. Due to its properties and its ease of use, SU-8 is an interesting option for many purposes, from pattern transfer applications (creating molds to be subsequently used with other materials as PDMS), to its direct use as a structural material for microelectromechanical systems (MEMS) [48, 51] and microfluidics [51]. Contrary to conventional resists, which are used for transfer patterns from a photolithographic mask to a solid layer, SU-8 has been used as a permanent building material to fabricate microcomponents such as cantilevers [52, 53], membranes [54], and microchannels [55]. During the patterning and post-exposure step, the SU-8 resist is cross-linked and becomes chemically resistant. This material has unique properties from a structural (thick structures and/or high aspect ratios can be obtained [49]), mechanical (low Young modulus of 4.02 GPa [48]) and optical (low absorbance in the near-UV range [56]) point of view. Thus, this material is extremely attractive for microfluidic systems that require high resistance against organic solvents and use light as readout mechanism.

Surprisingly, an in-depth study of the tolerance of the SU-8 against most common organic solvents is, to the best of our knowledge, yet to be reported. This may be caused by the fact that, despite these outstanding properties, the construction of sealed, SU-8 microchannels has been considered as a challenge. Some groups have approached the problem by sealing the defined microfluidic structures one-by-one to a glass coverslip with quick-setting glue [57, 58]. A wafer-scale sealing has also been proposed, requiring additional processing steps or through the use of dry thin-film laminates of SU-8 (SUEX) [59, 60]. The lamination of uncrosslinked SUEX films, which are provided in a flexible substrate, presents a main advantage. The flexibility of the film and its substrate during the transfer allows a more conformal contact and results in better adhesion. Therefore the bonding process becomes less sensitive to the thickness inhomogeneities compared to other bonding processes. This good adhesion permits the subsequent development of the structure (*e.g.* for the access holes) and also the possibility to stack many layers if required while keeping the yield at very high standards (and straightforwardly, reducing the overall cost of the fabricated systems).

In this context, SUEX covering seems to be a promising candidate that would allow obtaining chemically resistant microfluidics at wafer scale. Neverthless, no detailed information about the compatibility of such material against organic solvents has been reported either.

In addition to the compatibility of a SU-8/SUEX-based microfluidic with organic solvents, it is also important to simultaneously address the final objective, which is the use of this material to implement an arbitrary complex microfluidic network, defining a "micro total analysis system, μ-TAS". This concept, firstly introduced by Manz and coworkers [61] has major advantages. The great benefit of physically scaling down analytical systems is not only a reduction in size but rather an improvement of the analytical performance [62]. A continuous detection system enables not only feedback control to optimize reactant conversion in a chemical reaction, but also increases throughput in a system, facilitating the measurement of kinetic parameters as induction times for nucleation, allowing reaction kinetics to be obtained in situ. Nowadays, the μ-

TAS concept has been demonstrated using sensors with different detection methods, ranging from electrochemistry to mass spectroscopy or photonics/micro-optics. Among them, the latter (i.e. photonics/micro-optics, referred to as the so-called optofluidic systems, OFS) seems to be the most suitable for real time, high sensitive contactless monitoring of a liquid in a microfluidic network [63]. It is also important mentioning that, as opposite to the other working principles above mentioned, OFS may not require additional technological steps for its implementation, and hence the requested low cost issue prevails.

In this section of the present chapter, we propose the use of SU-8/SUEX optofluidic systems for their application in organic chemistry in general and in small molecule crystallization studies in particular. For that purpose, a simple OFS has been manufactured in SU-8 with a SUEX cover, as well as in PDMS (only for comparison purposes), and tested against 36 different commonly used solvents. Implemented micro-optical elements [64] allows swelling quantification of the materials, through the variation of the optical path, indirectly measured by UV-Vis spectrometry. Through this simple application, we show that the SU-8/SUEX OFS are resistant to many organic solvents and suitable for on-chip UV spectroscopy and, straightforwardly, both materials may be used with such organic solvents.

In addition to the compatibility with the structural materials, for droplet-based OFS it is also necessary to know the compatibility between the solvent and the carrier fluid in which solution droplets are generated. Immiscibility between solution and carrier fluid is a necessary condition for generating stable plugs. Again, no detailed information about the compatibility between the most commonly used carrier fluids for droplet based microfluidic experiments (FC-70 Fluorinert oil and silicone oil) and the organic solvents has been reported, making this information crucial for future organic solvent droplet-based OFS.

2. Experimental

Solvents and reagents

PDMS Sylgard 184 elastomer kit was supplied by Dow Corning (Midland, MI, USA). SU-8 polymer and propylene glycol methyl ether acetate developer (PGMEA) were supplied by MicroChem, Corp. (Newton, MA, USA). SUEX films were supplied by DJ DevCorp (Sudbury, MA, USA). FC-70 fluorinated oil and silicone oil were supplied by Hampton Research (Aliso Viejo, CA, USA). Thirty six solvents were chosen to evaluate their compatibility with SU-8 photoresist, Silicone oil and FC-70 Fluorinert oil. Solvents were chosen in the basis of their common use in crystallization experiments, their boiling point and their polarity. Changes in dielectric constant of the medium may have a dominant effect on the solubility of the ionizable solute, in which higher dielectric constant can cause more ionization of the solute and results in more solubilization [65]. The solvents used in this work are listed in Table 1 and all were purchased from commercial sources and used as received.

Table 1. Solvents used in this work

Solvent	Acronym	Boiling point (°C) †	Density (g/cm³) †	Relative permittivity †
Acetone	ACE	56.05	0.7845	21.01
Ethyl Acetate	ETA	77.11	0.9003	6.08
Acetonitrile	ACN	81.65	0.7857	36.64
Acetophenone	ACP	202	1.0281	17.44
Benzene	BZN	80.09	0.8765	2.28
1-Butanol	BUT	117.73	0.8095	17.84
Butanone	BNA	79.59	0.7999	18.56
Butyl Glycolate	BGL	188	1.0190	
Chlorobenzene	CLB	131.72	1.1058	5.69
Chloroform	CLF	61.17	1.4788	4.81
Cyclohexane	CLH	81	0.7740	2.02
Cyclopentane	CLP	49	0.7460	1.97
Cyclopentanone	CPN	131	0.9490	13.58
1,2-Dichloroethane	DCE	83.5	1.2454	10.42
Diisopropyl ether	DIE	68.4	0.7192	3.81
Dichlorometane	DCM	40	1.3266	8.93
Dimethyl acetamide	DMA	165	0.9372	38.85
N-methylformamide	NMF	199.51	1.011	189
N,N-Dimethylformamide	DMF	153	0.9945	38.25
Dimethyl Sulfoxide	DMSO	189	1.1010	47.24
Ethanol	EOH	78.29	0.7893	25.30
Diethyl Ether	DET	34.5	0.7138	4.27
Hexane	HEX	68.73	0.6606	1.89
Heptane	HEP	98.4	0.6795	1.92
Isoctane (2,2,4-Trimethylpentane)	ISO	99.22	0.6878	1.94
Isopropyl alcohol (2-Propanol)	ISP	82.3	0.7890	20.18
Methanol	MET	64.6	0.7914	33.00
Methyl Acetate	MAC	56.87	0.9342	7.07
1-Methyl-2-pyrrolidone	MPY	202	1.023	32.6
Nitrometane	NME	101.19	1.1371	37.27
Octane	OCT	125.67	0.6986	1.95
Pentane	PEN	36.06	0.6262	1.84
1-Propanol	1PR	97.2	0.7997	20.80
Tetrahydrofuran	THF	65	0.8833	7.52
Tetrahydropyran	THP	88	0.8810	5.66
Toluene	TOL	110.63	0.8668	2.38

† Data from [66]

Design and fabrication

The OFS for both PDMS and SU-8 retain the basic architecture, as shown in figure 1, albeit modifications in the micro-optical elements are required due to the ubiquitous fabrication procedures and their different refractive index. Ramifications of the inlet allow an homogeneous fluid velocity profile of the fluid when reaching the reactor, which has a width of 3 mm and a length of 5 mm (figures 1a and 1b). This width has been selected to avoid channel collapsing in case of swelling of the constructed material, whereas the length assures complete interaction between the organic solvent and the constituent material. From an optical point of view, the proposed OFS have three different optical interrogation channels (red arrows in figure 1a), located at 16%, 50% and 83% of the total length. At such locations is where the UV-Vis measurement is performed. Each interrogation channel comprises a self-alignment element for accurate fiber optics positioning (see figure 1b, beam trajectory represented in red) and a set of 2D microlenses that modulate the optical path (before and after propagating through the channel). All these components are fabricated in one single process step by replica molding with PDMS or by UV exposure when using SU-8.

A schematic illustration of the fiber inserts and lenses is shown in figure 2. Light is coupled into the system through a multimode optical fiber inserted into a self-alignment element, which allows solving the most crucial step to the design of the system: the positioning of the input optical fiber in relation to the micro-optical system and the microfluidics. As it can be observed in figure 2, the self-alignment element can be envisaged as a closed channel, with one end located exactly at the focal of the first microlens. Here, placing the fiber optics at the facet end wall will assure that the fiber optic is at the optical axis and at the appropriate position. The same applies for the output fiber which enables the collected light to reach the detector. At the end of these self-alignment elements, two micro-lenses made of the same material as the walls of the channels (PDMS/SU-8) are defined, according to their respective refractive indices [67, 68] ($n_{PDMS} = 1.42$ and $n_{su8} = 1.56$) and air ($n_{air} = 1.00$).

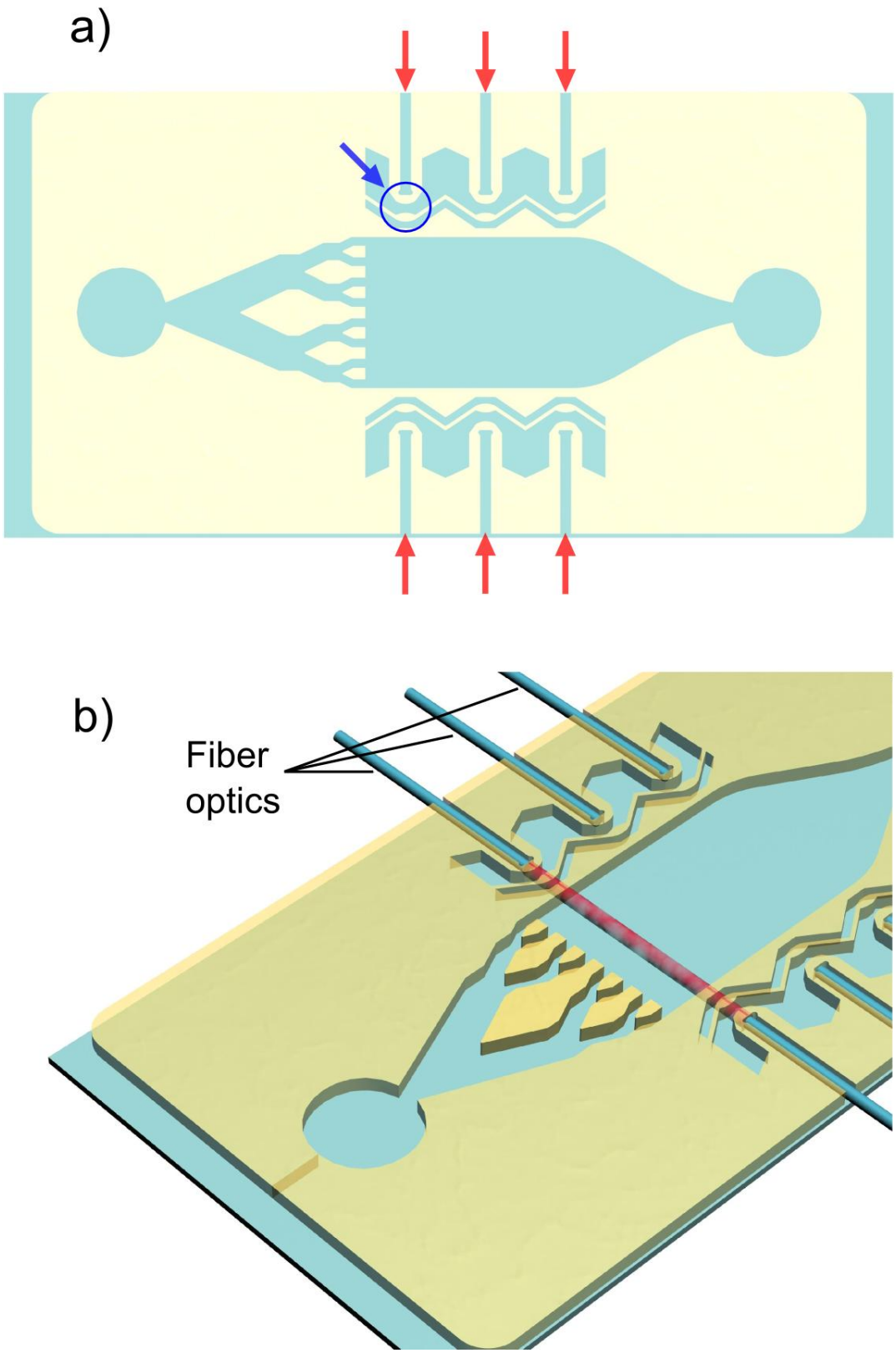

Figure 1. Schematic representation of the optofluidic system with a) interrogation channels marked with red arrows and one of the six microlenses array marked with a blue arrow, inside a circle; b) fiber optics inserted (optical path in red)

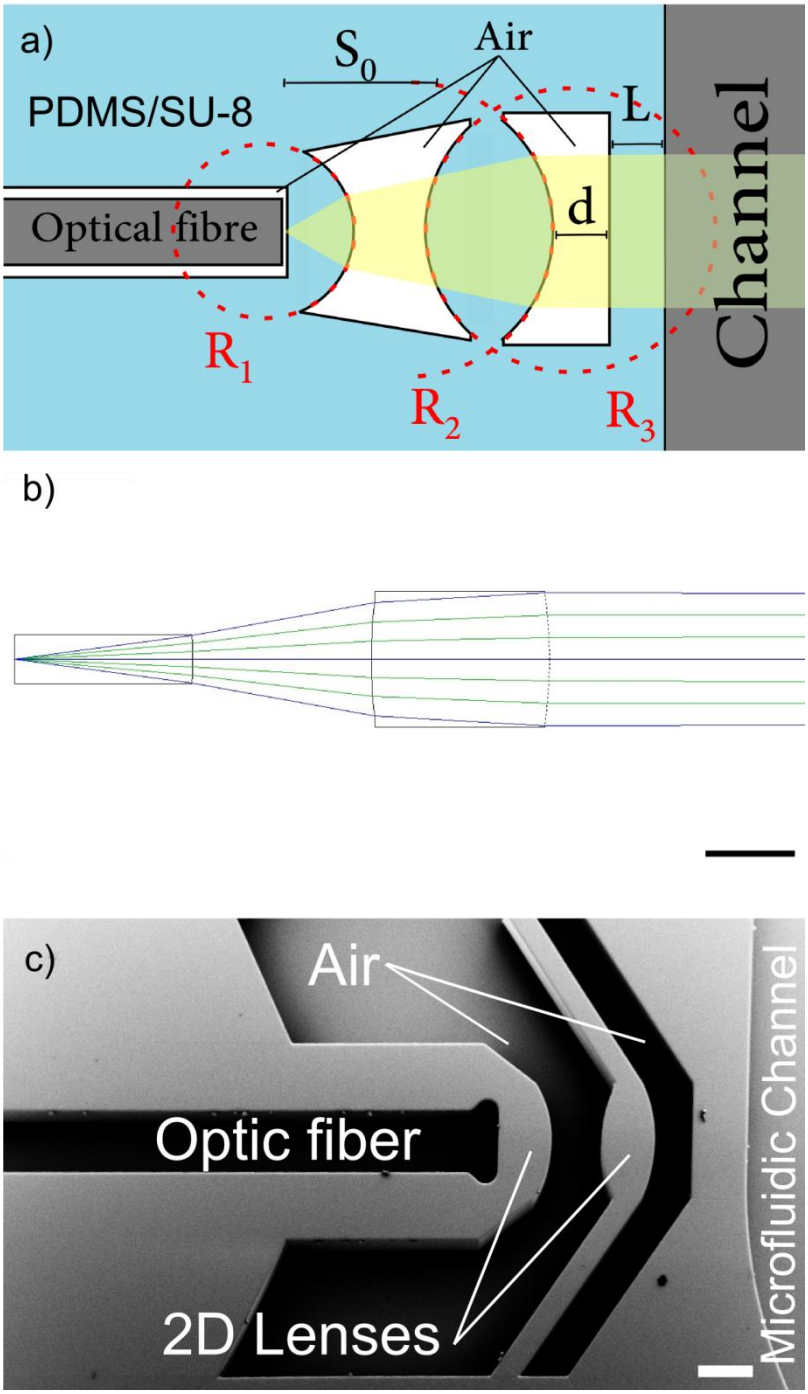

Figure 2. a) Detailed scheme of the optical fiber channel, the lenses and the prism for PDMS and SU-8 OFS. Optic fibers are stopped at a distance S0 which, considering the refractive index of PDMS/SU-8 and air, together with the curvature of the lenses R1 and R2-R3, allows having parallel beams at the biconvex second lens output. b) Ray tracing simulation performed by OSLO Edu software for the design of SU-8 lenses. Scalebar corresponds to a length of 100 µm; c) Detailed SEM image of an SU-8 optical interrogation channel, where the microlenses and the self-alignment channel are located in close proximity to the microfluidics. Scale bar corresponds to a length of 200 µm.

The first microlens reduces the numerical aperture of the light incoming from the fiber optics. This decrease allows the optical interrogation channels be set closer to the microfluidics. In turn, the second set of microlenses was designed to have parallel beams throughout the channels. The ray tracing simulations for the design of the lenses have been performed using OSLO Edu© software taking into account the numerical aperture of the used optic fibers (NA = 0,22). A screenshot of the performed ray tracing simulations is shown in figure 2b.

In accordance with the refractive indices of air and PDMS, and selecting the radius to be R_1^{PDMS} = 250 µm and R_2^{PDMS}=R_3^{PDMS} = 390 µm for PDMS, whereas R_1^{SU8} = 400 µm, R_2^{SU8}=R_3^{SU8} = 510 µm for SU-8, a distance S_0 = 400 µm for both materials should provide parallel beams through the optofluidic system. To separate the biconvex lens from the bulk regions, an air gap, with a minimum distance d = 30 µm, is left just after the lenses (d_{SU-8} = 150 µm, d_{PDMS} = 170 µm). No variation of the ray tilt is produced at the air–polymer interface due to the 90° incidence. Finally, in order to assure that the liquid inside the prism will not fill, due to leakage, the air gap, with a distance L, according to the properties of the materials (L_{SU-8} = 200 µm, L_{PDMS} = 500 µm) is left between the air gap and the channels. An example of the fabricated SU-8 optical interrogation channel is also shown in figure 2c.

PDMS OFS were fabricated by casting PDMS in an SU-8 master. The technology is extremely simple and it has been widely studied and reported [69], nevertheless, for completeness it is also reproduced here. After cleaning a low-cost 500 mm thick soda-lime glass, the substrate is dehydrated at 200 °C for 1 h prior to the spinning of an SU-8 layer with a thickness of 50 µm, which will act as a seed layer for the subsequent SU-8 layers. Afterwards, the substrates are baked at 95 °C for 30 minutes and exposed to UV light without using a mask and a post-exposure bake (PEB) at 95 °C is followed, with a slow cooling down to room temperature, in order to avoid any crack in the layer due to temperature stress. Then, with a single spin-on process using SU-8 2050, a thickness of 250 µm is obtained, in order to reach a sufficient height that allows a hassle-free insertion of the optical fibers (which have a diameter of 230 µm). A subsequent UV

exposure with a mask that defines the OFS is followed by another PEB and development of the structures in PGMEA, finishing the definition of the master. Finally, a 2 h hard bake (HB) at 120 °C relaxes all the structures and eliminates possible microfractures, increasing the long term stability. The PDMS pre-polymer was obtained by mixing the curing agent with the elastomer base in a 1:10 ratio (v:v). The resulting mixture was subsequently degassed to remove air bubbles, and a thin layer (between 0.5 and 1 mm) was poured over the master and cured for 60 min at 80 °C. Afterwards, the cured PDMS was peeled off from the master and the fluidic ports were opened. Then, both the PDMS and a second soda- lime glass substrate were exposed to an oxygen plasma [70] in a barrel etcher (Surface Technology Systems, Newport, UK). Immediately afterwards, both surfaces are brought in contact, causing its irreversible sealing. This covalent bonding between the PDMS and the soda-lime glass ends the fabrication process for the PDMS devices. A schematic representation of the process is depicted in figure 3.

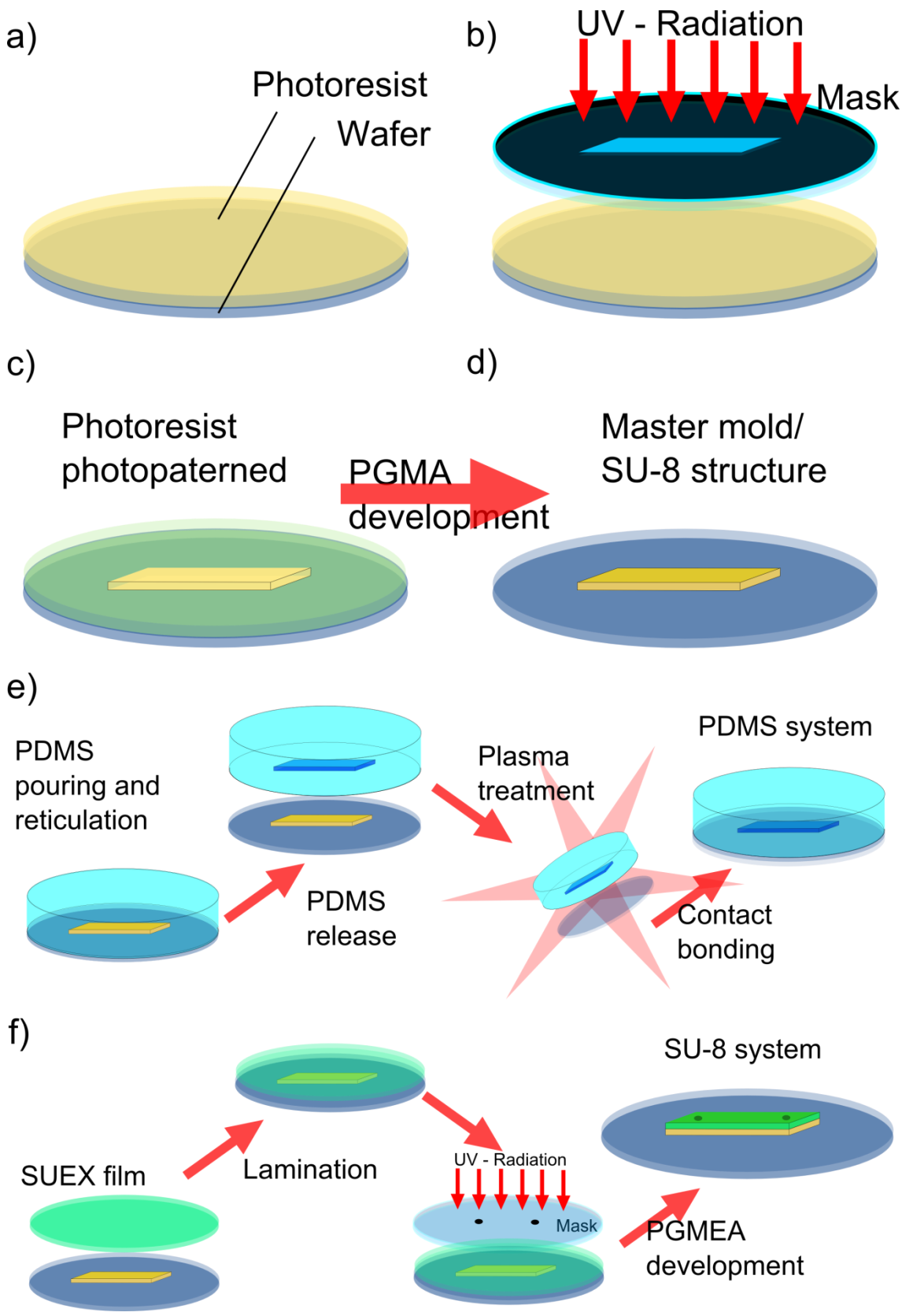

Figure 3. (a) - (e) Schematic representation of the fabrication of a SU-8 mold and the casting and fabrication of a PDMS based optofluidic system; a) to d) and f) schematic representation of the fabrication process for a SU-8 based optofluidic system.

The technology required for implementing the SU-8 OFS makes use of the above mentioned steps and is also schematized in figure 3. Concretely, using an appropriate mask, the walls and the micro-optical elements of the OFS made using SU-8 were defined with a thickness of 250 µm. The lid on such systems was done by laminating a 200 µm thick SUEX dry film by pressure and temperature with the help of a laminator (HeatSeal® H600 Pro from GBC®, USA). After the lamination process the SUEX film was exposed to UV light, using a mask that allows defining the fluid in/outlets. Figure 4 illustrates this process for a better understanding. PEB of the SUEX consisted on a first step at 40 °C for one hour with the SUEX cover side facing down in order to induce enough cure to inhibit lid sagging/bowing. Afterwards, the temperature was ramped up to 85 °C for 20 minutes [71]. Development was done using again PGMEA and then a HB at 120 °C for 2 hours was performed in order to obtain a residue-free device [71]. Chips were slowly cooled down to room temperature with the purpose of minimizing temperature stress, probably resulting in surface cracks and unbonding of the SUEX cover.

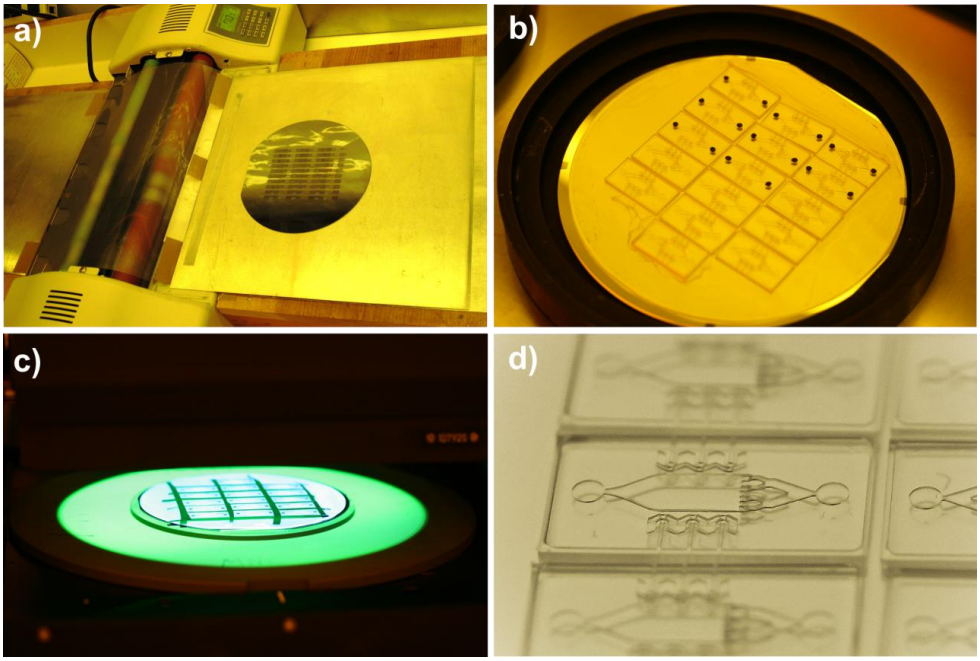

Figure 4. a) Image of the laminator with a silicon wafer over a Al sheet, used as a temporary lamination substrate; b) SUEX film laminated over a soda-lime glass wafer containing 16 pre-diced SU-8 systems; c) UV exposure of the SUEX film; d) array of SU-8 based systems ready for its use.

Carrier fluids Compatibility

The compatibility of FC-70 and silicone oils with the different organic solvents was tested in order to determine their suitability for future droplet based microfluidic experiments. With the purpose of examining their miscibility, 200 µL of each oil were energically mixed with 500 µL of each solvent in a 2 mL glass vial. The behavior of the mixture was observed in the first instants after mixing and vials were stored at room temperature. After 24 h vials were again monitored to check possible changes.

Characterization techniques

For compatibility tests, micro patterned samples fabricated in SU-8, comprising positive (blocks) and negative (wells, trenches) structures ranging from 1 to 100 µm, both isolated and in an array, as well as flood exposed and baked SUEX film were fabricated and immersed in 36 different solvents. After being immersed in the different organic solvents for 24 h, samples were subsequently dried at 30 °C on a hot plate and scanning electron microscopy experiments were performed using a Carl Zeiss AURIGA CrossBeam SEM (Germany). No metallization of the samples was carried out, in order to avoid any surface modificacion in the samples, thus allowing examination at micron scale. Also atomic force microscopy experiments were performed in a Veeco Nanoscope IV controller coupled to a Dimension 3100 head (UK), in order to determine its surface roughness at nanoscale. For that purpose, and to make roughness measurements comparable between the samples, all measurements were performed with the same scanning window size and resolution [72]. Three equal areas of 1x1 μm^2 randomly selected were scanned in contact mode with a resolution of 256x256 lines for each attacked sample, and for 10 different non attacked reference samples for each material. A first order flattening was applied for all the obtained images to fit each scanned line individually to center data and remove tilt, in order to obtain a significative measurement of the roughness. Figure 5 represents the same AFM image with no flattening, zero order flattening (centered data) and an order 1 flattening (centered data

and tilt removed). The roughness of a real surface is evaluated from the deviations of the two-dimensional measured profile (z values measured by means of the AFM technique on the surface) with respect to an ideal surface. Such deviations can be classified in three groups, depending on the value of the irregularity steps, as shown in Fig. 1, where the total profile (Fig. 1 – no flatten) includes the contributions of [73]:

– Nominal form: corresponding to macroscopic deviations from the mean line profile (nominal shape), cleaned out of the irregularities and characterized by a big sampling step

– Waviness: irregularities with large amplitude

– Roughness: irregularities with small amplitude

A zero order flattening removes the irregularities caused by the measurement deviations (existing in the non flattened nominal shape), revealing the nominal form, whilst a first order flattening also flattens the macroscopic deviations, revealing the roughness of the surface at the lower scales.

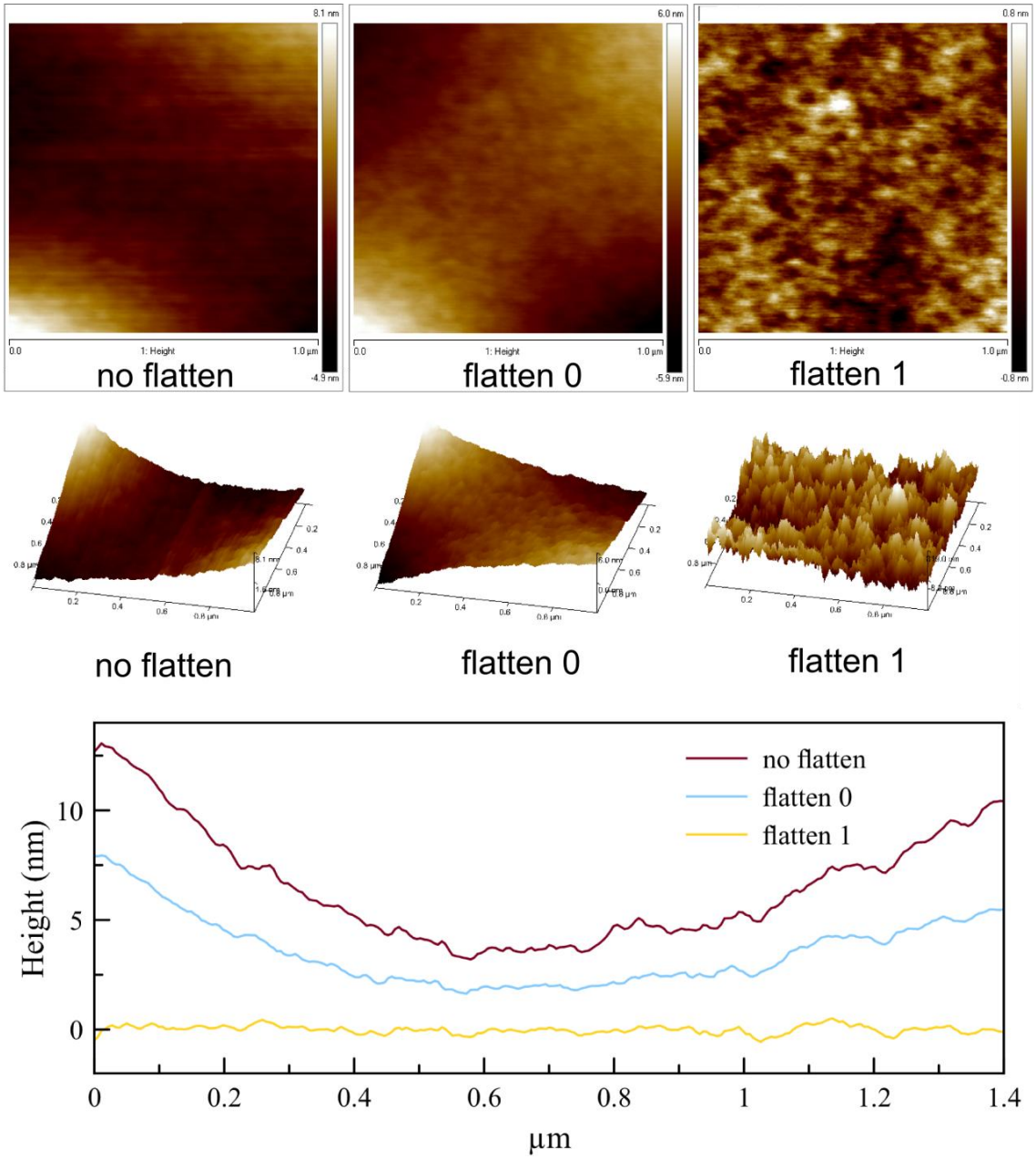

Figure 5. a) R AFM images of a SUEX 1x1 µm^2 surface with no flattening, order 0 flattening and order 1 flattening; b) diagonal z profile of the same images, displaying the nominal shape (no flatten), the nominal form (flatten 0) and the surface roughness at the lower scales (flatten 1).

From all the experiments, roughness in terms of average roughness (R_a, the arithmetic average of the absolute values of the surface height deviations measured from the mean plane), and root mean square (rms) roughness (R_q, root mean square average of height deviations taken from the mean data plane) were determined for all of the images

utilizing NanoScope Analysis software. These parameters are calculated through the following expressions:

$$R_a = \frac{1}{N}\sum_{i=1}^{N}|z_i - \bar{z}|,$$

$$R_q = \sqrt{\frac{\sum_{i=1}^{N}(z_i - \bar{z})^2}{N}},$$

where z_i is the height of the ith point with respect to the lowest point in the image and N is the total number of points comprised in the image. From each sample an average of the measurements and its standard deviation was determined in order to compare the roughness values with the averaged values obtained from the reference samples.

For a quantitative measurement of the swelling of the materials exposed to the organic solvents, a set of UV-Vis transmittance measurements were obtained using the previously described OFS. A Tungsten Halogen Light Source HL-2000-FHSA (Ocean Optics, Dunedin, FL, USA, USA), emitting at wavelengths ranging from 360 nm to 2000 nm was coupled to a multimode fiber optic with a diameter of 230 µm, (Thorlabs, Dachau, Germany), which was located in the self-alignment microchannels. Light emerging from the OFS was coupled to an identical fiber optic, directly connected to an Ocean Optics USB2000+ spectrophotometer (Ocean Optics, Dunedin, FL, USA). Such configuration enables obtaining the spectral response in the visible range for both SU-8 and PDMS OFS.

To check the compatibility against the solvents, 36 SU-8 OFS and 36 PDMS OFS were fabricated and the initial spectra of each one was acquired prior to being exposed to the solvent (T_0 Air in Figure 6). Then, each solvent was injected in one OFS and the spectral response was obtained again (T_0 Solvent in Figure 6). At this point, each OFS was placed in a flask containing the same solvent, and was left unperturbed for 24 h in a temperature-controlled chamber. Afterwards, the OFS was taken out of the flask and with the solvent still inside the OFS, the spectra was again acquired (T_{24} Solvent in

Figure 6). Finally, each OFS was blow dried and the final measurement was taken (T_{24} Air in Figure 6).

3. Results and discussion

Absorbance measurements

Figure 6 shows two typical spectra set which are representative of the experiments performed. Red and blue spectra in each set represent measured intensity through the empty OFS before and after 24 h immersion in the solvent. Both measurements are virtually equal (small differences are within the experimental error due to the manual insertion and alignment of optic fibers in the channels), demonstrating that the swelling process is reversible once all the solvent is evaporated [25]. All the spectra obtained for each solvent and for both PDMS and SU-8 OFSs can be found in the supporting information. Green and brown spectra correspond to OFS measurements once it has been filled with solvent, and after 24 hours immersion in the same solvent. Generally speaking, the spectra obtained when the OFS was filled with solvent had a higher number of counts per second (intensity) for any wavelength as compared than their identical measurements done with the OFS empty. This may be associated to the refractive index of the solvents, which are closer to those of PDMS and SU-8 than the air refractive index, reducing the beam broadening inside the OFS. The difference in intensity between T_0-Air and T_0-Solvent spectra (marked with a double black arrow in the figures) represents the change of optical path due to the presence of solvent in the channel, while the difference between T_0-Solvent and T_{24}-Solvent spectra (marked with a double red arrow) is caused by the change in the optical path due to swelling.

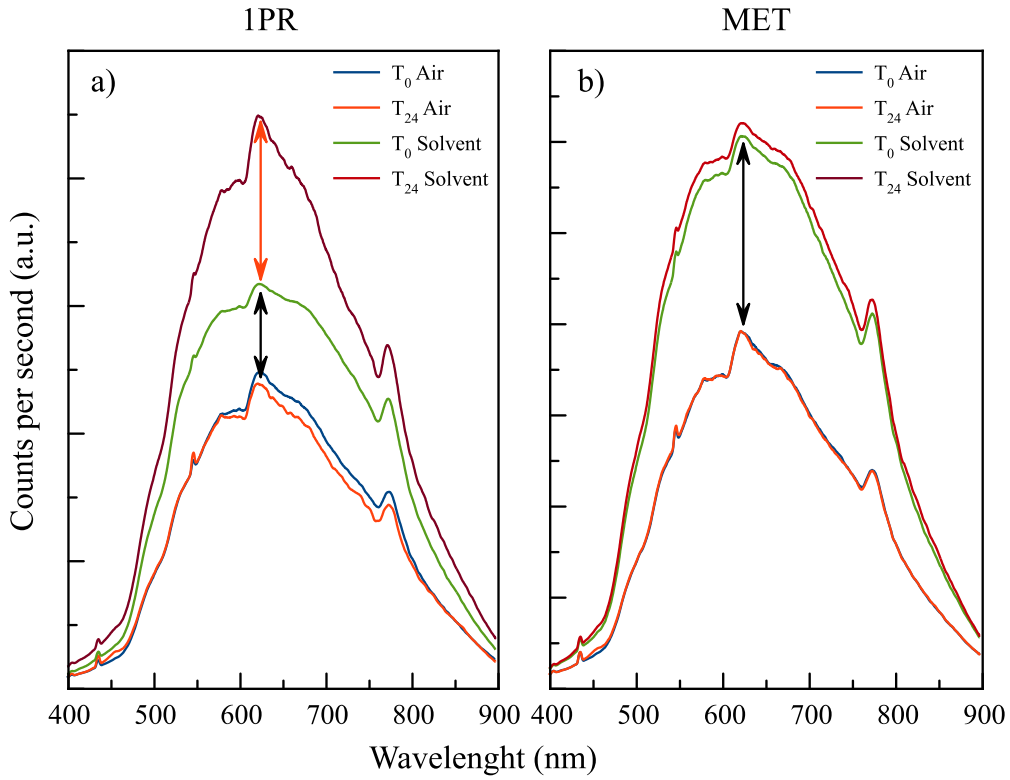

Figure 6. Typical spectra sets, representative for: a) a solvent that produces PDMS swelling (1-propanol); b) a solvent that do not produce measurable swelling in a PDMS device (methanol). Spectra sets measured in SU-8 devices are identical to the case described by b).

Swelling generates an increase of volume of the structures that form the chips, diminishing the width of the microfluidic channel and therefore the optical path. In equal conditions of emitted intensity and transmission media, the reduction of the optical path is transduced into an increase of detected intensity by the spectrometer. This variation in the optical path can be determined through Beer-Lambert law, which relates the absorption of light to the properties of the material through which the light is travelling. The Beer-Lambert law [74] states logarithmic dependence between the transmission of light through a substance, T, and the product of the absorption coefficient of the substance, α, and the path length (i.e., the distance the light travels through the material), ℓ. The absorption coefficient is also defined as a product of the molar absorptivity of the absorbing species, ε, and its molar concentration c. Equation can be written as $T = \frac{I}{I_o} = 10^{-\alpha\ell} = 10^{-\varepsilon c\ell}$, or in terms of absorbance: $A = -\log_{10}\left(\frac{I}{I_o}\right) = \alpha\ell =$

$\varepsilon c\ell$, where I_o is the intensity measured through the initial optical path, and I the intensity measured after optical path changes. Thus, the absorption coefficient, constant for the two absorbance measurements and the relative variation in the path length, with respect to the original one, can be deduced.

Absorbance measurements in PDMS OFS were not possible to be performed for all the studied solvents, due to tearing or desealing of the PDMS OFS bonded to the glass substrate. Once PDMS swells, it normally can deswell back to its original shape after the complete evaporation of the solvent. However, uneven evaporation, which happens when PDMS bonded to a surface is dried in air, creates a stress in the material. Evaporation rate is higher on the surface exposed to air, thus shrinking faster than the glass bonded part and leading to stress forces that tend to curl the PDMS surface. Moreover, under solvent contact, the bonds with the rigid substrate inhibits PDMS from swelling equally, also generating stress, which is relieved when the elastomer tears or deseals from the glass. In general, solvents with the lowest relative permittivity were found to swell PDMS the most, thus desealing from the glass substrate or tearing the channels. On the contrary, solvents with high relative permittivity did not exert important swelling effects. This behavior was also previously observed and reported, and it is explained by the affinity of PDMS (which has low polar contributions) with low polarity solvents [25], although it is not the only factor which affects swelling. The Hildebrand-Scatchard equation relates the solubility parameters of nonpolar liquids to the enthalpy change on mixing:

$$\Delta H_m = V_m(\delta_1 - \delta_2)^2 \varphi_1 \varphi_2,$$

where V_m is the volume of the mixture, δ_i is the solubility parameter of the component i, and φ_i is the volume fraction of i in the mixture [75]. For two components to be soluble in one another (i.e., for swelling to occur in a polymer-solvent system), the free energy of mixing, ΔG_m must be favorable, that is, $\Delta G_m < 0$. Since $\Delta G_m = \Delta H_m - T\Delta S_m$, and $\Delta H_m \propto (\delta_P - \delta_s)^2$, swelling is maximal when $(\delta_P - \delta_s)^2$ is 0, where δ_P and δ_s are the solubility parameters of the polymer and solvent. The solubility parameter can be expressed by a

sum of three forces: dispersion forces, δ_d, polar forces, δ_p, which are the ones mentioned above, and hydrogen-bonding forces, δ_h, within the material (Hansen's total solubility parameter) [75] that is, $\delta^2 = \delta_d^2 + \delta_p^2 + \delta_h^2$. Thus the effect of dispersion and hydrogen-bonding forces could explain the cases in which solvents with a high relative permittivity are causing swelling on PDMS, as can be observed for EOH and MPY solvents for example.

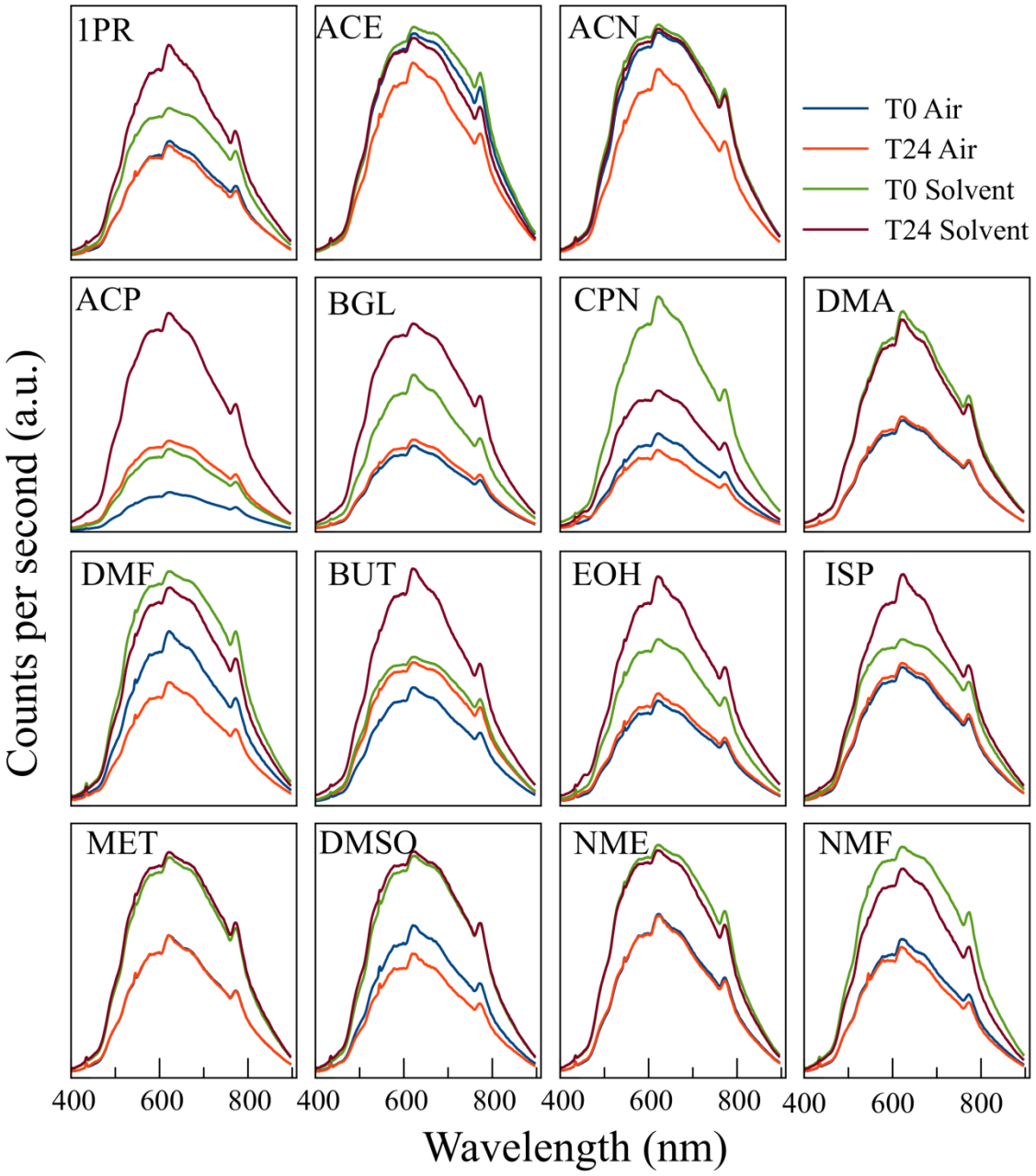

Figure 7. Spectra sets measured for the PDMS systems in contact with different solvents. Acronyms for each solvent correspond to the description in table 1.

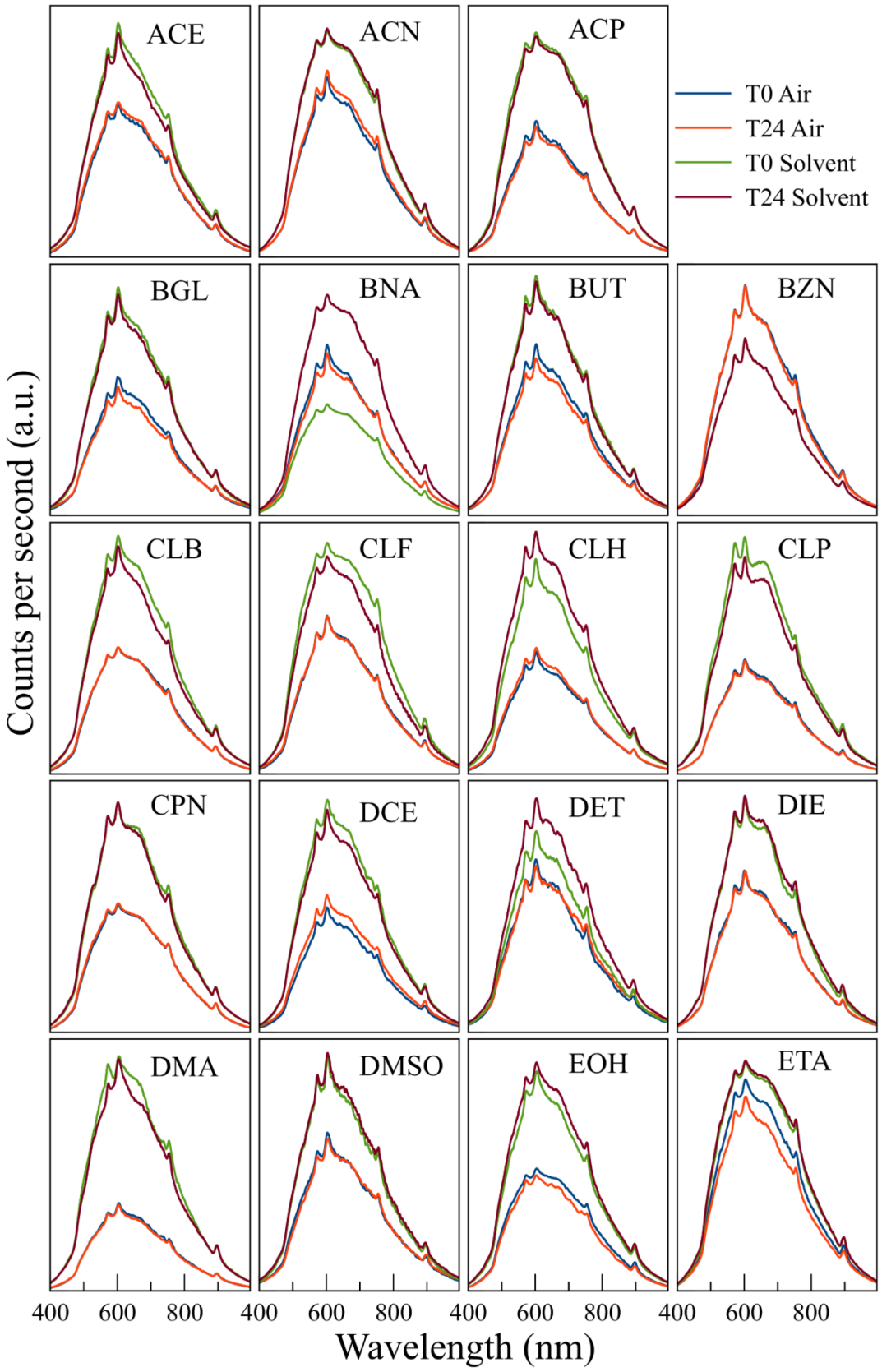

Figure 8. Spectra sets measured for the SU-8 systems in contact with different solvents. Acronyms for each solvent correspond to the description in table 1.

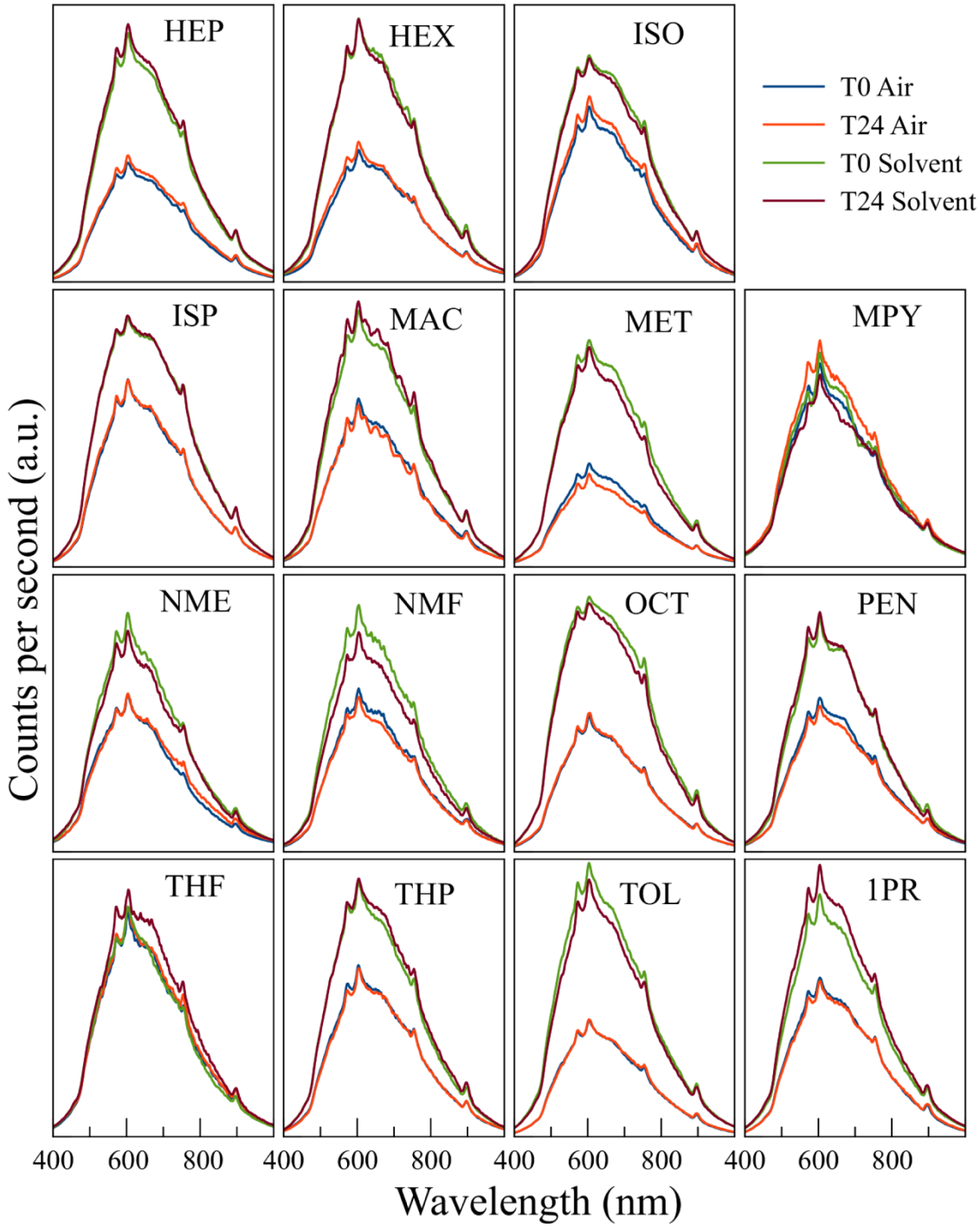

Figure 8 (continuation). Spectra sets measured for the SU-8 systems in contact with different solvents. Acronyms for each solvent correspond to the description in table 1.

In contrast with PDMS, SU-8 microchips only presented functional damage when exposed to DMF and DCM for 24 h, resulting in the tearing of the SUEX cover, impeding the filling of the chips for a second absorbance measurement. In spite of this problem in the cover, all the chips sufficiently maintained their integrity of the microfluidic channels.

Table 2 summarizes the measured optical path variations as a relative absorbance variation (in absorbance units, A.U.) with respect to the original channel width in PDMS and SU-8 OFS exposed to the solvents. Variations of ±0.6 dB were considered within experimental error after a series of preliminary experiments (note no negative values can be obtained for a real deformation of the channel walls, as the optical path can only be decreased by swelling). As it can be seen in figure 8, measurements through SU-8 systems only presented two different spectrum patterns, corresponding to air and solvent media, before and after 24 submersion in the solvents, revealing no quantifiable changes in the optical path and therefore no measurable swelling. That is to say that no measurable swelling effect was detected through absorbance measurements for most of the 34 remaining tested solvents. Only small variations, very close to the experimental error were found for the SU-8 OFS in the presence of DIE and DET solvents. The lower value of T_0 – Solvent in comparison with T_0 – Air for the SU-8 system exposed to BNA is probably due to the presence of air bubbles or any other foreign particle in the optical path when this measurement was performed.

Table 2. a) Swelling of PDMS and SU -8 chips exposed to 36 different solvents, measured by optical path variation determined by absorbance measurements through the microfluidic channel of the chips; and b) miscibility test for FC-70 and Silicone Oil with the same solvents.

	PDMS Chips	**SU-8 Chips**	**FC – 70 Compatibility**		**Silicone Oil Compatibility**	
Solvent	**Absorbance variation (A.U.x10)**[a]	**Absorbance variation (A.U.x10)** [a]	**t = 0**	**24 h**	**t = 0**	**24 h**
ACE	-0.21	-0.18	I	I	PM	PhS
ETA	Torn	0.03	I	I	M	=
ACN	0.09	0.05	I	I	I	I
ACP	4.3	0.05	I	I	I*	I
BZN	Torn	0.00	I	I	M	=
BUT	1.75	-0.11	I	I	M	=
BNA	Torn	2.98	I	I	M	=
BGL	1.52	-0.13	I*	I	PM	PhS
CLB	Desealed	-0.19	I	I	M	=
CLF	Desealed	-0,26	I*	I	M	=
CLH	Torn /desealed	0.52	I*	I	M	=
CLP	Torn /desealed	0.38	I*	I	M	=
CPN	-1,98	0.38	I	I	PM	PhS
DCE	Torn	-0.18	PM	E	M	=
DIE	Desealed	-0.77	I	I	M	=
DCM	Torn	Torn	I*	I	M	=
DMA	-0.15	-0.04	I*	I	I	I
NMF	-0.55	-0.51	I	I	I	I
DMF	-0.39	Torn	PM	E	I	I
DMSO	0.12	0.09	PM	E	PM	PhS
EOH	1.17	0.10	I	I	I	I
DET	Desealed	0.65***	I	I	M	=
HEX	Torn	-0.01	I	I	M	=
HEP	Torn	0.14	I*	I	M	=
ISO	Torn	-0.06	I*	I	M	=
ISP	1.10	0.02	I	I	M	=
MET	0.12	-0.13	I	I	I	I
MAC	Torn	0.15	I*	I	M	=
MPY	Torn	-0.49	I	I	I	I
NME	-0.1	-0.34	I	I	I	I
OCT	Desealed	-0.11	I*	I	M	=
PEN	Torn	0.11	I*	I	M	=
1PR	1.22	0.18	I	I	PM	PhS
THF	Torn	0.26	I*	I	M	=
THP	Torn	0.08	I*	I	M	=
TOL	Torn	0.27	I	I	M	=

"I"=Immiscible, "M"=Miscible, "E"=Emulsion, "PM"=partially miscible, "PhS"=Phase Separation

*Divides in small droplets when mixing energically but droplets quickly coalesce always maintaining a defined interface

[a]Measured at maximum intensity wavelength (603 nm)

The measured absorbance changes can be caused not only by OFS swelling, but also to other factors. Swelling generally reduces the width of microfluidic channel (and therefore in the optical path), resulting in a higher signal detected by the spectrometer. Nonetheless, it can also generate deformation of the polymeric lenses altering the shape and alignment of the lenses with the optical axis and changing the focal points. This would negatively affect the light intensity reaching the spectrometer. In addition, possible surface modification of the microfluidic walls due to solvent etching could increase the defects, enhancing the roughness and therefore hampering the wall transmittance, which again would decrease the spectrometer signal. Here, the measurements done using PDMS as a structural material have to be understood for validation and comparative purposes, with the final aim of demonstrating the validity of the SU-8 OFS. Yet keeping these aspects in mind, the fact of finding a better transmission of light after 24 h immersion in the solvents for the chips which presented swelling (and were measurable), makes us consider that the most important factor which is affecting the absorbance measurements is the variation in the optical path caused by swelling. As lenses are bound to the substrate, stress generated by its binding to the rigid substrate minimizes the possible deformation due to swelling, which should be lower than in the channel walls due to the small quantity of building material that forms the lenses. These facts make the possible effect of lens deformation negligible in the measurements, in comparison with channel deformation. Surface modification due to solvent etching will be discussed below.

Micro- and nano-scale surface etching

SU-8 micropatterns exposed to each of the solvents did not present noticeable surface etching at the micro scale. All the patterned samples remained apparently unaltered after 24 h exposition to the corresponding solvents. To illustrate this observation Figure 9 shows as an example 2x2 µm square patterns corresponding to the samples immersed in pentane (fig 9a) and N,N-dimethylformamide (fig 9b) as representative solvents of low and high relative permittivity, respectively. All the samples were also measured in the x and y dimensions and measurements were compared with non-immersed samples looking for a possible remaining deformation due to swelling. No variation in the pattern dimensions was found, which is in clear agreement with the absorbance measurements.

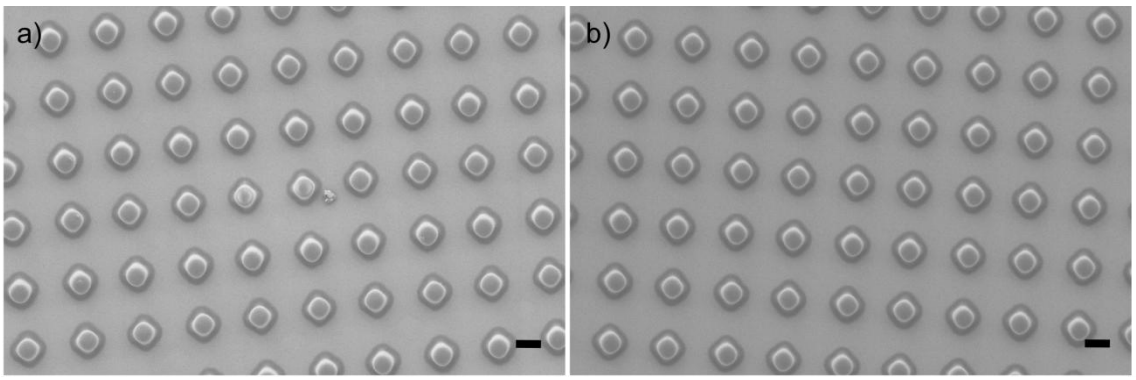

Figure 9. Illustrative SEM images of SU-8 micropatterns exposed to a) Pentane (PEN); b) N,N-Dimethylformamide (DMF). Scalebar – 2 µm. No signs of solvent attack were found for any of the patterns exposed to the 36 tested solvents.

While SEM observations and absorbance measurements have demonstrated that possible SU-8 etching (if it exists) should be within the studied wavelengths (as no variation in the spectra was observed), SUEX samples suffered obvious swelling, which caused the fracture of the samples for CLF, CLP, DCM, DMA, DMF, DMSO and MPY after 24 h etch. AFM roughness measurements over the rest of SUEX samples also revealed some roughness variation with respect to the reference samples. This difference observed between SUEX and SU-8 samples can be explained by the solvent etch of the polymer additives which are introduced in the SU-8 matrix to create SUEX dry films.

Table 3 shows the obtained R_a and R_q values (as defined in the experimental section) for all the SUEX samples, as well as the reference value calculated by an average of 3 independent measurements in a total of 10 SUEX reference samples, not exposed to any solvent. An important increase of roughness was found for SUEX samples attacked by CLB, CLH, CPN, DCE, NMF, HEP, 1PR and THF, revealing important dissolution at nano-scale. In contrast, small deviations with respect to the reference samples were found for those SUEX samples exposed to ACE, BUT, BNA, EOH, ISP and MAC. Roughness values measured for samples exposed to ETA, CAN, ACP, BZN, BGL, DET, HEX, ISO, MET, NME, OCT, PEN and TOL can be considered to be similar to reference value within the limits of experimental error. Finally measured values for DIE and THP were found to be slightly below, but very close to reference values. This observation suggests that probably a higher number of reference samples should have been considered for the estimation of the reference roughness value. Nevertheless, no roughness variation can be observed due to dissolution of SUEX exposed to DIE and THP.

Table 3. Measured values of Ra and Rq for the SUEX samples exposed to the different solvents

Solvent	**R_a (nm)**	**R_q (nm)**
Reference value	**0.49±0.04**	**0.61±0.06**
ACE	0.86 ± 0.09	1.06 ± 0.11
ETA	0.45 ± 0.12	0.56 ± 0.07
ACN	0.36 ± 0.14	0.73 ± 0.26
ACP	0.63 ± 0.15	0.81 ± 0.23
BZN	0.58 ± 0.21	0.76 ± 0.32
BUT	0.71 ± 0.11	0.92 ± 0.19
BNA	0.77 ± 0.05	0.98 ± 0.04
BGL	0.63 ± 0.12	0.81 ± 0.16
CLB	5.24 ± 2.27	6.50 ± 2.83
CLF	-	-
CLH	1.47 ± 0.36	1.89 ± 0.46
CLP	-	-
CPN	3.58 ± 2.10	4.35 ± 2.47
DCE	4.39 ± 0.34	5.47 ± 0.34
DIE	0.35 ± 0.07	0.44 ± 0.10
DCM	-	-
DMA	-	-
NMF	2.27 ± 0.89	2.93 ±1.24
DMF	-	-
DMSO	-	-
EOH	0.74 ± 0.11	0.93 ±0.14
DET	0.59 ± 0.10	0.75 ±0.13
HEX	0.38 ± 0.10	0.55 ±0.21
HEP	2.22 ± 0.38	3.22 ±0.84
ISO	0.39 ± 0.08	0.57 ±0.18
ISP	0.86 ± 0.09	1.09 ±0.12
MET	0.61 ± 0.14	0.76 ±0.16
MAC	0.98 ± 0.01	1.24 ±0.01
MPY	-	-
NME	0.48 ± 0.14	0.58 ±0.16
OCT	0.47 ± 0.08	0.61 ±0.12
PEN	0.39 ± 0.17	0.56 ±0.32
1PR	2.64 ± 0.99	3.22 ±1.27
THF	3.86 ± 0.59	4.82 ±0.77
THP	0.37 ± 0.02	0.49 ±0.04
TOL	0.58 ± 0.03	0.73 ±0.04

FC-70 and silicone oils compatibility

The miscibility test of FC-70 and silicone oils with all the studied organic solvents is summarized in Table 2. Fluorinert oil showed in general a better performance in contact with the different solvents than silicone oil. It was found to be immiscible with all of them, although it formed emulsions with DCE, DMSO and DMF. For some other cases, marked with a star (*) in the table, FC-70 separated into small droplets when mixed energically, but quickly coalesced again, always maintaining a well defined interface between oil and solvent. On the contrary, silicone oil was found to be miscible with most of the solvents, and immiscible just with 9 of 36 (ACN, ACP, DMA, NMF, DMF, EOH, MET, MPY and NME).

4. Conclusions

The use of SU-8 technology has been demonstrated as a low cost alternative to glass microfluidic systems for applications in organic chemistry. Here, poly(dimethylsiloxane) (PDMS) is not suitable due to its incompatibility with the commonly used organic solvents, which hampers its usability for studies ranging from active pharmaceutical ingredients to novel metal–organic frameworks. To validate this approach, an SU-8/SUEX based optofluidic system was designed, with the aim of providing optical and structural information regarding the compatibility of this material with 36 different organic solvents. Swelling quantification of the materials was obtained through the variation of the measured spectra across the system by using a white light source and a microspectrometer. PDMS swelling and lack of structural integrity were in accordance with previously reported observations, and it was not possible to measure the system after being immersed in most of the organic solvents (tearing or desealing occur). Conversely, SU-8/SUEX OFS showed a great robustness and mechanical stability against most of the tested solvents and no measurable swelling of the structures was optically detected. Solvent etch was also investigated at microscale by exposing a SU-8 micropattern to each solvent, and lastly analyzing its integrity by SEM observations.

SU-8 micropatterns exposed to each one of the solvents did not present noticeable surface corrosion at the micro scale. Finally, SUEX samples were also exposed to the solvents and surface modification was studied by roughness measurements performed by AFM. Important surface modifications were found for SUEX samples attacked by CLF, CLP, DCM, DMA, DMF, DMSO, MPY, CLB, CLH, DCE, NMF, HEP, 1PR and THF. Thus, the use of SU-8/SUEX systems with these solvents should be avoided or considered only for short periods of time, and not for a continuous use. In contrast, samples exposed to ACE, BUT, BNA, EOH, ISP and MAC displayed small roughness variations, and those samples exposed to ETA, CAN, ACP, BZN, BGL, DET, DIE, HEX, ISO, MET, NME, OCT, PEN, THP and TOL showed roughness values similar to the reference, within the experimental error. Therefore SU-8/SUEX systems can be safely used with these solvents, without expecting lack of structural integrity. In parallel, the compatibility of FC-70 and silicon oils with the same solvents has been tested. FC-70 was found to be compatible with all the tested solvents, except for DCE, DMF and DMSO. Silicon oil was found to be miscible and therefore not suitable with most of the solvents, except with ACN, ACP, DMA, NMF, DMF, EOH, MET, MPY and NME.

The results of this section have been recently submitted to:

- I. Rodríguez-Ruiz, A. Llobera, J. Vila-Planas, D. Johnson, J. Gómez-Morales, J. M. García-Ruiz. *Analysis of the structural integrity of SU-8 based optofluidic systems for small molecule crystallization studies.* Accepted in *Analytical Chemistry.*

Future perspectives

In this section we will describe a series of new tools for crystallization studies, developed during the last period of the project that involves the work presented somehow during the whole manuscript, but that *crystallized* in the last period. Although it has not been possible, up to now, to apply all the new developments to systems of interest, preliminary insights for some of them will be presented. For the rest of the devices described below, future experiments are programmed with the purpose of exploring their possibilities and capabilities. However, we consider its development as an important amount of work that is worthy of being presented by itself. The construction and design of an optofluidic flow reactor for cross-linked enzyme crystal catalyzed reactions and two droplet based optofluidic systems coupled to UV-Vis spectrometry for detection of nucleation events will be subsequently described. Nucleation in these systems can be triggered by direct mixing of reactant solutions, the use of precipitant agents, with the possible help of a plug factory to generate droplets, or by temperature variation. To use temperature as the variable to control the precipitation, a thermostatic peltier-based controller has been designed and constructed to host the optofluidic systems. More information about this hosting unit is described in the last subsection of this chapter.

Optofluidic flow reactor for cross-linked enzyme crystal catalyzed reactions

1. Cross-linked enzyme crystals

Biocatalysis allows the mild and selective formation of products using isolated enzymes. Compared with chemical methods biocatalysis shows excellent chemo-, regio- and stereoselectivity while retaining a small environmental footprint. Enzymes are widely applied in many different industries such as food processing (for human and animals)[76, 77], pharmaceuticals [78, 79], material processing (textiles, paper, detergents, etc.), waste treatment and also to produce biofuels [80, 81]. Similar level of development can be found in the application of enzymes in biosensor technologies [82, 83]. However, there are also drawbacks in enzyme-catalyzed reactions. They can exhibit a slow reaction rate, be unstable in practical operational conditions, their storage stability (or shelf life) can be poor, the downstream processing can be complex, the scale-up of enzymatic processes is often difficult, and the bulk supply of proteins is also often limited. On view of this, a major challenge in industrial biocatalysts is the development of stable, robust and preferably insoluble biocatalysts. These characteristics can generally be achieved by immobilization of the enzyme [84].

Enzyme immobilization [85-88] enhances biocatalytic processes due to their capacity to retain the activity or even to increase it; allows the recovering of the enzyme; augment the enzyme stability (vs. temperature, solvent nature, etc.), among other benefits. In spite of this, it is estimated that only a 20% of the biocatayitic processes involve immobilized enzymes. Traditionally there are three methods for enzyme immobilization: binding to a support (carrier), entrapment (encapsulation) and cross-linking. The first two can be grouped into the so called carrier-bound and the binding can be physical, ionic, or covalent in nature. However, physical bonding is generally too weak to keep the enzyme fixed to the carrier under industrial conditions of high reactant, product concentrations and high ionic strength. In this group the enzyme is immobilized or encapsulated with the help of polymers (silicon-based, typically alkyl-silane or poly-siloxane; epoxide; etc.) [85, 89], a solid support (cellulose, polyethyleneimine/sebacoyl

chloride, etc.) [90, 91], or a combination of both methodologies [85]. The use of a carrier inevitably suffers from dilution of volumetric and specific activities as carriers can account for 90% to >99% of the mass or volume of the catalyst, which results in lower space-time yields and productivities.

Hence, immobilization has only partially solved the problem of low enzyme activity for biotransformation in non-aqueous media. A second set of methodologies grouped as carrier-free has been developed to produce highly concentrated enzyme activity combined with high stability. Carrier-free are produced by cross-linking precipitated enzymes (aggregated or crystalline) by chemical means, typically using bidented ligands such as glutaraldehyde, aldehyde-dextran, hexametilendiisocianate, etc, to produce cross-linked enzyme crystals (CLECs) or cross-linked enzymes aggregates (CLEAs). Chemical cross-linking of enzyme crystals was first developed in the 1960's to stabilize enzyme crystals in order to facilitate the manipulation and X-ray crystallography data collection. However, it was soon recognized that cross-linked crystalline enzymes are catalytically active. Cross-linked enzyme crystals, or more generally cross-linked protein crystals (CLPCs), are created by the crystallization of the protein followed by a chemical cross-linking that "locks" the crystalline state outside the crystallization conditions. CLPCs can provide active, insoluble, mechanically robust, and micro-porous protein material under selected cross-linked conditions. CLPCs have been used as catalysts in various enzymatic production processes, as separation matrices and biosensors and as drug delivery vehicle [92-95].

Therefore, from the biocatalyst point of view carrier-free immobilized enzymes such as CLECs and CLEAs present numerous advantages versus carrier-bound or free enzyme: 10 to 1000 higher volumetric activities (U/g), higher stability against unnatural conditions (high temperature, organic solvents, etc.) and in particular cases higher selectivity. Although CLEAs are the easier and economical beneficial way to produce these highly active materials, they present two main disadvantages when compare with CLECs: the particle size and distribution are not controllable and they are not mechanically robust.

Crystallization is identified as the limiting step for the production of CLECs. In such environment, the main objective of the optofluidic device, described in this section, is to provide an unique platform for two subsequent steps: first, the production and immobilization of protein (enzyme) crystal that can be in situ cross-linked; and secondly, the use of the same device in which enzymes has been crystallized and cross-linked as a catalytic reactor for different biotechnological applications, monitored by UV-Vis spectroscopy.

2. Optofluidic reactor

A microfluidic flow reactor has been designed for performing crystallization and cross-linking of proteins and subsequently catalyzed reactions in presence of cross-linked enzyme crystals. A continuous UV-VIS detection system was designed and integrated along the flow reactor, enabling feedback control to optimize reactant conversion as a function of the input flow, increasing throughput in the system. This detection system also facilitates the measurement of kinetic parameters, allowing reaction kinetics to be obtained in situ, through molar absorptivity measurements. The great benefit of physically scaling down to microfluidic systems is not only a reduction in size and consumption of reactants, but rather an improvement of the analytical performance [62]. The global design of the optofluidic reactor (optical detection systems coupled to microfluidic devices) is shown in figure 10a and 10b and it can be explained by the sum of three components:

- Mixer: 3+1 Inputs permit the mixing of up to 3 different reactant solutions, while the 4th port is separated in two divergent channels for inserting a carrier immiscible fluid (oil) which downstream merges with the 3 solution channels. The use of an immiscible carrier fluid (if desired) converts the mixer in a plug factory, as described in the previous section. Subsequently, a passive zigzag mixer is also implemented in the design for homogenizing the mixtures. The effect of the passive mixer in the homogenization of reactant solutions

was characterized by an interferometry imaging experiment. A 0.5 M sodium citrate solution was mixed with pure water in the plug factory of an optofluidic system in order to provide enough contrast between mixing solutions (as a function of their refractive index) to be distinguished. Figure 11 shows an interferometric image of the mixing of the solutions and the zigzag homogenization channel. A clear mixing front is created between solution A (water) and solution B (sodium citrate), as depicted by red intermittent line in figures 11a, 11b and 11c, due to the laminar flow along the microfluidic channel. It can be noticed how the interferometric bands spread across the whole channel and become wider, diffusing the mixing front and revealing the homogenization of the solution along the zigzag channel.

- Detection Port: 3 pairs of fiber optics inserts (Figure 12c) are consecutively located in a channel at 3 different optical paths (channel width). This configuration offers the possibility of estimating the molar absorptivity of a substance by fitting the 3 obtainable measurements to a calibration curve.

- Droplet Storage: Finally a long serpentine channel allows the storing of thousands of droplets in each micro device. A trapping system was designed, permitting the location and storage of the droplets in a microwell array constructed over the main channel, but at a different high (figures 12d and 12e). Difference in fluid density allows carrier fluid to pass through the channel without disturbing the position of the droplets. Microchips with 200 µm and 500 µm width main channels (30 and 20 cm long), with droplet traps of 50x50 µm and 100x100 µm respectively, and 3 different heights (50, 100 and 200 µm) have been fabricated with the purpose of offering a wide range of possibilities for flow speed and droplet volume (from 125 pL to 2 nL) with the aim of lately optimizing the yield of the future reactions as a function of both parameters.

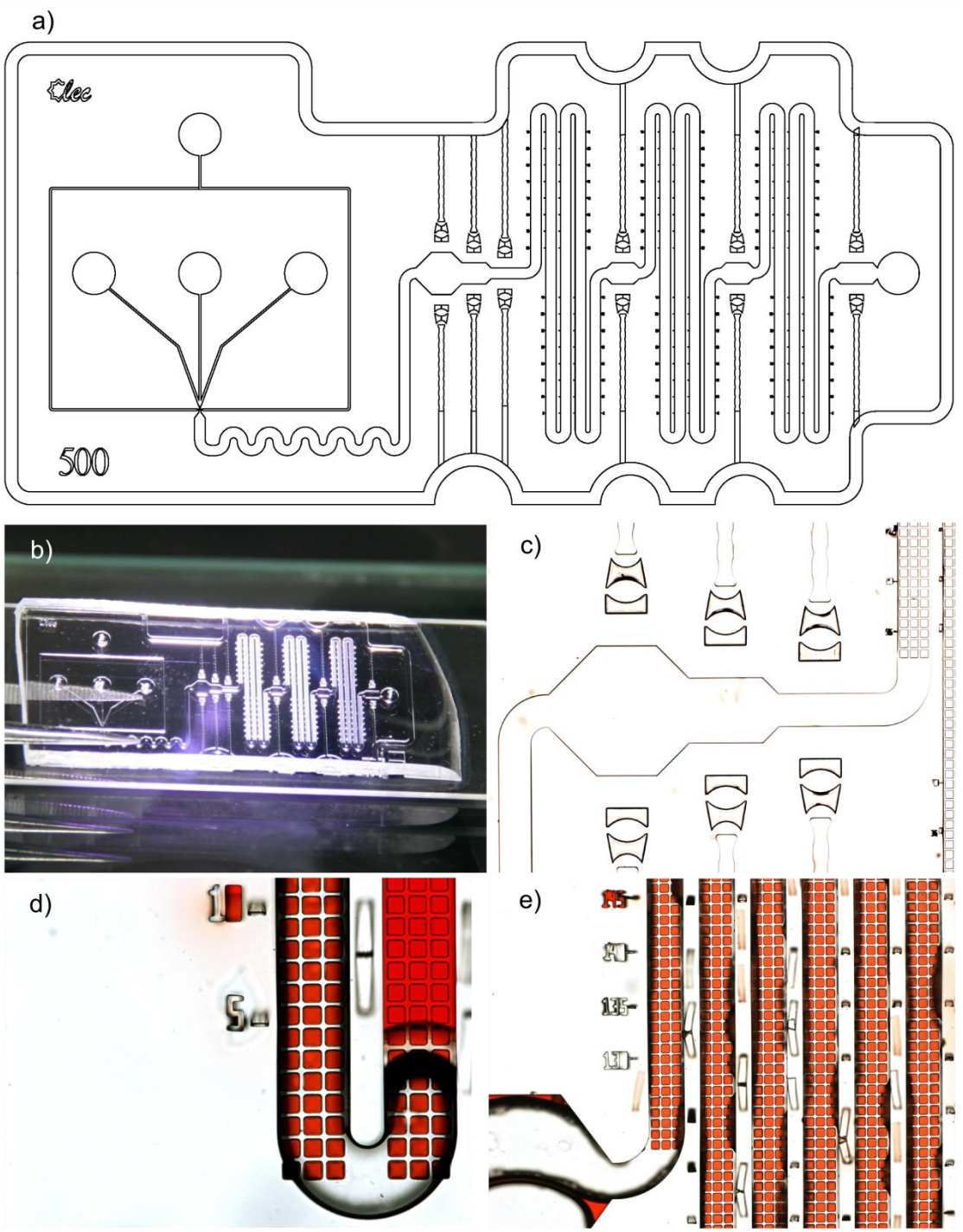

Figure 10. a) Scheme of a 500 µm width channel optofluidic reactor. Ports for optic fibers are distributed at equidistant lengths of the channel; b) Picture of the optofluidic microreactor manufactured in PDMS; c) Detail of the variation in the optical path of a 500 µm optofluidic reactor for molar absorptivity coefficient determination; d), e) Details of the microwell array. A colored solution is being pushed out of the main channel by a carrier fluid (FC-70 fluorinert oil).Droplets remain in the trapping system.

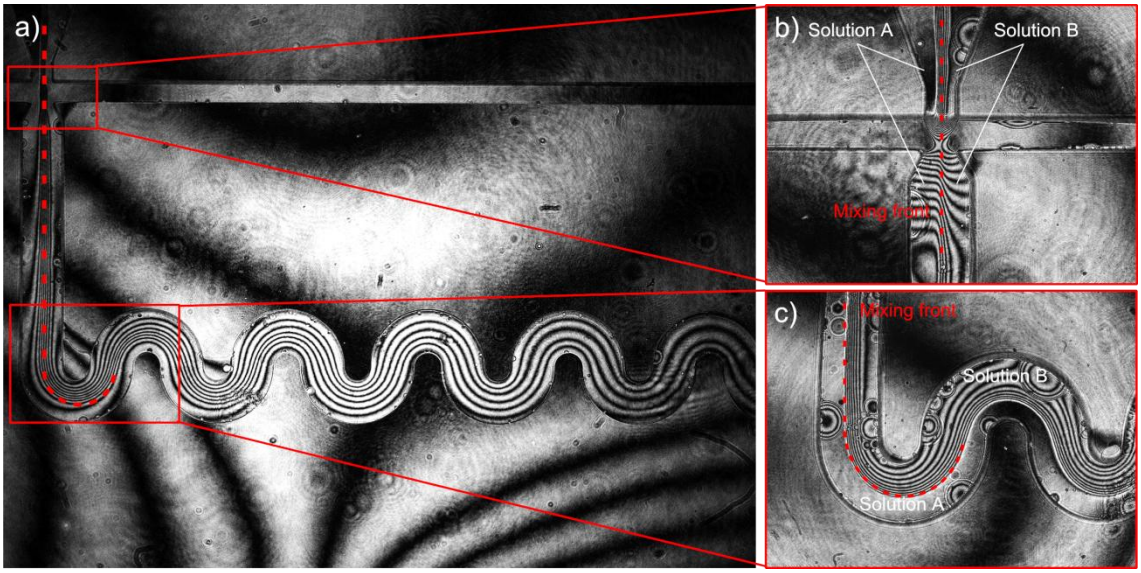

Figure 11. a) Interferometric image describing the homogenization of the mixing of solution A(water) and solution B (0.5 M sodium citrate) in the plug factory of an optofluidic system. b) and c) show details of the mixing front of both solutions in the first mixing instants (b) and at the beginning of the zigzag passive homogenization channel (c).

The strategy to crystallize proteins consists on coming across the optimal conditions where the protein solution can be displaced into a state of supersaturation followed by an equilibration process that favors minimal nucleation and optimal crystal growth. For the production of CLECs, some fine tune of the precipitant condition is needed to produce the desirable material while CLEAs can easily be generated if the set of conditions provoke a massive precipitation without affecting protein stability. There are a number of devices and procedures to bring a protein solution to a supersaturated state. One of the most common and successful method used to obtain protein crystals is the batch method [96, 97]. Batch crystallization entails the direct mixing of an undersaturated protein solution with a precipitant solution. Supersaturation is immediately achieved as the result of changes in protein solubility imposed by the precipitant solution. Consequently a crystalline solid state may form if the chemical and physical parameters were well selected. As the batch reaction is the most used method for the production of CLECs and CLEAS, the implementation of a mixer in our optofluidic system was considered to allow these batch reactions to be performed in order to achieve the supersaturation. Additionally, the scale down to microfluidics prevents inherent

buoyancy- driven convection during the crystal growth process due to solute depletion near the crystal surface and sedimentation in the crystal droplet [98]. Convection makes crystals grow in a heterogeneous environment compromising uniform growth and quality. This intrinsic effect of the techniques on protein crystal quality can be overcome by using a media in which mass transport is controlled by diffusion such microfluidic systems. Also a different implementation, usually called liquid-liquid diffusion or free-interface diffusion, has been considered to earn the advantage of a diffusive mass transport environment with the aim of reaching the critical supersaturation for nucleation very slowly, seeking for a single nucleation event [99, 100]. For this purpose, the microfluidic system is designed to operate in different modes: a) It can be loaded with a previously mixed metaestable solution containing protein and precipitant agent, (a red colored solution was used in figures 10d and 10e to illustrate this process). A second flow of immiscible inert oil removes solution from the channel while droplets of metaestable solution remain in the serpentine, locked in the trapping system (figure 10d) and ready to nucleate; It can also be filled up with a first flow of protein solution, and after the flow of inert oil, at last, a flow with a precipitant agent can get in contact with the trapped droplets, generating thousands of independent free-interface diffusion batch experiments; c) finally, for proteins with temperature dependent solubility, it is also possible to supersaturate a solution by a decrease of temperature with the help of a thermostated control, which will be described later, in the next subsection.

Once crystals of protein are obtained in the microwells by any of the previously described methods, a cross-linking agent solution can be introduced into the system, and once crystals are cross-linked, it is possible to introduce a continuous flow of reactant solution and follow the catalytic reaction by UV-Vis spectroscopy. For that purpose, fiber optics pairs are distributed at equidistant channel lengths allowing following the catalytic reactions in 3 different points of the reactor. Figure 12 shows a 3D representation of a light beam, inserted by a fiber optic, passing across one of the mentioned measurement points and collected by a second fiber optic that would connect to a micro spectrometer.

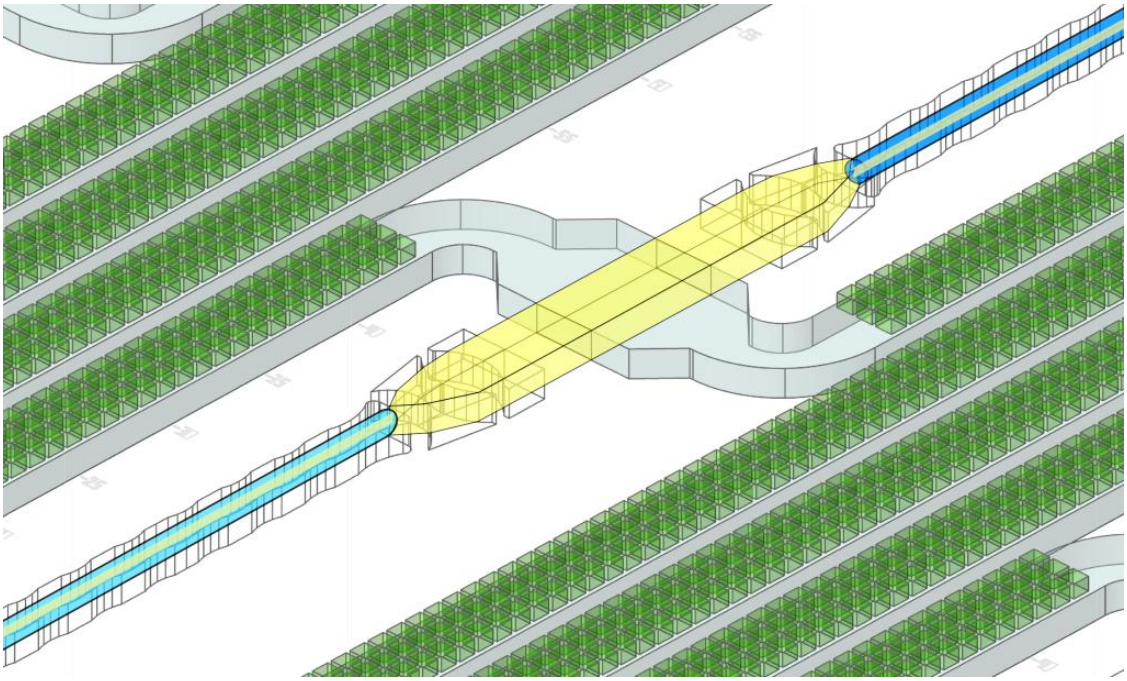

Figure 12. 3-D representation of a pair of fiber optics in the optofluidic reactor.

The application of the designed reactor is being first tested with a model protein, lysozyme, in order to develop and validate a reliable methodology for its application in other high added value products. Lysozyme catalyzes the hydrolysis of 4-methylumbelliferyl N,N',N''-triacetyl-b-chitotrioside ((GlcNAc)3-MeU,). The release of 4-methylumbelliferone can be followed by fluorescence measurements [101]. The catalytic hydrolyzation of (GlcNAc)3-MeU in presence of lysozyme crystals will be monitored through the fiber optics measurements of intensity emitted at 450 nm, using a 360 nm laser as the excitation light source. At the moment, the experiment of crystallization of lysozyme in the optofluidic system, as well as the subsequent cross-linking process has been succesfully performed. Figure 13 shows images of the lysozyme crystals precipitated in the microwell array of a 500 µm channel width reactor (figure 13 a-b), and its cross-linking (figure 13c-d), showing the typical groove marks and darkened colour of CLEC's, and remaining stable out of solution, in contact with air.

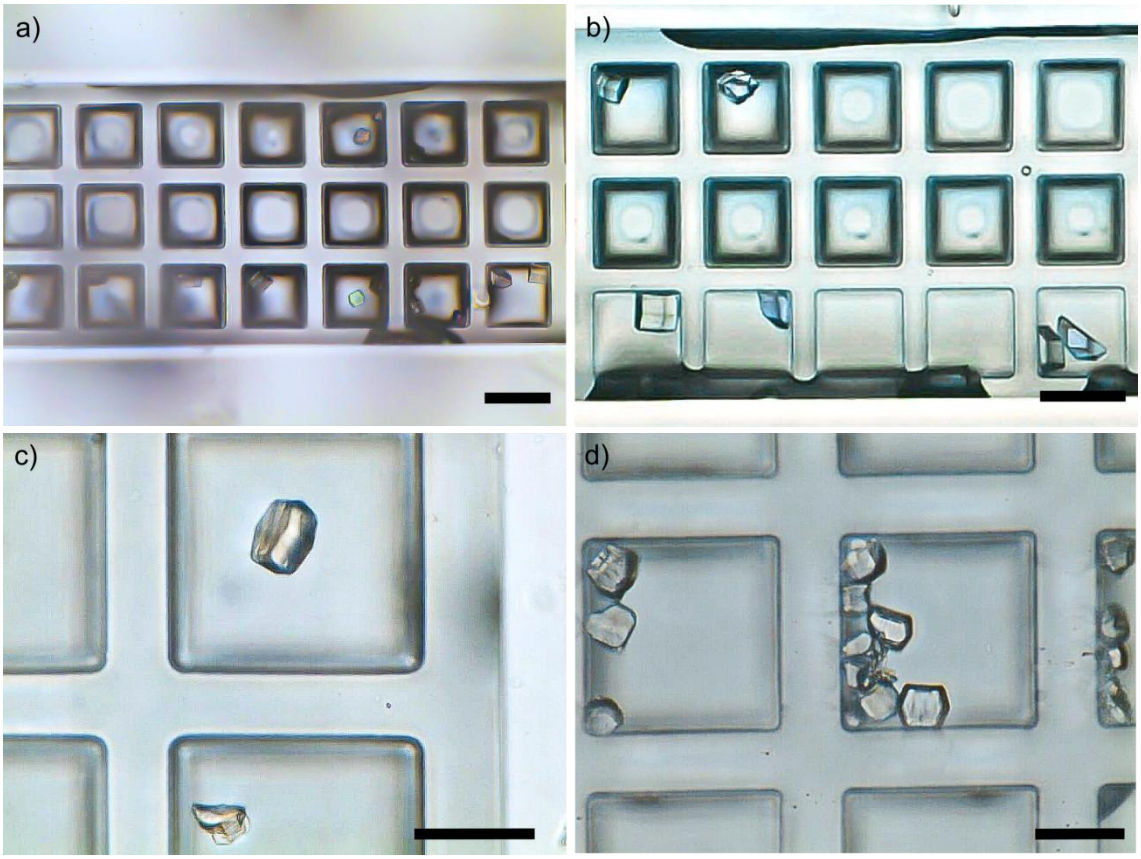

Figure 13. a,b) Lyzozyme crystals precipitated in a 500 µm channel width microfluidic reactor from a solution containing 15 mg/ml lyzozyme and 5% NaCl (0.1 % Triton X surfactant). Scale bars = 100 µm; c),d) crosslinked lysozyme crystals in the same reactor, after 5 min contact with a 5 % glutaraldehyde solution. Scale bars = 50 µm.

Subsequently, a second protein, formidase from *Bacillus cereus* CECT5050, will be cross-linked and crystallized in the optofluidic reactor. This enzyme catalyzes the conversion of formamide to formic acid liberating ammonia in the media, which can be followed spectrophotometrically, making this enzymatic reaction of interest for our purposes. Figure 13 shows the schematic reaction of formamide to formic acid, in presence of CECT5050.

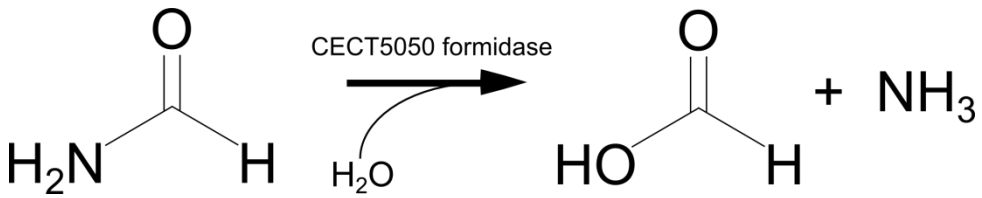

Figure 13. Catalytic conversion of formamide in the presence of CECT5050 formidase.

Finally, the enzymatic activity of lipase B (from *Candida Antarctica*), which is interesting for the production of biodiesel, will be quantified by the hydrolysis of p-Nitrophenyl butyrate, for the production of p-Nitrophenol. Figure 14 presents the chemical structure of p-Nitrophenyl butyrate and p-Nitrophenol in a schematic representation of the catalytic reaction. While p-Nitrophenyl butyrate is colorless, the catalytically produced amounts of 4-nitrophenol can be measured with a spectrophotometer at 415 nm.

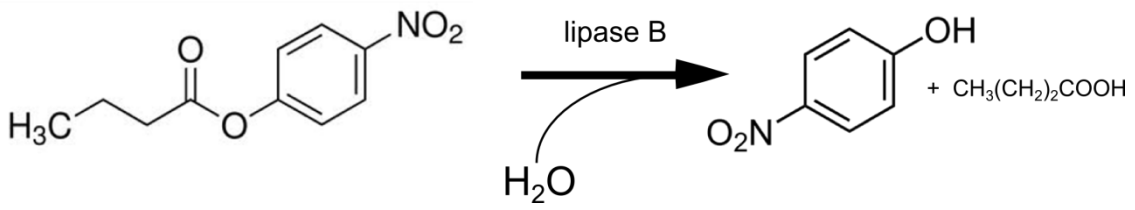

Figure 14. Catalytic hydrolysis of Nitrophenyl butyrate for the production of p-Nytrophenol in the presence of lipase B.

It is worth considering the interest of using lipase b, as well as other enzymes not only in aqueous media, but also with non-polar solvents. It has been known for some time that a variety of enzymes are catalytically active in apolar media, even presenting higher activity rates than in water media [102]. Some of these enzymes have been used for the transformation of water-insoluble substrates [103] (such as the transesterification of fats) and for peptide synthesis via reversal of the hydrolytic process [104]. Therefore, the next step for optimizing the versatility and applicability of our optofluidic reactor will be its fabrication with solvent resistant materials (SU8), which would permit the study and performance of organic solvent-mediated catalytic reactions for water insoluble substrates.

Plug-based optofluidic systems for the study of small molecule crystallization

The use of SU-8 based optofluidic systems for its use in organic chemistry applications has been studied and discussed along the first section of this chapter and, as commented at the end of the last section, it would have a special interest for the study of organic solvent-mediated enzymatic catalytic reactions. Additionally, crystallization from solution is a common process for the purification, separation, and control of polymorphism of pharmaceuticals, pigments, and other specialty compounds which are poorly soluble or not soluble in water. The supersaturation level is the driving force of the crystallization process and it has effects on the physic-chemical properties of the crystallized product (nucleating phase, morphology, size distribution, etc). Consequently, these physic-chemical properties are intrinsically related to the solubility of the solid phase in the solvent, and therefore, the use of different solvents could lead to precipitates with different properties, each one of them with important economic and medical interests from the pharmaceutical point of view.

Taking advantage of the chemical resistance of SU-8 based materials, which has been already demonstrated, different optofluidic systems have been developed and manufactured, following the same procedure described in the first section of this chapter, with the purpose of providing new tools and methodologies for the study of small molecule crystallization. Two plug based microfluidic systems have been designed with the purpose of performing crystallization studies for organic molecules, by monitoring nucleation using spectroscopy as a detection method. The first system was designed with 3 + 1 fluidic input 100 µm channels which merge into a single and wider one to generate a plug factory for droplet generation [5, 105-108]. Inputs permit the mixing of up to 3 different reactant solutions, while the fourth port is separated in two divergent channels for inserting a carrier immiscible fluid (oil) which downstream merges with the 3 solution channels for generating the droplets by “tweezing” the reactant solution. Subsequently, and due to the laminar flow and absence of convective forces existing at microfluidic scale [1, 2], a passive zigzag mixer is implemented in the design [3, 5, 105], allowing the fast homogenization of the droplets by constantly changing its flow direction. Schemes of

the whole system, the plug factory with the mixer, and a detail of a fiber optics insert, designed as previously explained in the preceding section, are depicted in Figure 15a.

With the purpose of providing a tunable detection system for nucleation, four different points for UV-Vis measurements have been positioned along the microfluidic channel. Droplets flow along the microfluidic channel at a speed and separation controlled by the velocity of the input flows and the solution/oil ratio respectively. First measurement position can be considered as a time = t_0 measurement, immediately after generation and mixing of the droplets. By coupling a light source and a micro-spectrophotometer at the end of the inserted fiber optics, Ocean Optics SpectraSuite^{TM} software captures the transmitted UV-Vis spectra in an interval up to 30 milliseconds, permitting the registration of the transmitted light spectra for each droplet passing across the light beam. The position of the fiber optics and the capture of the transmitted light allow absorbance measurements (absorption of light at a determined wavelength) and turbidimetry measurements as well (variation of intensity of the incoming light). After a determined length of microfluidic channel, which is periodically repeated, fiber optic inserts permit the measurement of the droplets at a time $t_0+\tau$, $t_0+2\tau$ and $t_0+3\tau$ respectively, being the value of τ tunable as a function of the input flows. This configuration allows online and continuous measurements for the detection of nucleated droplets for a determined time, and therefore allows determining nucleation frequency. The main interest of this system is the capability of working with a very small quantity of reactants, producing thousands of experiments which lead to very good statistical treatment of the data for obtaining a meaningful nucleation frequency value [11]. Representative SEM images of a SU-8 system are shown in figure 16. Figure 16a and 16 b illustrate the plug factory and the passive mixer, respectively. Figures 16c and 16d show the positioning of a pair of SU-8 lenses across a 100 μm width microfluidic channel.

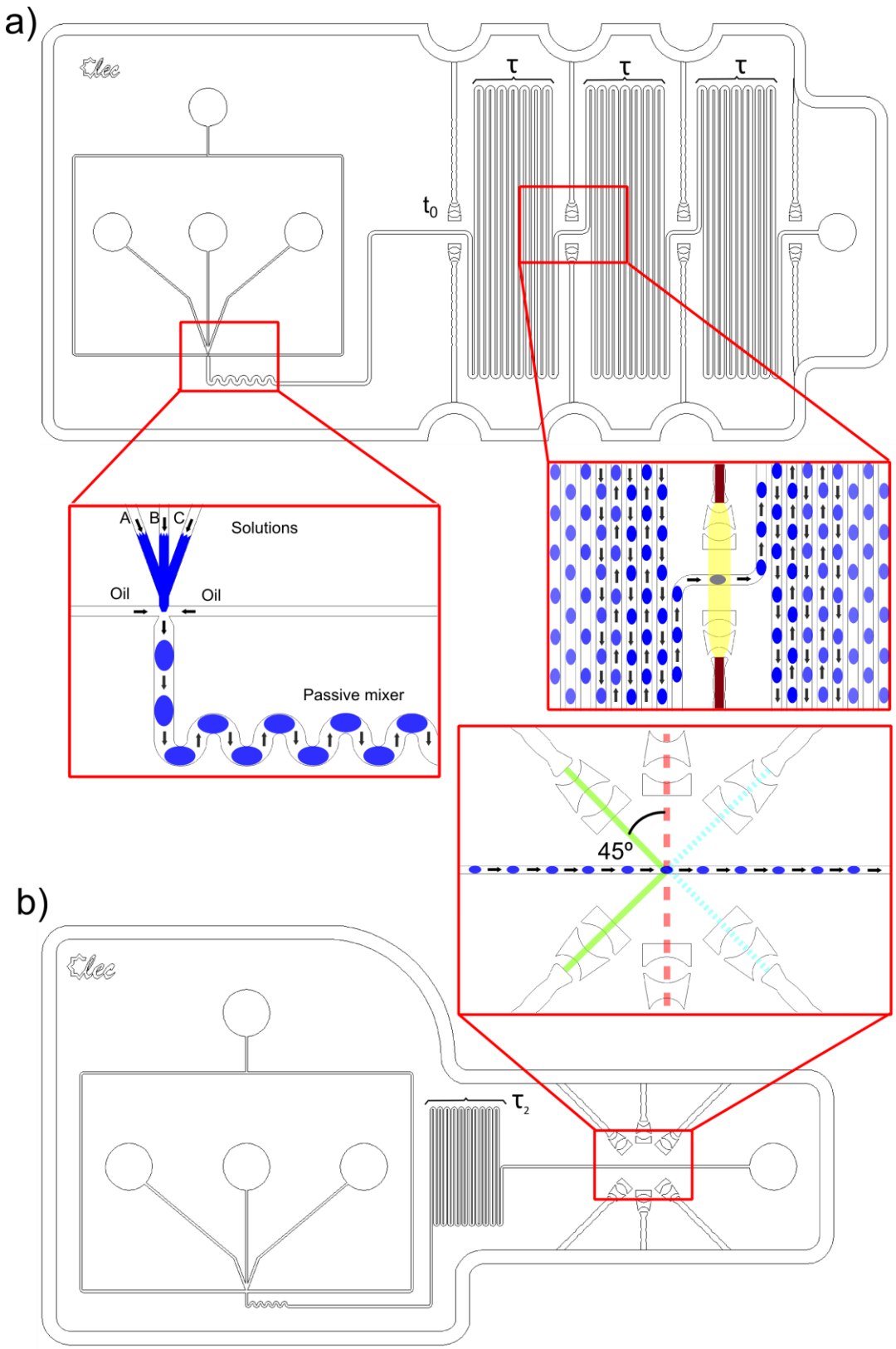

Figure 15. a) Optofluidic system developed for on line crystallization studies through spectrometry measurements. Details of the plug factory and a fiber optics insert for absorbance/turbidimetry measurements; b) Optofluidic system developed for the study of nucleation by light scattering measurements. Inset shows the magnification of the fiber optics configuration, allowing scattering measurements at 45, 90, and 135 ˚ .

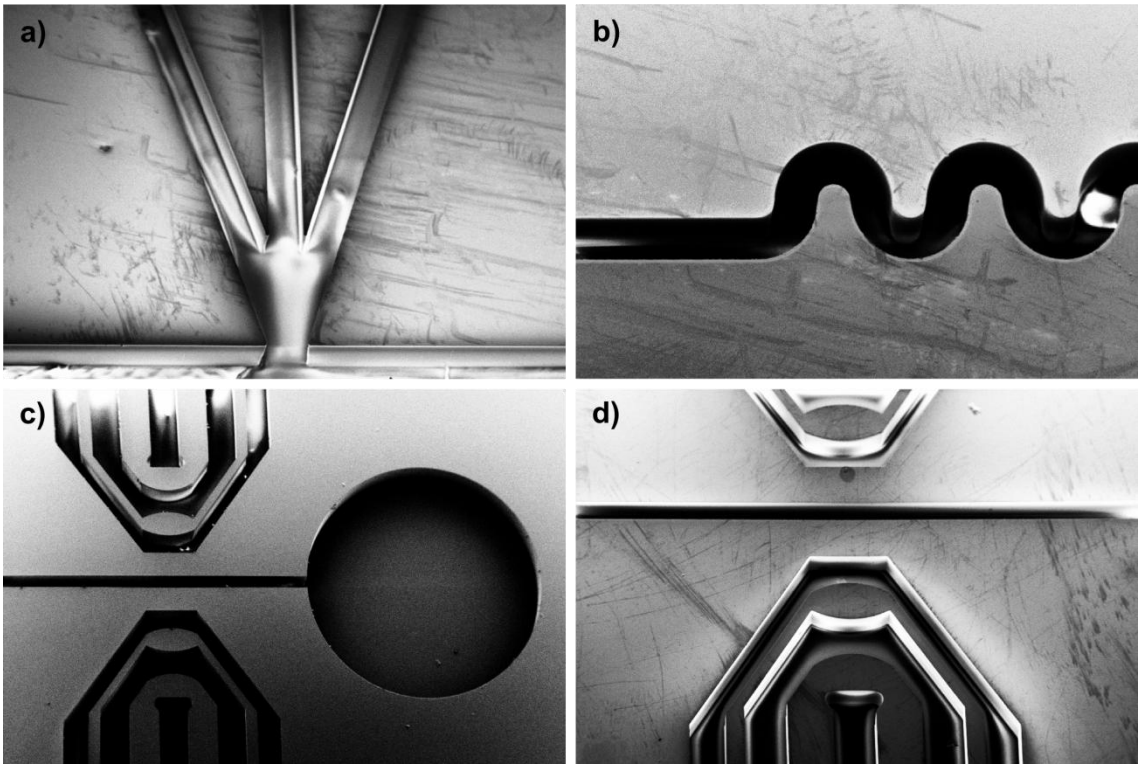

Figure 16. a) Detail of the plug factory for droplet generation. Channel width = 100 μm; b) passive 100 μm channel mixer; c) and d) positioning of a pair of SU-8 lenses across a 100 μm width microfluidic channel.

A second plug based system has also been designed with the purpose of implementing light scattering measurements in small volumes. In this case, and due to the special configuration required for the fiber optics positioning, only one measurement point has been considered, after a determined channel length, which is transduced in a residence time τ, tunable as a function of the input flows, as well. A scheme of this system is presented in figure 15b. As it can be observed in the inset of the figure, a "star" configuration of the fiber optics permit not only absorbance/turbidimetry measurements, but also 45°, 90° and 135° light scattering measurements.

"Plug and play" thermostated control for optofluidic devices

One of the most significant drawbacks of microfluidic systems is assuring a robust connection of the i/o flows, stable and without leakages. A precise control in the flows and connections allows a higher accuracy in the mixing and flow speed estimations, which are important in our case for correctly determining supersaturations and nucleation frequencies while carrying out experiments. With the aim of providing a useful tool for connecting our optofluidic systems, a hosting which allows the direct connection of the microfluidic ports to standard tubing has been designed. All of our optofluidic systems were normalized to a standard size with localized i/o ports, in order to correctly fit in an unique hosting system. Figure 17 shows a schematic representation of the main components of the hosting unit. It incorporates a peltier based thermostatic control with two independent areas, for setting and independently controlling temperature in the mixing and storing/analyzing areas of the optofluidic systems (figures 17b and 17c). Peltiers are refrigerated by a water cooling system (figure 17a), in order to be able to reach ΔTs higher than 20 $^{\circ}$C with respect to room temperature. The temperature control is performed through the use of two temperature sensors (one for each peltier element), located over the optofluidic systems (figure 17f in green), and connected to a PID controller. Temperature can be settled with the help of a commercial program with a stability of ± 0.01 $^{\circ}$C and a precision of ± 0.1 $^{\circ}$C. Respecting to the fluidic ports, inputs were designed for screwing standard tubing connections (figure 17g, blue circles), and 500 µm fluidic channels (figure 17f, magenta) conduct the flows to the system i/o ports. Channels were designed with the same total length in order to avoid pressure losses/variations for the incoming flows, and they end in a connection plug that fits with precision over the optofluidic systems (figure 17g, red circles), sealing by pressure when closing the hosting unit. In order to have a correct positioning to facilitate its connection, a location gap is designed with the precise standard dimensions of the systems (figures 17d and 17e).

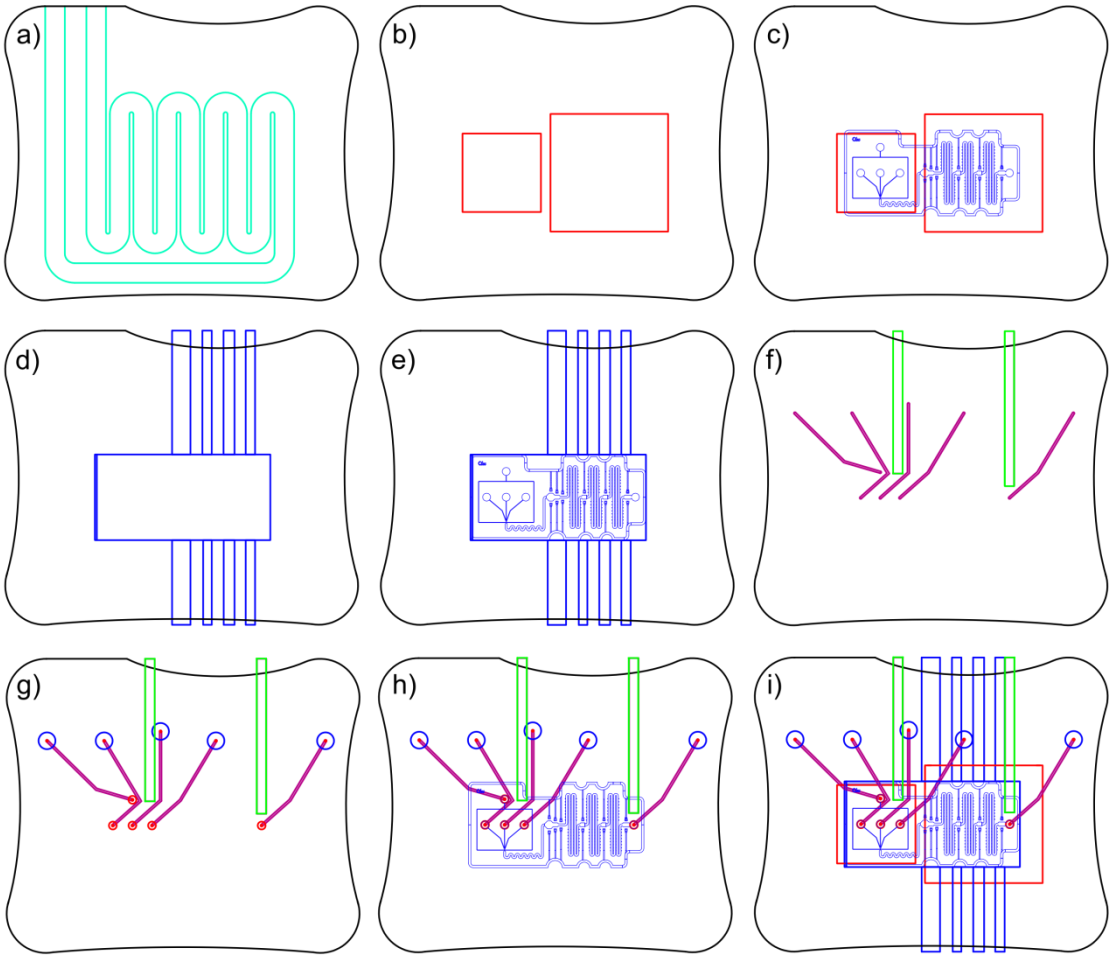

Figure 17. Different layers composing the "plug and play" hosting for optofluidic systems. a) refrigeration circuit for the peltier elements, which permit reaching ΔTs higher than 20 $^{\circ}$C with respect to room temperature; b), c) two peltier elements which allow independent temperature control for the plug factory/mixing area and the storing/analyzing area of the systems; d), e) location gap for a correct positioning of the optofluidic systems. It includes oriented channels for fiber optics insertion; f), g) h). Temperature sensors (green) for independently controlling temperature in the mixing and storing areas and 500 um channels (magenta) for connecting the i/o ports of the optofluidic systems. Channels are designed with the same total length in order to avoid pressure losses/variations for the incoming flows.

A first prototype has been fabricated in polymetyl metacrilate (PMMA) and aluminum and is shown in figure 18.

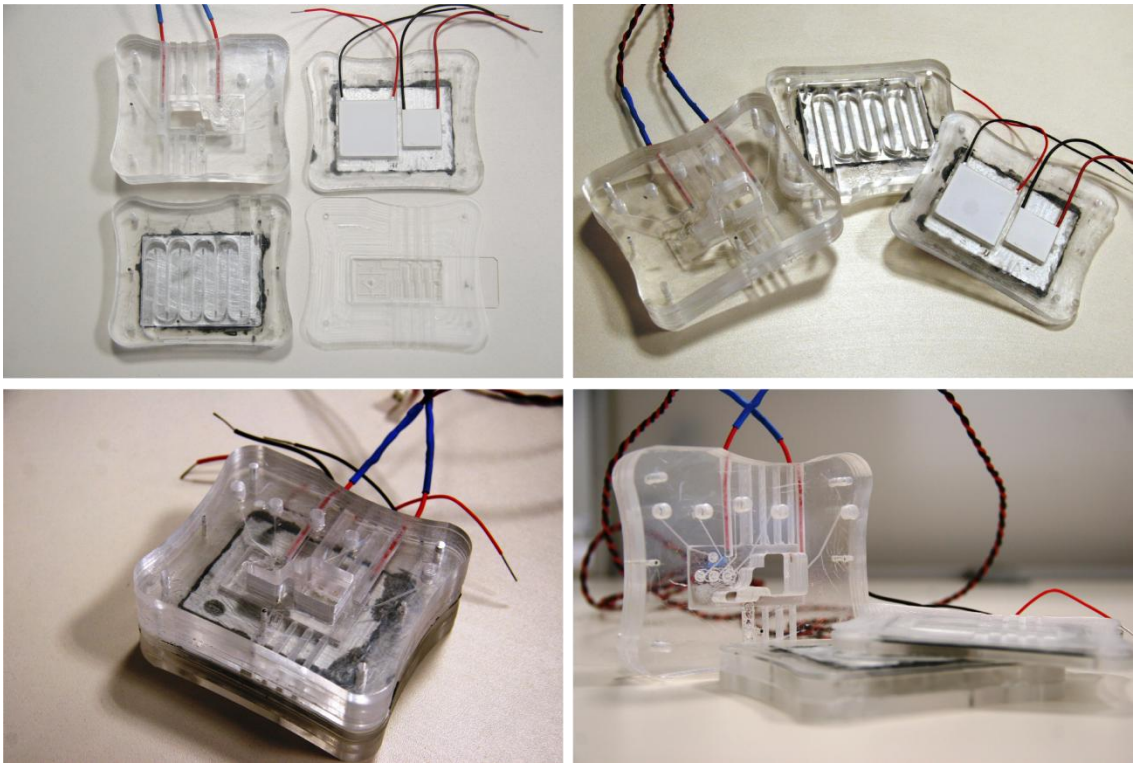

Figure 18. Different pictures of the first thermal control/hosting unit prototype, made of PMMA and aluminum.

Some of the technological developments presented in this section are in patent process

References

1. Bird R, Stewart W, Lightfoot E. Transport phenomena. 2nd. New York: John Wiley & Sons; 2002.

2. Bringer MR, Gerdts CJ, Song H, Tice JD, Ismagilov RF. Microfluidic systems for chemical kinetics that rely on chaotic mixing in droplets. Philos Trans R Soc London, Ser A. 2004;362(1818):1087-104.

3. Tung K-Y, Li C-C, Yang J-T. Mixing and hydrodynamic analysis of a droplet in a planar serpentine micromixer. Microfluid Nanofluid. 2009;7(4):545-57.

4. Yashina A, Meldrum F, Demello A. Calcium carbonate polymorph control using droplet-based microfluidics. Biomicrofluidics. 2012;6(2):22001-2200110.

5. Zheng B, Gerdts CJ, Ismagilov RF. Using nanoliter plugs in microfluidics to facilitate and understand protein crystallization. Curr Opin Struct Biol. 2005;15(5):548-55.

6. Theberge AB, Courtois F, Schaerli Y, Fischlechner M, Abell C, Hollfelder F, et al. Microdroplets in microfluidics: an evolving platform for discoveries in chemistry and biology. Angew Chem Int Ed. 2010;49(34):5846-68.

7. Vyawahare S, Griffiths AD, Merten CA. Miniaturization and Parallelization of Biological and Chemical Assays in Microfluidic Devices. Chem Biol. 2010;17(10):1052-65.

8. Seo M, Nie Z, Xu S, Mok M, Lewis PC, Graham R, et al. Continuous Microfluidic Reactors for Polymer Particles. Langmuir. 2005;21(25):11614-22.

9. Dendukuri D, Doyle PS. The Synthesis and Assembly of Polymeric Microparticles Using Microfluidics. Adv Mater. 2009;21(41):4071-86.

10. Li L, Mustafi D, Fu Q, Tereshko V, Chen DL, Tice JD, et al. Nanoliter microfluidic hybrid method for simultaneous screening and optimization validated with crystallization of membrane proteins. PNAS. 2006;103(51):19243-8.

11. Teychené S, Biscans B. Microfluidic Device for the Crystallization of Organic Molecules in Organic Solvents. Cryst Growth Des. 2011;11(11):4810-8.

12. Ildefonso M, Candoni N, Veesler S. A Cheap, Easy Microfluidic Crystallization Device Ensuring Universal Solvent Compatibility. Org Process Res Dev. 2012;16(4):556-60.

13. Effenhauser CS, Bruin GJM, Paulus A, Ehrat M. Integrated Capillary Electrophoresis on Flexible Silicone Microdevices: Analysis of DNA Restriction Fragments and Detection of Single DNA Molecules on Microchips. Anal Chem. 1997;69(17):3451-7.

14. Anderson JR, Chiu DT, Wu H, Schueller OJ, Whitesides GM. Fabrication of microfluidic systems in poly (dimethylsiloxane). Electrophoresis. 2000;21:27-40.

15. Leng J, Salmon J-B. Microfluidic crystallization. Lab Chip. 2009;9(1):24-34.

16. Zheng B, Tice JD, Roach LS, Ismagilov RF. A Droplet-Based, Composite PDMS/Glass Capillary Microfluidic System for Evaluating Protein Crystallization Conditions by Microbatch and Vapor-Diffusion Methods with On-Chip X-Ray Diffraction. Angew Chem Int Ed. 2004;43(19):2508-11.

17. Duffy DC, McDonald JC, Schueller OJ, Whitesides GM. Rapid Prototyping of Microfluidic Systems in Poly(dimethylsiloxane). Anal Chem. 1998;70(23):4974-84.

18. Dhouib K, Khan Malek C, Pfleging W, Gauthier-Manuel B, Duffait R, Thuillier G, et al. Microfluidic chips for the crystallization of biomacromolecules by counter-diffusion and on-chip crystal X-ray analysis. Lab Chip. 2009;9(10):1412-21.

19. Zhang Q, Zeng S, Qin J, Lin B. Microfluidic droplet trapping array as nanoliter reactors for gas–liquid chemical reaction. Electrophoresis. 2009;30(18):3181-8.

20. Shim J-u, Patil SN, Hodgkinson JT, Bowden SD, Spring DR, Welch M, et al. Controlling the contents of microdroplets by exploiting the permeability of PDMS. Lab Chip. 2011;11(6):1132-7.

21. Yin H, Ji B, Dobson PS, Mosbahi K, Glidle A, Gadegaard N, et al. Screening of Biomineralization Using Microfluidics. Anal Chem. 2008;81(1):473-8.

22. Sia SK, Whitesides GM. Microfluidic devices fabricated in Poly(dimethylsiloxane) for biological studies. Electrophoresis. 2003;24(21):3563-76.

23. Holden MA, Kumar S, Beskok A, Cremer PS. Microfluidic diffusion diluter: bulging of PDMS microchannels under pressure-driven flow. J Micromech Microeng. 2003;13(3):412.

24. Gervais T, El-Ali J, Gunther A, Jensen KF. Flow-induced deformation of shallow microfluidic channels. Lab Chip. 2006;6(4):500-7.

25. Lee JN, Park C, Whitesides GM. Solvent Compatibility of Poly(dimethylsiloxane)-Based Microfluidic Devices. Anal Chem. 2003;75(23):6544-54.

26. Lee J, Joon Kim M, Lee HH. Surface modification of poly(dimethylsiloxane) for retarding swelling in organic solvents. Langmuir. 2006;22(5):2090-5.

27. Toepke MW, Beebe DJ. PDMS absorption of small molecules and consequences in microfluidic applications. Lab Chip. 2006;6(12):1484-6.

28. Yakovleva J, Davidsson R, Lobanova A, Bengtsson M, Eremin S, Laurell T, et al. Microfluidic enzyme immunoassay using silicon microchip with immobilized antibodies and chemiluminescence detection. Anal Chem. 2002;74(13):2994-3004.

29. Oehrlein GS. Reactive-Ion Etching. Phys Today. 1986;39:26.

30. Shimbo M, Furukawa K, Fukuda K, Tanzawa K. Silicon-to-silicon direct bonding method. J Appl Phys. 1986;60(8):2987-9.

31. Albaugh KB, Cade PE, Rasmussen D, editors. Mechanisms of anodic bonding of silicon to pyrex glass. Solid-State Sensor and Actuator Workshop, 1988 Technical Digest, IEEE; 1988: IEEE.

32. Harris NR, Hill M, Beeby S, Shen Y, White NM, Hawkes JJ, et al. A silicon microfluidic ultrasonic separator. Sens Actuators, B. 2003;95(1–3):425-34.

33. Lin Y, Gerfen GJ, Rousseau DL, Yeh S-R. Ultrafast microfluidic mixer and freeze-quenching device. Anal Chem. 2003;75(20):5381-6.

34. Sanjoh A, Tsukihara T. Spatiotemporal protein crystal growth studies using microfluidic silicon devices. J Cryst Growth. 1999;196(2):691-702.

35. Becker H, Arundell M, Harnisch A, Hülsenberg D. Chemical analysis in photostructurable glass chips. Sens Actuators, B. 2002;86(2–3):271-9.

36. Mellors J, Gorbounov V, Ramsey R, Ramsey J. Fully integrated glass microfluidic device for performing high-efficiency capillary electrophoresis and electrospray ionization mass spectrometry. Anal Chem. 2008;80(18):6881-7.

37. Jia Z-J, Fang Q, Fang Z-L. Bonding of glass microfluidic chips at room temperatures. Anal Chem. 2004;76(18):5597-602.

38. Xuefeng Y, Hong S, Zhaolun F. A Simplified Microfabrication Technology for Production of Glass Microfluidic Chips. Chin J Anal Chem. 2003;31(1):116-9.

39. Kikutani Y, Horiuchi T, Uchiyama K, Hisamoto H, Tokeshi M, Kitamori T. Glass microchip with three-dimensional microchannel network for 2 [times] 2 parallel synthesis. Lab Chip. 2002;2(4):188-92.

40. Garcia-Egido E, Spikmans V, Wong SYF, Warrington BH. Synthesis and analysis of combinatorial libraries performed in an automated micro reactor system. Lab Chip. 2003;3(2):73-6.

41. Liu X, Du D, Mourou G. Laser ablation and micromachining with ultrashort laser pulses. IEEE J Quantum Electron. 1997;33(10):1706-16.

42. Becker H, Dietz W, Dannberg P. Microfluidic Manifolds by Polymer Hot Embossing for μ-Tas Applications. In: Harrison DJ, Berg A, editors. Micro Total Analysis Systems '98: Springer Netherlands; 1998. p. 253-6.

43. McCormick RM, Nelson RJ, Alonso-Amigo MG, Benvegnu DJ, Hooper HH. Microchannel electrophoretic separations of DNA in injection-molded plastic substrates. Anal Chem. 1997;69(14):2626-30.

44. Xu J, Locascio L, Gaitan M, Lee CS. Room-temperature imprinting method for plastic microchannel fabrication. Anal Chem. 2000;72(8):1930-3.

45. Attia U, Marson S, Alcock J. Micro-injection moulding of polymer microfluidic devices. Microfluid Nanofluid. 2009;7(1):1-28.

46. Martynova L, Locascio LE, Gaitan M, Kramer GW, Christensen RG, MacCrehan WA. Fabrication of Plastic Microfluid Channels by Imprinting Methods. Anal Chem. 1997;69(23):4783-9.

47. Becker H, Locascio LE. Polymer microfluidic devices. Talanta. 2002;56(2):267-87.

48. Lorenz H, Despont M, Fahrni N, LaBianca N, Renaud P, Vettiger P. SU-8: a low-cost negative resist for MEMS. J Micromech Microeng. 1997;7(3):121.

49. Lorenz H, Despont M, Fahrni N, Brugger J, Vettiger P, Renaud P. High-aspect-ratio, ultrathick, negative-tone near-UV photoresist and its applications for MEMS. Sens Actuators, A. 1998;64(1):33-9.

50. Shaw JM, Gelorme JD, LaBianca NC, Conley WE, Holmes SJ. Negative photoresists for optical lithography. IBM J Res Dev. 1997;41(1.2):81-94.

51. Llobera A, Seidemann V, Plaza JA, Cadarso VJ, Buttgenbach S. SU-8 optical accelerometers. J Microelectromech Syst. 2007;16(1):111-21.

52. Martin-Olmos C, Villanueva LG, van der Wal PD, Llobera A, de Rooij NF, Brugger J, et al. Conductivity of SU-8 Thin Films through Atomic Force Microscopy Nano-Patterning. Adv Funct Mater. 2012;22(7):1482-8.

53. Nordström M, Keller S, Lillemose M, Johansson A, Dohn S, Haefliger D, et al. SU-8 cantilevers for bio/chemical sensing; fabrication, characterisation and development of novel read-out methods. Sensors. 2008;8(3):1595-612.

54. Luo C, Govindaraju A, Garra J, Schneider T, White R, Currie J, et al. Releasing SU-8 structures using polystyrene as a sacrificial material. Sens Actuators, A. 2004;114(1):123-8.

55. Abgrall P, Conedera V, Camon H, Gue A-M, Nguyen N-T. SU-8 as a structural material for labs-on-chips and microelectromechanical systems. Electrophoresis. 2007;28(24):4539-51.

56. Lee KY, LaBianca N, Rishton SA, Zolgharnain S, Gelorme JD, Shaw J, et al., editors. Micromachining applications of a high resolution ultrathick photoresist. 1995: AVS.

57. L'Hostis E, Michel PE, Fiaccabrino GC, Strike DJ, de Rooij NF, Koudelka-Hep M. Microreactor and electrochemical detectors fabricated using Si and EPON SU-8. Sens Actuators, B. 2000;64(1):156-62.

58. Ayliffe HE, Bruno Frazier A, Rabbitt RD. Electric impedance spectroscopy using microchannels with integrated metal electrodes. J Microelectromech Syst. 1999;8(1):50-7.

59. Guerin LJ, Bossel M, Demierre M, Calmes S, Renaud P, editors. Simple and low cost fabrication of embedded micro-channels by using a new thick-film photoplastic. Solid State Sensors and Actuators, 1997 TRANSDUCERS '97 Chicago, 1997 International Conference on; 1997 16-19 Jun 1997.

60. Renaud P, Lintel H, Heuschkel M, Guérin L. Photo-Polymer Microchannel Technologies and Applications. In: Harrison DJ, Berg A, editors. Micro Total Analysis Systems '98: Springer Netherlands; 1998. p. 17-22.

61. Reyes DR, Iossifidis D, Auroux P-A, Manz A. Micro total analysis systems. 1. Introduction, theory, and technology. Anal Chem. 2002;74(12):2623-36.

62. Manz A, Graber N, Widmer HM. Miniaturized total chemical analysis systems: A novel concept for chemical sensing. Sens Actuators, B. 1990;1(1–6):244-8.

63. Llobera A, Demming S, Wilke R, Buttgenbach S. Multiple internal reflection poly(dimethylsiloxane) systems for optical sensing. Lab Chip. 2007;7(11):1560-6.

64. Llobera A, Wilke R, Buttgenbach S. Poly(dimethylsiloxane) hollow Abbe prism with microlenses for detection based on absorption and refractive index shift. Lab Chip. 2004;4(1):24-7.

65. Paruta AN, Sciarrone BJ, Lording. Correlation between solubility parameters and dielectric constants. J Pharm Sci. 1962;51:704-5.

66. Lide DR. CRC Handbook of Chemistry and Physics.: A Ready-Reference Book of Chemical and Physical Data: CRC PressI Llc; 2004.

67. Seo J, Lee LP, editors. Fluorescence amplification by self-aligned integrated microfluidic optical systems. TRANSDUCERS, Solid-State Sensors, Actuators and Microsystems, 12th International Conference on, 2003; 2003 8-12 June 2003.

68. Rabiei P, Steier WH, Zhang C, Dalton LR. Polymer Micro-Ring Filters and Modulators. J Lightwave Technol. 2002;20(11):1968.

69. Vila-Planas J, Fernández-Rosas E, Ibarlucea B, Demming S, Nogués C, Plaza JA, et al. Cell analysis using a multiple internal reflection photonic lab-on-a-chip. Nat Protoc. 2011;6(10):1642-55.

70. Jo BH, Van Lerberghe LM, Motsegood KM, Beebe DJ. Three-dimensional micro-channel fabrication in polydimethylsiloxane (PDMS) elastomer. J Microelectromech Syst. 2000;9(1):76-81.

71. Johnson D, Goettert J, Singh V, Yemane D. SUEX for High Aspect Ratio Micro-Nanofluidic Applications. Proc Microtech. 2012.

72. Méndez-Vilas A, Bruque JM, González-Martín ML. Sensitivity of surface roughness parameters to changes in the density of scanning points in multi-scale AFM studies. Application to a biomaterial surface. Ultramicroscopy. 2007;107(8):617-25.

73. D'Antonio P, Lasalvia M, Perna G, Capozzi V. Scale-independent roughness value of cell membranes studied by means of AFM technique. Biochimica et Biophysica Acta (BBA)-Biomembranes. 2012.

74. Swinehart DF. The Beer-Lambert Law. J Chem Educ. 1962;39(7):333.

75. Du Y, Xue Y, Frisch H. Solubility Parameters in: Physical Properties of Polymers Handbook. AIP. 1996;16:227.

76. Zhu Y, Rinzema A, Tramper J, Bol J. Microbial transglutaminase—a review of its production and application in food processing. Applied microbiology and biotechnology. 1995;44(3-4):277-82.

77. Haard NF. A review of proteotlytic enzymes from marine organisms and their application in the food industry. Journal of Aquatic Food Product Technology. 1992;1(1):17-35.

78. Vellard M. The enzyme as drug: application of enzymes as pharmaceuticals. Current Opinion in Biotechnology. 2003;14(4):444-50.

79. Zaks A, Dodds DR. Application of biocatalysis and biotransformations to the synthesis of pharmaceuticals. Drug Discovery Today. 1997;2(12):513-31.

80. Kirk O, Borchert TV, Fuglsang CC. Industrial enzyme applications. Current Opinion in Biotechnology. 2002;13(4):345-51.

81. Bommarius AS, Riebel BBR. Biocatalysis: fundamentals and applications: Wiley-Blackwell; 2004.

82. Karyakin AA, Karyakina EE. Prussian Blue-basedartificial peroxidase'as a transducer for hydrogen peroxide detection. Application to biosensors. Sens Actuators, B. 1999;57(1):268-73.

83. Delvaux M, Demoustier-Champagne S. Immobilisation of glucose oxidase within metallic nanotubes arrays for application to enzyme biosensors. Biosensors and Bioelectronics. 2003;18(7):943-51.

84. Katchalski-Katzir E, Kraemer DM. Eupergit® C, a carrier for immobilization of enzymes of industrial potential. Journal of Molecular Catalysis B: Enzymatic. 2000;10(1):157-76.

85. Brady D, Jordaan J. Advances in enzyme immobilisation. Biotechnol Lett. 2009;31(11):1639-50.

86. Bornscheuer U. Trends and Challenges in Enzyme Technology. In: Nielsen J, editor. Biotechnology for the Future: Springer Berlin Heidelberg; 2005. p. 181-203.

87. Cao L, Langen Lv, Sheldon RA. Immobilised enzymes: carrier-bound or carrier-free? Current Opinion in Biotechnology. 2003;14(4):387-94.

88. Tischer W, Kasche V. Immobilized enzymes: crystals or carriers? Trends in Biotechnology. 1999;17(8):326-35.

89. Subramanian A, Kennel SJ, Oden PI, Jacobson KB, Woodward J, Doktycz MJ. Comparison of techniques for enzyme immobilization on silicon supports. Enzyme and Microbial Technology. 1999;24(1):26-34.

90. Bickerstaff Jr GF. Immobilization of enzymes and cells: Springer; 1997.

91. Bahulekar R, Ayyangar N, Ponrathnam S. Polyethyleneimine in immobilization of biocatalysts. Enzyme and Microbial Technology. 1991;13(11):858-68.

92. Jegan Roy J, Abraham E. Strategies in making cross-linked enzyme crystals. Chemical Reviews. 2004;104(9):3705.

93. Margolin AL, Navia MA. Protein Crystals as Novel Catalytic Materials. Angew Chem Int Ed. 2001;40(12):2204-22.

94. Vaghjiani JD, Lee TS, Lye GJ, Turner MK. Production and Characterisation of Cross-Linked Enzyme Crystals (Clecs®) for Application as Process Scale Biocatalysts. Biocatalysis and Biotransformation. 2000;18(2):151-75.

95. St. Clair NL, Navia MA. Cross-linked enzyme crystals as robust biocatalysts. JACS. 1992;114(18):7314-6.

96. Chayen NE, Shaw Stewart P, Maeder D, Blow D. An automated system for micro-batch protein crystallization and screening. Journal of Applied Crystallography. 1990;23(4):297-302.

97. Durbin S, Feher G. Protein crystallization. Annual Review of Physical Chemistry. 1996;47(1):171-204.

98. Vekilov PG, Thomas BR, Rosenberger F. Effects of convective solute and impurity transport in protein crystal growth. The Journal of Physical Chemistry B. 1998;102(26):5208-16.

99. Hansen CL, Skordalakes E, Berger JM, Quake SR. A robust and scalable microfluidic metering method that allows protein crystal growth by free interface diffusion. PNAS. 2002;99(26):16531-6.

100. Li L, Du W, Ismagilov RF. Multiparameter screening on slipchip used for nanoliter protein crystallization combining free interface diffusion and microbatch methods. JACS. 2009;132(1):112-9.

101. Yang Y, Kuramitsu S, Hamaguchi K. Hydrolysis of 4-methylumbelliferyl N-acetyl-chitooligosaccharides catalyzed by human lysozyme. J Biochem. 1981;89(5):1357-66.

102. Chen C-S, Sih CJ. General Aspects and Optimization of Enantioselective Biocatalysis in Organic Solvents: The Use of Lipases [New Synthetic Methods (76)]. Angewandte Chemie International Edition in English. 1989;28(6):695-707.

103. Macrae AR. Lipase-catalyzed interesterification of oils and fats. J Am Oil Chem Soc. 1983;60(2):291-4.

104. Kullman W. Enzymatic Peptide Synthesis: CRC Press, Boca Raton; 1987.

105. Song H, Tice JD, Ismagilov RF. A Microfluidic System for Controlling Reaction Networks in Time. Angew Chem Int Ed. 2003;42(7):768-72.

106. Thorsen T, Roberts RW, Arnold FH, Quake SR. Dynamic Pattern Formation in a Vesicle-Generating Microfluidic Device. Phys Rev Lett. 2001;86(18):4163-6.

107. Yi GR, Thorsen T, Manoharan VN, Hwang MJ, Jeon SJ, Pine DJ, et al. Generation of Uniform Colloidal Assemblies in Soft Microfluidic Devices. Adv Mater. 2003;15(15):1300-4.

108. Link DR, Anna SL, Weitz DA, Stone HA. Geometrically Mediated Breakup of Drops in Microfluidic Devices. Phys Rev Lett. 2004;92(5):054503.

General conclusions

General conclusions

Summary of the main results

The work presented in this thesis spans different scaling down approaches for the study of nucleation phenomena. Special attention has been paid to the effects that confinement through the reduction of reaction volume exerts in crystallogenesis and crystal growth.

First we made use of reduction of volume to attain an optimal method to study gypsum ($CaSO_4 \cdot 2H_2O$) nucleation at low supersaturations and in absence of stirring. We were able to compare the results obtained by these differenced experimental conditions with those resulting from data reported in literature. Through a whole interpretation of the Classical Nucleation Theory, we could observe a common nucleation mechanism for all the experimental data reported to date, unifying the different estimations of gypsum interfacial energy in a single value.

Second, we have demonstrated the utility of scaling down for having access to different nucleation mechanisms, by using methods to achieve supersaturation state which are not accessible for large volumes. On this sense, we have analyzed and evaluated two different pathways to obtain nanosized biomimetic and full biocompatible apatite nanoparticles (whose composition of the model stoichiometric compound – hydroxyapatite – is Ca5(OH)(PO4)3), resulting from their heterogeneous nucleation and stabilization by the template effect of a precursor precipitate.

In addition, the effect of confinement in sodium chloride (NaCl) solutions and calcium carbonate ($CaCO_3$) precipitation was studied. High supersaturation values at very low (and constant) solution evaporation rates were reached prior to NaCl precipitation in nano-and picoliter volumes, for initially unsaturated solutions. This finding reveals one of the main mechanisms by which NaCl precipitates in the small pores and cracks of rocks and building materials, causing their degradation. Additionally, the precipitation of

$CaCO_3 \cdot 6H_2O$ (Ikaite) as a metaestable transient precursor for calcite ($CaCO_3$) precipitation was found in the same range of volumes. Ikaite only forms naturally at very low temperatures or high pressures and, to date, no pathway to its synthesis was found without using additives at room temperature.

Finally, the use of SU-8 technology has been demonstrated as a low cost alternative to glass microfluidic systems for applications in small molecule crystallization studies, where poly(dimethylsiloxane) (PDMS) is not suitable due to its incompatibility with the commonly used organic solvents. Moreover, we have validated the implementation of spectrophotometric detection systems in these microfluidic structures and we have designed and developed new microfluidic tools using this new technology for carrying out new crystallization studies.

In conclusion, we have demonstrated the convenience and utility of small volumes for studying nucleation phenomena in calcium sulfate and calcium phosphate salts, and we have found important stabilization effects, associated to confinement, in sodium chloride supersaturated solutions and metaestable precipitating calcium carbonate phases. Moreover, with a view to offer new platforms, based on microfluidics, for drug and macromolecule crystallization, we have presented new technological improvements which permit a wide series of crystallization experiments with very few amounts of reagents.

Conclusiones Generales

Resumen de los resultados principales

El trabajo presentado en esta tesis abarca el estudio de los fenómenos de nucleación, a través de diferentes aproximaciones, pero con un denominador común: la reducción de volumen en los experimentos. Se ha prestado una atención especial a los efectos que el confinamiento, a través de la reducción del volumen de reacción, ejerce en la formación de cristales y en el crecimiento cristalino.

En primer lugar se ha hecho uso de la reducción de volumen para encontrar un método óptimo para el estudio de la nucleación de yeso ($CaSO_4 \cdot 2H_2O$), en ausencia de agitación y a bajas sobresaturaciones. Los resultados obtenidos en estos experimentos han sido comparados con los resultantes de experimentos publicados con anterioridad. A través de una interpretación íntegra de la teoría clásica de la nucleación hemos podido establecer un mecanismo de nucleación común para todos los experimentos publicados hasta la fecha, unificando en un solo valor las distintas estimaciones existentes para la energía interfacial del yeso en solución.

Posteriormente se ha demostrado la utilidad de la reducción de volumen para lograr acceso a diferentes mecanismos de nucleación: la reducción de escala ha permitido el uso de métodos para crear sobresaturación que no son aplicables a grandes volúmenes. En este sentido, se han analizado y evaluado dos vías diferentes para la obtención de nanocristales biomiméticos y biocompatibles de apatito (cuya fórmula estequiométrica del compuesto modelo – hidroxiapatito – es $Ca_5(OH)(PO_4)_3$) como resultado, en ambos casos, de un proceso de nucleación heterogénea sobre un precipitado precursor que actúa como estabilizador de dichos nanocristales, evitando su agregación.

Asimismo se ha estudiado el efecto que el confinamiento en pequeños volúmenes ejerce sobre soluciones saturadas de cloruro sódico (NaCl), y sobre la precipitación del carbonato cálcico ($CaCO_3$). Altos valores de sobresaturación, generados mediante una

evaporación controlada de la disolución, a una velocidad muy lenta y constante, han sido alcanzados como paso previo a la nucleación de cloruro sódico en gotas en el rango de volúmenes de nano- y picolitros. Este hallazgo muestra uno de los mecanismos principales por los que esta sal precipita en los pequeños poros y grietas de las rocas y algunos materiales de construcción, causando su degradación. Adicionalmente, y para el mismo rango de volúmenes, se detectó la nucleación de ikaita ($CaCO_3 \cdot 6H_2O$) como un precursor metaestable de la precipitación de calcita ($CaCO_3$). En medios naturales, la ikaita solo se forma a muy bajas temperaturas o altas presiones y, hasta la fecha, no se había encontrado una vía para su síntesis a temperatura ambiente, sin el uso de aditivos.

Finalmente, el uso de tecnologías basadas en la resina fotosensible SU-8 ha demostrado ser una alternativa de bajo coste a los sistemas microfluídicos fabricados en vidrio, para su aplicación en estudios de cristalización de fármacos y otras pequeñas moléculas. El poli(dimetilsiloxano) (PDMS), como alternativa de bajo coste, no es un material apto para estos estudios, dada su incompatibilidad con la mayoría de los disolventes orgánicos que se usan normalmente. Conjuntamente, se ha validado el uso de sistemas de detección espectrofotométrica, integrados en las estructuras microfluídicas, y se han diseñado y desarrollado nuevas herramientas para realizar estudios de cristalización utilizando estas nuevas tecnologías.

En resumen, se ha demostrado la conveniencia y utilidad de los pequeños volúmenes para estudiar los fenómenos de nucleación del sulfato cálcico y los fosfatos cálcicos, y hemos encontrado importantes efectos de estabilización, asociados con el confinamiento en pequeños volúmenes, en disoluciones sobresaturadas de cloruro sódico, y en la precipitación de fases metaestables de carbonato cálcico. Además, con la intención de ofrecer nuevas plataformas para el desarrollo de estudios de cristalización de fármacos y macromoléculas, hemos presentado nuevos desarrollos y mejoras tecnológicas, basadas en técnicas microfluídicas, que potencialmente permiten un amplio abanico de experimentos de cristalización en disolventes orgánicos con cantidades ínfimas de reactivos.

Appendixes

Appendix I

pH-Responsive delivery of doxorubicin from citrate-apatite nanocrystals with tailored carbonate content

Langmuir

Article

pubs.acs.org/Langmuir

pH-Responsive Delivery of Doxorubicin from Citrate−Apatite Nanocrystals with Tailored Carbonate Content

Isaac Rodríguez-Ruiz,[†,‡] José Manuel Delgado-López,[†,‡] Miguel A. Durán-Olivencia,[†] Michele Iafisco,[§] Anna Tampieri,[§] Donato Colangelo,[∥] Maria Prat,[∥,*] and Jaime Gómez-Morales[†,*]

[†]Laboratorio de Estudios Crystalográficos, IACT (CSIC-UGR), Avenida de las Palmeras, 4. 18100 Armilla, Granada, Spain

[§]Institute of Science and Technology for Ceramics (ISTEC), National Research Council (CNR), Via Granarolo 64, 48018 Faenza (RA), Italy

[∥]Dipartimento di Scienze della Salute, Università del Piemonte Orientale "A.Avogadro", Via Solaroli 17, 28100 Novara, Italy

Supporting Information

ABSTRACT: In this work, the efficiency of bioinspired citrate-functionalized nanocrystalline apatites as nanocarriers for delivery of doxorubicin (DOXO) has been assessed. The nanoparticles were synthesized by thermal decomplexing of metastable calcium/citrate/phosphate solutions both in the absence (Ap) and in the presence (cAp) of carbonate ions. The presence of citrate and carbonate ions in the solution allowed us to tailor the size, shape, carbonate content, and surface chemistry of the nanoparticles. The drug-loading efficiency of the two types of apatite was evaluated by means of the adsorption isotherms, which were found to fit a Langmuir−Freundlich behavior. A model describing the interaction between apatite surface and DOXO is proposed from adsorption isotherms and ζ-potential measurements. DOXO is adsorbed as a dimer by means of a positively charged amino group that electrostatically interacts with negatively charged surface groups of nanoparticles. The drug-release profiles were explored at pHs 7.4 and 5.0, mimicking the physiological pH in the blood circulation and the more acidic pH in the endosome-lysosome intracellular compartment, respectively. After 7 days at pH 7.4, cAp-DOXO released around 42% less drug than Ap-DOXO. However, at acidic pH, both nanoassemblies released similar amounts of DOXO. *In vitro* assays analyzed by confocal microscopy showed that both drug-loaded apatites were internalized within GTL-16 human carcinoma cells and could release DOXO, which accumulated in the nucleus in short times and exerted cytotoxic activity with the same efficiency. cAp are thus expected to be a more promising nanocarrier for experiments *in vivo*, in situations where intravenous injection of nanoparticles are required to reach the targeted tumor, after circulating in the bloodstream.

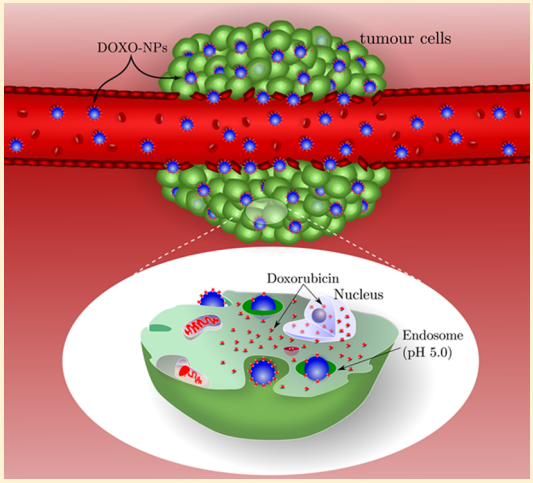

1. INTRODUCTION

In the latest years, nanomaterial science has attracted a dramatic and exponentially increasing interest in the biomedical field, in particular for their potential applications in drug delivery for cancer therapies.[1−5] One of the key challenges of such an application is the efficient delivery of the drug to the tumor region, while reducing as far as possible the toxic side effects. Due to their size (<100 nm), nanoparticles can escape capture by macrophages, being able to remain in the bloodstream for prolonged time and to pass through endothelial cells lining blood vessels, which are more permeable in the tumor region (i.e., enhanced permeability and retention effect, Figure 1A), and then to cross cell membranes.[4,6] Moreover, nanoparticles may protect the drug component from a premature degradation and may deliver poorly water-soluble chemotherapeutic drugs directly to tumor cells. They are also very efficient carriers since their high surface/volume ratio allows them to incorporate large amounts of drugs.[1−5]

Size, shape, and surface chemistry can dictate the behavior of nanoparticles at the nano-biointerface.[7] The shape of nanoparticles has been shown to have an impact on various processes including circulation, vascular adhesion and phagocytosis.[8] Spheres show an appreciable advantage over rods in termsof cell uptake, in fact with the increase of the nanorod aspect ratio, the total cell uptake decreases.[9] Otherwise, needle-shaped nanoparticles seem to induce cell membrane disruption and increased cell mobility.[10] To date, the precise effects of nanoparticle shape on cells is still a controversial issue and deserves further investigations *in vitro* and especially *in vivo*.

Received: March 5, 2013
Revised: May 6, 2013
Published: June 4, 2013

   dx.doi.org/10.1021/la4008334 | *Langmuir* 2013, 29, 8213−8221

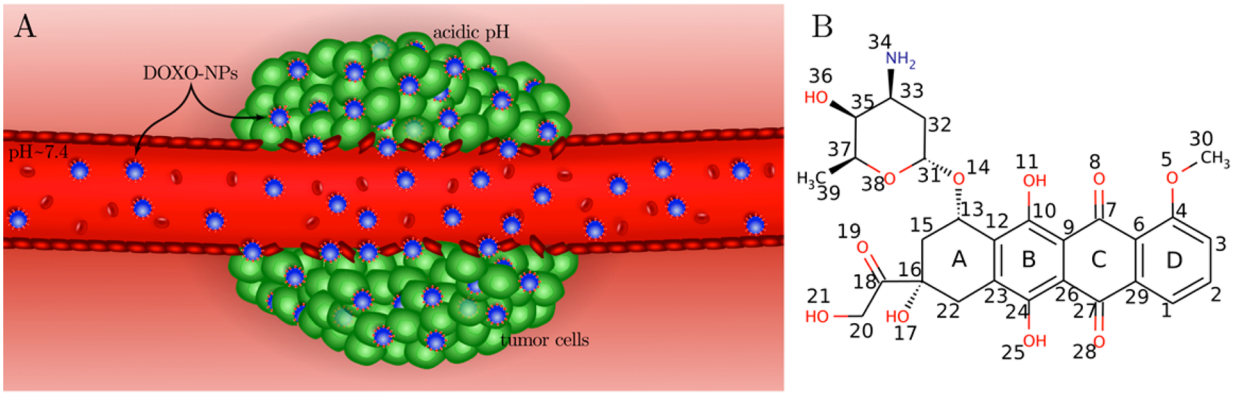

Figure 1. (A) Schematic representation of the use of nanoparticles (NPs) as passive targeting due to the enhanced permeability and retention (EPR) effect in the tumor region. The extracellular tumor environment and the intracellular lysosome exhibit acidic pH, facilitating the selective release of the drug within tumor cells. (B) Molecular structure of DOXO. Groups involving oxygen atoms and amino groups are marked in red and blue colors, respectively.

Delivery systems for therapeutics range from liposome complexes to nanoparticles made up of various materials, including ceramics, polymers and metals.[11−13] However, several concerns regarding the biodegradability of such materials, the toxicity of degradation byproducts or the toxic structural characteristics of the nanoparticles themselves have been hindering their clinical translation.[14] The possibility to use nanocrystalline apatites as carriers for local and controlled supply of drugs is very attractive, due to their peculiar properties such as biocompatibility, biodegradability, easily tunable physical-chemical properties (i.e., size and surface composition),[15,16] lower toxicity than other nanomaterials (such as silica, quantum dots, carbon nanotubes, or metallic magnetic particles), low production costs, excellent storage abilities (not easily subjected to microbial degradation), and pH-dependent dissolution.[17] This latter feature is particularly interesting since pHs lower than the one observed in normal tissues are found in the extracellular environments of solid tumors and in particular within the endosome-lysosome cell compartment, where it reaches values around 5,[18] thus enabling a preferential active drug release from apatite surface in a pH-dependent way in the tumor region (Figure 1A).

Recently, Nancollas et al. suggested that the use of citrate in the crystallization of nanocrystalline apatite can be considered an interesting strategy inspired from nature to control the synthesis of this material.[19] Solid state NMR studies have recently reassessed the role of citrate in stabilizing the size and morphology of bone apatite, where it accounts for about 5.5 wt % of the total organic component.[20] We have recently demonstrated that the use of citrate as calcium-complexing ions provides fully biocompatible bioinspired nanocrystalline apatites by thermal decomplexing batch crystallization method.[21]

Doxorubicin (DOXO), an anthracycline antibiotic with three planar and aromatic hydroxyanthraquinonic rings (Figure 1B),[22] has been used in this paper because it is commonly used in cancer chemotherapies due to its broad spectrum of antitumor activity.[23] Through its chromophore group it intercalates between two stacked DNA base pairs,[24] interfering with nucleic acid synthesis in the *S* phase of cell cycle.[25−27] A major problem associated with DOXO administration involves its significant side effects, concerning in particular cardiac function, and hepatic toxicity.[28−30] These nonspecific side effects could be dramatically reduced by the use of drug delivery nanocarriers and this work can open new perspectives in this domain.

Therefore, in this paper we have assessed the efficiency of two types of bioinspired citrate-functionalized apatite nanocrystals differing for size, shape, carbonation degree and surface chemistry as nanocarriers for the loading and controlled release of DOXO. The cellular uptake and the cytotoxic activity of DOXO-loaded nanoparticles were also analyzed *in vitro* against the human carcinoma GTL-16 cell line.

2. EXPERIMENTAL SECTION

2.1. Reagents. Calcium chloride dihydrate ($CaCl_2{\cdot}2H_2O$, Bioxtra, ≥ 99.0% pure), sodium citrate tribasic dihydrate ($Na_3(Cit){\cdot}2H_2O$ where Cit = citrate = $C_6H_5O_7$, ACS reagent, ≥ 99.0% pure), sodium phosphate dibasic (Na_2HPO_4, ACS reagent, ≥ 99.0% pure), sodium carbonate monohydrate ($Na_2CO_3{\cdot}H_2O$, ACS reagent, 99.5% pure), doxorubicin hydrochloride ($C_{27}H_{29}NO_{11}HCl$, 98.0−102.0% HPLC grade), sodium acetate ($C_2H_3O_2Na$, 99.0%), hydrochloric acid (HCl, ACS reagent, ≥37%), acetic acid (CH_3CO_2H, ACS reagent, 99.7%), sodium hydroxide (NaOH, ACS reagent, ≥ 99.5% pure) and phosphate buffered saline (PBS) were purchased from Sigma-Aldrich. Ultrapure water (0.22 μS, 25 °C, Milli-Q, Millipore) was used in all of the experiments.

2.2. Synthesis of Apatite Nanocarriers. The apatite nanocarriers were synthesized by the batch crystallization method consisting in the thermal decomplexing of metastable calcium/citrate/phosphate/carbonate solutions as described elsewhere.[21] The nanoparticles denoted as Ap were obtained in the absence of Na_2CO_3 in the mother solution whereas those obtained in the presence of 100 mM Na_2CO_3 are referred to as cAp. After the precipitation, the nanoparticles were repeatedly washed with water by centrifugation (Hettich Universal 32R) and freeze-dried at −60 °C under vacuum (3 mbar) overnight.

2.3. Characterization Techniques. Transmission electron microscopy (TEM) analyses were performed with a STEM Philips CM 20 microscope operating at 80 kV. The powder samples were ultrasonically dispersed in ultrapure water and then few droplets of the slurry were deposited on conventional copper microgrids. A surface area analyzer (Sorpty 1750, Carlo Erba, Milan, Italy) was used to measure the N_2 adsorption/desorption isotherms of Ap and cAp at the temperature of 50 °C. The specific surface areas (SSA) of the samples were calculated using the Brunauer−Emmett−Teller (BET) method from the nitrogen adsorption data at a relative pressure of 0.03 Torr. Fourier Transform Infrared (FTIR) spectra were recorded on a Thermo Nicolet 380 FTIR spectrometer. Each powdered sample (~1 mg) was mixed with about 200 mg of anhydrous KBr and pressed into 7 mm diameter discs. Pure KBr discs were used as background. The infrared spectra were registered from 4000 to 400 cm^{-1} with a

dx.doi.org/10.1021/la4008334 | *Langmuir* 2013, 29, 8213−8221

resolution of 4 cm^{-1}. Raman spectra were collected with a LabRAM-HR spectrometer (Jobin-Yvon, Horiba, Japan). The excitation line was provided by a diode laser emitting at a wavelength of λ = 785.4 nm and a Peltier cooled charge-couple device (CCD) (1064 × 256 pixels) were used as detector. Spectrometer resolution was higher than 3 cm^{-1}. For each acquisition and depending on the quality of the spectra, signal averaging of three spectra and acquisition time between 100 and 300 s was performed. The Raman intensity was represented as counts per seconds (cps). The electrophoretic mobility (ζ-potential) measurements were performed with a Zetasizer Nano analyzer (Malvern, UK) using disposable folded capillary cells at 25 °C. The pH evolution of the ζ-potential was measured by using a MPT-2 autotitrator (Malvern, UK) connected to the analyzer. Diluted HCl and NaOH solutions (0.25 and 0.1 M, respectively) were used as titration agents.

2.4. Drug Adsorption and Release Experiments. The adsorption kinetic of DOXO on the nanoparticles was determined by mixing 5 mg of nanoparticles with 1 mL of aqueous DOXO solution (1 mg/mL). The mixtures were incubated at 37 °C for different times, up to a maximum of 48 h. Incubation was done under agitation in the dark since DOXO is sensitive to photolytic decomposition.[31]

For the study of the adsorption isotherms, 5 mg of apatite were mixed with 1 mL of different concentrations (from 0.03 to 1 mg mL^{-1}) of aqueous DOXO solutions. Mixtures were then incubated under agitation at 37 °C for 24 h. Drug loaded samples were separated from unbound drug molecules by centrifugation at 10.000 rpm for 5 min. Afterward samples were carefully washed three times with a 1 mL of ultrapure water to remove the physically adsorbed drug molecules. The amount of nonadsorbed DOXO in the supernatant was measured by UV−vis spectroscopy with a Cary 1E UV−vis spectrophotometer (Varian, USA) at a wavelength of λ = 480 nm. This latter amount was considered as the equilibrium concentration (C_e) whereas the difference between the initial amount of DOXO and this latter value was used to calculate the adsorbed amount of DOXO per unit mass of adsorbent (Q). The molar absorptivity of DOXO in solution was estimated from the slope of a standard calibration straight line as 18.4 ± 0.3 mg mL^{-1} cm^{-1}. The washing solutions containing the DOXO molecules detached from functionalized nanoparticles (physically adsorbed) were also quantitatively analyzed and the result was taken into account for the calculation of Q.

The isotherm data were fitted to different models in order to obtain comparable and physically interpretable parameters describing the adsorption process. The models of Langmuir and Langmuir−Freundlich (LF) were tested for the isotherms. The curves were fitted to the experimental data using a nonlinear least-squares fitting algorithm to obtain the model parameters (see Supporting Information S1). The Langmuir adsorption model[32] considers an energetically homogeneous surface in which the maximum drug adsorption capacity is defined by a full monolayer of adsorbed drug wherein no interaction between adsorbed neighbors is considered.[33,34] The Langmuir model is represented by eq 1

$$Q = \frac{Q_{max}(K_L C_e)}{1 + (K_L C_e)} \quad (1)$$

where Q is the surface coverage, C_e is the equilibrium concentration of adsorbate in solution, Q_{max} is the drug loading capacity and K_L is the Langmuir affinity constant.[35] The LF model, shown in eq 2, describes an adsorption condition in which interaction between adsorbed neighbors (cooperativity) is considered. Constant K_{LF} represents the LF affinity constant in eq 2 and coefficient r represents the cooperativity coefficient. Generally, if $r > 1$, cooperativity is defined as positive, and if $r < 1$, cooperativity is negative.

$$Q = \frac{Q_{max}(K_{LF} C_e)^r}{1 + (K_{LF} C_e)^r} \quad (2)$$

Drug release from functionalized nanoparticles was analyzed both at the physiological pH 7.4 and at the acidic pH 5.0. The functionalized nanocrystals (5 mg) were washed twice with ultrapure water and freeze-dried overnight, then they were resuspended either in HEPES buffer (10 mM, 10 mL, pH 7.4) or Acetate buffer (10 mM, 10 mL, pH 5.0) solutions containing NaCl in the range 0.18−0.20 M. Suspensions were constantly stirred at 37 °C and at scheduled times the samples were centrifuged and aliquots of supernatants were analyzed by UV−vis spectroscopy. After the measurement the supernatants were restored to the suspensions.

The release efficiency, D_R, was described as the ratio (%wt) between the amount of drug released at time t ($Q_{(t)}$) and the drug loading capacity, Q_{max}.

$$D_R = \frac{Q_{(t)}}{Q_{max}} \times 100 \quad (3)$$

2.5. Cellular Internalization of Nanoparticles. In all the experiments with cells, the human carcinoma GTL-16 cells,[36] which are cultured in Dulbecco's modified Eagle's medium containing 10% heat-inactivated fetal calf serum (FCS), 50 U mL^{-1} penicillin, and 50 μg mL^{-1} streptomycin, were used. Cells (2.2×10^4) were seeded on glass coverslips (12 mm diameter) in 24-well plates and after 24 h free DOXO or nanoparticle suspensions were added. After incubation at 37 °C for 3 h, glass coverslips were washed twice with fresh PBS to remove any free DOXO or nanoparticles. Cells were fixed with paraformaldehyde (4%) in PBS, pH 7.2, permeabilized with Triton-X100 (1%) in PBS, containing bovine serum albumin (2%) and their nuclei stained with To-Pro3 (Life Technologies, Monza MB, Italy). Accumulation of free DOXO or nanoparticle samples in GTL-16 cells was detected using a Zeiss LSM510 confocal microscope. The excitation wavelength used for DOXO and To-Pro3 were 476 and 633 nm respectively. Their emissions were detected between 575 and 630 nm (DOXO) and between 650 and 750 nm (To-Pro3). Images were taken at 630x magnification.

2.6. Cytotoxicity Assays. GTL-16 cells (10×10^3/0.4 cm^2 microwell) were incubated for 24 h and afterward, different concentrations of DOXO and DOXO-coupled nanoparticles, ranging from 0.01 to 100 μg mL^{-1}, were added in 100 μL. After 3 days incubation, cells viability was evaluated by the 3-(4,5-*Di*methylthiazol-2-yl)-2,5-*di*phenyltetrazolium bromide) (MTT, Sigma) colorimetric assay. Briefly, 20 μL of MTT solution (5 mg mL^{-1} in a PBS solution) were added to each well. The plate was then incubated at 37 °C for 3 h. After the removal of the solution, 0.2 N HCl acidified isopropanol was added for dissolution of formazan crystals. Optical density was measured in a multiwell reader (2030 Multilabel Reader Victor TM X4, PerkinElmer) at 570 nm. Experiments were performed 4 times using 3 replicates for each sample. One-way ANOVA with Dunnett's post test was performed using GraphPad Prism version 4.00 for Windows, GraphPad Software (GraphPad Prism, San Diego, CA).

3. RESULTS

3.1. Characterization of the Nanocarriers. Figure 2 shows TEM micrographs of the Ap (A) and cAp (B) nanoparticles. Ap are needle-like nanoparticles elongated along the *c*-axis with an average length of ca. 100 nm whereas cAp are more isomorphic with shorter average length (ca. 30 nm). The main physical-chemical properties of both types of apatites are summarized in Table 1. Figure 2C and D display the FTIR spectra of Ap and cAp, respectively. They exhibit a main feature at ca. 1030 cm^{-1} with shoulders at ca. 1046 and 1075 cm^{-1} due to the triply degenerated asymmetric stretching mode of the apatitic PO_4 groups (ν_3PO_4). This band is slightly red-shifted with respect to that of stoichiometric hydroxyapatite, mainly in the cAp, most likely due to the presence of CO_3^{2-}, and/or HPO_4^{2-} ions incorporated into the crystal lattice.[21] The presence of carbonate replacing both OH^- (A-type) and PO_4^{3-} (B-type) positions in the crystal lattice of cAp is witnessed by the bands at ca. 1550, 1452, 1465 (as a shoulder), 1415, 880, and 873 cm^{-1} (Figure 2D).[21] Indeed, the disappearance of the OH librational mode at 631 cm^{-1} in the

dx.doi.org/10.1021/la4008334 | Langmuir 2013, 29, 8213−8221

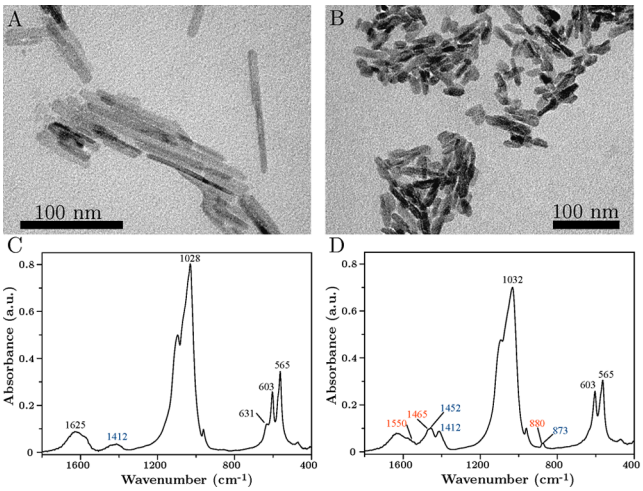

Figure 2. TEM micrographs of apatite nanocrystals obtained (A) in the absence and (B) in the presence of Na_2CO_3. FTIR spectra of the (C) Ap and (D) cAp nanoparticles. Red and blue peaks are due to A-type and B-type carbonate substitutions, respectively.

Table 1. Morphological (Length (L), Width (W), Aspect Ratio (R)) and Physical-chemical Features (i.e., Citrate and Carbonate Content, Ca/P Ratio and Specific Surface Area (SSA)) of Ap and cAp Nanoparticles

	Ap	cAp
L [nm][a,b]	104 ± 40	29 ± 10
W [nm][a,b]	15 ± 6	12 ± 3
R[a]	8 ± 3	2 ± 1
Citrate [%wt][b]	2.0 ± 0.1	2.1 ± 0.1
Carbonate [%wt][b]	1.0 ± 0.1	2.9 ± 0.2
Ca/P[b]	1.54 ± 0.02	1.58 ± 0.01
SSA [$m^2 g^{-1}$]	90 ± 9	93 ± 9

[a]Values obtained from TEM observations of more than 100 nanoparticles of different experiments. [b]Data extracted from ref 21.

spectra of cAp is due to substitution of OH apatitic groups by carbonate (A-type substitutions).

The presence of a limited amount of carbonate in the Ap nanoparticles (1.0 ± 0.1 wt %, Table 1) is derived from unintentionally dissolved CO_2 in the preparation media and/or from CO_2 adsorbed onto the surface materials during the storage. More detailed information of the physical-chemical properties of these nanoparticles has been previously reported.[21]

The nanoparticles synthesized with this precipitation method are covered by citrate ions[21,37] similarly to bone apatite.[20] These compositional features, together with their specific surface areas (SSA), which are similar to the SSA of the biological apatites (87 ± 0.6 $m^2 g^{-1}$),[38] confirm that both Ap and cAp, are biomimetic bone-like nanocrystalline apatites.[39,40]

3.2. DOXO Adsorption Isotherms and Release Profiles. The adsorption isotherms of DOXO onto Ap and cAp nanoparticles are depicted in Figure 3A and B, respectively. DOXO adsorption kinetics on apatites was previously evaluated in order to find out the time required to reach the adsorption equilibrium (Supporting Information S2).

The test of Scatchard, the plot of Q/C_e as a function of Q,[41] was carried out to evaluate the presence of cooperative effects in drug adsorption (insets in Figure 3). The nonlinearity of the Scatchard plot suggests the presence of cooperative effects during the adsorption, excluding thus a Langmurian behavior. It is presumable that the adsorption sites on the apatite surface are energetically heterogeneous due to the different chemical species (calcium, phosphates, citrate) present on its surface.[34] Hence, the isotherms were fitted according to the LF model,[42] which introduces the effects of the surface energetic heterogeneities by means of the exponent r.[35]

The Q_{max}, K_{LF} and r parameters (Table 2) were obtained by fitting the experimental data with the Langmuir–Freundlich eq 2. The value of coefficient r indicates the existence of cooperativity in the binding interaction on both types of

Table 2. Adsorption Parameter Obtained from NWLS Curve Fitting of Experimental Data According to Langmuir–Freundlich Equation

parameter	Ap-DOXO	cAp-DOXO
K_{LF} [mL mg^{-1}]	8 ± 2	8.0 ± 0.9
Q_{max} [mg mg^{-1}]	0.41 ± 0.06	0.44 ± 0.02
r	1.3 ± 0.2	1.4 ± 0.1

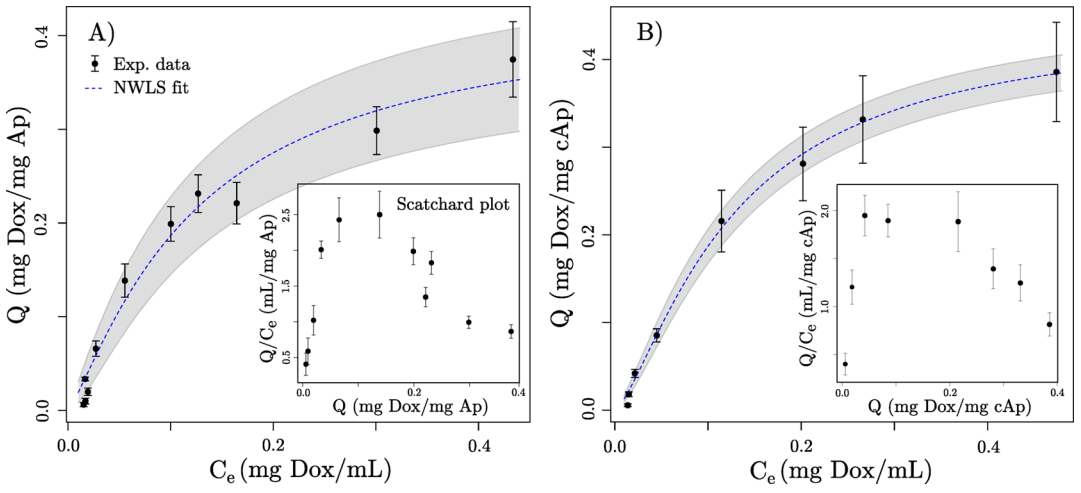

Figure 3. Adsorption isotherms of DOXO on nanocrystalline (A) Ap and (B) cAp. Dotted blue line represents the nonlineal weighted least-squares (NWLS) fitting of the experimental data by using Langmuir–Freundlich equation. (Insets) Scatchard plots of the same data.

dx.doi.org/10.1021/la4008334 | Langmuir 2013, 29, 8213–8221

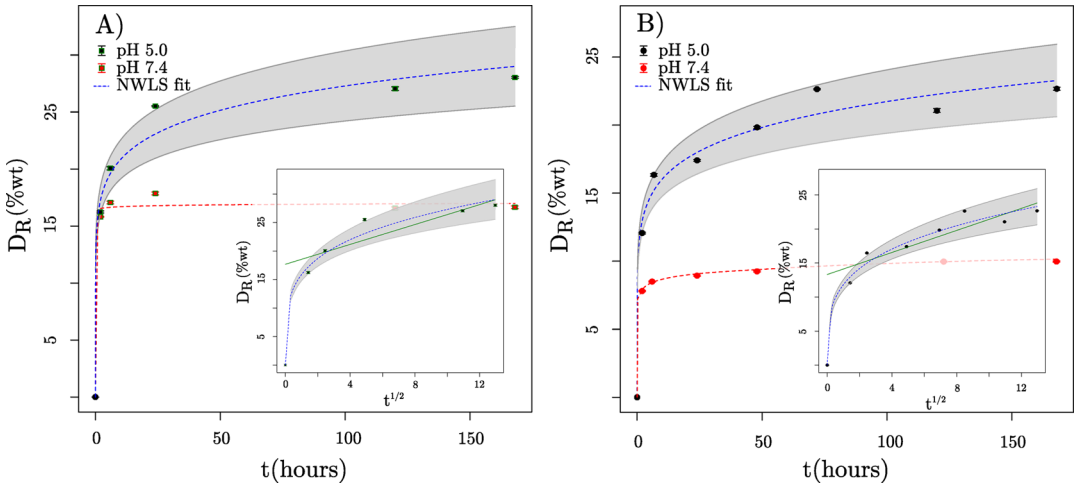

Figure 4. Kinetics of DOXO release from (A) Ap and (B) cAp at pH 7.4 and pH 5.0. (Insets) Plot of D_R as a function of $t^{1/2}$, indicating that the release of DOXO follows a subdiffusive regime.

nanoparticles.[34] This finding reveals that adsorbed molecules are not only interacting with the substrate, but they are also lowering the adsorption energy through positive interactions between themselves. K_{LF} and Q_{max} are very similar for Ap and cAp. Thus, taking into account the experimental error, it can be assumed that both types of particles showed similar drug loading capacity.

The release of DOXO from drug-loaded Ap and cAp was found to be strongly pH dependent (Figure 4). In fact, the release was much higher at pH 5.0 than at pH 7.4. Specifically, after 7 days the amount of DOXO released at physiological pH 7.4 was 17 and 10% of the total drug amount loaded on Ap and cAp, respectively. In the acidic media, the drug was released faster, reaching values of about 29 and 23% of the total DOXO loaded on Ap and cAp, respectively. The lower amount of drug released from cAp with respect to Ap suggests that the bond between DOXO and cAp nanoparticle is stronger, possibly because of the presence of higher amount of carbonated groups at the cAp surface.

3.3. Characterization of the DOXO−Nanocarriers Complexes. Raman spectroscopy was used to confirm that DOXO was successfully adsorbed on the surface of the nanoparticles. Raman spectra collected for cAp, DOXO in aqueous solution and DOXO-functionalized cAp are depicted in Figure 5. The spectrum of Ap-DOXO (not shown) was similar to that obtained for cAp-DOXO. The spectrum of cAp (spectrum a in Figure 5) displayed typical Raman peaks of carbonate-apatite nanoparticles.[21,43] The spectrum of DOXO in aqueous solution (spectrum b in Figure 5) exhibited Raman peaks assignable to vibrational modes of free DOXO.[44] In particular, the broad peaks centered at ca. 1579 and 1640 cm^{-1} can be assigned to the stretching vibrations of the C═O groups of the anthracene ring (ring C in Figure 1B).[44,45] The Raman bands in the region 1460−1410 cm^{-1} are due to the C═C and C−C stretches of the aromatic hydrocarbons.[44,45] The bands in the region 1200−1300 cm^{-1} are assignable to the vibrations involving in-plane C−O, C−O−H and C−H bending modes.[44] The peaks in the lower Raman shift region are most probably due to the deformation of CO groups and skeletal vibrations.[46] Similar features can be distinguished in the Raman spectrum of the DOXO-functionalized cAp (spectrum c in Figure 5), confirming the existence of adsorbed DOXO onto the cAp surface.

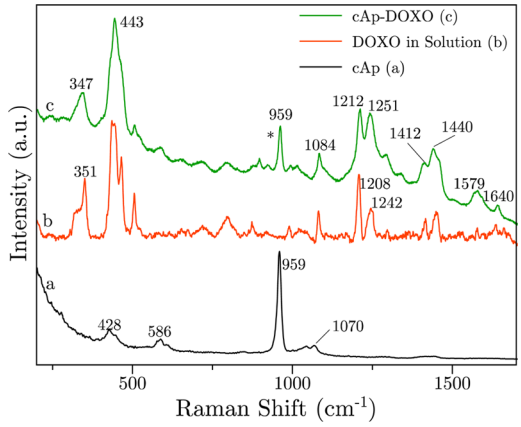

Figure 5. Raman spectra of (a) cAp, (b) DOXO in aqueous solution and (c) DOXO-functionalized cAp (0.32 mg DOXO/mg cAp). The asterisk denotes the main peak of cAp (related to the symmetric stretching of PO_4 groups[21,43]).

The ζ-potential evolution, as a function of C_e, of Ap-DOXO and cAp-DOXO suspended in ultrapure water is reported in Figure 6A. The ζ-potentials of the bare Ap and cAp nanoparticles were −33.9 ± 4.5 and −36.4 ± 4.9 mV, respectively. The adsorption of DOXO produced a gradual increase of the ζ-potential, which reached positive values with the maximum amount of adsorbed DOXO. Different profiles of the ζ-potential were found in both types of functionalized apatites with higher ζ-potential values for cAp-DOXO than Ap-DOXO for the same C_e. Nonetheless, the same ζ-potential was attained for both once the surface was completely saturated.

The ζ-potential of the DOXO-loaded cAp decreased with increasing pH, as shown in Figure 6B. Similar behavior was found also for the Ap-DOXO (data not shown). The point of zero charge (pzc) of cAp-DOXO was around 8.1, which is very close to the pK_a of DOXO (8.2),[47,48] which means that the apatite surface is almost covered by the drug.

3.4. Cellular Internalization of Nanoparticles. The endocytotic behavior of DOXO-loaded nanoparticles, as well as of soluble free DOXO with cells was analyzed at the confocal laser microscopy (CLM), after cells were incubated with these compounds for 3 h in serum-containing cell media. Figure 7 shows that in these conditions DOXO (false red color), either

dx.doi.org/10.1021/la4008334 | Langmuir 2013, 29, 8213−8221

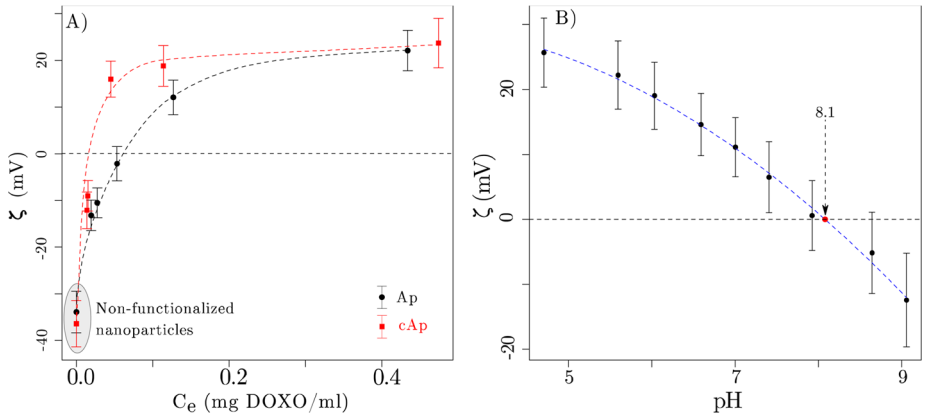

Figure 6. (A) Plot of the ζ-potential of DOXO-functionalized Ap and cAp as a function of C_e. (B) Plot of the ζ-potential of cAp-DOXO (0.32 mg DOXO/mg cAp) as a function of the pH. The point of zero charge of cAp-DOXO is 8.1.

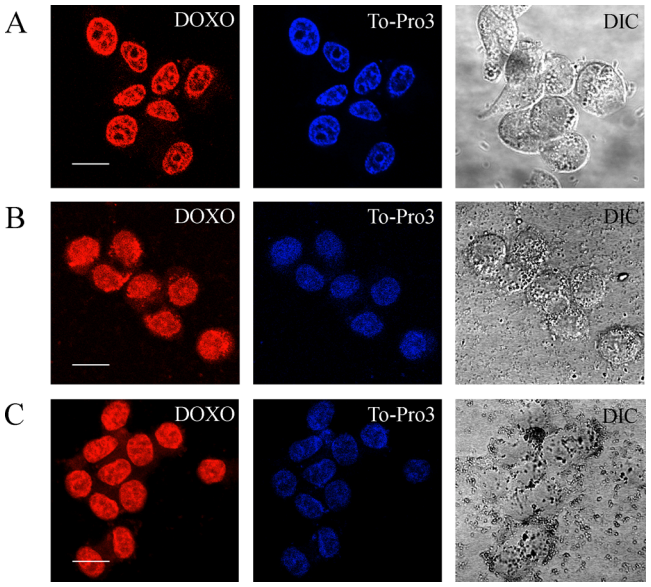

Figure 7. Intracellular localization of DOXO (in false red color) in GTL-16 cultured for 3h in serum-containing media added with (A) free DOXO, (B) Ap-DOXO complex and (C) cAp-DOXO complex, as visualized by confocal laser scanning microscopy (CLSM). Nuclei stained with To-Pro3 appear in false blue color. DIC = Differental Interference Contrast. Bar = 25 μm.

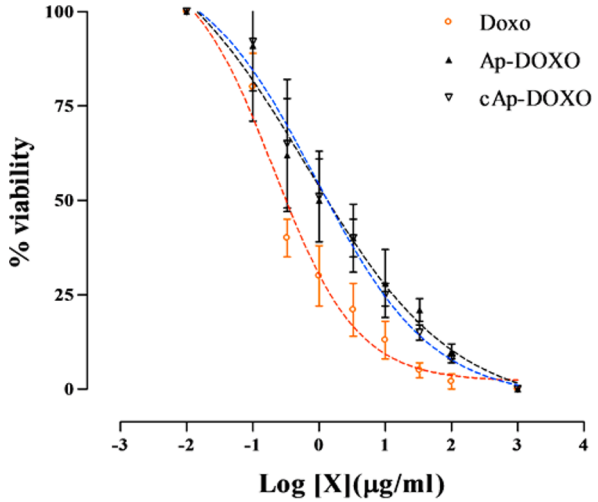

Figure 8. Effects of DOXO coupled to the two nanoparticles Ap and c-Ap (Ap-DOXO and cAp-DOXO complexes) on GTL-16 viability compared to the soluble DOXO after 3 days continuous treatment. Uncoupled nanoparticles reduced cell viability to about 90−95%, only at the concentrations higher than 33 μg/mL. Log[X] indicates the DOXO concentration in each sample and data are expressed as viability compared to the untreated control at the same time point.

in soluble form (A) or complexed at the surface of nanoparticles (B and C), is internalized. In all cases, it is mainly localized within the nucleus (false blue color). Comprehensive analysis of a series of images collected along the *z*-axis shows that, especially in the case of nanoparticles, some DOXO is detected also within the cytoplasm. Moreover, while in the case of soluble DOXO the latter is detected mainly with a diffuse pattern, in the case of nanoparticles, dots corresponding to DOXO stain are also visualized, especially in the case of Ap-DOXO nanoassemblies. This result suggests that nanoapatites carrying DOXO have been internalized and that after internalization DOXO migrated to the nucleus.

3.5. Cytotoxicity Assays. In order to analyze the biological effects of the DOXO-loaded nanoparticles, we measured their effects on cell proliferation. The cytotoxic activity of the soluble DOXO and DOXO coupled to nanoparticles at different concentrations was assessed on GTL-16 cell line by MTT assay (Figure 8). The measure of the IC50 revealed a different behavior of the compounds. In fact, while DOXO IC_{50} was 0.25 μg mL^{-1}, Ap-DOXO and cAp-DOXO IC_{50} were 1.11 and 1.04 μg mL^{-1}, respectively, thus indicating a lower efficiency of the complexes when compared to the soluble DOXO. The IC_{50} equivalent amounts of DOXO were 0.44, 1.94 and 1.82 μM, respectively.

One-way ANOVA and Dunnett's post-test revealed slightly significant differences ($p \leq 0.05$) between the soluble DOXO and the DOXO coupled to nanoparticles, with no significant difference between the two type of nanoassemblies.

4. DISCUSSION

DOXO molecules form dimers in aqueous solutions in the concentration range used in this work, being the antiparallel (i.e., with the $-NH_3^+$ groups in opposite directions, Supporting Information S4) the most stable configuration.[49] Since the pH used in the loading experiments is much lower than the pK_a of DOXO, the amino groups are protonated. Interaction of DOXO with apatite is of electrostatic nature and adsorption of antiparallel dimers of DOXO with the rings perpendicular to

dx.doi.org/10.1021/la4008334 | *Langmuir* 2013, 29, 8213−8221

the apatite surface is supported by ζ-potential values described above. The positively charged $-NH_3^+$ groups of the DOXO dimers electrostatically interact with the negatively charged free carboxylate groups of adsorbed citrate and also, in a minor extent, with the surface $>PO_4^{\delta-}$, $>CO_3^{\delta-}$, $>OH^{\delta-}$ groups, whereas the other amino group, in antiparallel position, will contribute to the positive values of the ζ-potential. The pH-dependent ζ-potential measured for cAp-DOXO confirms the existence of free amino-groups being protonated or deprotonated as a function of the pH (Figure 6 B). DOXO adsorbed with the rings oriented parallel to the apatite surface can be discharged since the theoretical total number of DOXO dimers estimated for this configuration greatly varies from the total number of adsorbed dimers experimentally measured (the amount of 0.44 mg DOXO adsorbed on 1 mg of cAp is equal to 2.44×10^{20} dimers of DOXO per gram of cAp, Supporting Information S4). It can be concluded that there are not significant differences between Ap and cAp in terms of drug loading capacities, in particular if they are functionalized in saturating conditions.

The stability of the nanoparticles functionalized with DOXO and, from the other side, the release of DOXO is an important issue to be considered, since nanoparticles would encounter different pHs *in vivo*, namely the physiological pHs (around 7.4) in the blood circulation and the more acidic pHs in the tumor microenvironment and in the endosome-lysosome intracellular compartment (around 5.0), if internalization occurs. Ideally antitumor drug delivery based on pH-responsive effect requires the drug carriers to retain most of the cargo drug in the bloodstream for several hours or even longer until they can reach the target.

The pH-responsive release mechanism occurred under a subdiffusive desorption regime that fits well with pseudo empirical Korsmeyer's power law (Supporting Information S5). Differences were observed in the DOXO release capability of the two types of nanoassemblies. Apparently the binding of DOXO to cAp was slightly stronger, since the amount of drug released from cAp was lower than from Ap. In the case of bare cAp, a higher amount of carbonate groups at the surface compared to Ap might be responsible for the slightly more negative ζ-potential (Figure 6A). The more negative surface charge would favor a stronger electrostatic interaction with the NH_3^+ groups of the DOXO. The fact that cAp-DOXO is more stable than Ap-DOXO at physiological pH can be advantageously exploited, since this would reduce the amount of soluble DOXO in the blood circulation and thus its side effects. On the other hand, although cAp-DOXO released lower amount of DOXO than Ap-DOXO at acidic pH, both nanoassemblies exhibited similar toxic activity *in vitro* against a gastric carcinoma cell line.

Both functionalized apatites were uptaken by cells and were able to carry inside their bound DOXO. Indeed, in this case DOXO could be visualized also as a dotted pattern, besides a diffuse pattern, which, by contrast, was the only one detectable in the case of treatment of cells with soluble DOXO. Nanoassemblies should have been uptaken by cells through an endocytotic mechanism,[50,51] while soluble DOXO could easily and more quickly diffuse through the plasma membrane due its lipophilic properties.[52] The different pathways in the internalization process could also explain the observation that a lower level of DOXO was detectable within the cytoplasm, relative to the nucleus, in the case of soluble DOXO treatments. In any case the final destination of DOXO was the nucleus, where indeed it was easily visualized. It cannot be excluded that a certain amount of free DOXO escaped from the cell through the multidrug-resistance (MDR) pump,[53] since it is not known if these cells express this molecule. In general the fact that nanoparticles are internalized through vesicle with the endocytic pathway protects in a certain way DOXO from being released from the cells in case of the presence of MDR and this is an advantage of drug-nanocarriers.

The internalized DOXO-apatites were able to exert their cytotoxic activity on GTL-16 cells, since they blocked their proliferation, although being somehow less efficient than soluble DOXO. DOXO is one of the most popular chemotherapeutic molecules and thus has been used as a reference molecule in different contexts. It has been used also coupled to many different carriers, and depending on which one it was coupled to, contradictory results were reported, since in some cases it was more potent than soluble DOXO,[54,55] while in others it was less efficient,[56] suggesting that the carrier used may affect the final toxic activity. In any case, the fact that the DOXO coupled to apatite is less toxic—as shown here—can be an advantage, since normal healthy cells could be more easily spared. Moreover, in this context, the fact that cAp-DOXO released lower amount of DOXO at the physiological pH suggest that they might be safer to healthy cells in comparison to Ap-DOXO. In summary, cAp should represent an efficient drug carrier for tumor cells. Their selectivity for tumor cells, which depends on the enhanced permeation retention effect operating in the tumor microenvironment, could be increased if these nanoparticles are functionalized with other moieties, such as ligands or monoclonal antibodies targeting molecules preferentially expressed at the surface of tumor cells.[57]

5. CONCLUSIONS

In this work we studied the drug-loading and releasing efficiency of citrate functionalized nanocrystalline apatites as nanocarriers for controlled delivery of doxorubicin. Apatites were chosen as carriers since they are highly biomimetic, biocompatible and biodegradable, being the major inorganic constituents of hard tissues in vertebrates.[15] The thermal decomplexing of metastable Ca/citrate/phosphate/carbonate solutions provided bone-like apatite nanocrystals with carbonation degree within 1−4%. They are coated by citrate, similarly to that recently found in bone apatites where citrate ions, which account for about 5.5 wt % of the total organic component in bone, were strongly bound to the apatite nanocrystals surface.[20] Two types of nanoparticles grown in the absence (Ap) or in the presence (cAp) of sodium carbonate were functionalized with DOXO. Although the two types of apatite revealed different shapes and sizes, which can be ascribed to the incorporation of carbonate into the apatitic crystal lattice,[58,59] they exhibited similar SSA. By contrast, their chemical composition and surface properties were different, which was then reflected in their DOXO adsorptive and release capabilities. The adsorption isotherms of DOXO on both types of nanocrystalline apatites fit remarkably well to LF model suggesting, in conjunction with ζ-potential measurements, the adsorption of DOXO dimers in an antiparallel configuration. $-NH_3^+$ DOXO groups interact with the negatively charged free carboxylate groups of adsorbed citrate and also, in a minor extent, with the surface $>PO_4^{\delta-}$, $>CO_3^{\delta-}$, $>OH^{\delta-}$ groups. The other free $-NH_3^+$ group of the dimer contributes to the positive ζ-potential values.

dx.doi.org/10.1021/la4008334 | *Langmuir* 2013, 29, 8213−8221

Both nanoassemblies exhibited a pH-responsive release mechanism under a subdiffusive desorption regime that fits well with pseudo empirical Korsmeyer's power law. After 7 days, at physiological pH, cAp-DOXO released around 42% less DOXO than Ap-DOXO. However, at pH 5.0, comparable amounts of DOXO were released from both surfaces. Additionally, both were efficiently internalized by cells with subsequent intracellular release of DOXO, followed by its transport into the nucleus killing thus the carcinoma GTL-16 cells. These properties make these nanocrystalline apatites the starting block to build multifunctional devices for targeted delivery of DOXO for cancer treatment.

■ ASSOCIATED CONTENT

Supporting Information

This material is available free of charge via the Internet at http://pubs.acs.org.

■ AUTHOR INFORMATION

Corresponding Author

*E-mail: jaime@lec.csic.es; mprat@med.unipmn.it.

Author Contributions

‡I.R.R. and J.M.D.-L. equally contributed to this work. Both should be considered as first authors. The manuscript was written through contributions of all authors. All authors have given approval to the final version of the manuscript.

Notes

The authors declare no competing financial interest.

■ ACKNOWLEDGMENTS

We gratefully thank Dr. Ezio Perucco for his help in the experiments of confocal microscopy. This work has been carried out within the framework of the projects CRYSFUN-BIO MAT2011-28543 (Spanish Ministerio de Ciencia e Innovación (MICINN)), Project I+D+i CEI-BioTic (UGR), Spanish-Italian Integrated Action (ref. IT2009-00028), and 30258/DB2001 (Ricerca Finalizzata 2009 from Regione Piemonte). J.M.D.-L. and J.G.-M. belong to the research team "Factoría de Cristalización" (Consolider Ingenio 2010) of the Spanish Ministerio de Ciencia e Innovación. J.M.D.-L. and I.R.-R. also thank to the Consejo Superior de Investigaciones Científicas (CSIC) for their postdoctoral JAE-DOC and JAE-Pre research contract, respectively, within the program "Junta para la Ampliación de Estudios" cofinanced by the European Social Fund (ESF). M.I. and A.T. acknowledge the PNR-CNR Aging Program 2012-2014 and the Flagship Project NanoMAX (PNR-CNR 2011-2013).

■ REFERENCES

(1) Grossman, J. H.; McNeil, S. E. Nanotechnology in cancer medicine. *Phys. Today* **2012**, *65*, 38−42.

(2) Heath, J. R.; Davis, M. E. Nanotechnology and cancer. *Annu. Rev. Med.* **2008**, *59*, 251−265.

(3) Ferrari, M. Cancer nanotechnology: opportunities and challenges. *Nat. Rev. Cancer* **2005**, *5*, 161−171.

(4) Pietronave, S.; Iafisco, M.; Locarno, D.; Rimondini, L.; Prat, M. Functionalized nanomaterials for diagnosis and therapy of cancer. *J. Appl. Biomater. Biomech.* **2009**, *7*, 77−89.

(5) Schroeder, A.; Heller, D. A.; Winslow, M. M.; Dahlman, J. E.; Pratt, G. W.; Langer, R.; Jacks, T.; Anderson, D. G. Treating metastatic cancer with nanotechnology. *Nat. Rev. Cancer* **2012**, *12*, 39−50.

(6) Manzoor, A. A.; Lindner, L. H.; Landon, C. D.; Park, J. Y.; Simnick, A. J.; Dreher, M. R.; Das, S.; Hanna, G.; Park, W.; Chilkoti, A.; Koning, G. A.; Ten Hagen, T. L. M.; Needham, D.; Dewhirst, M. W. Overcoming limitations in nanoparticle drug delivery: Triggered, intravascular release to improve drug penetration into tumors. *Cancer Res.* **2012**, *72*, 5566−5575.

(7) Albanese, A.; Tang, P. S.; Chan, W. C. The effect of nanoparticle size, shape, and surface chemistry on biological systems. *Annu. Rev. Biomed. Eng.* **2012**, *14*, 1−16.

(8) Gratton, S. E. A.; Ropp, P. A.; Pohlhaus, P. D.; Luft, J. C.; Madden, V. J.; Napier, M. E.; DeSimone, J. M. The effect of particle design on cellular internalization pathways. *Proc. Natl. Acad. Sci. U.S.A.* **2008**, *105*, 11613−11618.

(9) Qiu, Y.; Liu, Y.; Wang, L.; Xu, L.; Bai, R.; Ji, Y.; Wu, X.; Zhao, Y.; Li, Y.; Chen, C. Surface chemistry and aspect ratio mediated cellular uptake of Au nanorods. *Biomaterials* **2010**, *31*, 7606−19.

(10) Doshi, N.; Mitragotri, S. Needle-shaped polymeric particles induce transient disruption of cell membranes. *J. R. Soc. Interface* **2010**, *6*, 26.

(11) Koo, O. M.; Rubinstein, I.; Onyuksel, H. Role of nanotechnology in targeted drug delivery and imaging: a concise review. *Nanomed. Nanotechnol. Biol. Med.* **2005**, *1*, 193−212.

(12) Forrest, M. L.; Kwon, G. S. Clinical developments in drug delivery nanotechnology. *Adv. Drug Delivery Rev.* **2008**, *60*, 861−862.

(13) Amiji, M. M. Nanotechnology for targeted drug and gene delivery. *Nanomed.-Nanotechnol.* **2006**, *2*, 299−300.

(14) Doane, T. L.; Burda, C. The unique role of nanoparticles in nanomedicine: imaging, drug delivery and therapy. *Chem. Soc. Rev.* **2012**, *41*, 2885−2911.

(15) Gómez-Morales, J.; Iafisco, M.; Delgado-López, J. M.; Sarda, S.; Drouet, C. Progress on the preparation of nanocrystalline apatites and surface characterization: Overview of fundamental and applied aspects. *Prog. Cryst. Growth Charact.* **2013**, *59*, 1−46.

(16) Iafisco, M.; Palazzo, B.; Martra, G.; Margiotta, N.; Piccinonna, S.; Natile, G.; Gandin, V.; Marzano, C.; Roveri, N. Nanocrystalline carbonate-apatites: role of Ca/P ratio on the upload and release of anticancer platinum bisphosphonates. *Nanoscale* **2012**, *4*, 206−17.

(17) Al-Kattan, A.; Girod-Fullana, S.; Charvillat, C.; Ternet-Fontebasso, H.; Dufour, P.; Dexpert-Ghys, J.; Santran, V.; Bordere, J.; Pipy, B.; Bernad, J.; Drouet, C. Biomimetic nanocrystalline apatites: Emerging perspectives in cancer diagnosis and treatment. *Int. J. Pharm.* **2012**, *423*, 26−36.

(18) Zheng, C.; Xu, J.; Yao, X.; Xu, J.; Qiu, L. Polyphosphazene nanoparticles for cytoplasmic release of doxorubicin with improved cytotoxicity against Dox-resistant tumor cells. *J. Colloid Interface Sci.* **2011**, *355*, 374−382.

(19) Xie, B.; Nancollas, G. H. How to control the size and morphology of apatite nanocrystals in bone. *Proc. Natl. Acad. Sci. U.S.A.* **2010**, *107*, 22369−22370.

(20) Hu, Y. Y.; Rawal, A.; Schmidt-Rohr, K. Strongly bound citrate stabilizes the apatite nanocrystals in bone. *Proc. Natl. Acad. Sci. U.S.A.* **2010**, *107*, 22425−22429.

(21) Delgado-López, J. M.; Iafisco, M.; Rodríguez, I.; Tampieri, A.; Prat, M.; Gómez-Morales, J. Crystallization of bioinspired citrate-functionalized nanoapatite with tailored carbonate content. *Acta Biomater.* **2012**, *8*, 3491−3499.

(22) Wood, J. Doxorubicin. In *The Cytotoxics Handbook*, 4th ed.; Allwood, A. S., Wright, P., Eds.; Radcliffe Medical Press Ltd: Oxon, UK, 2002; p 8.

(23) Beretta, G.; Zunino, F. Molecular Mechanisms of Anthracycline Activity. In *Anthracycline Chemistry and Biology II*; Krohn, K., Ed.; Springer: Berlin/Heidelberg, 2008; Vol. *283*, pp 1−19.

(24) Pindur, U.; Haber, M.; Sattler, K. Antitumor active drugs as intercalators of deoxyribonucleic acid: Molecular models of intercalation complexes. *J. Chem. Educ.* **1993**, *70*, 263.

(25) Pigram, W. J.; Fuller, W.; Hamilton, L. D. Stereochemistry of intercalation: interaction of daunomycin with DNA. *Nat. New Biol.* **1972**, *235*, 17−19.

(26) Aubel-Sadron, G.; Londos-Gagliardi, D. Daunorubicin and doxorubicin, anthracycline antibiotics, a physicochemical and biological review. *Biochimie* **1984**, *66*, 333−352.

(27) Liao, L. B.; Zhou, H. Y.; Xiao, X. M. Spectroscopic and viscosity study of doxorubicin interaction with DNA. *J. Mol. Struct.* **2005**, *749*, 108−113.
(28) Kremer, L. C. M.; van Dalen, E. C.; Offringa, M.; Voûte, P. A. Frequency and risk factors of anthracycline-induced clinical heart failure in children: a systematic review. *Ann. Oncol.* **2002**, *13*, 503−512.
(29) Longhi, A.; Ferrari, S.; Bacci, G.; Specchia, S. Long-term follow-up of patients with doxorubicin-induced cardiac toxicity after chemotherapy for osteosarcoma. *Anticancer Drugs* **2007**, *18*, 737−744.
(30) Elliott, P. Pathogenesis of cardiotoxicity induced by anthracyclines. *Semin. Oncol.* **2006**, *33*, S2−S7.
(31) Beijnen, J. H.; van der Houwen, O. A. G. J.; Underberg, W. J. M. Aspects of the degradation kinetics of doxorubicin in aqueous solution. *Int. J. Pharm.* **1986**, *32*, 123−131.
(32) Langmuir, I. The adsorption of gases on plane surfaces of glass, mica and platinum. *J. Am. Chem. Soc.* **1918**, *40*, 1361−1403.
(33) El Shafei, G. M. S.; Moussa, N. A. Adsorption of some essential amino acids on hydroxyapatite. *J. Colloid Interface Sci.* **2001**, *238*, 160−166.
(34) Luo, Q.; Andrade, J. D. Cooperative adsorption of proteins onto hydroxyapatite. *J. Colloid Interface Sci.* **1998**, *200*, 104−113.
(35) Rill, C.; Kolar, Z. I.; Kickelbick, G.; Wolterbeek, H. T.; Peters, J. A. Kinetics and thermodynamics of adsorption on hydroxyapatite of the [160Tb]terbium complexes of the bone-targeting ligands DOTP and BPPED. *Langmuir* **2009**, *25*, 2294−2301.
(36) Giordano, S.; Ponzetto, C.; Renzo, M. F. D.; Cooper, C. S.; Comoglio, P. M. Tyrosine kinase receptor indistinguishable from the c-met protein. *Nature* **1989**, *339*, 155−156.
(37) López-Macipe, A.; Gómez-Morales, J.; Rodríguez-Clemente, R. Nanosized hydroxyapatite precipitation from homogeneous calcium/citrate/phosphate solutions using microwave and conventional heating. *Adv. Mater.* **1998**, *10*, 49−53.
(38) Misra, D. N.; Bowen, R. L.; Mattamal, G. J. Surface area of dental enamel, bone, and hydroxyapatite: Chemisorption from solution. *Calcif. Tissue Int.* **1978**, *26*, 139−142.
(39) Lowenstam, H. A.; Weiner, S. *On Biomineralization*; University Press: Oxford, 1989.
(40) Mann, S. *Biomineralization: principles and concepts in bioinorganic materials chemistry*; University Press: Oxford, 2001.
(41) Sharma, S.; Agarwal, G. P. Interactions of proteins with immobilized metal ions: role of ionic strength and pH. *J. Colloid Interface Sci.* **2001**, *243*, 61−72.
(42) Sips, R. On the Structure of a Catalyst Surface. *J. Chem. Phys.* **1948**, *16*, 490−495.
(43) Ramírez-Rodríguez, G. B.; Delgado-López, J. M.; Gómez-Morales, J. Evolution of calcium phosphate precipitation in hanging drop vapor diffusion by in situ Raman microspectroscopy. *CrystEngComm* **2013**, *15*, 2206−2212.
(44) Beljebbar, A.; Sockalingum, G. D.; Angiboust, J. F.; Manfait, M. Comparative FT SERS, resonance Raman and SERRS studies of doxorubicin and its complex with DNA. *Spectrochim. Acta Part A: Mol. Biomol. Spectrosc.* **1995**, *51*, 2083−2090.
(45) Barick, K. C.; Nigam, S.; Bahadur, D. Nanoscale assembly of mesoporous ZnO: A potential drug carrier. *J. Mater. Chem.* **2010**, *20*, 6446−6452.
(46) Das, G.; Nicastri, A.; Coluccio, M. L.; Gentile, F.; Candeloro, P.; Cojoc, G.; Liberale, C.; De Angelis, F.; Di Fabrizio, E. FT-IR, Raman, RRS measurements and DFT calculation for doxorubicin. *Microsc. Res. Tech.* **2010**, *73*, 991−995.
(47) Sturgeon, R. J.; Schulman, S. G. , Electronic absorption spectra and protolytic equilibria of doxorubicin: Direct spectrophotometric determination of microconstants. *J. Pharm. Sci.* **1977**, *66*, 958−961.
(48) Land, E. J.; Mukherjee, T.; Swallow, A. J.; Bruce, J. M. One-electron reduction of adriamycin: Properties of the semiquinone. *Arch. Biochem. Biophys.* **1983**, *225*, 116−121.
(49) Agrawal, P.; Barthwal, S. K.; Barthwal, R. Studies on self-aggregation of anthracycline drugs by restrained molecular dynamics approach using nuclear magnetic resonance spectroscopy supported by absorption, fluorescence, diffusion ordered spectroscopy and mass spectrometry. *Eur. J. Med. Chem.* **2009**, *44*, 1437−51.
(50) Rajendran, L.; Knolker, H.-J.; Simons, K. Subcellular targeting strategies for drug design and delivery. *Nat. Rev. Drug Discovery* **2010**, *9*, 29−42.
(51) Sahay, G.; Alakhova, D. Y.; Kabanov, A. V. Endocytosis of nanomedicines. *J. Controlled Release* **2010**, *145*, 182−195.
(52) Minotti, G.; Menna, P.; Salvatorelli, E.; Cairo, G.; Gianni, L. Anthracyclines: Molecular Advances and Pharmacologic Developments in Antitumor Activity and Cardiotoxicity. *Pharmacol. Rev.* **2004**, *56*, 185−229.
(53) Ambudkar, S. V.; Kimchi-Sarfaty, C.; Sauna, Z. E.; Gottesman, M. M. P-glycoprotein: from genomics to mechanism. *Oncogene* **2003**, *22*, 7468−7485.
(54) Chang, J.-E.; Shim, W.-S.; Yang, S.-G.; Kwak, E.-Y.; Chong, S.; Kim, D.-D.; Chung, S.-J.; Shim, C.-K. Liver cancer targeting of doxorubicin with reduced distribution to the heart using hematoporphyrin-modified albumin nanoparticles in rats. *Pharm. Res.* **2012**, *29*, 795−805.
(55) Padhye, S. S.; Guin, S.; Yao, H. P.; Zhou, Y. Q.; Zhang, R.; Wang, M. H. Sustained expression of the RON receptor tyrosine kinase by pancreatic cancer stem cells as a potential targeting moiety for antibody-directed chemotherapeutics. *Mol. Pharm.* **2011**, *8*, 2310−9.
(56) Shi, M.; Ho, K.; Keating, A.; Shoichet, M. S. Doxorubicin-conjugated immuno-nanoparticles for intracellular anticancer drug delivery. *Adv. Funct. Mater.* **2009**, *19*, 1689−1696.
(57) Iafisco, M.; Delgado-López, J. M.; Varoni, E. M.; Tampieri, A.; Rimondini, L.; Gómez-Morales, J.; Prat, M. Cell surface receptor targeted biomimetic apatite nanocrystals for cancer therapy. *Small* **2013**, DOI: 10.1002/smll.201202843.
(58) Legeros, R. Z.; Trautz, O. R.; Legeros, J. P.; Klein, E.; Shirra, W. P. Apatite crystallites: effects of carbonate on morphology. *Science* **1967**, *155*, 1409−1411.
(59) Rey, C.; Combes, C.; Drouet, C.; Sfihi, H.; Barroug, A. Physico-chemical properties of nanocrystalline apatites: Implications for biominerals and biomaterials. *Mater. Sci. Eng., C* **2007**, *27*, 198−205.

Supplementary Information for

pH-Responsive Delivery of Doxorubicin from Citrate-Apatite Nanocrystals with Tailored Carbonate Content

Isaac Rodríguez-Ruiz[a,†], José Manuel Delgado-López[a,†], Miguel A. Durán-Olivencia[a], Michele Iafisco[b], Anna Tampieri[b], Donato Colangelo[c], Maria Prat[c,], Jaime Gómez-Morales[a,*]*

[a]Laboratorio de Estudios Cristalográficos, IACT (CSIC-UGR). Avda. de las Palmeras, 4. 18100 Armilla, Granada, Spain.

[b]Institute of Science and Technology for Ceramics (ISTEC), National Research Council (CNR), Via Granarolo 64, 48018 Faenza (RA), Italy.

[c]Dipartimento di Scienze della Salute. Università del Piemonte Orientale "A.Avogadro". Via Solaroli 17, 28100 Novara, Italy.

* Address correspondence to:

Jaime Gómez Morales, email: jaime@lec.csic.es;

Maria Prat, e-mail: mprat@med.unipmn.it

†Isaac Rodríguez-Ruiz and José Manuel Delgado-López equally contributed to this work.

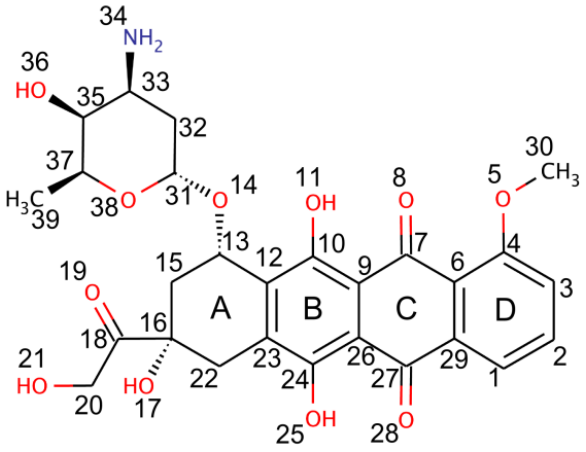

Figure S1. Molecular structure of DOXO. Groups involving oxygen atoms and amino group are marked in red and blue colours, respectively.

S1. Data fitting and error analysis

The errors of the measurements, shown as bars in graphics, were evaluated by using the first-order Taylor method for propagating uncertainties.[1, 2] The experimental data were fitted by non-linear Weighted Least Square (NWLS), shown as dashed lines in the respective plots. These calculations were computed with *R*,[3] a free software environment for statistical computing and graphics, and the *R*-package *nls*.

It is worth to note that the evaluation of the goodness of a NWLS fitting curve is not as simple as in the linear case, where it is absolutely determined by the R^2 coefficient. However, this drawback was overcome by introducing the parameters obtained from the NWLS method in a linearized version of the model equation and, then, computing the corresponding R^2 (denoted hereafter as R_{lin}^2). The confidence intervals of the fittings were represented as shaded areas.

As an example, the goodness of the fitting of the adsorption isotherms to the LF model (Equation 2) was evaluated by means of the R_{lin}^2 coefficient associated with the following linear equation

$$ln\left(\frac{Q}{Q_{max}-Q}\right) = r\ ln\ K_{LF} + r\ ln\ C_e \qquad \text{(S1)}$$

The obtained coefficients are shown in Table S1 and the plots of the linearized Langmuir-Freundlich curve are depicted in Figure S2. It can be clearly observed as the R^2 coefficient overestimates the accuracy of the NWLS fitting in comparison to the R_{lin}^2.

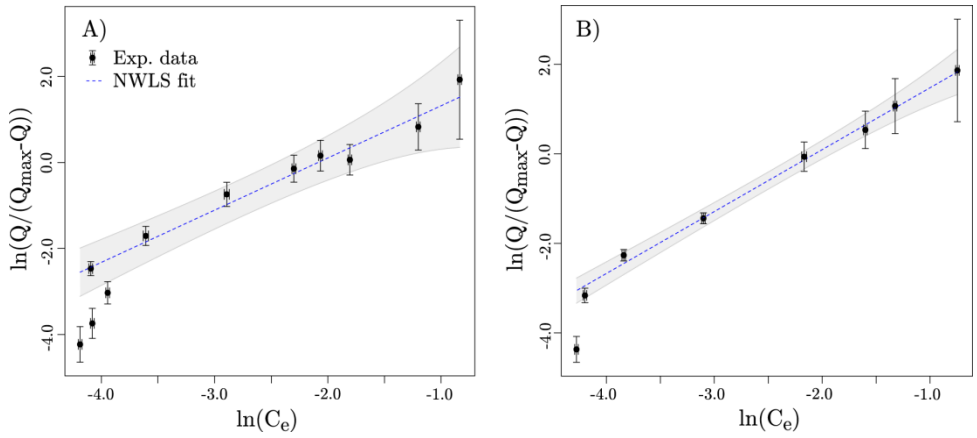

Figure S2. Plots of the experimental values obtained during DOXO adsorption isotherms on Ap (A) and cAp (B) and the corresponding linearized Langmuir-Freundlich fitting curve (dotted blue line) with its confidence intervals of (shaded areas).

Table S1. R values obtained from NWLS curve fitting of experimental data to Langmuir-Freundlich equation.

Parameter	Ap	cAp
R^2	0.9627	0.9970
R_{lin}^2	0.8827	0.9489

S2. Kinetics of the adsorption: Lagergren behaviour

The adsorption of an adsorbate from an aqueous solution can be modelled through Lagergren's equation,[4] consisting in a pseudo-first order rate equation

$$\frac{dQ(t)}{dt} = \frac{1}{\tau}\left(Q_{max} - Q(t)\right) \qquad \text{(S2)}$$

with Q the amount of DOXO on the nanoapatite surface and τ the time required to reach approximately a 63% of Q_{max}. By integrating equation (S2) from $t = 0$ to $t = t$ and imposing the initial condition $Q(0) = 0$, one readily gets

$$Q(t) = Q_{max}\left(1 - e^{-t/\tau}\right) \qquad \text{(S3)}$$

or equivalently

$$\frac{Q_{max} - Q(t)}{Q_{max}} = e^{-t/\tau} \qquad \text{(S4)}$$

The latter equation was employed to compute the associated R_{lin}^2 =0.8953 in order to coefficient.

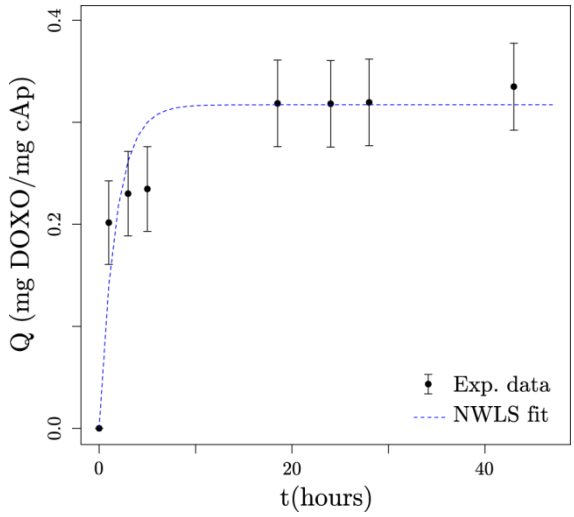

Figure S3. Adsorption kinetics of DOXO on cAp nanocrystals.

The time evolution of the adsorbed amount of DOXO on cAp at 37 °C is depicted in Figure S3). The maximum adsorbed amount resulting from fitting calculations is Q_{max}= 0.32 ± 0.02 mg DOXO mg cAp^{-1} and the characteristic time is τ = (1.7 ± 0.3) hours. Therefore, the time required to reach the 99.32% of the Q_{max} is 5τ = (9 ± 1) hours. Thus, we can consider that after that time Q is almost constant (the system reached the equilibrium).

S3. Assignments of Raman peaks to vibrational modes of DOXO

The interpretation of the Raman spectrum of DOXO in aqueous solutions was based on the comparison of the experimental frequencies with the harmonic frequencies calculated by density functional theory (DFT). Theoretical harmonic vibrational frequencies of DOXO were obtained from Density Functional Theory (DFT) calculations using the B3LYP functional as implemented in the Gaussian 03 code. [5] This functional is a combination of Becke's three-parameter hybrid exchange functional[6] and the Lee-Yang-Parr correlation functional (LYP).[7] The choice of this functional has been motivated by its remarkably good performance for obtaining vibrational frequencies at a computational cost significantly lower than those for MP2 or other post-Hartree-Fock (HF) methods. The C, N, O and H atoms were described at the 6-311G level.[8, 9] The harmonic frequencies were calculated for the molecule in aqueous solutions within the polarizable continuum solvation model (SCRF-PCM)[10, 11] and for adsorbed DOXO on a cluster with the (10-10) orientation of the hexagonal hydroxyapatite but considering only Ca atoms to reduce the computational time. Ca atoms were described with the LANL2DZ effective core potential. All frequency values are given without applying any scaling factor. The assignments of the observed bands to the main vibrational modes of DOXO based on DFT simulations are summarized in Table S2. The peaks with a shift higher than the spectral resolution (3 cm^{-1}), comparing DOXO in solution and adsorbed, have been underlined.

Table S2. Raman shift of DOXO in solution and adsorbed onto cAp surface. The assignments of the experimental frequencies to the vibrational modes were done on the basis of the harmonic frequencies calculated at the B3LYP/6-311G level within the SCRF-PCM solvation model. The peaks with a shift higher than the spectral resolution (3 cm^{-1}), comparing DOXO in solution and adsorbed, have been underlined.

B3LYP/6-311G [cm^{-1}]	DOXO in solution [cm^{-1}]	Adsorbed DOXO [cm^{-1}]	Assignment [a] [b]
347.0	<u>351</u>	<u>347</u>	r $N\text{-}H_3^+$
455.9	443	443	ωRingA,B,C $\omega C^{32}\text{-}H_2$
457.8	465	465	ωRingA,B,C,D $\omega C^{32}\text{-}H_2$
512.2	505	505	ωC^{16}-OH ωC [18] $\omega C^{20}{=}H_2$
1063.1	1081	1084	$\delta_{as}C^{39}\text{-}H_3\delta N\text{-}H_3^+\delta C^1C^3\text{-}H$
1212.5	<u>1208</u>	<u>1212</u>	δC^3-H δC [22]-$H_2\delta OH(C^{10})$
1249.4	<u>1251</u>	<u>1242</u>	$\delta C^{32}\text{-}H_2\delta$ $C^1C^{33}C^{35}$-H $\nu C^{10}C^{24}$-OH
1295.9	1297	1295	$\delta OH(C^{10}C^{24})$ νRings
1394.9	1412	1412	νC^6C^{29} $\nu C^9C^{26}\delta OH(C^{10}C^{24})$ $\delta C^{22}\text{-}H_2$
1435.6	1440	1440	$\delta_s C^{30}\text{-}H_3\delta C^1C^2\text{-}H_2$ νC^6C^{29}
1569.5	<u>1574</u>	<u>1579</u>	$\nu Rings\delta OH(C^{10}C^{24})$ δC^1C^3H
1608.2	<u>1634</u>	<u>1640</u>	$\nu C^7{=}0$

[a] r, $\delta_{(s\text{-}as)}$, ν, ω belong to the rocking, bending (symmetric and asymmetric), stretching and wagging vibrations, respectively. [b] C_xH_y represents carbon in position "x" bounded to a number "y" (y =1 2 3) of hydrogens

S4. Estimation of the area occupied by adsorbed DOXO with different orientations

The maximum number of adsorbed dimers can be roughly estimated by calculating the surface area occupied by one dimer adsorbed with a certain orientation. The dimer was considered as a rectangular prism with the following dimensions 18.2x14.5x2.5 $Å^3$ (Figure S4), values extracted from Agrawal et. al.[12]). An area of 18.2x14.5 $Å^2$ was occupied for a *parallel* adsorption, with the cromophore ring parallel to the surface. On the other hand, the occupied area was 18.2x2.5 $Å^2$ for a *perpendicular* adsorption, with the cromophore ring perpendicular to the surface. The number of dimers for each orientation (D_1) is obtained from the ratio between the SSA of the nanoparticles and the area occupied by one dimer for each orientation. This value can be compared with the number of dimers (D_2) adsorbed at equilibrium, Q_{max}, obtained experimentally from the adsorption isotherms. The results are summarized in Table S4. The variation (in percentage) depicted in table S4 was calculated as $(D_1-D_2)/D_2$. The value obtained for the perpendicular orientation is comparable to D_2 whereas the value obtained for the parallel is much lower.

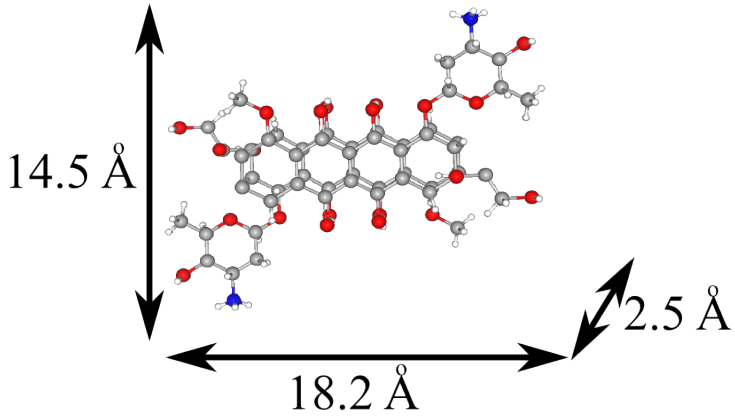

Figure S4. Dimensions of the DOXO dimer.

Table S4. Calculated molecules for the DOXO dimer and estimated variation from the theoretical number of binding sites on cAp nanoparticles

Orientation	D_1 (dimers g^{-1})	% variation*
Perpendicular	2.1 x 10^{20}	16.04
Parallel	3.5 x 10^{19}	85.48

*The number of dimers per gram of cAp calculated from Q_{max} was D_2=2.4x10^{20}.

S5. Kinetics of the desorption

Most of desorption processes (e.g. drug release from a nano-carrier) can be understood as thermally activated escape processes where the energy barrier depends on thermodynamic parameters such as pH, temperature, etc. Under this assumption, the percentage of drug released, $D_R(t)$, with respect to the initial concentration loaded on the surface of a slab-like nanoparticle, Q_0, should increase following the exact analytical solution of Fick's equation[13]

$$D_R(t) = 1 - \frac{8}{\pi^2}\sum_{n=0}^{\infty}\frac{exp\left[-D\pi^2(2n+1)^2 t/L^2\right]}{(2n+1)^2} \qquad \text{(S5)}$$

since the matrix is slab-like shaped and the drug can be considered homogeneously distributed along the surface of the nanoparticle. In order to avoid the use of infinite series, Equation S5 can be approximated as[13, 14]

$$D_R(t) \simeq 4\left(\frac{Dt}{\pi L^2}\right)^{\frac{1}{2}} \qquad \text{short times} \qquad \text{(S6)}$$

$$D_R(t) \simeq 1 - \frac{8}{\pi^2} exp\left(\frac{-\pi^2 Dt}{L^2}\right) \qquad \text{long times} \qquad \text{(S7)}$$

The non-linearity of the plot of D_R(t) as a function of $t^{1/2}$ (insets in Fig 4A and B for Ap and cAp, respectively) demonstrates that our experimental data does not follow a fickian behaviour. The non-fickian response of drug release is a well-known problem commonly termed as subdiffusive-limited regime, usually associated with complex systems. This regime has been experimentally detected in several environments, such as porous media, glasses, transport through cell membranes and other biological systems.[15-17] Korsmeyer et al. proposed a semi-empirical potential law which includes both fickian and non-fickian behaviors [18-20],

$$D_R(t) \simeq \mathcal{K} t^{\gamma} \gamma \leq 1 \qquad \text{(S8)}$$

where $\mathcal{K}$ is the effective diffusion constant and γ is the diffusional exponent. In nearly fickian diffusive systems defects on the geometry of the substrate could yield values of γ lower than 1/2, but this effect should not be dominant and, hence, this deviation should be negligible leading to γ = 1/2. Ritger observed that γ might also be influenced by size distributions.[21, 22] Hence, the non-fickian behaviour could be due to the broad size distribution shown by the nanoapatites. Additionally, values of γ lower than 1/2 might also be explained considering the drug transport as a subdiffusion-limited reaction governed by Fick's law with memory effects[15-17] and hence, by the semi-empirical Korsmeyer's potential-law (equation SP8).

Table S3 summarizes the parameters extracted from the NWLS fitting to the Korsmeyer's potential-law of the experimental data obtained for the release of DOXO from Ap and cAp at pHs 7.4 and 5.0.

Table S3. Values of the release profiles obtained from NWLS curve fitting of experimental data Korsmeyer's power-law.

Parameter	Ap		cAp	
	pH5.0	pH 7.4	pH5.0	pH 7.4
$\mathcal{K}$	15.87 ± 1.09	16.46 ± 0.76	11.81 ± 0.79	7.58 ± 0.09
γ	0.11 ± 0.02	0.01 ± 0.01 [a]	0.13 ± 0.02	0.05 ± 0.01
R_{lin}^2	0.925	0.1023 [a]	0.914	0.984

[a] The evolution to the steady state occurred very fast and therefore there is not enough information about the relaxation process being almost impossible to obtain valuable kinetic data.

It is not expected the dissolution of both types of nanoparticles in solution at pH 7.4. Thus, the drug release takes place by the previously explained sub-diffusive regime from the apatitic

surface to the solution, and controlled by the equilibrium concentration. However, at acidic pH the nanoparticles could be slightly dissolved and consequently modify the drug release mechanism. Nonetheless, the release from both types of nanoassemblies at acidic pH fits well to the sub-diffusive regime described by the pseudo empirical Korsmeyer's potential law. This finding suggests the dissolution of nanoparticles is almost negligible for both types of nanoparticles and at both pH values.

References

1. Mekid, S.; Vaja, D., Propagation of uncertainty: Expressions of second and third order uncertainty with third and fourth moments. *Measurement* **2008,** 41, (6), 600-609.

2. Fornasini, P., Uncertainty in Indirect Measurements. The Uncertainty in Physical Measurements. In Springer New York: 2009; pp 149-162.

3. Development Core Team, R: A language and environment for statistical computing. R Foundation for Statistical Computing, Vienna, Austria. ISBN 3-900051-07-0. In 2005.

4. Lagergren, S., About the theory of so-called adsorption of soluble substances. *Kungliga Svenska Vetenskapsakademiens* **1898,** 24, (4), 1-39.

5. Frisch, M. J.; Trucks, G. W.; Schlegel, H. B.; Scuseria, G. E.; Robb, M. A.; Cheeseman, J. R.; Montgomery, J. A. J.; Vreven, T.; Kudin, K. N.; Burant, J. C.; Millam, J. M.; Iyengar, S. S.; Tomasi, J.; Barone, V.; Mennucci, B.; Cossi, M.; Scalmani, G.; Rega, N.; Petersson, G. A.; Nakatsuji, H.; Hada, M.; Ehara, M.; Toyota, K.; Fukuda, R.; Hasegawa, J.; Ishida, M.; Nakajima, T.; Honda, Y.; Kitao, O.; Nakai, H.; Klene, M.; Li, X.; Knox, J. E.; Hratchian, H. P.; Cross, J. B.; Bakken, V.; Adamo, C.; Jaramillo, J.; Gomperts, R.; Stratmann, R. E.; Yazyev, O.; Austin, A. J.; Cammi, R.; Pomelli, C.; Ochterski, J. W.; Ayala, P. Y.; Morokuma, K.; Voth, G. A.; Salvador, P.; Dannenberg, J. J.; Zakrzewski, V. G.; Dapprich, S.; Daniels, A. D.; Strain, M. C.; Farkas, O.; Malick, D. K.; Rabuck, A. D.; Raghavachari, K.; Foresman, J. B.; Ortiz, J. V.; Cui, Q.; Baboul, A. G.; Clifford, S.; Cioslowski, J.; Stefanov, B. B.; Liu, G.; Liashenko, A.; Piskorz, P.; Komaromi, I.; Martin, R. L.; Fox, D. J.; Keith, T.; Al-Laham, M. A.; Peng, C. Y.; Nanayakkara, A.; Challacombe, M.; Gill, P. M. W.; Johnson, B.; Chen, W.; Wong, M. W.; Gonzalez, C.; Pople, J. A. *Gaussian 03*, revision B.01; Pittsburgh, PA: Gaussian, Inc., 2003.

6. Becke, A. D., Density-functional thermochemistry. III. The role of exact exchange. *J. Chem. Phys.* **1993,** 98, (7), 5648-5652.

7. Lee, C.; Yang, W.; Parr, R. G., Development of the Colle-Salvetti correlation-energy formula into a functional of the electron density. *Phys. Rev. B* **1988,** 37, (2), 785-789.

8. Krishnan, R.; Binkley, J. S.; Seeger, R.; Pople, J. A., Self-consistent molecular orbital methods. XX. A basis set for correlated wave functions. *J. Chem. Phys.* **1980,** 72, (1), 650-654.

9. Clark, T.; Chandrasekhar, J.; Spitznagel, G. W.; Schleyer, P. V. R., Efficient diffuse function-augmented basis sets for anion calculations. III. The 3-21+G basis set for first-row elements, Li–F. *J. Comput. Chem.* **1983,** 4, (3), 294-301.

10. Barone, V.; Cossi, M.; Tomasi, J., A new definition of cavities for the computation of solvation free energies by the polarizable continuum model. *J. Chem. Phys.* **1997,** 107, (8), 3210-3221.

11. Cossi, M.; Scalmani, G.; Rega, N.; Barone, V., New developments in the polarizable continuum model for quantum mechanical and classical calculations on molecules in solution. *J. Chem. Phys.* **2002,** 117, (1), 43-54.

12. Agrawal, P.; Barthwal, S. K.; Barthwal, R., Studies on self-aggregation of anthracycline drugs by restrained molecular dynamics approach using nuclear magnetic resonance spectroscopy supported by absorption, fluorescence, diffusion ordered spectroscopy and mass spectrometry. *Eur. J. Med. Chem.* **2009,** 44, (4), 1437-51.

13. Siepmann, J.; Siepmann, F., Modeling of diffusion controlled drug delivery. *J. Control. Release* **2012,** 161, (2), 351-62.

14. Fu, Y.; Kao, W. J., Drug release kinetics and transport mechanisms of non-degradable and degradable polymeric delivery systems. *Expert Opin. Drug Deliv.* **2010,** 7, (4), 429-444.

15. Hernández, D.; Varea, C.; Barrio, R. A., Dynamics of reaction-diffusion systems in a subdiffusive regime. *Physical Review E* **2009,** 79, (2), 026109.

16. Ferreira, J. A.; Oliveira, P., Looking for the Lost Memory in Diffusion-Reaction Equations. Advances in Mathematical Fluid Mechanics. In Rannacher, R.; Sequeira, A., Eds. Springer Berlin Heidelberg: 2010; pp 229-251.

17. Yuste, S. B.; Lindenberg, K.; Ruiz-Lorenzo, J. J., Subdiffusion-Limited Reactions. In *Anomalous Transport*, Wiley-VCH Verlag GmbH & Co. KGaA: 2008; pp 367-395.

18. Korsmeyer, R. W.; Lustig, S. R.; Peppas, N. A., Solute and penetrant diffusion in swellable polymers. I. Mathematical modeling. *J. Polym. Sci., Part B: Polym. Phys.* **1986,** 24, (2), 395-408.

19. Korsmeyer, R. W.; Von Meerwall, E.; Peppas, N. A., Solute and penetrant diffusion in swellable polymers. II. Verification of theoretical models. *J. Polym. Sci., Part B: Polym. Phys.* **1986,** 24, (2), 409-434.

20. Arifin, D. Y.; Lee, L. Y.; Wang, C.-H., Mathematical modeling and simulation of drug release from microspheres: Implications to drug delivery systems. *Adv. Drug Delivery Rev.* **2006,** 58, (12–13), 1274-1325.

21. Ritger, P. L.; Peppas, N. A., A simple equation for description of solute release I. Fickian and non-fickian release from non-swellable devices in the form of slabs, spheres, cylinders or discs. *J. Control. Release* **1987,** 5, (1), 23-36.

22. Ritger, P. L.; Peppas, N. A., A simple equation for description of solute release II. Fickian and anomalous release from swellable devices. *J. Control. Release* **1987,** 5, (1), 37-42.

Appendix II

List of publications

Appendix II

List of publications

1. M. Iafisco, J. M. Delgado-López, J. Gómez-Morales, M. A. Hernández-Hernández, I. Rodríguez-Ruiz, N. Roveri (2011): "*Formation of calcium phosphates by vapour diffusion in highly concentrated ionic micro-droplets*", Crystal Research Technology Vol. 46(8), pages 841 – 846

2. J. M. Delgado-Lopez, M. Iafisco, I. Rodríguez-Ruiz, A. Tampieri, M. Prat, J. Gomez-Morales (2012): "*Crystallization of bioinspired citrate-functionalized nanoapatite with tailored carbonate content*", Acta biomaterialia Vol. 8(9), pages 3491-3499.

3. I. Rodríguez-Ruiz, J. M. Delgado-Lopez, M. A. Durán-Olivencia, M. Iafisco, A. Tampieri, D. Colangelo, M. Prat, J. Gomez-Morales (2013): "*pH-Responsive Delivery of Doxorubicin from Citrate-Apatite Nanocrystals with Tailored Carbonate Content*" Langmuir. Vol. 29, pages 8213−8221.

4. I. Rodríguez-Ruiz, Z. Hammadi, R. Grossier, J. Gómez-Morales, J. M. García-Ruiz, S. Veesler. "*Monitoring picoliter sessile microdroplet dynamics shows that size doesn't matter*". Accepted in Langmuir.

5. I. Rodríguez-Ruiz, St. Veesler, J. Gómez-Morales, J. M. Delgado-López, O. Grauby, Z. Hammadi, N. Candoni, J. M. García-Ruiz. "*Transient calcium carbonate hexahydrate (ikaite) temporarily stabilized in confined nano- and picovolumes*". Submitted to Journal of the American Chemical Society.

6. I. Rodríguez-Ruiz, A. Llobera, J. Vila-Planas, D. Johnson, J. Gómez-Morales, J. M. García-Ruiz. "*Analysis of the structural integrity of SU-8 based optofluidic systems for small molecule crystallization studies*". Accepted in Analytical Chemistry.